CRANFIELD UNIVERSITY

GABRIELE DESSENA

IDENTIFICATION OF FLEXIBLE STRUCTURES DYNAMICS

SCHOOL OF AEROSPACE, TRANSPORT AND MANUFACTURING
Aerospace

Doctor of Philosophy
Academic Year: 2019–2023

Supervisors: Dr D. I. Ignatyev, Prof J. F. Whidborne, and Dr L. Zanotti Fragonara
6th April 2023

CRANFIELD UNIVERSITY

SCHOOL OF AEROSPACE, TRANSPORT AND MANUFACTURING

Aerospace

Doctor of Philosophy

Academic Year: 2019–2023

GABRIELE DESSENA

Identification of Flexible Structures Dynamics

Supervisors: Dr D. I. Ignatyev, Prof J. F. Whidborne, and Dr L. Zanotti Fragonara

6th April 2023

This thesis is submitted in partial fulfilment of the requirements for the degree of Doctor of Philosophy.

Abstract

The pursuit of aerodynamic efficiency and the advances in materials technology, particularly in composite material, has contributed to shifting the paradigm of wing design to high aspect ratio wings. Increasing the span, for decreasing drag, and using composite lightweight materials make the new wing very flexible and prone to nonlinear dynamic behaviour. With nonlinearities, increasing challenges arise for the identification and modelling of the wing. These challenges cannot be overlooked for flexible structures as these models are critical for the prediction of aeroelastic phenomena. Hence, it is fundamental to expand the knowledge of the behaviour of these structures through the identification and modelling of sample flexible wing models. In this work, a series of methods and approaches are proposed and employed for the identification and modelling of a flexible wing. First, a system identification technique in the frequency domain, the Loewner Framework, is applied for modal parameters extraction in mechanical systems for structural health monitoring. This new technique, with a linear reduced order model, is used to characterise the flutter behaviour of a flexible wing. The results are compared to similar techniques. A thorough experimental campaign is run on a flexible wing model to characterise its nonlinear behaviour and the underlying linear system. In particular, nonlinearities are detected, identified and quantified. Then, a meta-model technique based on Kriging, the refined Efficient Global Optimisation, is proposed for finite element model updating. First, the technique is used for damage detection in benchmark structures, then, it is employed for the validation of component-based strategies for model updating of a flexible wing.

Keywords

Finite Element Analysis; Structural Dynamics; Nonlinear Dynamics; Modal Analysis; Structural Health Monitoring; System Identification; Aeronautical Structures; Flexible Wings; High Aspect Ratio Wings

Contents

List of Figures

List of Tables

Acknowledgements

First, I'm extremely grateful to Dr Luca Zanotti Fragonara and Dr Mudassir Lone for giving me the opportunity to pursue doctoral research at Cranfield University with a founded studentship from the Engineering and Physical Sciences Research Council (EPSRC grant number 2277626). I would like to express my sincere appreciation to my current supervisors, Dr Dmitry Ignatyev and Prof James Whidborne, for stepping up to the role when most needed and for their continuous guidance and support during this research.

I would like to express my deepest appreciation to Dr Alessandro Pontillo, now at the University of Bristol, and Dr Marco Civera, at the Politecnico di Torino, for their mentorship, guidance and fruitful collaborations during this research. I am also thankful to Dr Ivan Petrunin for his helpfulness in providing the facilities and part of the equipment used for the experimental tests within this research.

I would be remiss in not mentioning Prof Colin Pilbeam and Dr Argyrios Zolotas, chair and reviewer of the progress review team, for their feedback and support.

I would like to thank everyone within the Autonomous Systems Dynamics & Control Research Group and the Dynamics Simulation and Control Group for their support and encouragement during my PhD. I also would like to thank all the friends I spent time with during these three years at Cranfield University for their support and for sharing valuable experiences and memories.

I am grateful for the support and encouragement received from my friends and family back home during these three years. In particular, I would like to

acknowledge the immense support I have received from my parents during these seven years spent in the UK for my studies. This endeavour would not have been possible without them.

Foreword

Cranfield University offers the possibility to choose between two doctoral thesis formats: the, classic, monograph and the collection of papers (or paper-format). In this thesis, the latter approach is followed.

In accordance with Cranfield University *Senate Handbook: Research Students' Handbook*[1], the thesis is organised as follows:

1. Introduction:
    - Here the context and a short background on the work area is given, followed by the project's aims and objectives, a list of published, submitted, or completed works and how they link together;
2. Papers:
    - A series, usually three to five, of chapters, which are self-contained (e.g. a global literature review is not required);
3. Conclusions and Suggestions for Future Work:
    - As usual, pointing out the findings and weighing them against the problem, presented in the Introduction, and previous works.

[1] Senate Handbook: Research Students' Handbook: https://www.cranfield.ac.uk/-/media/files/corporate_documents/research-students-handbook.ashx [Accessed on 15/09/2022]

Chapter 1

Introduction

The development of significant technological advancements within the aerospace industry has led to a new concept in wing design: high aspect ratio flexible wings. The likes of Airbus A350 and Boeing 787 Dreamliner are the proof of these improvements as they feature more flexible and slenderer wings than legacy aircraft within the same class, having much more lightweight structures, thanks to the extensive use of composite materials [1]. Despite full-scale aircraft historically being seen as linear structures, these later changes introduce new challenges from nonlinear flight dynamics and aeroelastic perspectives [2].

Within this context lies a framework developed within Cranfield University, known as Beam Reduction and Dynamic Scaling [3–7] for the creation of a tool suitable for the early stages of design. In this setting, having an accurate flight physics model is of paramount importance. Numerous computationally expensive modelling tools exist today, but there is a lack of "fast" numerical tools that can be used in the conceptual design stages.

Typically, a nonlinear finite element model with hundreds of degrees-of-freedoms is used, but when dealing with transient responses several iterations are necessary to guarantee convergence and hence these are unsuitable for real-time health monitoring, digital twin or pilot-in-the-loop simulations.

In order to establish these tools a thorough knowledge of the structural behaviour of flexible wings needs to be acquired, particularly concerning the nonlinear regime [8]. This work thoroughly examines a flexible wing model, both experimentally and numerically. To facilitate these tasks, new experimental, for modal parameters extraction, and numerical, a surrogate-based optimisation routine, techniques are developed to study and characterise the flexible wing and assess the health state of other structures.

1.1 Aims and Objectives

The main scientific aim of this thesis is to develop computationally efficient techniques for the identification and modelling of the structural behaviour of a flexible wing.

Considering the overall aim of this work, three sub-aims and related objectives, complementary to each other, can be defined:

A1. Development of a computationally efficient technique for system identification (SI) in structural dynamics:

- **O1a.** Development of a numerical algorithm for SI based on the Lowener Framework (LF);
- **O1b.** Assessing LF's capability, in terms of precision, reliability, and robustness to noise, for the Structural Health Monitoring (SHM) of mechanical systems against established techniques;
- **O1c.** Validating, in terms of precision and robustness, the LF to existing methods for the prediction of aeroelastic phenomena onset speed for the flexible wing.

A2. Generation of an experimental data set of the flexible wing model via vibration testing for experimental validation:

O2a. Conducting experimental vibration test on the flexible wing and handling experimental data;

O2b. Carrying out Experimental Modal Analysis (EMA) of the flexible wing at different input amplitude for the preliminary assessment of nonlinear behaviour;

O2c. Identifying and characterising the nonlinear behaviour of the flexible wing model with Nonlinear Modal Analysis (NLMA) to describe the origin of the nonlinearity.

A3. Development a computationally efficient technique for the model updating of flexible wings:

O3a. Implementing a new global-local surrogate-based optimisation algorithm and validating it against existing methods;

O3b. Introducing a computationally efficient FEM updating (FEMU) technique and assessing its precision and reliability for damage detection against existing methods;

O3c. Validating the technique for the FEMU of the flexible wing model using experimental data from A2.

Please note, the acronyms used for identifying the aims (A) and objectives (O) are used in the following section to introduce the relevant research outputs.

1.2 Contribution to Knowledge

The main and secondary contributions of this thesis are identified according to the aims and objectives structure in Section 1.1. In particular, a main contribution per sub-aim and a secondary contribution per objective are identified. They can be summarised as follows:

A1. Development of a computationally efficient technique for SI in structural dynamics:

SI is the founding block of system characterisation from experimental campaigns as it allows to build of useful models from experimental data. In this work, SI is an important tool in extracting modal parameters from relevant data. Hence, prior to moving to the experimental work itself, it is should be considered by itself before diving into experimental work. In particular, this involves considering existing SI techniques and implementing new ones:

O1a A MATLAB algorithm for SI via the LF is developed;

O1b The LF's precision, reliability, and robustness to noise is assessed for the SHM of numerical and experimental mechanical systems;

O1c The LF is validated to existing SI techniques for aeroelastic phenomena onset speed prediction the flexible wing model.

A2. Generation of an experimental data set of the flexible wing model via vibration testing for experimental validation:

EMA and NLMA are the constituent blocks of the testing campaigns that involve the wing model. Their main scope is to extract useful information, such as modal parameters or nonlinear characteristics, from vibration testing. The term Ground Vibration Testing (GVT) is used interchangeably with EMA during this thesis:

O2a The GVT, for linear vibration testing, and decay from resonance techniques, for nonlinear vibration testing, are employed to carry out the vibration testing on the wing;

O2b The modal parameters of the flexible wing are extracted from test data at different input amplitudes and experimental conditions;

O2c A nonlinear model of the flexible wing is identified using the Nonlinear Normal Modes (NNMs) theory. This includes backbone curve extraction, time-frequency analysis and analytical modelling.

A3. Development a computationally efficient technique for the model updating of flexible wings:

After having acquired experimental data and obtained valuable metrics through SI techniques a suitable model of the structure under scrutiny can be built. This objective deals with building an accurate finite element model (FEM) of the flexible wing model:

O3a The refined Efficient Global Optimisation (rEGO) is implemented as an optimisation technique in MATLAB and validated against evolutionary techniques;

O3b The rEGO is introduced for the SHM of numerical and experimental systems;

O3c The rEGO is validated for the FEMU of the flexible wing with different component-based approaches.

1.3 Thesis Structure

As mentioned in the foreword, this thesis is in the paper-format. This means that rather than having a monograph structure, chapters take the form of self-contained journal papers. Hence, a literature review chapter is not part of this thesis, rather each chapter has a self-contained literature review. In order to reflect the self-contained nature of the paper-format thesis references are provided in order of appearance per chapter, but a global bibliography is available at the end of the thesis with all cited works in alphabetical order with respect to authors' last names.

The chapter structure follows the same direction of Section 1.2, two papers are included for each sub-aim and their order is the following:

A1. Development of a computationally efficient technique for SI in structural dynamics:

Chapter 2. A Loewner-based System Identification and Structural Health Monitoring Approach for Mechanical Systems;

Chapter 4. Comparative study on novel modal parameters extraction methods for aeronautical structures;

A2. Generation of an experimental data set of the flexible wing model via vibration testing for experimental validation:

Chapter 3. Ground Vibration Testing of a Flexible Wing: A Benchmark and Case Study;

Chapter 5. Identification of Nonlinearity Sources in a Flexible Wing: a Case Study;

A3. Development a computationally efficient technique for the model updating of flexible wings:

Chapter 6. A Global-local Meta-modelling Technique for Model Updating;

Chapter 7. An Iterative Approach for the Model Updating of Flexible Wings.

In the following paragraphs, the abstracts for the aforementioned papers are listed.

Chapter 2. Data-driven SHM requires precise estimates of the target system behaviour. In this sense, SHM by means of modal parameters is strictly linked to SI. However, existing frequency domain SI techniques have several theoretical and practical drawbacks. This chapter proposes using an input-output SI technique based on rational interpolation, known as the LF, to estimate the modal properties of mechanical systems. Pioneeringly, the LF mode shapes and natural

frequencies estimated by LF are then applied as damage-sensitive features for damage detection. To assess its capability, the LF is validated on both numerical and experimental datasets and compared to established system identification techniques. Promising results are achieved in terms of accuracy and reliability.

Chapter 3. Beam-like flexible structures are of interest in many fields of engineering, particularly aeronautics, where wings are frequently modelled and represented as such. Experimental modal analysis is commonly used to characterise the wing's dynamical response. However, unlike other flexible structure applications, no benchmark problems involving high-aspect-ratio flexible wings have appeared in the open literature. To address it, this chapter reports on ground vibration testing results for a flexible wing and its sub-assembly and parts. The experimental data can be used as a benchmark and are available to the aeronautical and structural dynamics community. Furthermore, non-linearities in the structure, where present, were detected. Tests were performed on the whole wing as well as parts and sub-assembly, providing four specimens. These were excited with random vibration at three different amplitudes from a shaker table. The modal properties of a very flexible high-aspect-ratio wing model, its sub-assembly and parts, were extracted, non-linear behaviour was detected and the experimental data are shared in an open repository.

Chapter 4. Experimental modal analysis in general, and ground vibration testing in particular for Aerospace applications, are a vital part of the design and certification process for civil and military aircraft. Two recently developed system identification techniques in the frequency domain, Fast Relaxed Vector Fitting and Loewner Framework, have been successfully applied to civil and mechanical systems for the extraction of modal parameters. In this work, both are used for the extraction of the modal parameters in aeronautically relevant structures for damage detection and aeroelastic modelling; respectively, a numerical model of a small fixed-wing unmanned aerial system spar and an experimental case

study of a high aspect ratio flexible wing. The signals from different damage and loading scenarios for the numerical system are corrupted with different levels of noise to assess the sensitivity, to changes in the structure, and the robustness to noise of the modal parameters obtained from the methods. Results are benchmarked against the known exact values. Then, the modal parameters identified from the experimental data are used to build a reduced-order model to characterise aeroelastic phenomena onset speeds. The modal parameters identified by the techniques are compared to those derived from a well-established method: Numerical algorithms for subspace state space system identification (N4SID). In addition, the experimental data from the ground vibration testing of the high aspect ratio wing is made available in an open repository.

Chapter 5. Nonlinearities exist, to different extents, in all real systems. In aeronautics, flexible high aspect ratio wings have become the new state-of-the-art in wing design, pushed by the pursuit for greater aerodynamic efficiency, by decreasing drag, and lighter aircraft, thanks to the use of composite materials. Nevertheless, accounting for nonlinearities in the design and testing phase of an aeronautical product development is still a challenge. In this work, a flexible wing that showed unusual, softening, behaviour during two previous ground vibration testing campaigns is considered. In order to determine the nature of the nonlinearity, the wing backbone curve is extracted from the free-decay from resonance data, along with the time-frequency spectrogram and the Hilbert spectrum. The softening behaviour is confirmed and further testing and visual inspections on the sub-assemblies and components are carried out to pinpoint the main sources of nonlinearity.

Chapter 6. The finite element model updating procedure of large or complex structures is a challenge for engineering practitioners and researchers. Iterative methods, such as genetic algorithms and response surface models, have a high computational burden for these problems. In this work, an enhanced ver-

sion of the well-known Efficient Global Optimisation technique is introduced to address this issue. The enhanced method, refined Efficient Global Optimisation or rEGO, exploits a two-step refinement and selection technique to expand the global search capability of the original method to a global-local, or hybrid, search capability. rEGO is tested and validated on four optimisation test functions against the original methods and genetic algorithms with different settings. Good results in terms of precision and computational performance are achieved, so an application to model updating is sought. A penalty function for the finite element model updating is identified in residuals of the modified total modal assurance criterion, which uses the modal parameters from an existing structure and compares them to those of the model. The choice process is carried out using a numerical system and comparing five suitable penalty functions as candidates. Finally, rEGO for finite element model updating is implemented on a hybrid, numerical and experimental, case study based on a well-known experimental dataset. A finite element model of the structure is built and then tuned to the experimental data, then a numerical study, based on the numerical model, is carried out for damage detection and lastly the same task is done for experimental data. Satisfactory results in terms of precision and computational performance are achieved when compared to the original methods and genetic algorithms.

Chapter 7. Finite element models hardly ever represent out of the box the real behaviour of the structure they are meant to characterise. In aeronautics, this mismatch is not acceptable as finite element models are a fundamental part of the development of an aircraft. Even more now, with the advent of flexible wings as the new state-of-the-art, the need for precise modelling to avoid unexpected behaviour is high. Finite element model updating can be expensive for complex structures and surrogate models can be employed for reducing the computational burden. In this work, a recently introduce surrogate-based technique, the refined Efficient Global Optimisation, is used for the model updating of a flexible wing

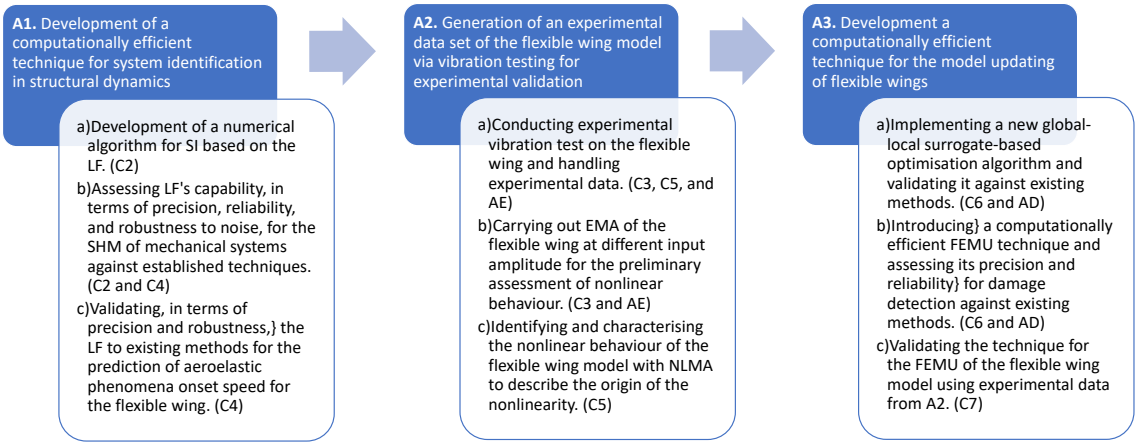

Figure 1.1: Objectives and thesis structure. C# and A#, respectively, define the Chapter number and Appendix letter.

following two component-based approaches to validate their merits. Good results are achieved in terms of model errors and computational efficiency.

Apart from full articles, also two other research outputs are made within this doctoral research in the form of Conference Proceedings. The first work is a preliminary version of the work in Chapter 2 dealing with rEGO, while the second is related to some additional testing carried out on the wing. The former is related to A3 and it can be found in Appendix D, while the latter is to A2 and it is found in Appendix E.

Even if the thesis is a collection of self-contained works, these works are strongly linked. First, the three main objectives are strictly complementary. In fact, first SI is considered (A1), before applying the techniques to experimental data (A2) and finally, using the data from A2, to build a reliable model (A3). Figure 1.1 condenses the relation between all of the chapters and the thesis structure.

The remaining of this Chapter recaps on the research output linked to this thesis, then Chapters 2 to 7 will include the above-mentioned works. Finally, this research is closed by the conclusions and some final remarks on future works in Chapter 8.

1.4 List of Research Outputs

There are two types of research outputs within this thesis: journal articles and conference proceedings. The following journal articles have been completed, submitted or published:

Dessena, G., Civera, M., Zanotti Fragonara, L., Ignatyev, D.I., Whidborne, J.F. (2023). A Loewner-based system identification and structural health monitoring approach for mechanical systems, *[Accepted] Structural Control and Health Monitoring* - (Chapter 2)

Dessena, G., Ignatyev, D.I., Whidborne, J.F., Pontillo, A., Zanotti Fragonara, L. (2022). Ground vibration testing of a flexible wing: A benchmark and case study. Aerospace, 9(8), 438. DOI: 10.3390/aerospace9080438 - (Chapter 3)

Dessena, G., Civera, M., Ignatyev, D.I., Whidborne, J.F., Zanotti Fragonara, L. (2023). Comparative study on novel modal parameters extraction methods for aeronautical structures, *in preparation* [aimed at *Aerospace Science and Technology*] - (Chapter 4)

Dessena, G., Pontillo A., Ignatyev, D.I., Whidborne, J.F., Zanotti Fragonara, L. (2023). Identification of nonlinearity sources in a flexible Wing: a case study, *in preparation* [aimed at *Journal of Aerospace Engineering*] - (Chapter 5)

Dessena, G., Ignatyev, D.I., Whidborne, J.F,, Zanotti Fragonara, L. (2023). A global-local meta-modelling technique for model updating, *[Submitted]* Computer Methods in Applied Mechanics and Engineering - (Chapter 6)

Dessena, G., Pontillo A., Ignatyev, D.I., Whidborne, J.F., Zanotti Fragonara, L. (2023). An iterative approach for the model updating of flexible wings, *in preparation* [aimed at *Chinese Journal of Aeronautics*] - (Chapter 7)

In addition, two Conference Proceedings are added in Appendices D and E:

Dessena, G., Ignatyev, D.I., Whidborne, J.F., Zanotti Fragonara, L. (2023). A Kriging Approach to Model Updating for Damage Detection. In: Rizzo, P., Milazzo,

A. (eds) European Workshop on Structural Health Monitoring. EWSHM 2022. Lecture Notes in Civil Engineering, vol 254. Springer, Cham. DOI: 10.1007/978-3-031-07258-1_26 - (Appendix D)

Dessena, G., Ignatyev, D.I., Whidborne, J.F., Pontillo, A., Zanotti Fragonara, L. (2022). Ground Vibration Testing of a High Aspect Ratio wing with Revolving Clamp. *In:* 33rd Congress of the International Council of the Aeronautical Sciences (ICAS) – Stockholm, 4–9 September 2022. DOI: 10.17862/cranfield.rd.20486229 - (Appendix E)

Authors' contributions information are available, in the CRediT taxonomy[1] format, in Appendix A.

References

[1] M. Civera, L. Zanotti Fragonara, and C. Surace, "Using video processing for the full-field identification of backbone curves in case of large vibrations," *Sensors*, vol. 19, no. 10, p. 2345, 2019, ISSN: 1424-8220, DOI: 10.3390/s19102345 (cit. on p. 1).

[2] S. Malik, S. Ricci, and L. Riccobene, "Aeroelastic analysis of a slender wing," *CEAS Aeronautical Journal*, vol. 11, no. 4, pp. 917–927, 2020, ISSN: 1869-5582, DOI: 10.1007/s13272-020-00459-6 (cit. on p. 1).

[3] A. Pontillo *et al.*, "Flexible high aspect ratio wing: low cost experimental model and computational framework," in *2018 AIAA Atmospheric Flight Mechanics Conference*, Kissimmee, FL: American Institute of Aeronautics and Astronautics, 2018, pp. 1–15, ISBN: 978-1-62410-525-8, DOI: 10.2514/6.2018-1014 (cit. on p. 1).

[1] L. Allen, A. O'Connell, and V. Kiermer, "How can we ensure visibility and diversity in research contributions? How the Contributor Role Taxonomy (CRediT) is helping the shift from authorship to contributorship", Learned Publishing, vol. 32, no. 1. Wiley, pp. 71–74, 2019. DOI: 10.1002/leap.1210.

[4] S. Y. Yusuf, D. Hayes, A. Pontillo, M. A. Carrizales, G. X. Dussart, and M. M. Lone, "Aeroelastic Scaling for Flexible High Aspect Ratio Wings," in *AIAA Scitech 2019 Forum*, Reston, Virginia: American Institute of Aeronautics and Astronautics, 2019, pp. 1–14, ISBN: 978-1-62410-578-4, DOI: 10.2514/6.2019-1594 (cit. on p. 1).

[5] D. Hayes, A. Pontillo, S. Y. Yusuf, M. M. Lone, and J. Whidborne, "High aspect ratio wing design using the minimum energy destruction principle," in *AIAA Scitech 2019 Forum*, Kissimmee, FL: American Institute of Aeronautics and Astronautics, 2019, ISBN: 978-1-62410-578-4, DOI: 10.2514/6.2019-1592 (cit. on p. 1).

[6] A. Pontillo, "High Aspect Ratio Wings on Commercial Aircraft: a Numerical and Experimental approach," PhD Thesis, Cranfield University, 2020 (cit. on p. 1).

[7] S. Y. Yusuf, "On System Identification and Dynamic Scaling of a Flexible Aircraft," PhD Thesis, Cranfield University, 2019 (cit. on p. 1).

[8] J. P. Nöel, L. Renson, G. Kerschen, B. Peeters, S. Manzato, and J. Debille, "Nonlinear dynamic analysis of an F-16 aircraft using GVT data," in *IFASD 2013 - International Forum on Aeroelasticity and Structural Dynamics*, 2013, pp. 1–13 (cit. on p. 2).

Chapter 2

A Loewner-based System Identification and Structural Health Monitoring Approach for Mechanical Systems[1]

Abstract

Data-driven Structural health monitoring (SHM) requires precise estimates of the target system behaviour. In this sense, SHM by means of modal parameters is strictly linked to system identification (SI). However, existing frequency domain SI techniques have several theoretical and practical drawbacks. This paper proposes using an input-output system identification technique based on rational interpolation, known as the Loewner framework (LF), to estimate the modal properties of mechanical systems. Pioneeringly, the Loewner framework mode shapes and natural frequencies estimated by LF are then applied as damage-sensitive

[1] This is an adapted version of the following journal article accepted to *Structural Control and Health Monitoring* on the 27th February 2023: Dessena, G., Civera, M., Zanotti Fragonara, L., Ignatyev, D. I., Whidborne, J. (2023). A Loewner-based System Identification and Structural Health Monitoring Approach for Mechanical Systems

features for damage detection. To assess its capability, the Loewner framework is validated on both numerical and experimental datasets and compared to established system identification techniques. Promising results are achieved in terms of accuracy and reliability.

2.1 Introduction

The use of vibration-based data in structural health monitoring (SHM) is an important topic, traditionally based on the identification of modal parameters [1, 2] obtained through system identification (SI). Thus, effective and precise SI is of paramount importance for damage detection; yet several alternative strategies exist for SI.

These SI methods can be divided into many categories, depending on the data domain (time or frequency) and the identification procedure (input-output or output only). Input-output data are usually obtained by experimental modal analysis (EMA) [3], while output-only data are collected with operational modal analysis (OMA) techniques [4]. Recent advances have focused on frequency domain techniques and EMA for the SHM of engineering systems [5–7]. Output-only SI was applied for monitoring multi-span bridges by [8] and for arch dams by [9].

In this context, the input-output SI method applied in this work is the Loewner framework (LF): an interpolation-based SI method for the model order reduction (MOR) of large-scale dynamical systems first introduced by Antoulas and co-authors in electrical engineering [10, 11].

This work aims to demonstrate the LF's suitability as an efficient means for the extraction of modal parameters, by comparing it to other state-of-the-art techniques for SHM purposes modal parameters-based damage detection, as it will be shown in the later sections of this paper. Sensitivity, accuracy, and precision

of the identified modal parameters are fundamental for their use in damage detection. Therefore, the SHM problem is the perfect platform for the validation of the LF against existing and well-known SI techniques.

The main contributions of this work are:

(i) The use of the LF to extract the modal parameters of mechanical systems;

(ii) The application of the LF for SHM.

To the authors' best knowledge, this is the first time these have been attempted. To this aim, the LF implementation proposed in [10–12] is modified to accommodate for the extraction of modal parameters, such as natural frequencies (ω_n), damping ratios (ζ_n) and mode shapes ($\boldsymbol{\phi}_n$). The goodness of the proposed method is evaluated on a numerical system, where the robustness to noise is also tested, and on a well-known experimental benchmark.

In the rest of this section, a brief recall of the two concepts of SI and SHM is given. For comparability, two well-known alternatives, numerical algorithms for subspace state space system identification (N4SID) in the time domain and a frequency domain version of least-squares complex exponential (LSCE) are here recalled as well, before moving to the discussion of LF in the next section.

2.1.1 System identification

This subsection focuses on *linear* SI from input-output data in the time and frequency domain. Readers interested in a more comprehensive review are directed to [13].

Subspace state space system identification (SSI) methods, particularly N4SID, are, predominantly, time domain methods for SI and are regarded as the state-of-the-art methods for *linear* experimental and operational modal analysis (EMA and OMA) in all fields of industrial and civil engineering. For this work, N4SID is

considered, since input-output data is used. *Linear* SSI methods, like N4SID, aim to characterise systems in state space form of a linear time-invariant (LTI) system under known excitation [14, 15]:

$$\begin{aligned} \boldsymbol{x}_{k+1} &= \boldsymbol{A}\boldsymbol{x}_k + \boldsymbol{B}\boldsymbol{u}_k + \boldsymbol{w}_k \\ \boldsymbol{y}_k &= \boldsymbol{C}\boldsymbol{x}_k + \boldsymbol{D}\boldsymbol{u}_k + \boldsymbol{v}_k \end{aligned} \quad \text{with} \quad \hat{\boldsymbol{E}}\left[\begin{pmatrix} \boldsymbol{w}_p \\ \boldsymbol{v}_p \end{pmatrix} (\boldsymbol{w}_q^T \boldsymbol{v}_q^T)\right] = \begin{pmatrix} \boldsymbol{Q} & \boldsymbol{S} \\ \boldsymbol{S}^T & \boldsymbol{R} \end{pmatrix} \delta_{pq} \geq 0 \qquad (2.1)$$

$\boldsymbol{A} \in \mathbb{R}^{n\times n}$ is the system matrix, $\boldsymbol{B} \in \mathbb{R}^{n\times m}$ is the input matrix, $\boldsymbol{C} \in \mathbb{R}^{l\times n}$ is the output matrix and $\boldsymbol{D} \in \mathbb{R}^{l\times m}$ direct feed-through matrix. m is the number of inputs, while l is the number of outputs and n is the order of the unknown system. The vectors $\boldsymbol{u}_k \in \mathbb{R}^{m\times 1}$ and $\boldsymbol{y}_k \in \mathbb{R}^{l\times 1}$ are the measurements at time instant k of, respectively, the inputs and outputs of the process. The vector $\boldsymbol{x}_k$ is the state vector of the process at discrete time instant k and $\boldsymbol{v}_k \in \mathbb{R}^{l\times 1}$ is the measurement noise and $\boldsymbol{w}_k \in \mathbb{R}^{n\times 1}$ is called the process noise. $\boldsymbol{v}_k$ and $\boldsymbol{w}_k$ are assumed to be zero mean, stationary white noise vector sequences and uncorrelated with the inputs $\boldsymbol{u}_k$. The matrices $\boldsymbol{Q} \in \mathbb{R}^{n\times n}$, $\boldsymbol{S} \in \mathbb{R}^{n\times l}$, and $\boldsymbol{R} \in \mathbb{R}^{l\times l}$ are the covariance matrices of $\boldsymbol{v}_k$ and $\boldsymbol{w}_k$, while $\hat{\boldsymbol{E}}$ is the expected value operator and δ_{pq} is the Kronecker delta.

In brief, the identification procedure of N4SID can be seen as a two-step process: in the first instance, the input-output data is used to develop, via projection and SVDs, the extended observability matrix and an estimate of the state sequence. This, with a given set of weights specific to N4SID, is used to solve a simple set of overdetermined equations, in the least squares sense, to obtain the state space matrices and noise model.

The interested reader is referred to [14–16] for a comprehensive theoretical background on SSI and N4SID. No further theoretical background on the method is provided in the remainder of the article, as N4SID is only considered as a benchmark method for the scope of this article.

Another industry standard method [17] chosen for this work is a frequency

domain variant of LSCE. LSCE identification is an evolution of the complex exponential (CE) [18, 19] method which overcomes the single-input single-output (SISO) limitation of the latter, acquiring single-input multi-output (SIMO) capabilities. The LSCE implementation used within this work starts by computing, via inverse Fourier transform, the impulse response functions (IRFs) from the acquired frequency response functions (FRFs) and by fitting to the response a set of complex damped sinusoids using Prony's method; hence, allowing to find the poles of the systems and its mode shapes. the decrease of [20, 21] for a more mathematical-based background of the method. The algorithms used within this work to implement N4SID and LSCE are, respectively, adaptations of MATLAB's `n4sid` and `modalfit` functions.

2.1.2 Structural health monitoring

Damage, generally, is defined as a change in a system which undermines or affects its operational capability [1, 22]. The process of implementing a damage detection strategy for aerospace [23], civil [24] and mechanical engineering infrastructure [25] is known as SHM. SHM strategies can be divided into two categories: direct and indirect methods [26]. The latter involves model-based methods [27] and the former often relies on data-driven (especially vibration-based) strategies [2].

In the latter case, modal parameters, such as ω_n, ζ_n, and $\boldsymbol{\phi}_n$, are chosen as damage indicators, because they are easily identifiable from vibrational data [28] and have a direct relationship with the mass and stiffness of the target structure [2, 29]. These can serve different purposes, for instance, damage severity assessment and damage localisation. ω_n work best for identifying the severity of the damage, but less so for the localisation as they can easily be buried by environmental and operational variations [30], since the change in frequency is usually very small. On the other hand, $\boldsymbol{\phi}_n$ are more suited for damage localisa-

tion, which is, usually, done by detecting a difference between the baseline and damaged $\boldsymbol{\phi}_n$. ζ_n are usually the least-used modal parameter as a standalone damage indicator, because it can be misleading due to its nature. In fact, ζ_n has a strong dependence on non-structural factors, so it is difficult to extract the extent of the change which is due to damage and which is not [6, 31].

For the scope of this work, ω_n is be used to assess the damage severity and $\boldsymbol{\phi}_n$ for damage localisation, while ζ_n is only used to evaluate the goodness of the identification with and without damage. Damage quantification is obtained by computing the relative change of the corresponding ω_n between the baseline and damaged cases, while localisation is achieved by comparing the baseline and damaged $\boldsymbol{\phi}_n$. These approaches are well documented in the literature.

The remainder of the article is organised as follows. As anticipated, the LF theory for SI is discussed in the next section, starting from the Loewner matrix. Then, the LF is used on a numerical example, a 9 DoF system, to assess both the effect of noise on the LF identification and its sensitivity to damage. The results on the noise-free cases are also compared with N4SID and LSCE. Next, the LF SI capability is experimentally compared to N4SID and LSCE on the three-storey structure from the Engineering Institute (EI) at Los Alamos National Laboratory (LANL), where the LF is able to correctly identify modal properties and damage over the 17 cases of the dataset. Finally, the article ends with the Conclusions.

2.2 The Loewner framework

Only recently has the LF been applied for SI of electrical [10, 11] and aerodynamic [32] systems. Here it is proposed for mechanical systems, in particular for the detection of modal properties and, so, for SHM purposes. To the knowledge of the authors, this has not been previously proposed. In this section, the mathematical background of the LF is provided. The discussion starts by introducing the

Loewner matrix ($\mathbb{L}$), then the Loewner pencil ($\mathbb{L}, \mathbb{L}_s$). Finally, the realisation problem based on the Loewner pencil is discussed. The section ends by introducing the authors' contribution to this framework.

The LF actively fits a set of frequency domain data, in the form of FRFs, via rational interpolation, which aims at representing a given function as the quotient of two polynomials. In this case, the Loewner interpolant, matrix L, is then used to create, or realise, a state space representation of the data for a given order k.

The final goal does not differ from more established techniques for mechanical systems, like rational fraction polynomial (RFP) [33], or from the recently developed [6, 7] Fast Relaxed Vector Fitting (FRVF) [34], which is an evolution of the well known Vector Fitting (VF) [35]. Nevertheless, the LF's main attribute is to provide a trade-off between accuracy of fit and complexity of the model by overcoming the severely ill-conditioning of current fitting processes [10, 36]. The LF is a *linear* SI method, despite some extensions being developed for limited nonlinear problems, such as the Hammerstein cascaded dynamical systems [37]. For this work, the classical *linear* LF is considered.

2.2.1 Loewner Matrix

The matrix $\mathbb{L}$ is defined as follows [38]:

Given a row array of pairs of complex numbers (μ_j,$\boldsymbol{v}_j$), $j = 1,...,q$, and a column array of pairs of complex numbers (λ_i,$\boldsymbol{w}_j$), $i = 1,...,k$, with λ_i, μ_j distinct, the associated $\mathbb{L}$, or divided-differences matrix is:

$$\mathbb{L} = \begin{bmatrix} \frac{\boldsymbol{v}_1 - \boldsymbol{w}_1}{\mu_1 - \lambda_1} & \cdots & \frac{\boldsymbol{v}_1 - \boldsymbol{w}_k}{\mu_1 - \lambda_k} \\ \vdots & \ddots & \vdots \\ \frac{\boldsymbol{v}_q - \boldsymbol{w}_1}{\mu_q - \lambda_1} & \cdots & \frac{\boldsymbol{v}_q - \boldsymbol{w}_k}{\mu_q - \lambda_k} \end{bmatrix} \in \mathbb{C}^{q \times k} \tag{2.2}$$

If there is a known underlying function $\boldsymbol{\phi}$, then $\boldsymbol{w}_i = \boldsymbol{\phi}(\lambda_i)$ and $\boldsymbol{v}_j = \boldsymbol{\phi}(\mu_j)$.

Loewner established a connection between $\mathbb{L}$ and rational interpolation, also known as Cauchy interpolation. This allows interpolants based on determinants of submatrices of $\mathbb{L}$ [39]. In fact, rational interpolants can be derived from $\mathbb{L}$, according to [36, 40, 41], from the Loewner pencil and this approach is considered for the remainder of this work. The Loewner pencil comprises ($\mathbb{L}$,$\mathbb{L}_s$), where $\mathbb{L}_s$ is the *Shifted Loewner matrix*, which is defined later.

The concept of interpolation and rational interpolation is not be discussed any further, as they are out of the scope of this work; for further reading, the interested reader is referred to [42, 43].

2.2.2 The Loewner realisation

Let us consider an LTI dynamical system $\boldsymbol{\Sigma}$ with m inputs and p outputs, and k internal variables in descriptor-form representation which is given by:

$$\begin{aligned} \boldsymbol{\Sigma}: \ \boldsymbol{E}\frac{d}{dt}\boldsymbol{x}(t) &= \boldsymbol{A}\boldsymbol{x}(t)+\boldsymbol{B}\boldsymbol{u}(t) \\ \boldsymbol{y}(t) &= \boldsymbol{C}\boldsymbol{x}(t)+\boldsymbol{D}\boldsymbol{u}(t) \end{aligned} \tag{2.3}$$

where $\boldsymbol{x}(t) \in \mathbb{R}^k$ is the internal variable, $\boldsymbol{u}(t) \in \mathbb{R}^m$ is the function's input and $\boldsymbol{y}(t) \in \mathbb{R}^p$ is the output. The constant matrices are:

$$\boldsymbol{E},\boldsymbol{A} \in \mathbb{R}^{k\times k},\ \boldsymbol{B} \in \mathbb{R}^{k\times m}\ \boldsymbol{C} \in \mathbb{R}^{p\times k}\ \boldsymbol{D} \in \mathbb{R}^{p\times m} \tag{2.4}$$

when the matrix $\boldsymbol{A}-\lambda\boldsymbol{E}$ is non singular for a given finite value λ, such that $\lambda \in \mathbb{C}$, a Laplace transfer function, $\boldsymbol{H}(s)$, of $\boldsymbol{\Sigma}$ can be defined in the form of a $p \times m$ rational matrix function:

$$\boldsymbol{H}(s) = \boldsymbol{C}(s\boldsymbol{E}-\boldsymbol{A})^{-1}\boldsymbol{B}+\boldsymbol{D} \tag{2.5}$$

Let us consider the more general case of tangential interpolation, also known as rational interpolation along tangential directions [44]. The right interpolation data

are:

$$(\lambda_i; \boldsymbol{r}_i, \boldsymbol{w}_i),\ i = 1, \ldots, \rho \qquad \left.\begin{array}{c} \boldsymbol{\Lambda} = \text{diag}[\lambda_1, \ldots, \lambda_k] \in \mathbb{C}^{\rho \times \rho} \\ \boldsymbol{R} = [\boldsymbol{r}_1\ \ldots \boldsymbol{r}_k] \in \mathbb{C}^{m \times \rho} \\ \boldsymbol{W} = [\boldsymbol{w}_1\ \ldots\ \boldsymbol{w}_k] \in \mathbb{C}^{\rho \times \rho} \end{array}\right\} \tag{2.6}$$

Likewise, the left interpolation data:

$$(\mu_j, \boldsymbol{l}_j, \boldsymbol{v}_j),\ j = 1, \ldots, v \qquad \left.\begin{array}{c} \boldsymbol{M} = \text{diag}[\mu_1, \ldots, \mu_q] \in \mathbb{C}^{v \times v} \\ \boldsymbol{L}^T = [\boldsymbol{l}_1\ \ldots \boldsymbol{l}_v] \in \mathbb{C}^{p \times v} \\ \boldsymbol{V}^T = [\boldsymbol{v}_1\ \ldots\ \boldsymbol{v}_q] \in \mathbb{C}^{m \times v} \end{array}\right\} \tag{2.7}$$

λ_i and μ_j are the values at which $\boldsymbol{H}(s)$ is evaluated. The vectors $\boldsymbol{r}_i$ and $\boldsymbol{l}_j$ are, respectively, the right and left tangential general directions, which are selected randomly in practice [32], and $\boldsymbol{w}_i$ and $\boldsymbol{v}_j$ are the right and left tangential data. The rational interpolation problem is solved when the transfer function $\boldsymbol{H}$, associated with realisation $\boldsymbol{\Sigma}$ in Equation (2.3), is linked to $\boldsymbol{w}_i$ and $\boldsymbol{v}_j$:

$$\boldsymbol{H}(\lambda_i)\boldsymbol{r}_i = \boldsymbol{w}_i,\ j = 1 \ldots, \rho \quad \text{and} \quad \boldsymbol{l}_i \boldsymbol{H}(\mu_j) = \boldsymbol{v}_j,\ i = 1, \ldots, v \tag{2.8}$$

such that Equation (2.8) is satisfied via the Loewner pencil.

Now, let us consider a set of points $Z = \{z_1, \ldots, z_N\}$ within the complex plane, a rational function $\boldsymbol{y}(s)$, such that $\boldsymbol{y}_i := \boldsymbol{y}(z_i), i = 1, \ldots, N$, and let $Y = \{\boldsymbol{y}_1, \ldots, \boldsymbol{y}_N\}$. Then by considering the left and right data partition as:

$$Z = \{\lambda_1, \ldots, \lambda_\rho\} \cup \{\mu_1, \ldots, \mu_v\} \quad \text{and} \quad Y = \{\boldsymbol{w}_1, \ldots, \boldsymbol{w}_\rho\} \cup \{\boldsymbol{v}_1, \ldots, \boldsymbol{v}_v\} \tag{2.9}$$

with $N = p + v$; hence, the matrix $\mathbb{L}$ becomes:

$$\mathbb{L} = \begin{bmatrix} \frac{\boldsymbol{v}_1\boldsymbol{r}_1 - \boldsymbol{l}_1\boldsymbol{w}_1}{\mu_1 - \lambda_1} & \cdots & \frac{\boldsymbol{v}_1\boldsymbol{r}\rho - \boldsymbol{l}_1\boldsymbol{w}\rho}{\mu_1 - \lambda\rho} \\ \vdots & \ddots & \vdots \\ \frac{\boldsymbol{v}_v\boldsymbol{r}_1 - \boldsymbol{l}_v\boldsymbol{w}_1}{\mu_v - \lambda_1} & \cdots & \frac{\boldsymbol{v}_v\boldsymbol{r}\rho - \boldsymbol{l}_v\boldsymbol{w}\rho}{\mu_v - \lambda\rho} \end{bmatrix} \in \mathbb{C}^{v\times\rho} \tag{2.10}$$

Since $\boldsymbol{v}_v\boldsymbol{r}_p$ and $\boldsymbol{l}_v\boldsymbol{w}_p$ are scalars, $\mathbb{L}$ satisfies the Sylvester equation in such a fashion:

$$\mathbb{L}\boldsymbol{\Lambda} - \boldsymbol{M}\mathbb{L} = \boldsymbol{L}\boldsymbol{W} - \boldsymbol{V}\boldsymbol{R} \tag{2.11}$$

Now, Let us define the *shifted Loewner matrix*, $\mathbb{L}_s$, as the $\mathbb{L}$ corresponding to $s\boldsymbol{H}(s)$:

$$\mathbb{L}_s = \begin{bmatrix} \frac{\mu_1\boldsymbol{v}_1\boldsymbol{r}_1 - \lambda_1\boldsymbol{l}_1\boldsymbol{w}_1}{\mu_1 - \lambda_1} & \cdots & \frac{\mu_1\boldsymbol{v}_1\boldsymbol{r}_\rho - \lambda_\rho\boldsymbol{l}_1\boldsymbol{w}_\rho}{\mu_1 - \lambda_\rho} \\ \vdots & \ddots & \vdots \\ \frac{\mu_v\boldsymbol{v}_v\boldsymbol{r}_1 - \lambda_1\boldsymbol{l}_v\boldsymbol{w}_1}{\mu_v - \lambda_1} & \cdots & \frac{\boldsymbol{v}_v\boldsymbol{r}_\rho - \boldsymbol{l}_v\boldsymbol{w}_\rho}{\mu_v - \lambda_\rho} \end{bmatrix} \in \mathbb{C}^{v\times\rho} \tag{2.12}$$

Likewise, the Sylvester equation is satisfied as follows:

$$\mathbb{L}_s\Lambda - \boldsymbol{M}\mathbb{L}_s = \boldsymbol{L}\boldsymbol{W}\boldsymbol{\Lambda} - \boldsymbol{M}\boldsymbol{V}\boldsymbol{R} \tag{2.13}$$

Let us consider Equation (2.5) and, particularly, matrix $\boldsymbol{D}$. As shown in [41], the $\boldsymbol{D}$-term is incorporated in the other matrices as it does not influence interpolation; hence, $\boldsymbol{D}$ is set to 0 per convention. So, Equation (2.5) becomes:

$$\boldsymbol{H}(s) = \boldsymbol{C}(s\boldsymbol{E} - \boldsymbol{A})^{-1}\boldsymbol{B} \tag{2.14}$$

A realisation of the smallest possible dimension exists only when it is completely controllable and observable. Hence, when the data is assumed to be sampled from a system for which the transfer function can be described by Equation (2.14), the generalised tangential observability, $\mathscr{O}_v$, and generalised tangen-

tial controllability, $\mathscr{R}_\rho$, are defined as follows [11]:

$$\mathscr{O}_v = \begin{bmatrix} \boldsymbol{l}_1\boldsymbol{C}(\mu_1\boldsymbol{E}-\boldsymbol{A})^{-1} \\ \vdots \\ \boldsymbol{l}_v\boldsymbol{C}(\mu_q\boldsymbol{E}-\boldsymbol{A})^{-1} \end{bmatrix} \in \mathbb{R}^{v\times n} \tag{2.15}$$

$$\mathscr{R}_\rho = \begin{bmatrix} (\lambda_1\boldsymbol{E}-\boldsymbol{A})^{-1}\boldsymbol{B}\boldsymbol{r}_1 & \cdots & (\lambda_\rho\boldsymbol{E}-\boldsymbol{A})^{-1}\boldsymbol{B}\boldsymbol{r}_\rho \end{bmatrix} \in \mathbb{R}^{n\times\rho} \tag{2.16}$$

Now, let us incorporate Equations (2.15) and (2.16) into, respectively, Equations (2.10) and (2.12):

$$\mathbb{L}_{j,i} = \frac{\boldsymbol{v}_j\boldsymbol{r}_i - \boldsymbol{l}_j\boldsymbol{w}_i}{\mu_j-\lambda_i} = \frac{\boldsymbol{l}_j\boldsymbol{H}(\mu_i)\boldsymbol{r}_i - \boldsymbol{l}_j\boldsymbol{H}(\lambda_i)\boldsymbol{r}_i}{\mu_j-\lambda_i} = -\boldsymbol{l}_j\boldsymbol{C}(\mu_j\boldsymbol{E}-\boldsymbol{A})^{-1}\boldsymbol{E}(\lambda_i\boldsymbol{E}-\boldsymbol{A})^{-1}\boldsymbol{B}\boldsymbol{r}_i \tag{2.17}$$

$$(\mathbb{L}_s)_{j,i} = \frac{\mu_j\boldsymbol{v}_j - \lambda_i\boldsymbol{l}\boldsymbol{w}_i}{\mu_j-\lambda_i} = \frac{\mu_j\boldsymbol{l}_j\boldsymbol{H}(\mu_i)\boldsymbol{r}_i - \lambda_i\boldsymbol{l}_j\boldsymbol{H}(\lambda_i)\boldsymbol{r}_i}{\mu_j-\lambda_i} = -\boldsymbol{l}_j\boldsymbol{C}(\mu_j\boldsymbol{E}-\boldsymbol{A})^{-1}\boldsymbol{A}(\lambda_i\boldsymbol{E}-\boldsymbol{A})^{-1}\boldsymbol{B}\boldsymbol{r}_i \tag{2.18}$$

First, let us first consider the case of minimal amount of data, where it is assumed $p = v$. The assumption is based on the fact that no duplicated data is allowed in $\boldsymbol{R}$ and $\boldsymbol{L}$. Thus, rearranging Equations (2.15) and (2.16) into (2.17) and (2.18):

$$\mathbb{L} = -\mathscr{O}_v\boldsymbol{E}\mathscr{R}_\rho \qquad\qquad \mathbb{L}_s = -\mathscr{O}_v\boldsymbol{A}\mathscr{R}_\rho \tag{2.19}$$

Then, letting the Loewner pencil be a regular pencil, in the sense of $\mathrm{eig}((\mathbb{L},\mathbb{L}_s)) \neq (\mu_i,\lambda_i)$:

$$\boldsymbol{E} = -\mathbb{L}, \qquad \boldsymbol{A} = -\mathbb{L}_s, \qquad \boldsymbol{B} = \boldsymbol{V}, \qquad \boldsymbol{C} = \boldsymbol{W} \tag{2.20}$$

Accordingly, the interpolating rational function is described as:

$$\boldsymbol{H}(s) = \boldsymbol{W}(\mathbb{L}_s - s\mathbb{L})^{-1}\boldsymbol{V} \tag{2.21}$$

The aforementioned derivation refers to the minimal amount of data instance, which is rarely the case when dealing with real data. Nevertheless, the LF is extendable to redundant data. Firstly, let us assume:

$$\operatorname{rank}[\zeta\mathbb{L} - \mathbb{L}_s] = \operatorname{rank}[\mathbb{L}\,\mathbb{L}_s] == \operatorname{rank}\begin{bmatrix}\mathbb{L}\\ \mathbb{L}_s\end{bmatrix} = k,\ \forall\zeta \in \{\lambda_j\} \cup \{\mu_i\} \tag{2.22}$$

Secondly, the short Singular Value Decomposition (SVD) of $\zeta\mathbb{L} - \mathbb{L}_s$ is computed:

$$\operatorname{svd}(\zeta\mathbb{L} - \mathbb{L}_s) = \boldsymbol{Y}\boldsymbol{\Sigma}_l\boldsymbol{X} \tag{2.23}$$

where $\operatorname{rank}(\zeta\mathbb{L} - \mathbb{L}_s) = \operatorname{rank}(\boldsymbol{\Sigma}_l) = \operatorname{size}(\boldsymbol{\Sigma}_l) = k, \boldsymbol{Y} \in \mathbb{C}^{v\times k}$ and $\boldsymbol{X} \in \mathbb{C}^{k\times\rho}$. Thirdly, note that:

$$-\boldsymbol{A}\boldsymbol{X} + \boldsymbol{E}\boldsymbol{X}\boldsymbol{\Sigma}_l = \boldsymbol{Y}^*\mathbb{L}_s\boldsymbol{X}^*\boldsymbol{X} - \boldsymbol{Y}^*\mathbb{L}\boldsymbol{X}^*\boldsymbol{X}\boldsymbol{\Sigma}_l = \boldsymbol{Y}^*(\mathbb{L}_s - \mathbb{L}\boldsymbol{\Sigma}_l) = \boldsymbol{Y}^*\boldsymbol{V}\boldsymbol{R} = \boldsymbol{B}\boldsymbol{R} \tag{2.24}$$

and likewise, $-\boldsymbol{Y}\boldsymbol{A} + \boldsymbol{M}\boldsymbol{Y}\boldsymbol{E} = \boldsymbol{L}\boldsymbol{C}$ such that $\boldsymbol{X}$ and $\boldsymbol{Y}$ are, respectively, the generalised controllability and observability matrices for the system $\boldsymbol{\Sigma}$ with $\boldsymbol{D} = 0$. After checking for the right and left interpolation conditions, the Loewner realisation for redundant data is:

$$\boldsymbol{E} = -\boldsymbol{Y}^*\mathbb{L}\boldsymbol{X}, \qquad \boldsymbol{A} = -\boldsymbol{Y}^*\mathbb{L}_s\boldsymbol{X}, \qquad \boldsymbol{B} = \boldsymbol{Y}^*\boldsymbol{V}, \qquad \boldsymbol{C} = \boldsymbol{W}\boldsymbol{X} \tag{2.25}$$

The formulation of Equation (2.25) – i.e. the Loewner realisation for redundant data – is going to be considered in the remainder of this work. The interested

reader is referred to [36, 41] for a more in-depth discussion of each step.

2.2.3 The algorithm

Having outlined the general process to characterise a system, in the form of Equation (2.25), the general application is applied to the specific case of frequency domain data. Of particular interest is the application in [10, 11] and its MATLAB implementation [45] for a MIMO system. These advances were of service to the authors to develop their application to mechanical systems. Particularly, the implementation deviates from that proposed in [10, 11, 45] as it introduces the identification of modal parameters, thus making the LF a viable instrument for the identification of modal parameters of *linear* mechanical system. The implementation is outlined in Algorithm 1 and a MATLAB implementation is available from a Cranfield Online Research Data (CORD) entry [46].

Algorithm 1: The LF for mechanical systems algorithm

Input: The system's FRFs as $\boldsymbol{H}(\omega)$, the frequency vector as ω, and the LF order as n

Output: A matrix with the modal properties (ω_n, ζ_n, and $\boldsymbol{\phi}_n$), the Loewner realisation, and $[\boldsymbol{E},\boldsymbol{A},\boldsymbol{B},\boldsymbol{C},\boldsymbol{D}]$

1 $[\mathbb{L},\mathbb{L}_s,\boldsymbol{V},\boldsymbol{W},\mu,\lambda] = \texttt{loewner}(j\omega,\boldsymbol{H},\omega)$;[11, 45]
2 $[\boldsymbol{X},\boldsymbol{Y}]$ = svd($\mathbb{L}$) and enforce order k of the LF: $\boldsymbol{X}_k = \boldsymbol{X}(:,1:k)$; $\boldsymbol{Y}_k = \boldsymbol{Y}(:,1:k)$;
3 Find $[\boldsymbol{E},\boldsymbol{A},\boldsymbol{B},\boldsymbol{C}]$ as per Equation (2.25)
4 Ensure poles stability: if necessary, turn $\boldsymbol{E}$ into an identity matrix;
5 Set $\boldsymbol{D} = 0$;
6 Obtain $[\boldsymbol{E},\boldsymbol{A},\boldsymbol{B},\boldsymbol{C},\boldsymbol{D}]$ and the Loewner realisation;
7 Convert from descriptor state-space model to continuous state-space model;
8 Compute the system poles and obtain ω_n, ζ_n, and $\boldsymbol{\phi}_n$.

In Algorithm 1, the function `loewner` creates $\mathbb{L}$, $\mathbb{L}_s$, and the interpolation data matrices, $\boldsymbol{V}$ and $\boldsymbol{W}$ by following the process outlined in Equations (2.6) to (2.13). The data in $\boldsymbol{H}$ is sampled in the right and left data vectors, respectively, in such a fashion: `1:2:end` and `2:2:end` (using MATLAB notation). Then, the generalised

tangential directions vectors are generated as random vectors, using the `randn` MATLAB function. After having established the right and left data, it is trivial, by following the abovementioned proofs, to obtain the $\mathbb{L}$, $\mathbb{L}_s$ and the interpolation data matrices, $\boldsymbol{V}$ and $\boldsymbol{W}$, and progress in the algorithm. The authors' main contribution is outlined in points 7 and 8 of the Algorithm.

2.3 Numerical case study

In order to investigate the goodness of fit and the effect of noise on the results of the LF-based SI, a numerically simulated 9 DoF mass-spring-damper system, as shown in Figure 2.1, is developed. The system consists of nine masses, such that $m_n = 1$ kg, adjacently linked with springs, such that $k_n = 5000$ Nm^{-1}, and dampers, characterised by the critical damping ratio of $\zeta_n = 1\% \forall n$.

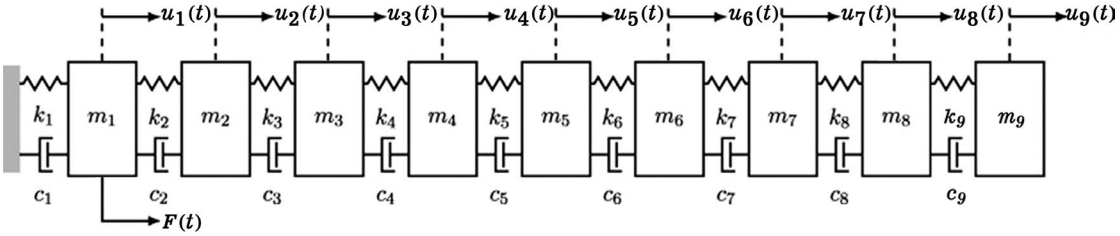

Figure 2.1: 9 DoF system: schematic diagram.

The numerical model is excited with a unit $(1$ N) rectangular impulse applied to the first mass as input force, the data are recorded at a sampling frequency $f_s = 200$ Hz, with a frequency resolution of $\Delta f = 0.05$ Hz. According to the Nyquist criterion, only frequencies up to 100 Hz are inspected, this is however not an issue since all nine modes fall into this frequency range. The receptance FRFs are extracted by dividing the fast Fourier transform (FFT) of the output displacement recordings by the input force FFT, at each output channel (i.e. at each mass and DoF). Note that the algorithm can be applied both in a SISO or a SIMO fashion. For brevity, only the results for a SIMO application (considering all the available output channels at once) are reported and discussed.

The response of the modelled system is considered with and without artificially added additive white Gaussian noise, to test its robustness to measurement noise. The error is calculated with respect to the known numerical results. For the idealised noise-free scenario, the LF is able to correctly identify ω_{1-9}, with a maximum discrepancy of 0.025%, ζ_{1-9}, and $\boldsymbol{\phi}_{1-9}$, demonstrated [47] with a MAC (Modal Assurance Criterion) of unity for all modes. The MAC is computed with the usual [48] formulation:

$$MAC(\boldsymbol{\phi}_b, \boldsymbol{\phi}_e) = \frac{\left(\boldsymbol{\phi}_b^T \boldsymbol{\phi}_e\right)^2}{\left(\boldsymbol{\phi}_b^T \boldsymbol{\phi}_b\right)\left(\boldsymbol{\phi}_e^T \boldsymbol{\phi}_e\right)} \tag{2.26}$$

where the b and e subscripts respectively represent the baseline and the mode shape to be compared.

Before introducing the investigation of noise effects in the numerical system, it is beneficial to compare the precision of LF with that of N4SID and LSCE against the known ground truth (benchmark). In Tables 2.1 to 2.3 ω_n, ζ_n, and $\boldsymbol{\phi}_n$ are compared for the noiseless case.

Table 2.1: Natural frequencies, in Hz, identified via LF, N4SID, and LSCE and their relative difference to the numerical values.

Natural Frequency [Hz] - (relative difference - %)									
Mode	Benchmark	LF	N4SID	LSCE	Mode	Benchmark	LF	N4SID	LSCE
#1	1.859	1.859	1.859	2.647	#6	17.762	17.766	17.762	16.144
	-	(0.025)	(-)	(42.394)		-	(0.025)	(-)	(-9.106)
#2	5.525	5.527	5.525	5.963	#7	19.795	19.800	19.795	19.046
	-	(0.025)	(-)	(7.923)		-	(0.025)	(-)	-3.784
#3	9.041	9.044	9.041	9.311	#8	21.288	21.294	21.288	21.705
	-	(0.025)	(-)	(2.982)		-	(0.025)	(-)	1.956
#4	12.311	12.314	12.311	12.012	#9	22.201	22.206	22.201	22.694
	-	(0.025)	(-)	(-2.425)		-	(0.025)	(-)	2.219
#5	15.244	15.248	15.244	15.420					
	-	(0.025)	(-)	(1.150)					

ω_n, ζ_n, and $\boldsymbol{\phi}_n$

From Tables 2.1 to 2.3, it is clear that the parameters identified via LF and N4SID are extremely coherent with the numerical values. In fact, N4SID is virtually identical for every parameter, while LF shows a very slight (0.025 %) differ-

Table 2.2: Damping ratios identified via LF, N4SID, and LSCE and their relative difference to the numerical values.

Damping Ratio [-] - (relative difference - %)									
Mode	Benchmark	LF	N4SID	LSCE	Mode	Benchmark	LF	N4SID	LSCE
#1	0.010	0.010	0.010	0.096	#6	0.010	0.010	0.010	0.019
	-	(-)	(-)	(864.412)	-		(-)	(-)	(90.889)
#2	0.010	0.010	0.010	0.056	#7	0.010	0.010	0.010	0.017
	-	(-)	(-)	(456.304)	-		(-)	(-)	(69.254)
#3	0.010	0.010	0.010	0.036	#8	0.010	0.010	0.010	0.013
	-	(-)	(-)	(261.094)	-		(-)	(-)	(25.981)
#4	0.010	0.010	0.010	0.025	#9	0.010	0.010	0.010	0.011
	-	(-)	(-)	(149.527)		-	(-)	(-)	(12.645)
#5	0.010	0.010	0.010	0.002					
	-	(-)	(-)	(-81.580)					

Table 2.3: MAC values between the mode shapes obtained from LF, N4SID, and LSCE and the numerical value.

MAC value (computed with respect to the benchmark). [-]									
Mode	Benchmark	LF	N4SID	LSCE	Mode	Benchmark	LF	N4SID	LSCE
#1	1	1	1	0.979	#6	1	1	1	0.124
#2	1	1	1	0.110	#7	1	1	1	0.025
#3	1	1	1	0.034	#8	1	1	1	0.001
#4	1	1	1	0.005	#9	1	1	1	0.018
#5	1	1	1	0.110					

ence for ω_n, but perfect adherence to the numerical values for ζ_n, and $\boldsymbol{\phi}_n$. On the other hand, LSCE performance is very poor. Errors for the ω_n identification are above 40 % and 800 % for ζ_n. This tendency is also confirmed for $\boldsymbol{\phi}_n$, for which only the first mode is acceptably coherent with the numerical results. The poor performance of LSCE could be explained by the closely spaced modes included in the dataset. Due to its computation steps, LSCE is only able to build a rank-deficient matrix and so misinterpret the closely-spaced modes. As is shown later in the experimental case study, LSCE works fine for sparser modes.

It can be said that for noiseless scenarios, even for closely spaced modes, the LF can perform similarly to the most established technique, N4SID, and better than others e.g. LSCE. This is the first step toward proving the feasibility of LF as a SI method. A test of the LF robustness to noise follows and anticipates a potential application for SHM. The same numerical system as above is used for these studies.

2.3.1 Investigation of noise effects

The effects of noise on the Loewner-based SI are investigated numerically as follows. The signal is corrupted at the input, at the output, and/or at both with a noise range between 0 and 25 with intervals of 1%, totalling 75 independent cases. The percentage of noise is defined as a fraction of the signal's standard deviation, σ. As an overall metric of fitness between the numerically derived receptance FRF and the Loewner realisation, a deviation quantity is introduced as local Root Mean Square Error (RMSE_{ij}) between the FRFs' columns at a given frequency step and is defined with the following formulation:

$$\text{RMSE}_{ij} = \sqrt{\left| \left(f_i^{fit}(j) - f_i(j) \right) \right|^2} \tag{2.27}$$

where $f_i^{fit}(j)$ indicated as the Loewner realisation's column at the given frequency vector index j, likewise $f_i(j)$ as the FRFs' columns at at the corresponding frequency and the subscript i the given FRF column. Alongside RMSE_{ij}, the global Root Mean Square Error (RMSE) is introduced with its usual formulation:

$$\text{RMSE} = \sqrt{\frac{1}{I}\sum_{i=1}^{I}\frac{1}{K}\sum_{j=1}^{K}\left| \left(f_i^{fit}(j) - f_i(j) \right) \right|^2} \tag{2.28}$$

where I is the number of FRFs'columns and the other notation is consistent with Equation (2.27). The number of frequency points, K, is given by $f_s/2/\Delta f$, which returned 2000. The results on the goodness of fit of the model for input-output 0, 1, and 5% noise are presented in in Figure 2.2, Figure 2.3 shows the effect of noise, in all cases, for the correlation of ω_n, ζ_n and $\boldsymbol{\phi}_n$ and, lastly, Figure 2.4 shows the effect of noise on the overall RMSE, mean of the RMSE over its samples, per given noise level and iteration.

By analysing Figure 2.2, the FRFs of the nine channels are superimposed for conciseness, with the numerical data represented by a blue line and the fitted

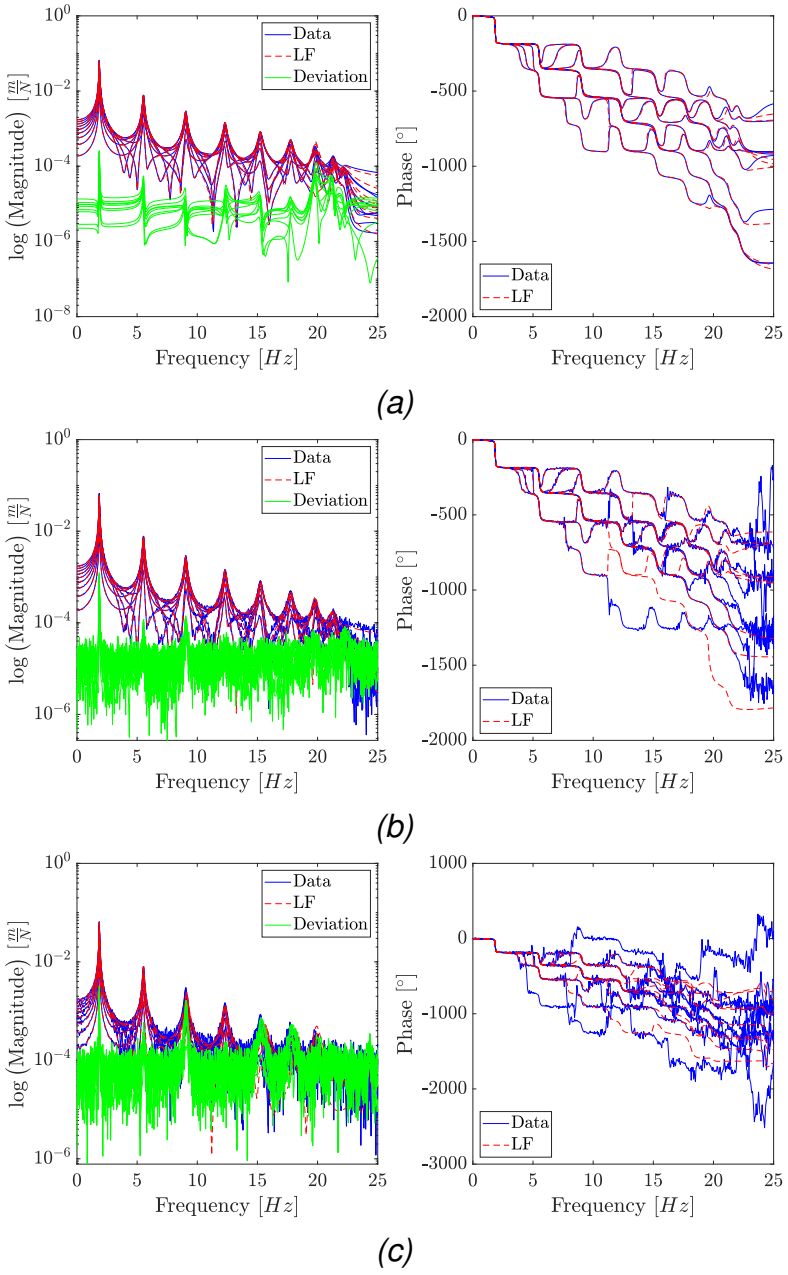

Figure 2.2: 9 DoF system: the 9 DoF system numerical receptance FRF is compared with LF's transfer function results for the 0% (Figure 2.2a), 1% (Figure 2.2b), and 5% (Figure 2.2c) input-output noise cases. In each subfigure, from left to right, the gain's absolute value and the phase angle are presented, for conciseness all 9 channels are superimposed.

model by a dashed red line. As expected, the deviation, indicated by the green line, increases with the noise, particularly for high DoF. However, the absolute value of the deviation does not rise significantly with increasing noise, excluding the noise-free scenario. Considering these early results on a numerical model, it

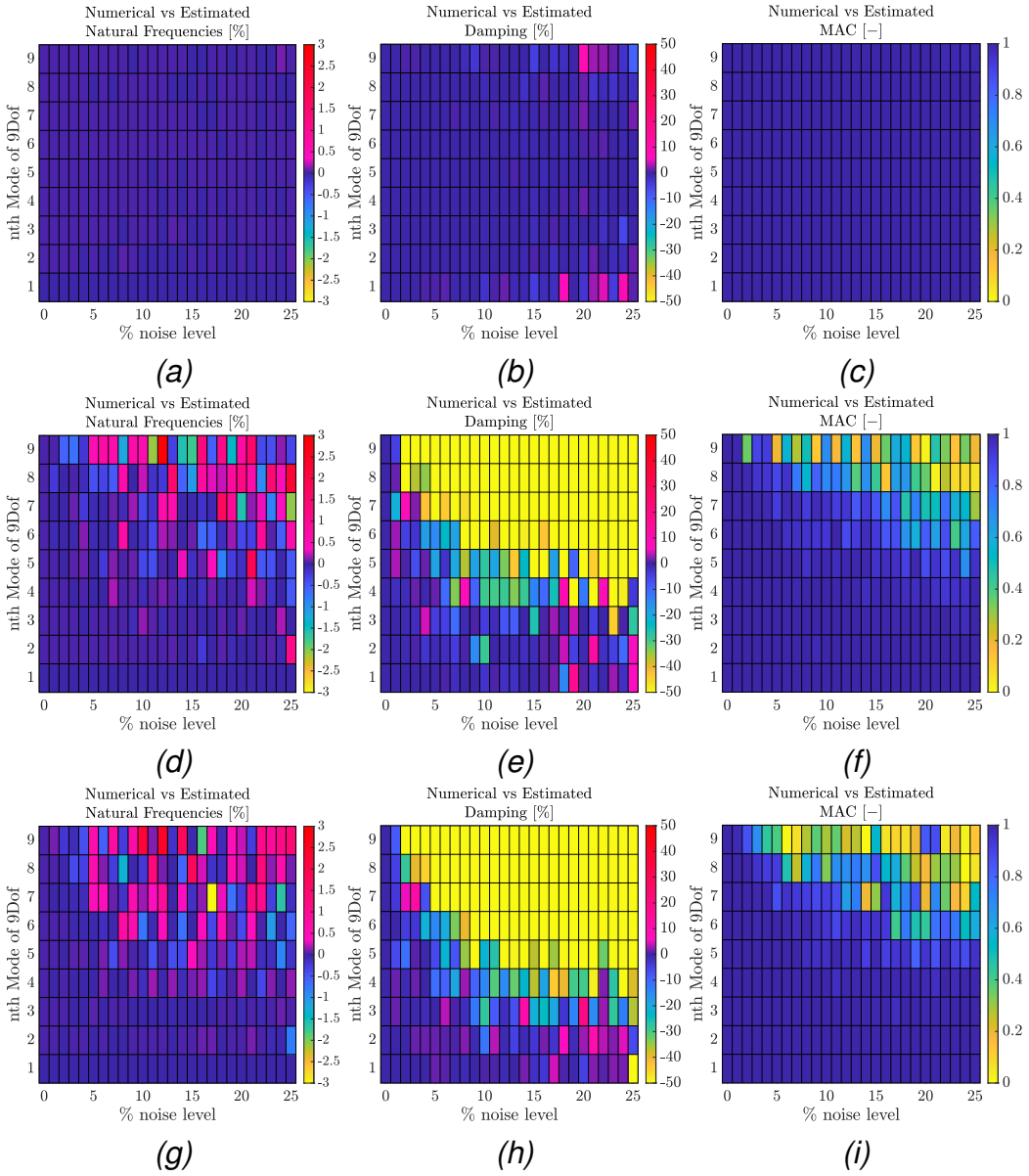

Figure 2.3: 9 DoF system: In Figures 2.3a to 2.3c the effect of input only noise on ω_n is investigated , while in Figures 2.3d to 2.3f and Figures 2.3g to 2.3i the effect of output only and input-output noise is taken under scrutiny. The first column refers to the relative difference in ω_n, in $\%$, relevant to the numerical results. Likewise, for the second column, but referring to the ζ_n, while the third column reports on the MAC Value between the numerical and the estimated value of $\boldsymbol{\phi}_n$.

could be asserted that, for the LF, phase modelling is more sensitive to noise than peak amplitude. However, it should be noted that the deviation does not have a constant value, particularly referring to Figure 2.2b. In fact, it seems linearly related to the frequency. A qualitative explanation of this phenomenon could be

traced back to the nature of the LF as an interpolation matrix. The sum of multiple interpolation errors along the FRF could justify the deviation increase over frequency. The minimum order case $k = 18$ (for the LF, the minimum order should be two times the number of modes to be discovered in the frequency interval) is considered in Figure 2.2b. However, the decay in performance over noise does not constitute a problem, as shown in Figure 2.2, when addressing modal parameters as the order k of the Loewner realisation is raised accordingly and a stabilisation diagram is used to detect the stable poles.

Figure 2.3 compares the correlation between numerical and estimated data when subjected to noise. Figures 2.3a to 2.3c, show the results for the case of input noise, Figures 2.3d to 2.3f for output noise, and, lastly, Figures 2.3g to 2.3i show the input-output noise case. The main modal quantities, ω_n, ζ_n, and $\boldsymbol{\phi}_n$, are considered. ω_n and ζ_n estimation results are presented as the relative difference (Δ), in percentage, calculated by:

$$\Delta = \frac{x_e - x_b}{x_b}\% \tag{2.29}$$

where x_e and x_b represent. respectively, the estimated and baseline quantities.

As expected, the increase in noise is linked to a decrease in the identification of the precision of the modal parameters by the LF. However, it should be noted that input noise has a negligible effect compared to output only and input-output noise. As shown in Figures 2.3a to 2.3c, for the input-only noise, the correlation between the numerical and estimated properties is almost uninfluenced by any noise level, even the most severe. Conversely, for output only and input-output noise the ω_n are almost always correctly identified for all cases and the $\boldsymbol{\phi}_n$ always show good correlation for the first 5 modes. The ζ_n, as expected, appear to be the most problematic quantity; in fact, for any case where noise is higher than 2% and a mode higher than 3, considerable errors, exceeding 50%, are identified.

Nevertheless, the ζ_n are correctly identified for all modes only with the 0% and 1% noise.

In Figure 2.4, the effect of the noise on the global RMSE is investigated over five iterations, for statistical significance. It should be noted that the LF order was set to its minimum order k. As already discussed, the global RMSE of the input only noise is considerably lower, about five times, than the output and input-output cases. In fact, while all three cases increase linearly with noise, the latter two have a very similar trend and magnitude. Hence, output noise has a greater effect on the goodness of the Loewner realisation than input noise.

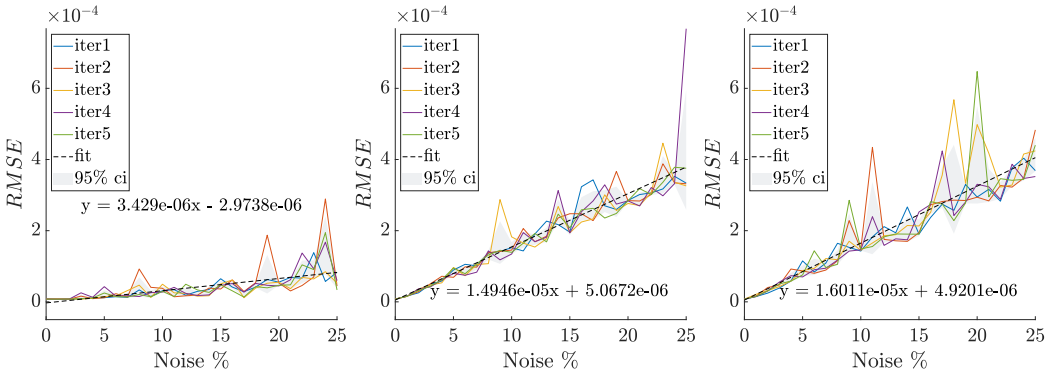

Figure 2.4: 9 DoF system: Relationship between the noise level for input-only (Figure 2.4a), output-only (Figure 2.4b), and input-output (Figure 2.4c) noise and global RMSE. 95% ci stands for 95% confidence interval.

Overall, the above-mentioned results show that the LF is a promising method for the identification of mechanical systems. Importantly, the value of global RMSE never exceeds 5×10^{-4} and Figure 2.4 shows that, for small enough values of noise, the modal properties are correctly identified. This is also confirmed in Figures 2.2 and 2.3, where, as the level of noise increases the fitted model deviated from the numerical data; however, this is particularly true for phase data and ζ_n rather than amplitude, ω_n and $\boldsymbol{\phi}_n$.

From these numerical results, it can be said that the LF is able to correctly identify the modal parameters of the numerical system even when it is artificially

corrupted with noise. In particular, in the given study, the LF is virtually unaffected by input noise; while output-only and input-output noise are found to have a similar influence. Notably, the first three modes are always correctly identified, exception made for ζ_n at high noise levels, at all noise levels. Notably, $\boldsymbol{\phi}_n$ are the least affected parameter by noise and they are followed by ω_n. However, ζ_n is the most severely affected quantity by noise. In conclusion, the LF is a suitable alternative, in terms of robustness to noise and precision, for the identification of the modal parameters of mechanical systems. In addition, the robustness to noise of the ω_n and $\boldsymbol{\phi}_n$ identification makes makes the LF sensitive enough to detect small variations under realistic conditions. This property makes it a valid candidate for the SHM of mechanical systems, as is shown in the following subsection.

2.3.2 Investigation of structural damage effects

Having assessed the capability of the LF to identify mechanical systems, this section investigates its ability to be employed as a SHM method, i.e. the capacity of the LF to detect changes in ω_n, ζ_n, and $\boldsymbol{\phi}_n$ according to a damage scenario. For this scope, the 9 DoF system shown in Figure 2.1 is considered. In order to simulate damage, the stiffness of the fifth element (k_6) is reduced by 5, 10 and 30%. It should be made clear that ζ_n levels, in terms of damping ratio, are not modified in the damaged system as they are heavily influenced by noise; hence, comparison on ζ_n is deferred to the experimental example in the following section. Noise is also taken into consideration; however, for SHM scopes, only the input-output noise case is considered, as it is shown that input-only noise has negligible effect and that output-only has a similar effect to input-output noise. The same noise intervals as in the previous subsection are considered; hence, giving 26 cases per damage step and a total, over the three damage scenarios, of 78. The results in this subsection are presented by comparing the identified ω_n, in Hz, with the numerical damaged counterpart, the same is done for ζ_n.

In order to measure $\boldsymbol{\phi}_n$'s correlation with the numerical damaged case, the MAC value between the numerical and the identified $\boldsymbol{\phi}_n$, computed as per Equation (2.26), is selected as the figure of merit. Table 2.4 shows the ω_n of the baseline and damaged numerical cases, which serves as a source of comparison with the data in Figure 2.5.

Table 2.4: 9 DoF system: natural frequencies, in Hz, of the numerical undamaged and damaged cases.

	Natural frequency [Hz]			
Mode #	Undamaged	5%	10%	30%
1	1.859	1.855	1.851	1.827
2	5.525	5.500	5.4719	5.327
3	9.041	9.040	9.039	9.030
4	12.311	12.243	12.170	11.796
5	15.244	15.235	15.226	15.176
6	17.762	17.693	17.617	17.239
7	19.795	19.737	19.677	19.433
8	21.288	21.261	21.231	21.095
9	22.201	22.098	22.010	21.784

Figure 2.5 shows that the LF detects all the damaged cases correctly for all modes with noise level less than 3%, except for ζ_n, which confirms it to be the parameter most influenced by noise. It is seen that for all noise level and damage cases ω_n, ζ_n, and $\boldsymbol{\phi}_n$ show good correlation, with the expected results, for the first four modes. In addition, ω_n and $\boldsymbol{\phi}_n$ are well correlated for the first eight modes. A case of specific interest is the 5% stiffness reduction scenario, as it allows to prove the capability of the LF to detect small changes in ω_n, as highlighted in Table 2.4, thus demonstrating the feasibility of the method for SHM. In addition, Figure 2.6 shows the effect of the three different damage scenarios, which, for brevity's sake, includes only the first three modes' modal parameters. Since ζ_n is left unchanged, Figures 2.6a and 2.6b, respectively, portray Δ changes, as per Equation (2.29), between the ω_{1-3} and plot $\boldsymbol{\phi}_{1-3}$ between the estimated undamaged and damaged noiseless case. As shown, there is a clear relationship between the increase in

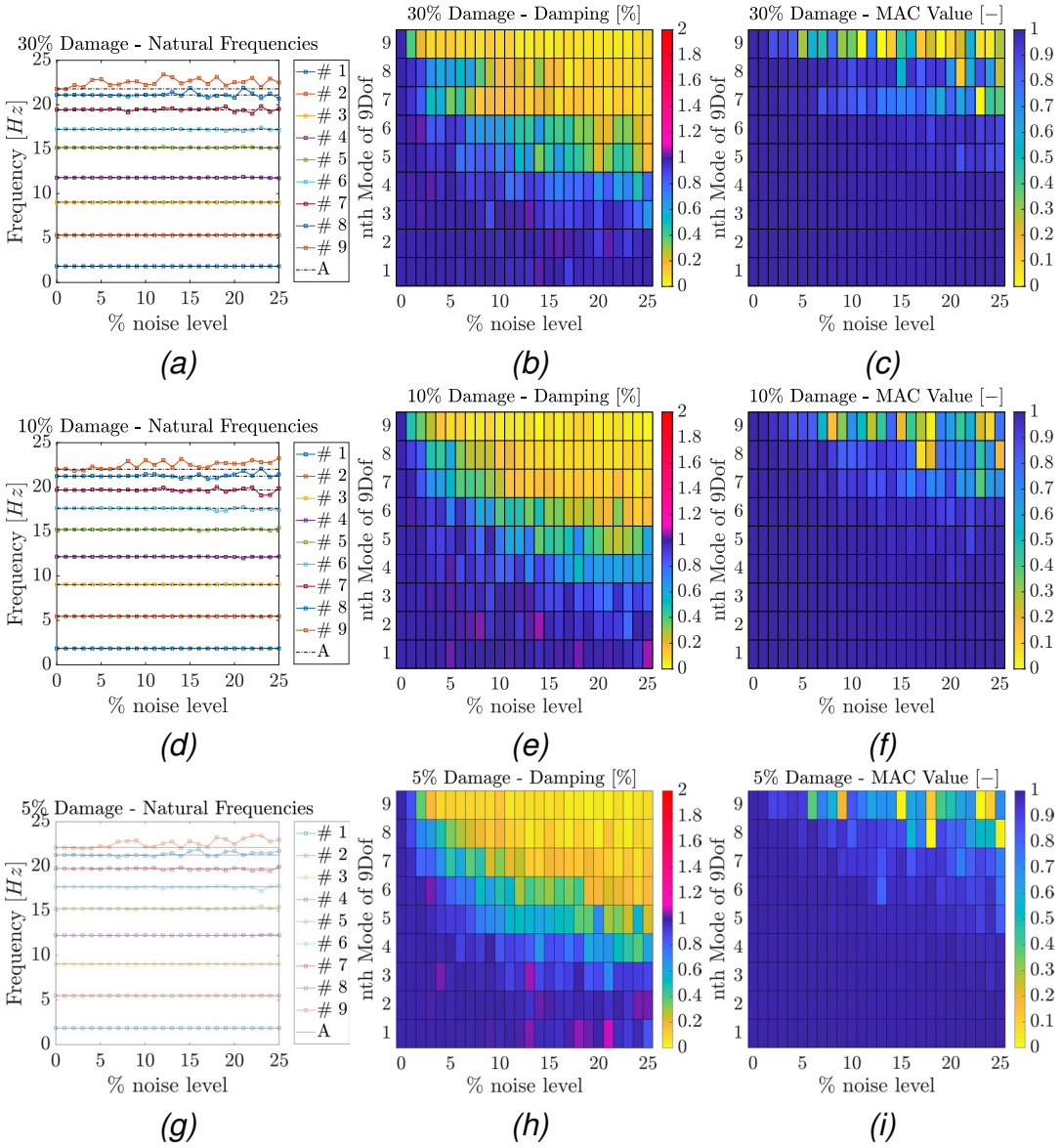

Figure 2.5: 9 DOF system - 30% damage (top), 10% damage (middle), 5% damage (bottom): Results of the numerical study on the numerical case effected by input-output noise: In Figures 2.5a, 2.5d and 2.5g the effect on ω_n identification, while in Figures 2.5b, 2.5e and 2.5h on ζ_n and, lastly, in Figures 2.5c, 2.5f and 2.5i on $\boldsymbol{\phi}_n$. In the legend A stays for numerical results and # n stands for Mode # n.

damage and ω_{1-3}'s Δ and in $\boldsymbol{\phi}_{1-3}$ trajectories. The difference between the baseline and damaged ω_{1-3} increases and the $\boldsymbol{\phi}_{1-3}$ trajectory deviation gets more pronounced as the damage increases; this allows, at least qualitatively, damage severity assessment, in addition to damage detection. Moreover, the most significant deviation in the $\boldsymbol{\phi}_n$ trajectories happen within the fifth node; thus, allowing for the use of LF for damage localisation as well.

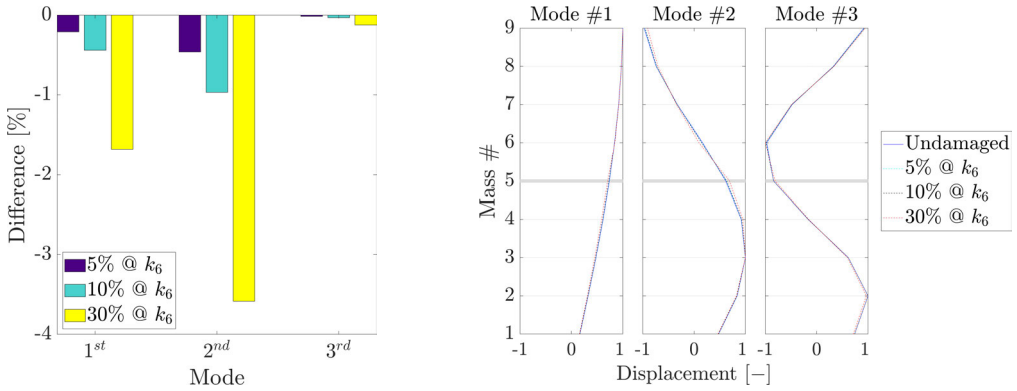

(a) *(b)*

Figure 2.6: 9 DoF system: Relative difference, in percentage, between baseline and damaged cases in ω_n for the first three modes (Figure 2.6a) and the first three $\boldsymbol{\phi}_n$ for the numerical baseline and damaged cases (Figure 2.6b). The data refers to the noiseless case identified by LF and the thicker grid line remarks the damage location.

To summarise this set of results, the performance of the LF has been numerically evaluated for the detection of changes in ω_n and $\boldsymbol{\phi}_n$ induced by progressive stiffness reductions. As preliminarily shown for the baseline scenario, the identification of the damaged scenarios is coherent with the expected values for low levels of noise. This translates to the possibility of using the extracted modal parameters for damage detection and localisation. As expected, the SI approach is able to track the decrease of the three modes and it is shown that the expected relationship between damage and caused by the stiffness reduction; the identified modal coordinates reflect the $\boldsymbol{\phi}_n$'s deviated trajectories, according to the severity and location of the damage. This proves that the LF is precise and robust enough to be used for damage detection in mechanical systems.

In the following section, the LF is again compared to N4SID, in the time domain, and to LSCE, in the frequency domain, to evaluate its SI and SHM capabilities on a benchmark experimental case study.

2.4 Experimental case study

Since the results presented for the numerical case demonstrate that the LF can be a feasible alternative for the SI and SHM of mechanical systems, this study is to test the reliability of the method against real data. The experimental case study selected to extensively test the LF's capabilities to detect and track changes in the mechanical properties of the system (both mass and stiffness), even under noisy conditions and with nonlinearities added to the system, is the well-known [4, 49–51] three-storey frame structure benchmark experiment performed at the EI at the LANL [52, 53].

The three-storey structure, Figure 2.7, is made of four plates ($30.5 \times 30.5 \times 2.5$ cm) linked to the correspondent vertex by a column assembled by bolted joints. A total of 12 columns ($17.7 \times 2.5 \times 0.6$ cm) is used to make up the frame and an additional one ($15.0 \times 2.5 \times 2.5$ cm) is suspended from the top floor and was used to simulate nonlinear effects, intended to mimic a breathing crack mechanism [54], with its interaction with a bumper placed on the second floor (see the zoomed-in particular in Figure 2.7). The base plate is constrained on rails which allow movement in the transverse direction only, which is also the direction of the input force, acting on the base plate. The structure can be regarded as a 4 DoF system, with each DoF corresponding to a floor, or plate. The frame structure and the shaker are mounted on the same baseplate ($76.2 \times 30.5 \times 2.5$ cm). The input force from the shaker to the structure is measured via a load cell with a nominal sensitivity of 2.2 mV/N. Four accelerometers with nominal sensitivities of $1{,}000$ mV/g are attached at the centerline of each floor. Data is collected and processed by the means of a Dactron Spectrabook and the shaker is driven by a Techron 5530 Power Supply Amplifier. The structure is excited with a band-limited random excitation in the range of $20 - 150$ Hz. The lower limit is selected to avoid the rigid body mode of the structure. A 2.6 V RMS in the Dactron system, approximately

20 N RMS measured at the input, is set as the excitation level.

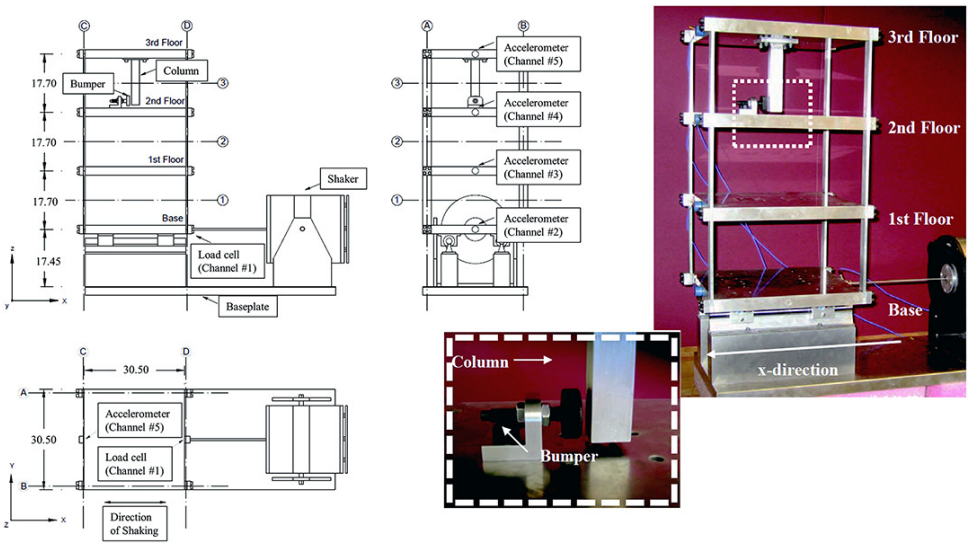

Figure 2.7: Three-storey frame structure: Experimental test set-up and schematic diagrams of the the three-storey frame structure. (Adapted from [7, 52])

Table 2.5 lists all the scenarios, 17, that were tested. The first is the baseline configuration, 2-3 changes in environmental conditions by the means of adding mass, 4-9 stiffness reductions by changing columns thickness and 10-17 nonlinear cases. Nonlinearity, as above-mentioned, is introduced with the extra columns and bumper and it is regulated by the distance between the two. Notably, cases 10-14 are nonlinear only configurations, while 15-17 are nonlinear and environmentally conditioned configurations. It is worth noting that LF is a *linear* SI method; hence, nonlinearity, for the scope of this work, was considered as a noise-like disturbance and not as a per se phenomenon. Hence, the identified parameters for this case refer to the underlying linear system and not to the bi-linear stiffness induced by the bumper-stopper interaction. A total of 850 realisations, 50 for each case, exist, this allowed for an exhaustive statistical comparison of the identification methods results. Each instance comes with a recorded input (in terms of force, N, time histories - THs) and the four respective outputs (as acceleration THs, in g); consequently, 50 SIMO accelerance FRFs (considering all the available output channels) are at disposal for any of the 17 cases. For adherence

with the *Système international* of units, the output's THs in g were converted to ms^{-2}.

Table 2.5: Three-storey frame structure: damage scenarios.

Case	Description	Case	Description
1	Linear baseline	10	Nonlinear, distance between bumper and column tip 0.20 mm
2	Linear, added mass of 1.2 kg at the base	11	Nonlinear, distance between bumper and column tip 0.15 mm
3	Linear, added mass of 1.2 kg at the first floor	12	Nonlinear, distance between bumper and column tip 0.13 mm
4	Linear, 87.5% stiffness reduction in one column of the first inter-storey	13	Nonlinear, distance between bumper and column tip 0.10 mm
5	Linear, 87.5% stiffness reduction in two columns of the first inter-storey	14	Nonlinear, distance between bumper and column tip 0.05 mm
6	Linear, 87.5% stiffness reduction in one column of the second inter-storey	15	Nonlinear, bumper 0.20 mm from column tip, 1.2 kg added at the base
7	Linear, 87.5% stiffness reduction in two columns of the second inter-storey	16	Nonlinear, bumper 0.20 mm from column tip, 1.2 kg added on the first floor
8	Linear, 87.5% stiffness reduction in one column of the third inter-storey	17	Nonlinear, bumper 0.10 mm from column tip, 1.2 kg added on the first floor
9	Linear, 87.5% stiffness reduction in two columns of the third inter-storey		

For the scope of this work, the first mode of the three-storey structure is not considered, because, as reported in literature [52, 53], it is not a vibration mode but a rigid-body motion, for which there is no interest for the proposed applications of the LF.

2.4.1 Results

In Figure 2.8 the Loewner realisation corresponding to the minimum order, $k = 6$, is compared with the accelerance FRF of selected cases, in this instance scenarios # 1, # 4, and # 14; hence, taking under consideration the baseline scenario, a damaged scenario, and a nonlinear scenario. This comparison features a single instance of a given scenario for conciseness. Table 2.6 presents the μ values of the identified ω_n and ζ_n for the three cases of interest in Figure 2.8 alongside benchmark [52] and literature [7], identified via FRVF, data. Also for conciseness, Table 2.6 and Figure 2.9 present the modal parameters identified by the LF, LSCE, and N4SID for the selected cases. A more statistical approach was considered for the ω_n and ζ_n in Figure 2.10's box plots, where LF results are measured against the value obtained by N4SID. Lastly, Figure 2.11 compares the Δ, as per Equation (2.29), between the identified ω_n and ζ_n values of three damaged cases, 4, 5, and 9, and the baseline scenario, case # 1 and Figure 2.12 plots the $\boldsymbol{\phi}_n$ of the cases just mentioned.

Figure 2.8 presents the results of the LF fitting over the accelerance FRFs of a single instance of cases # 1 (Figure 2.8a), 4 (Figure 2.8b) and 14 (Figure 2.8c). For all cases shown, the maximum deviation (green line) is, by an order of magnitude, less than the unity for the gain amplitude. The red dashed line represents the Loewner realisation and the blue line is the accelerance FRFs. Both amplitude and phase seem to be correctly modelled by the LF; nevertheless, case # 14 shows that the noising effect of nonlinearity had a tangible effect on LF, particularly on phase modelling.

As can be seen in Table 2.6, ω_n values are very close for the three methods; nevertheless, the ζ_n identification is not consistent for the last case for the LF. In fact, case # 14's ζ_n is severely underestimated by the LF, if compared with N4SID and LSCE. As it will be discussed in depth later, this is also the case with the other nonlinear scenarios. It should be noted that for the three cases under

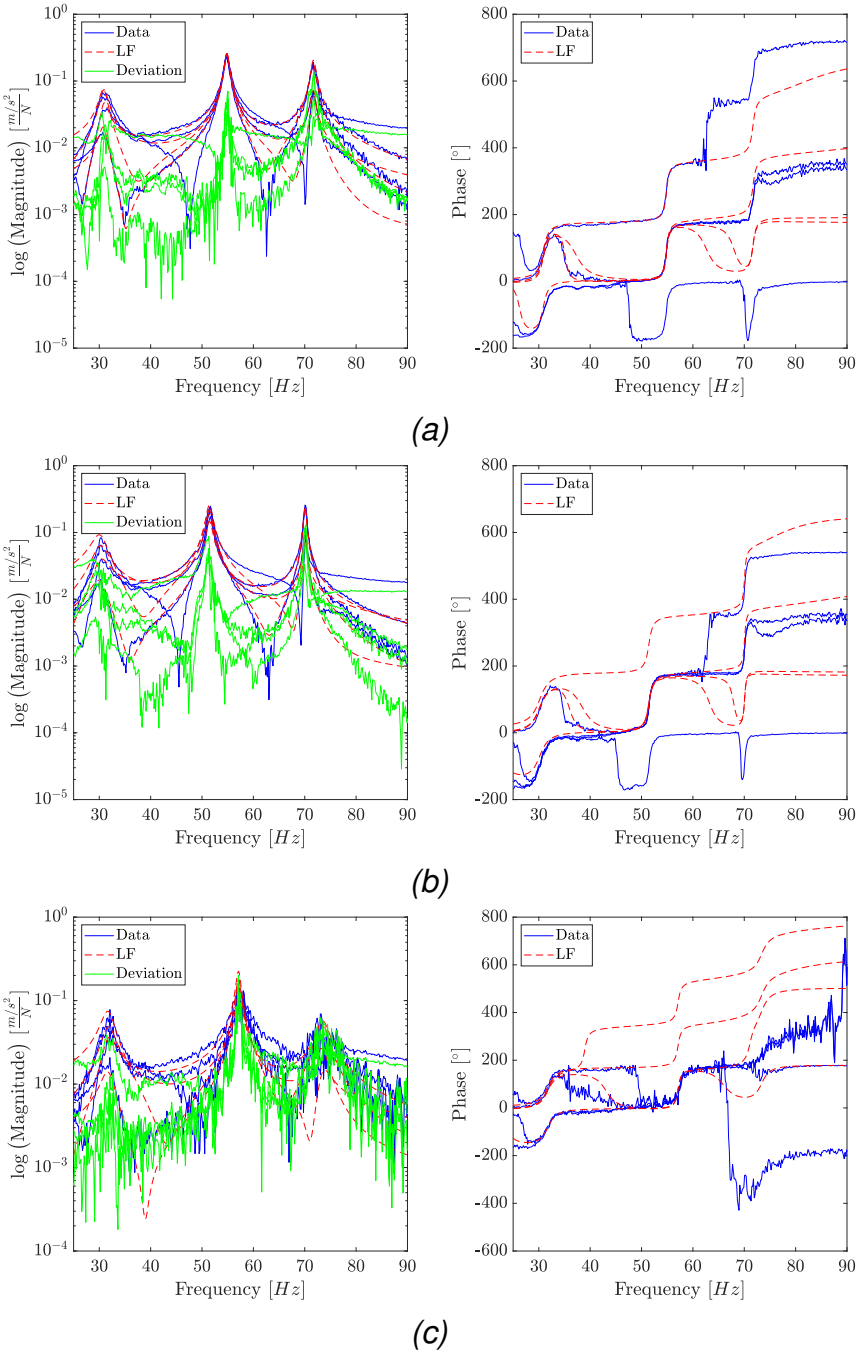

Figure 2.8: Three-storey structure: The FRF computed from the test data is compared with the LF's transfer function, for a single instance of cases # 1 (2.8a), 4 (2.8b) and 14 (2.8c). The absolute gain (left) and the phase angle (left)are presented with all 4 channels superimposed for conciseness.

scrutiny, LSCE overestimates ζ_{1-2}, compared to N4SID. A good agreement is detected between the modal parameters identified via LF within this paper and the benchmark and literature results.

Table 2.6: Three-storey structure: identified ω_n, in Hz, and ζ_n of the scenarios # 1, 4, and 14 from benchmark [52], literature (FRVF [7]), N4SID, LSCE and LF.

Natural Frequency [Hz]				
Scenario #	Mode #	2	3	4
1	Benchmark	30.700	54.200	70.100
	FRVF	30.890	54.740	71.610
	N4SID	30.980	54.731	71.542
	LSCE	30.992	54.594	71.432
	LF	30.986	54.751	71.574
4	Benchmark	30.9	51.2	69.2
	FRVF	30.65	51.54	70.05
	N4SID	30.742	50.919	70.026
	LSCE	30.735	51.103	70.041
	LF	30.700	51.532	70.013
14	Benchmark	33.5	57.6	74.2
	FRVF	31.73	56.98	73.71
	N4SID	31.520	57.532	72.872
	LSCE	32.093	57.886	73.886
	LF	31.667	57.577	73.110
Damping Ratio [-]				
Scenario #	Mode #	2	3	4
1	Benchmark	0.063	0.020	0.010
	FRVF	0.034	0.008	0.007
	N4SID	0.033	0.008	0.006
	LSCE	0.038	0.014	0.007
	LF	0.029	0.007	0.006
4	Benchmark	0.071	0.022	0.006
	FRVF	0.036	0.009	0,004
	N4SID	0.033	0.011	0.003
	LSCE	0.038	0.015	0.003
	LF	0.028	0.009	0.003
14	Benchmark	0.071	0.022	0.010
	FRVF	0.530	0.055	0.030
	N4SID	0.035	0.018	0.017
	LSCE	0.035	0.019	0.009
	LF	0.016	0.005	0.001

Nevertheless, the LF is able to correctly identify the first three $\boldsymbol{\phi}_n$ of the non rigid-body modes of the three-storey structure, as shown in Figure 2.9. The values plotted are the μ values of the identified modal displacements for each method. The blue solid line represents the N4SID identification, LF the red

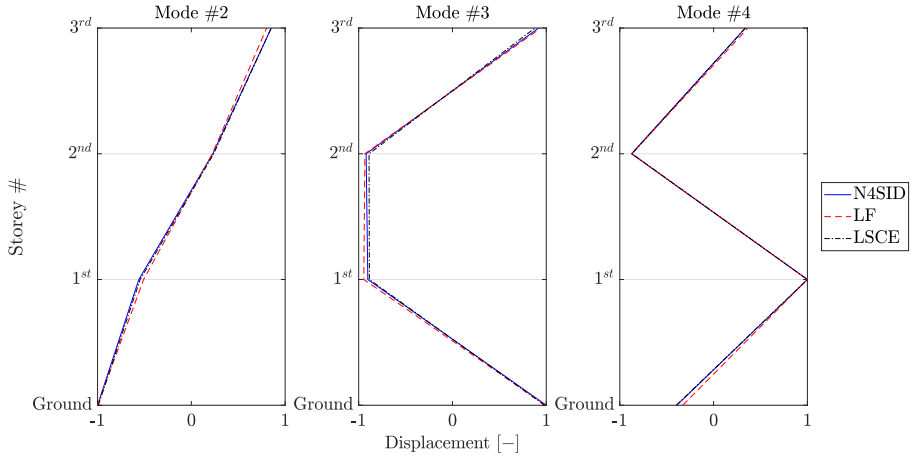

Figure 2.9: Three-storey structure: Mode shapes of non rigid-body motion modes identified via N4SID, LSCE, and LF.

dashed line, and LSCE the black dashed-dotted line. The coherence within the $\boldsymbol{\phi}_n$ is confirmed by the MAC matrix diagonal values between the identified $\boldsymbol{\phi}_n$ (N4SID vs LSCE, N4SID vs LF, and LSCE vs LD) being unity, showing perfect correlation.

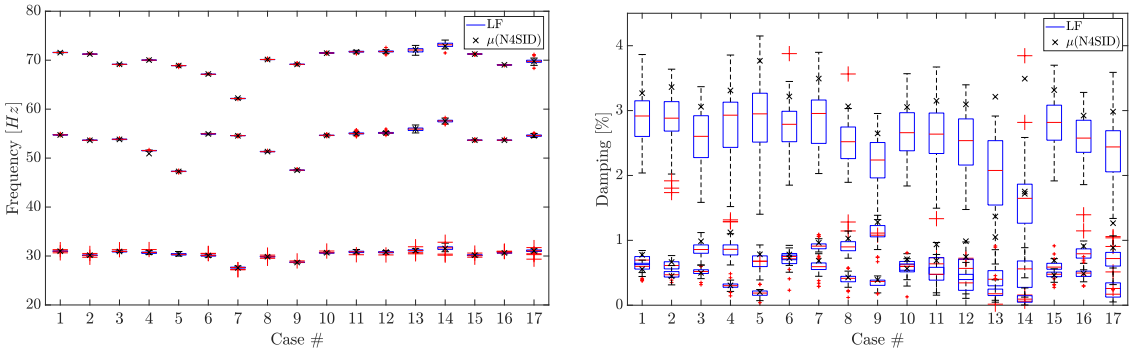

(a) *(b)*

Figure 2.10: Three-storey structure: Box plot of the ω_n (a) and ζ_n (b) for each case (over 50 instances). The median value is represented by the central red line, the bottom and top blue edges of the box indicate the 25th and 75th percentiles and the whiskers the largest and smallest data points not considered outliers. The red plus symbol indicates the outlier values. The black saltire represents the mean values identified via N4SID.

Lastly, the results of the LF identification of the 850 instances are weighted against the μ values of the corresponding N4SID identification in Figure 2.10. In Figures 2.10a and 2.10b the median value is represented by the central red line, the bottom and top blue edges of the box show the 25^{th} and 75^{th} percentiles, the whiskers the largest and smallest data points not considered outliers and

the red Greek cross indicates the outlier values. These metrics give statistical significance to the parameters identified via the LF. The identified ω_n matches the N4SID identified counterpart, while for ζ_n the LF struggles to match the N4SID result. Generally, the LF underestimates in all scenarios the ζ_n, when compared for N4SID; nevertheless, the difference is small, except for cases # 5, 13, and 14. Cases # 13, and 14 also show the biggest difference between their 25^{th} and 75^{th} percentiles for the ω_n. The cause of this issue can be traced back to the high nonlinearity of these two cases, which is perceived as noise by the LF, which is sensitive to high noise levels. In general, the identified ω_n are quite stable, except for the mentioned cases. This is not the case for the ζ_n, particularly for the first non rigid-body mode.

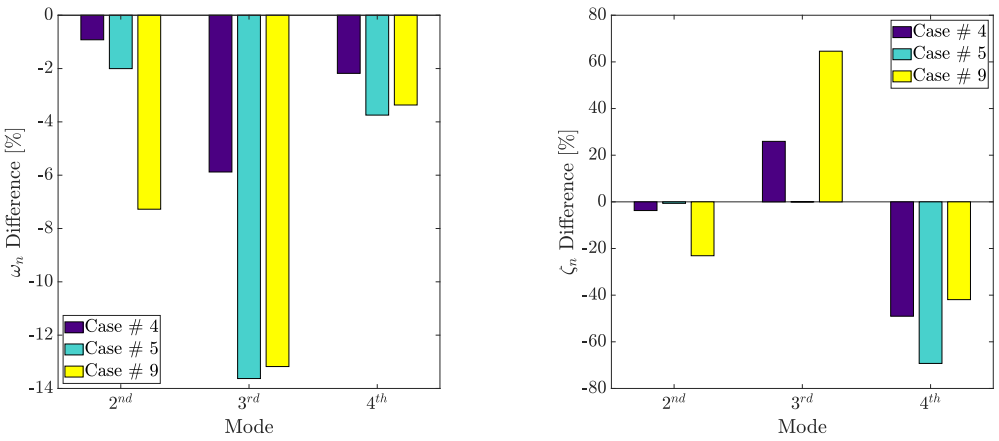

(a) *(b)*

Figure 2.11: Three-storey structure: ω_n (Figure 2.11a) and ζ_n (Figure 2.11b) of the undamaged and damaged settings, the y-axis indicates the relative change (Δ) in percentage.

Figure 2.11 shows the Δ between cases 4, 5, and 9 and the baseline case, # 1. Cases # 4 and 5 are two similar damaged cases. The former experience a stiffness reduction in one column of the first inter-storey, the latter in two columns of the same inter-storey. Hence, their damage differs only in severity rather than localisation, which is the case for scenario # 9: featuring a stiffness reduction in two columns of the third inter-storey. These facts are well represented in Figure 2.11a,

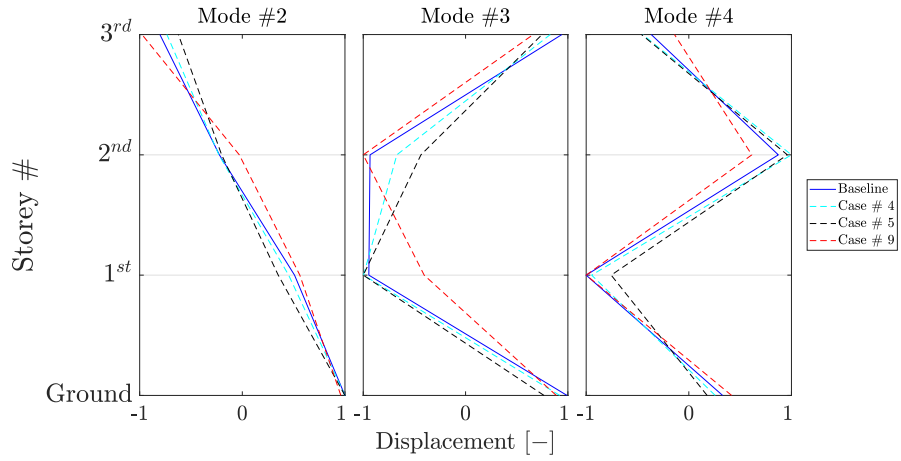

Figure 2.12: Three-storey structure: $\boldsymbol{\phi}_n$ of the undamaged and damaged (cases # 4, 5, and 9) settings.

as the Δ of the identified ω_n increases in between cases # 4 and 5 and case # 9 experience a negative Δ, as expected in a damaged scenario. On the ζ_n side, Figure 2.11b reports on the Δ between the identified ζ_n in the damaged cases and the baseline cases. However, as is well-known, changes in modal damping generally provide little useful information for damage detection. In fact, no strong correlation between $\Delta\zeta_n$ and increasing damage is visible, independently of the considered System Identification algorithm.

Finally, Figure 2.12 plots the identified $\boldsymbol{\phi}_n$ of the baseline and the damaged cases # 4, 5, and 9. The difference in values between the data from cases # 4 and 5 increases with damage, but the mode shape still retains the same trajectory, as expected for a decrease of stiffness, while for case # 9 the variation is more consistent, as a pointwise source of nonlinearity is added at the top floor.

To summarise the experimental validation, the extensive benchmark dataset of the three-storey frame structure allowed for a thorough validation of the SI procedure for the precise extraction of modal parameters with different levels of increasing damage. The modal parameters extracted via LF are generally coherent to those extracted by N4SID, LSCE, and FRVF, as well as to the benchmark results reported in the scientific literature. This is particularly valid for all the ω_n and $\boldsymbol{\phi}_n$ values. In sparse occasions, the benchmark ζ_n results are not fully coher-

ent with the LF-identified parameters; however, this is also true for N4SID, LSCE, and FRVF results. Hence, the precision of the LF-identified modal parameters allows for damage severity assessment and localisation, at least to the same extent as the other three techniques.

2.5 Conclusions

In this work, the suitability of the Loewner Framework (LF) as an input-output System Identification (SI) method for the extraction of modal parameters has been numerically and experimentally verified. Furthermore, the viability of such precise estimates for damage detection has been investigated as well, applying them to classic SHM procedures. To the authors' best knowledge, this work is the first attempt at extracting modal parameters (ω_n, ζ_n, and $\boldsymbol{\phi}_n$) via LF and also the first application of LF for Structural Helth Monitoring (SHM) purposes.

First, the LF is validated with a numerical model of a 9 degrees-of-freedom system against the same parameters as identified via N4SID and LSCE. This displayed the limitations of LSCE for closely-spaced modes, while instead proving the accuracy and precision of the LF. Furthermore, an investigation of the effects of measurement noise has been carried out on the same numerical case study, also considering the case of developing damage. The signals are corrupted with additive white Gaussian noise and three damaged scenarios (5%, 10%, and 30% stiffness reduction on the fifth element) are generated. The LF is able to correctly identify the modal parameters and find the differences between different damage states.

Lastly, the LF is compared to N4SID and LSCE on an experimental three-storey frame structure dataset from LANL, which features 17 different structural scenarios. Once again, the LF reliably returned the modal parameters of the structure under investigation, even with noisy measurement or in presence of

damage-induced nonlinearities, such as for cases $\#14-17$. These identifications were found to be accurate enough to allow for damage detection, localisation, and severity assessment, thus for a full damage diagnosis and assessment procedure.

To summarise the main findings, the main advantage of the LF over the existing methods, in particular over LSCE, is a more consistent ζ_n estimation. It must be said that, as it happens for similar techniques, the ζ_n remains the most difficult modal parameter to estimate accurately. The results for the three-storey structure show great agreement with the benchmark and literature examples.

Another point to consider is that the identification is more influenced by output noise rather than input noise; therefore, accurate sensing devices should be used, as usual for any experimental setup. Given the requirement for precise and accurate modal parameters for SHM and considering the aforementioned results and discussion, the LF is clearly validated for SI and SHM applications to mechanical systems. The only real practical limitation for LF lies in being an input-output method, which is generally less practical than output-only approaches for the OMA of large structures. This aspect will be addressed in future works.

References

[1] C. R. Farrar, S. W. Doebling, and D. A. Nix, "Vibration–based structural damage identification," *Philosophical Transactions of the Royal Society of London. Series A: Mathematical, Physical and Engineering Sciences*, vol. 359, no. 1778, N. A. J. Lieven and D. J. Ewins, Eds., pp. 131–149, 2001, ISSN: 1364-503X, DOI: 10.1098/rsta.2000.0717 (cit. on pp. 15, 18).

[2] A. Rytter, "Vibrational based inspection of civil engineering structures," Ph.D. dissertation, Aalborg University, 1993 (cit. on pp. 15, 18).

[3] G. Dessena, D. I. Ignatyev, J. F. Whidborne, A. Pontillo, and L. Zanotti Fragonara, "Ground vibration testing of a flexible wing: a benchmark and case study," *Aerospace*, vol. 9, no. 8, p. 438, 2022, ISSN: 2226-4310, DOI: 10.3390/aerospace9080438 (cit. on p. 15).

[4] M. Civera, V. Mugnaini, and L. Zanotti Fragonara, "Machine learning-based automatic operational modal analysis: A structural health monitoring application to masonry arch bridges," *Structural Control and Health Monitoring*, no. May, pp. 1–23, 2022, ISSN: 1545-2255, DOI: 10.1002/stc.3028 (cit. on pp. 15, 39).

[5] M. Richardson and B. Schwarz, "Modal parameter estimation from operating data," *Sound and Vibration Magazine*, 2003, ISSN: 15410161 (cit. on p. 15).

[6] M. Civera, G. Calamai, and L. Zanotti Fragonara, "System identification via Fast Relaxed Vector Fitting for the Structural Health Monitoring of masonry bridges," *Structures*, vol. 30, no. January, pp. 277–293, 2021, ISSN: 23520124, DOI: 10.1016/j.istruc.2020.12.073 (cit. on pp. 15, 19, 20).

[7] M. Civera, G. Calamai, and L. Zanotti Fragonara, "Experimental modal analysis of structural systems by using the fast relaxed vector fitting method," *Structural Control and Health Monitoring*, vol. 28, no. 4, pp. 1–23, 2021, ISSN: 1545-2255, DOI: 10.1002/stc.2695 (cit. on pp. 15, 20, 40, 42, 44).

[8] M. T. A. Chaudhary and Y. Fujino, "System identification of bridges using recorded seismic data and its application in structural health monitoring," *Structural Control and Health Monitoring*, vol. 15, no. 7, pp. 1021–1035, 2008, ISSN: 15452255, DOI: 10.1002/stc.249 (cit. on p. 15).

[9] X. Zhi-Qian, P. Jian-Wen, W. Jin-Ting, and C. Fu-Dong, "Improved approach for vibration-based structural health monitoring of arch dams during seismic events and normal operation," *Structural Control and Health*

Monitoring, vol. 29, no. 7, pp. 1–19, 2022, ISSN: 1545-2255, DOI: 10.1002/stc.2955 (cit. on p. 15).

[10] S. Lefteriu and A. C. Antoulas, "Modeling multi-port systems from frequency response data via tangential interpolation," in *2009 IEEE Workshop on Signal Propagation on Interconnects*, IEEE, 2009, pp. 1–4, ISBN: 978-1-4244-4490-8, DOI: 10.1109/SPI.2009.5089847 (cit. on pp. 15, 16, 19, 20, 26).

[11] S. Lefteriu and A. C. Antoulas, "A new approach to modeling multiport systems from frequency-fomain data," *IEEE Transactions on Computer-Aided Design of Integrated Circuits and Systems*, vol. 29, no. 1, pp. 14–27, 2010, ISSN: 0278-0070, DOI: 10.1109/TCAD.2009.2034500 (cit. on pp. 15, 16, 19, 24, 26).

[12] A. C. Ionita and A. C. Antoulas, "Case Study: Parametrized Reduction Using Reduced-Basis and the Loewner Framework," in *Reduced Order Methods for Modeling and Computational Reduction*, A. Quarteroni and G. Rozza, Eds., Cham: Springer International Publishing, 2014, ch. 2, pp. 51–66, DOI: 10.1007/978-3-319-02090-7_2 (cit. on p. 16).

[13] L. Zadeh, "On the identification problem," *IRE Transactions on Circuit Theory*, vol. 3, no. 4, pp. 277–281, 1956, ISSN: 0096-2007, DOI: 10.1109/TCT.1956.1086328 (cit. on p. 16).

[14] P. Van Overschee and B. De Moor, "N4SID: Subspace algorithms for the identification of combined deterministic-stochastic systems," *Automatica*, vol. 30, no. 1, pp. 75–93, 1994, ISSN: 00051098, DOI: 10.1016/0005-1098(94)90230-5 (cit. on p. 17).

[15] W. Favoreel, B. De Moor, and P. Van Overschee, "Subspace state space system identification for industrial processes," *Journal of Process Control*,

vol. 10, no. 2-3, pp. 149–155, 2000, ISSN: 09591524, DOI: 10.1016/S0959-1524(99)00030-X (cit. on p. 17).

[16] S. J. Qin, "An overview of subspace identification," *Computers & Chemical Engineering*, vol. 30, no. 10-12, pp. 1502–1513, 2006, ISSN: 00981354, DOI: 10.1016/j.compchemeng.2006.05.045 (cit. on p. 17).

[17] F. Dezi, F. Gara, and D. Roia, "Dynamic Characterization of Open-ended Pipe Piles in Marine Environment," in *Applied Studies of Coastal and Marine Environments*, InTech, 2016, pp. 169–204, DOI: 10.5772/62055 (cit. on p. 17).

[18] F. R. Spitznogle and A. H. Quazi, "Representation and analysis of time-limited signals using a Complex Exponential algorithm," *The Journal of The Acoustical Society of America*, vol. 47, no. 5 (Part I), pp. 1150–1155, 1970 (cit. on p. 18).

[19] F. R. Spitznogle, J. M. Barrett, C. I. Black, T. W. Ellis, and W. L. LaFuze, "Representation and analysis of sonar signals. Volume I. Improvements in the Complex Exponential signal analysis computational algorithm.," Office of Naval Research- Contract No. NOOO14-69-C0315,1971, Tech. Rep., 1971, p. 47 (cit. on p. 18).

[20] D. L. Brown, R. J. Allemang, R. Zimmerman, and M. Mergeay, "Parameter estimation techniques for modal analysis," in *1979 Automotive Engineering Congress and Exposition*, Univ.of Cincinnati, 1979, p. 19, DOI: 10.4271/790221 (cit. on p. 18).

[21] N. M. M. Maia, "Extraction of valid modal properties from measured data in structural vibrations," PhD Thesis, Imperial College London, 1988, p. 380 (cit. on p. 18).

[22] C. R. Farrar and K. Worden, "An introduction to structural health monitoring," *Philosophical Transactions of the Royal Society A: Mathemati-*

cal, Physical and Engineering Sciences, vol. 365, no. 1851, pp. 303–315, 2007, ISSN: 1364503X, DOI: 10.1098/rsta.2006.1928 (cit. on p. 18).

[23] L. Gelman, I. Petrunin, C. Parrish, and M. Walters, "Novel health monitoring technology for in-service diagnostics of intake separation in aircraft engines," *Structural Control and Health Monitoring*, vol. 27, no. 5, pp. 1–14, 2020, ISSN: 15452263, DOI: 10.1002/stc.2479 (cit. on p. 18).

[24] P. Rizzo and A. Enshaeian, "Challenges in bridge health monitoring: a review," *Sensors*, vol. 21, no. 13, p. 4336, 2021, ISSN: 1424-8220, DOI: 10.3390/s21134336 (cit. on p. 18).

[25] H. Sohn, C. R. Farrar, D. D. Shunk, D. W. Stinemates, B. R. Nadler, and J. Czarnecki, "A Review of Structural Health Monitoring Literature: 1996–2001," Los Alamos National Laboratory (LANL), Los Alamos, CA, Tech. Rep., 2004 (cit. on p. 18).

[26] N. F. Alkayem, M. Cao, Y. Zhang, M. Bayat, and Z. Su, "Structural damage detection using finite element model updating with evolutionary algorithms: a survey," *Neural Computing and Applications*, vol. 30, no. 2, pp. 389–411, 2018, ISSN: 0941-0643, DOI: 10.1007/s00521-017-3284-1 (cit. on p. 18).

[27] G. Dessena, D. I. Ignatyev, J. F. Whidborne, and L. Zanotti Fragonara, "A Kriging Approach to Model Updating for Damage Detection," in *EWSHM 2022*, P. Rizzo and A. Milazzo, Eds., LNCE 254, Singapore: Springer, 2023, ch. 26, pp. 245–255, DOI: 10.1007/978-3-031-07258-1_26 (cit. on p. 18).

[28] A. Cancelli, S. Laflamme, A. Alipour, S. Sritharan, and F. Ubertini, "Vibration-based damage localization and quantification in a pretensioned concrete girder using stochastic subspace identification and particle swarm model

updating," *Structural Health Monitoring*, vol. 19, no. 2, pp. 587–605, 2020, ISSN: 1475-9217, DOI: 10.1177/1475921718820015 (cit. on p. 18).

[29] R. Cardoso, A. Cury, and F. Barbosa, "A robust methodology for modal parameters estimation applied to SHM," *Mechanical Systems and Signal Processing*, vol. 95, pp. 24–41, 2017, ISSN: 08883270, DOI: 10.1016/j.ymssp.2017.03.021 (cit. on p. 18).

[30] Wei Fan and Pizhong Qiao, "Vibration-based damage identification methods: A Review and comparative study," *Structural Health Monitoring*, vol. 10, no. 1, pp. 83–111, 2011, ISSN: 1475-9217, DOI: 10.1177/1475921710365419 (cit. on p. 18).

[31] E. Reynders, R. Pintelon, and G. De Roeck, "Uncertainty bounds on modal parameters obtained from stochastic subspace identification," *Mechanical Systems and Signal Processing*, vol. 22, no. 4, pp. 948–969, 2008, ISSN: 08883270, DOI: 10.1016/j.ymssp.2007.10.009 (cit. on p. 19).

[32] D. Quero, P. Vuillemin, and C. Poussot-Vassal, "A generalized state-space aeroservoelastic model based on tangential interpolation," *Aerospace*, vol. 6, no. 1, p. 9, 2019, ISSN: 2226-4310, DOI: 10.3390/aerospace6010009 (cit. on pp. 19, 22).

[33] M. H. Richardson and D. L. Formenti, "Global curve fitting of frequency response measurements using the rational fraction polynomial method.," *Proceedings of the International Modal Analysis Conference & Exhibit*, vol. 1, pp. 390–397, 1985 (cit. on p. 20).

[34] B. Gustavsen, "Relaxed Vector Fitting Algorithm for Rational Approximation of Frequency Domain Responses," in *2006 IEEE Workship on Signal Propagation on Interconnects*, IEEE, 2006, pp. 97–100, ISBN: 1-4244-0454-1, DOI: 10.1109/SPI.2006.289202 (cit. on p. 20).

[35] B. Gustavsen and A. Semlyen, "Rational approximation of frequency domain responses by vector fitting," *IEEE Transactions on Power Delivery*, vol. 14, no. 3, pp. 1052–1061, 1999, ISSN: 08858977, DOI: 10.1109/61.772353 (cit. on p. 20).

[36] A. C. Antoulas, S. Lefteriu, and A. C. Ionita, "A Tutorial Introduction to the Loewner Framework for Model Reduction," in *Model Reduction and Approximation*, Philadelphia, PA: Society for Industrial and Applied Mathematics, 2017, ch. 8, pp. 335–376, DOI: 10.1137/1.9781611974829.ch8 (cit. on pp. 20, 21, 26).

[37] D. S. Karachalios, I. V. Gosea, and A. C. Antoulas, "The Loewner framework for nonlinear identification and reduction of Hammerstein cascaded dynamical systems," *PAMM*, vol. 20, no. 1, pp. 2020–2022, 2021, ISSN: 1617-7061, DOI: 10.1002/pamm.202000337 (cit. on p. 20).

[38] K. Löwner, "Über monotone matrixfunktionen," *Mathematische Zeitschrift*, vol. 38, no. 1, pp. 177–216, 1934, ISSN: 0025-5874, DOI: 10.1007/BF01170633 (cit. on p. 20).

[39] B. Anderson and A. Antoulas, "Rational interpolation and state-variable realizations," *Linear Algebra and its Applications*, vol. 137-138, no. C, pp. 479–509, 1990, ISSN: 00243795, DOI: 10.1016/0024-3795(90)90140-8 (cit. on p. 21).

[40] A. C. Antoulas, "A tutorial introduction to the Loewner framework for model reduction," in *9th Elgersburg Workshop Mathematische Systemtheorie*, 2014 (cit. on p. 21).

[41] A. Mayo and A. Antoulas, "A framework for the solution of the generalized realization problem," *Linear Algebra and its Applications*, vol. 425, no. 2-3, pp. 634–662, 2007, ISSN: 00243795, DOI: 10.1016/j.laa.2007.03.008 (cit. on pp. 21, 23, 26).

[42] J. Meinguet, *On the solubility of the Cauchy interpolation problem* (Institut de Mathématique Pure et Appliquée Louvain: Rapport). Univ. Cathol., 1969 (cit. on p. 21).

[43] C. Schneider and W. Werner, "Some new aspects of rational interpolation," *Mathematics of Computation*, vol. 47, no. 175, p. 285, 1986, ISSN: 00255718, DOI: 10.2307/2008095 (cit. on p. 21).

[44] B. Kramer and S. Gugercin, "Tangential interpolation-based eigensystem realization algorithm for MIMO systems," *Mathematical and Computer Modelling of Dynamical Systems*, vol. 22, no. 4, pp. 282–306, 2016, ISSN: 1387-3954, DOI: 10.1080/13873954.2016.1198389 (cit. on p. 21).

[45] A. C. Ionita, *System identification*, 2013, [Online]. Available: http://aci.rice.edu/system-identification/ (visited on 2021) (cit. on p. 26).

[46] G. Dessena, *A tutorial on the Loewner-based system identification and structural health monitoring approach for mechanical systems.* Cranfield, 2022, DOI: 10.17862/cranfield.rd.16636279 (cit. on p. 26).

[47] D. J. Ewins, *Modal Testing Theory, Practice and Application*, 2nd. Baldock, UK: Research Studies Press, 2000, p. 562, ISBN: 978-0-863-80218-4 (cit. on p. 28).

[48] R. J. Allemang and D. L. Brown, "A correlation coefficient for modal vector analysis," in *Proceedings of the 1st International Modal Analysis Conference*, Orlando: Union Coll, 1982, pp. 110–116 (cit. on p. 28).

[49] M. Civera, L. Zanotti Fragonara, and C. Surace, "Using video processing for the full-field identification of backbone curves in case of large vibrations," *Sensors*, vol. 19, no. 10, p. 2345, 2019, ISSN: 1424-8220, DOI: 10.3390/s19102345 (cit. on p. 39).

[50] D. Martucci, M. Civera, and C. Surace, "The Extreme Function Theory for Damage Detection: An Application to Civil and Aerospace Structures," *Applied Sciences*, vol. 11, no. 4, p. 1716, 2021, ISSN: 2076-3417, DOI: 10.3390/app11041716 (cit. on p. 39).

[51] M. Civera and C. Surace, "A Comparative Analysis of Signal Decomposition Techniques for Structural Health Monitoring on an Experimental Benchmark," *Sensors*, vol. 21, no. 5, p. 1825, 2021, ISSN: 1424-8220, DOI: 10.3390/s21051825 (cit. on p. 39).

[52] E. Figueiredo, G. Park, J. Figueiras, C. Farrar, and K. Worden, "Structural health monitoring algorithm comparisons using standard data sets," Los Alamos National Laboratory (LANL), Los Alamos, NM (United States), Tech. Rep., 2009, DOI: 10.2172/961604 (cit. on pp. 39–42, 44).

[53] E. Figueiredo, G. Park, C. R. Farrar, K. Worden, and J. Figueiras, "Machine learning algorithms for damage detection under operational and environmental variability," *Structural Health Monitoring*, vol. 10, no. 6, pp. 559–572, 2011, ISSN: 1475-9217, DOI: 10.1177/1475921710388971 (cit. on pp. 39, 41).

[54] A. Bovsunovsky and C. Surace, "Non-linearities in the vibrations of elastic structures with a closing crack: A state of the art review," *Mechanical Systems and Signal Processing*, vol. 62-63, pp. 129–148, 2015, ISSN: 08883270, DOI: 10.1016/j.ymssp.2015.01.021 (cit. on p. 39).

Chapter 3

Ground Vibration Testing of a Flexible Wing: A Benchmark and Case Study[1]

Abstract

Beam-like flexible structures are of interest in many fields of engineering, particularly aeronautics, where wings are frequently modelled and represented as such. Experimental modal analysis is commonly used to characterise the wing's dynamical response. However, unlike other flexible structure applications, no benchmark problems involving high-aspect-ratio flexible wings have appeared in the open literature. To address it, this paper reports on ground vibration testing results for a flexible wing and its sub-assembly and parts. The experimental data can be used as a benchmark and are available to the aeronautical and structural dynamics community. Furthermore, non-linearities in the structure, where present, were detected. Tests were performed on the whole wing as well as parts and

[1] This is an adapted version of the following Open Access journal article: Dessena, G., Ignatyev, D. I., Whidborne, J. F., Pontillo, A., Zanotti Fragonara, L. (2022). Ground vibration testing of a flexible wing: A benchmark and case study. Aerospace, 9(8), 438. The final authenticated version is available at: https://doi.org/10.3390/aerospace9080438

sub-assembly, providing four specimens. These were excited with random vibration at three different amplitudes from a shaker table. The modal properties of a very flexible high-aspect-ratio wing model, its sub-assembly and parts, were extracted, non-linear behaviour was detected and the experimental data are shared in an open repository.

3.1 Introduction

As aeronautical technology progressed over the last 70 years, the increasing use of lightweight and composite materials has allowed designers and manufacturers to create a new state of the art for aircraft design. The likes of Boeing 787 and Airbus A350 have a higher proportion of composite and lightweight structures than ever before, driven by the need for, more efficient, high-aspect-ratio (HAR) wings [1]. Nevertheless, this approach has its shortcomings, particularly concerning the prediction and modelling of such flexible structures. Hence, new tools and procedures are needed. To address these issues, projects such as the Beam Reduction and Dynamic Scaling (BeaRDS) framework [2–5] were carried out to help the development of the aircraft, particularly wings, of the future. However, the issue remains largely open not only from an industrial point of view, but also from the academic side. In fact, while it is trivial to find benchmarks and open datasets for structural health monitoring or seismic vibration, the same cannot be said for flexible wings. The authors propose closing this gap by introducing a case study, benchmark and datasets for a flexible wing. Hence, this work aims to (i) report on the Ground Vibration Testing (GVT) results for a flexible wing and its sub-assembly and parts, (ii) detect, if any, non-linearities in the structure and (iii) share the experimental data to be used as a benchmark by the aeronautical and structural dynamics community.

The specimens used in this work were developed within the BeaRDS frame-

work and include the eXperimental BeaRDS-2 (XB-2) HAR wing, its sub-assembly and its parts. These were tested with a random vibration at three different amplitudes, the data were post-processed and the modal parameters were extracted via Least Squares Complex Exponential (LSCE) [6, 7] from the systems' Frequency Response Functions (FRFs). The modal parameters and the near resonance FRF region were also used for the detection of non-linear behaviour. In addition, the experimental data were shared in an open repository and can be accessed via the Data Availability Statement.

Structural integrity is of paramount importance in engineering, and the knowledge and control of the vibrations of a system is a common part of the design of many products, such as fuel pumps [8] and suspended bridges [9]. For these objectives, refined Finite Element Models (FEMs) and experimental testing were carried out. In particular, *linear* Experimental Modal Analysis (EMA) was used to obtain the structure's modal parameters, such as natural frequencies (ω_n), damping ratios (ζ_n) and mode shapes ($\boldsymbol{\phi}_n$) [10]. These data are used for various applications, such as damage detection [11] and model updating [12].

In aeronautics, the term GVT is preferred over EMA. GVT is a rather standard procedure in the final stages of an aircraft project development and certification [13], and can also be used to detect inconsistencies in the building processes and materials used [14].

GVT is usually undertaken on entire craft, such as fighter jets [15], civil airliners [16] and unmanned aerial vehicles [17], or parts of them, such as helicopter blades [18]. The main objective of these procedures in aeronautics is the extraction of modal parameters used to update FEMs [19], rather than for damage detection. The usual procedure is to couple the FEM with an aerodynamic model to obtain the aeroelastic behaviour [20]. In order to obtain good correlation between the FEM and the real structure, the FEM needs to be tuned according to the results obtained via GVT, ensuring the final concept is compliant with the

aeroelastic properties and dynamical response obtained from FEMs [21].

Damage detection would be impractical, as GVTs are usually lengthy and costly procedures performed in experimental settings on the ground. Nevertheless, it is still important to assess the state of a system [22]. This can be achieved with Operational Modal Analysis (OMA) [23]. OMA allows for the collection of experimental data during the operational life of a structure and allows us to obtain modal parameters [24] that can be either used for direct or model-based damage assessment. In particular, such model-based approaches can be used not only to obtain information about the health of the structure, but also about its new dynamics, such as aeroelastic onset speeds [25]. However, any OMA application is not considered here because GVT is the scope of this work.

In *linear* EMA, three main excitation techniques are usually used: sweep sine, random vibration and impulse testing. Each of them has advantages and disadvantages, which are beyond the scope of this paper; the reader can consult [26, 27] for a deeper insight. As this work deals with a flexible wing, structural non-linearities should also be considered. In the last 30 years, major advances have been made in the development of *Non-linear* Modal Analysis (NLMA), which can be described as a three-step procedure [28]: detection, (ii) characterisation and (iii) parameter estimation. This work focuses only on the first of the three steps. Both sine sweep [29] and random vibration [30] have been used to detect non-linearities. Since non-linearity in sine sweep approaches is detected via distortions in the FRF [27] and these distortions can also depend on the sweep rate (e.g., too fast) [26], random vibration is selected as the chosen input for this work. The trend, and difference in modal parameters, predominantly ω_n, and the near resonance regions of the FRFs of the experiments at different input amplitudes are used to detect non-linearities, as proposed in [27]. The reader interested in a more in-depth review of NLMA and non-linear dynamics in general is referred to the classical reviews [28, 31] and the book [27], while for practical applications,

the following works are suggested [15, 32, 33].

Modal parameters identification was carried out with a single method, as it is customary for vibration testing campaigns [34], and because it was shown, for a related structure [24], that the modal parameters are independent of the technique used. The method selected is a frequency domain implementation of the industry-standard method LSCE [35]. LSCE was introduced to overcome, acquiring single-input multiple-output capability, the single-input single-output limitations of the Complex Exponential Method [6, 7]. The LSCE method requires, as a starting point, the Impulse Response Functions (IRFs) of the system, which are then fitted with a set of complex damped sinusoids via Prony's method [36, 37]. This allows the poles of the systems and the modal parameters to be found. In this implementation, the IRF is computed via inverse Fourier transform from the FRF. The LSCE implementation used in this work was adapted from MATLAB's function `modalfit` to be used in conjunction with an in-house-developed stabilisation diagram routine.

The remainder of this article is organised as follows. In Section 3.2 the specimens used within this work are outlined, a set of numerical and theoretical predictions is given, then the test set-up is described and, finally, the data processing and the identification procedure are shown. Section 3.3 presents the results obtained, Section 3.4 discusses the results and Section 3.5 presents the conclusions and closing remarks.

3.2 Materials and Methods

This section is concerned with the description of the specimens and the context behind their design and manufacture. Theoretical and numerical predictions, alongside data from a previous testing campaign, are presented as a source for comparison. The experimental setup is shown and, finally, the data processing

and the parameters identification strategy are outlined.

3.2.1 The XB-2 High Aspect Ratio Wing

The XB-2 HAR wing was designed under the BeaRDS framework, Figure 3.1, a project developed within Cranfield University which aimed to establish a process for the design, manufacture and testing of dynamically scaled HAR wings for use in Cranfield University's 8'×6' wind tunnel. The XB-2 was a scaled-down version of an optimised full-scale wing designed to minimise induced drag on an A320-like aircraft [4], which was scaled down for wind tunnel testing [3]. The wing consists of four main components: the main spar, the stiffening tube (or the tube), the additional brass masses for the purpose of dynamic scale parameters matching (or the masses) and the skin. However, for the purpose of this study, the masses are removed.

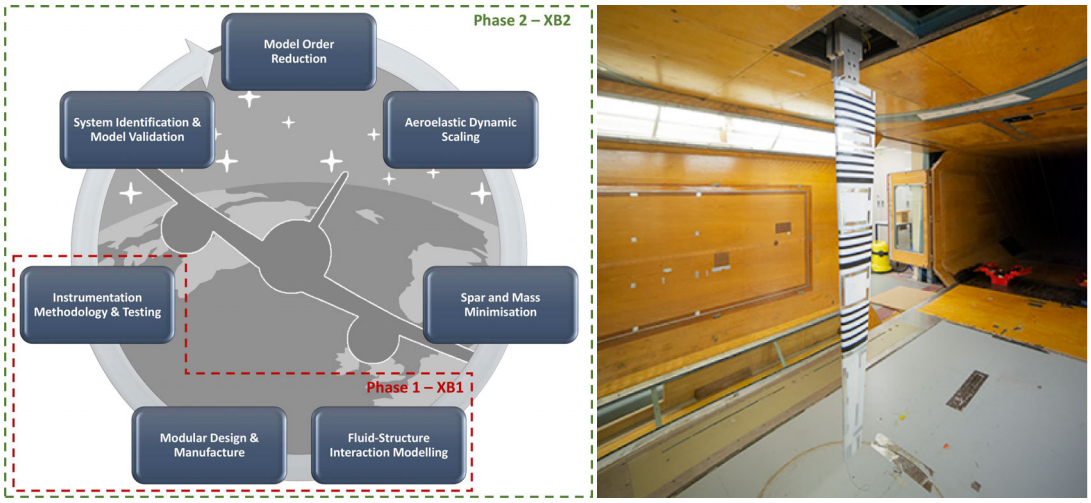

(a) *(b)*

Figure 3.1: BeaRDS work flow (Retrieved from [2]) and XB-2 in the 8'×6' Cranfield University's wind tunnel (Retrieved from [5]).

The XB-2 spar is made of 6082-T6 Aluminium. The tube and the connections are made of Stainless Steel, and the skin is made of strips of 3D printed Digital-ABS [38] and Agilus 30 [39], a rubber-like material printed together to guarantee

the structural continuity of the wing skin (no gaps). Figure 3.2 shows the skin's Digital-ABS and Agilus 30 sections, respectively, in white and black. The bespoke skin constitutes the aerodynamic surface of the wing, which is outlined by a NACA 23015 aerofoil and spans 1.5 m. The mean aerodynamic chord is 0.017 m with a taper ratio of 0.35, a Leading Edge sweep (Λ_{LE}) of 1.49° and a sweep $c/4$ ($\Lambda_{c/4}$) of 0°. The wing does not feature any dihedral or twist. The materials and physical properties are presented in Table 3.1. The subsequent subsection introduces the XB-2 wing's parts in detail.

Figure 3.2: XB-2 wing top view.

Table 3.1: Materials and physical properties.

Material	**Young Modulus [GPa]**	**Poisson Ratio [-]**	**Density [kgm^{-3}]**
6082-T6 Aluminium	70	0.33	2700
Stainless Steel	193	0.33	8000
Digital ABS	2.6–3.0	0.33 [14]	1170–1180
Agilus 30	NA	NA	1140
Property	**Details**	**Unit**	
Semi span	1.5	m	
$\bar{c}$	172	mm	
λ	0.35	-	
Λ_{LE}	14.9	°	
$\Lambda_{c/4}$	0	°	
Aerofoil	NACA 23015	-	
Mass	3.024	kg	

The Spars

The spar is made of 6082-T6 Aluminium Alloy, and it can be divided into three sections according to its spanwise position and geometric characteristics: root, mid-span and tip.

As shown in Figure 3.3, the spar features a Saint George's cross-shaped cross-section, which changes proportions along the span, and a rectangular cross-section in the root section, where the spar can be clamped. The three locations of interest along the span (root, mid-span and tip) are given in Table 3.2, where positions are with respect to the centroid of the root section's extremity: X-axis is in span-wise direction and positive in the outward direction, Y-axis describes the vertical placement with the positive direction upwards and the Z-axis is the depth, positive in the LE to TE (Trailing Edge) direction, as shown in Figure 3.3. Due to a manufacturing constraint, the spar was machined from two separate aluminium blocks, which were welded at mid-span and secured by a bolted bridge plate.

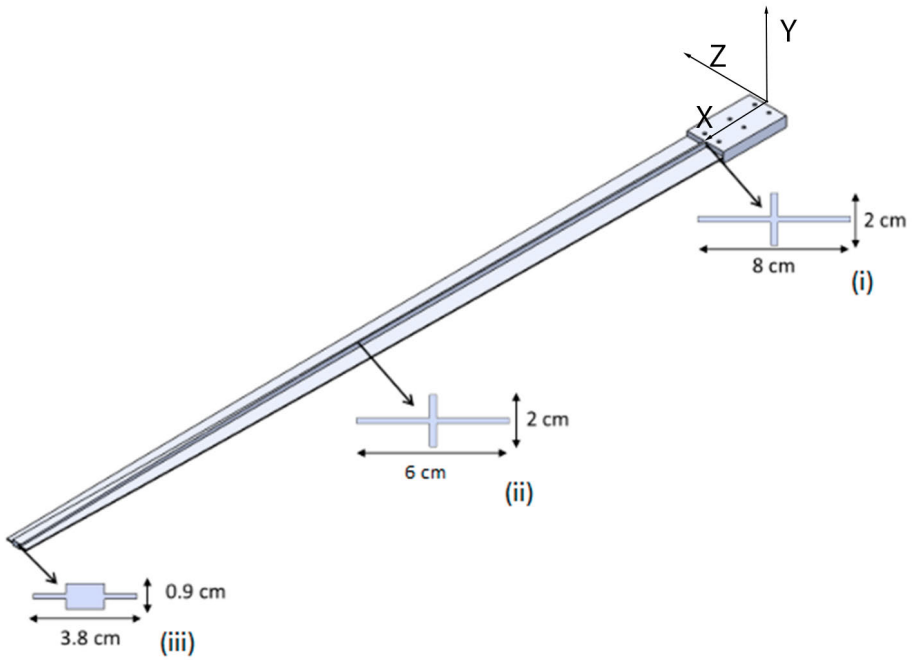

Figure 3.3: Main spar CAD model with section view at the location of interest: (**i**) root, (**ii**) mid-span, and (**iii**) tip (adapted from [3]).

Table 3.2: Spar's interest points location.

Section	**X [m]**	**Y [m]**	**Z [m]**
Root	0.125	0	0
Mid-span	0.875	0	0
Tip	1.45	0	0

Two identical samples of the spar specimen were manufactured, which we will refer to as the main spar and the twin spar for the remainder of the article. The twin spar was used for ground testing within BearDS, while the main spar is the specimen that served as the spar of the model tested in the wind tunnel. Their main difference is in the way the two halves are joined. The main spar features a reinforced bridge plate, featuring a “L” profile, rather than the simple plate used for the twin spar, as shown in Figure 3.4.

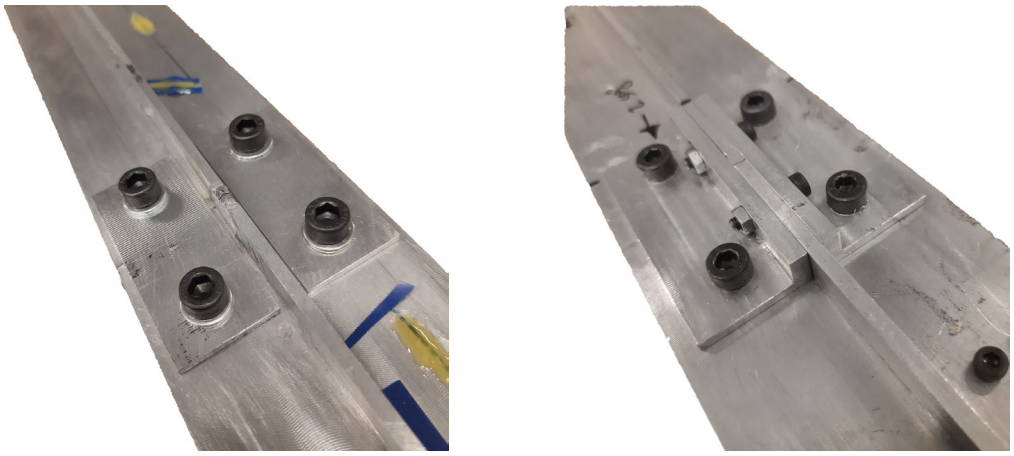

(a) *(b)*

Figure 3.4: Figure 3.4a shows the reinforced plate of the twin spar, while Section 3.2.1 shows the bridge of the main spar.

Another difference emerged when XB-2 was disassembled; the main spar was plastically deformed near the root, resulting in a 55 mm vertical deviation at the tip. The twin spar weighs 1.220 kg and the main spar 1.225 kg. Table 3.3 remarks on the differences between the twin and main spar.

Table 3.3: Spars descriptions.

Specimen	Description	Mass [kg]
Twin spar	The twin spar is a spar that was manufactured for ground testing only and it is recognisable from the main, or actual, spar for its bridge plate, as shown in Figure 3.4a.	1.220
Main spar	This is the spar used for the wind tunnel testing of XB-2 and its recognisable from the twin spar for its deformed shape and L profiled bridge plate, Figure 3.4b.	1.225

The Tube

The tube was introduced in the original scaling process of the full-scale wing to stiffen the wing sub-scale model and prevent flutter onset during wind tunnel testing [3]. It is placed parallel to the main spar, and it is attached to it at three points, as shown in Figure 3.5. The tube and links are made of Stainless Steel. The tube has an outer diameter of 10 mm and a thickness of 1 mm. The three rigid links and the tube's ends are positioned as per Table 3.4, where the reference is the same as considered for Table 3.2. The tube weighs 0.130 kg, and after its assembly with the main spar, shown in Figure 3.5, it weighs 1.362 kg.

Figure 3.5: The spar and tube assembly.

Table 3.4: Spar's interest points location.

Section	X [m]	Y [m]	Z [m]
Tube inner end	0.157	−0.002	0.045
First link	0.170	0	0.045
Second link	0.430	0	0.045
Third link	0.690	0	0.045
Tube outer end	0.707	−0.002	0.045

The Skin

The wing's skin is divided into four sections made up of 47 different subsections, which were 3D printed in Digital ABS and Agilus 30. The skin provides the aerodynamic shape of the wing and transfers the aerodynamic loads to the underlying structure. As shown in Figures 3.1b and 3.2, the black stripes on the wing are the rubber-like Agilus 30 strips, while the rest of the skin is made of Digital ABS. Remarkably, each section is printed using two different materials within the same print by using the Polyjet technique and not requiring glueing, or any other form of assembly, between the different stripes. With this arrangement in mind, the Agilus 30 stripes allow the skin to be flexible without compromising its integrity. The full wing assembly, as shown in Figure 3.2, weighs 3.024 kg.

3.2.2 Theoretical and Numerical Predictions

Prior to testing, a theoretical and numerical prediction of the first three bending modes was performed. The numerical prediction was achieved via the Euler-Bernoulli beam theory by calculating the first three theoretical bending frequencies of the main spar, as per the following Equation [40]:

$$f_i = \frac{\lambda_i^2}{2\pi \mathrm{L}^2}\sqrt{\frac{\mathrm{EI}}{m}} \qquad i = 1,2,3$$
$$\text{for } \lambda_{1-3} = \{1.87510407, 4.69409113, 7.85475744\} \tag{3.1}$$

where λ is the natural frequency parameter, L is the beam length, E is the Young Modulus, I is the second moment of inertia of the beam section, averaged over the beam span, and m is the mass per unit length. The value of λ corresponding to the mode of interest can be found in Equation (3.1) and they are related to the boundary conditions, which for this case is fixed to one end (cantilever beam). The value of L corresponds to the beam's span outboard of the clamp, so it is 1.325 m, and likewise for m. The mass of the beam without the root section was

estimated to be 650 g, and was divided by L to obtain m.

The numerical prediction was carried out with a FEM of the main spar, with the aim of identifying the first three bending modes' natural frequencies. The main spar was modelled as a tapered beam, with elements BEAM188 in ANSYS Mechanical APDL and the bridge at mid-span as a lumped mass of 44 g. As a further source of comparison, the results of a previous GVT campaign [3] on the twin spar are reported. Nevertheless, the testing setup was different because the previous campaign used a stinger shaker, rather than a shaker table, which influences the identified results. In fact, it was found in [41], on a similar structure, that the ω_n identified from a stinger shaker were higher than those from a shaker table experiment, due to the interaction between the structure and the stinger. Table 3.5 shows the first three bending modes' natural frequencies of the twin spar from predictions and the previous testing campaign of the twin spar [3]. The results show that the FEM and the previous GVT values are consistent with the theoretical prediction. In fact, the ω_1's value is almost the same across the different cases and for the remaining modes, they are within 10%.

Table 3.5: Results of the spar's natural frequencies' prediction and previous testing campaign.

Bending Mode	**Theoretical**	**Numerical**	**GVT [3]**
1st	5.166	5.183	5.27
2nd	32.373	30.837	27.12
3rd	90.646	106.060	83.39

3.2.3 Experimental Setup

A random verification at three increasing input scenarios was carried out for the twin spar, main spar, main spar and tube and full configuration of XB-2, as outlined in Table 3.6.

The specimens were driven by a Data Physics® Signal Force™ modal shaker

Table 3.6: Specimens of the testing campaign.

Specimen	Description	Mass [kg]
Twin spar	The twin spar is a spar that was manufactured for ground testing only, and it is recognisable from the main, or actual, spar for its bridge plate, as shown in Figure 3.4a.	1.220
Main spar	This is the spar used for the wind tunnel testing of XB-2 (Figure 3.4b).	1.225
Spar and tube	The spar and tube is the torque box of XB-2, which includes the main spar and the tube (Figure 3.5).	1.362
Full wing	This is the XB-2 wing, comprising spar, tube and skin (Figure 3.2).	3.024

controlled by DP760™ closed-loop control software running on a consumer-grade laptop. The data were collected by nine accelerometers, as per Table 3.7, and positioned along the span, as per Figure 3.6. One further accelerometer was placed on the clamp, serving as feedback for the shaker. The accelerometers are connected to a National Instruments cDAQ-9178, saving the data on a desktop machine via a LabVIEW program developed in-house. The experimental setup schematic is found in Figure 3.7. The accelerometer's span-wise position was decided using a sensor placement routine based on a genetic algorithm [42]. The FEM model used for the theoretical predictions was employed as a baseline, and a genetic algorithm minimised the sum of the off-diagonal terms of the autoMAC (Modal Assurance Criterion between the modes themselves) by varying the sensors' position along the span.

A random verification of different amplitude was used. A low, medium and high input level corresponded, respectively, to 0.305, 1.034 and 1.712 g RMS values. These input scenarios are referred to, respectively, as the low-, medium- and high-input scenarios for the remainder of this article. The random input signal was bandwidth limited between 2 and 400 Hz and had a 20 min duration.

Table 3.7: Accelerometers specifications.

ID #	Accelerometers Model	Sensitivity [mVg^{-1}]	Mass [g]
0	PCB Piezotronics® model: 352C23	4.88	0.2
1R	PCB Piezotronics® model: 356A16	96.50	7.4
1L	Isotron® accelerometer model 7251A	10.30	10.5
2R	PCB Piezotronics® model: 356A16	97.20	7.4
2L	Isotron® accelerometer model 7251A	10.08	10.5
3R	PCB Piezotronics® model: 356A45	100.20	4.2
3L	Isotron® accelerometer model 7251A	10.34	10.5
4R	Brüel & Kjær® accelerometer type 4507-002	94.12	4.8
4L	Brüel & Kjær® accelerometer type 4507-002	95.52	4.8

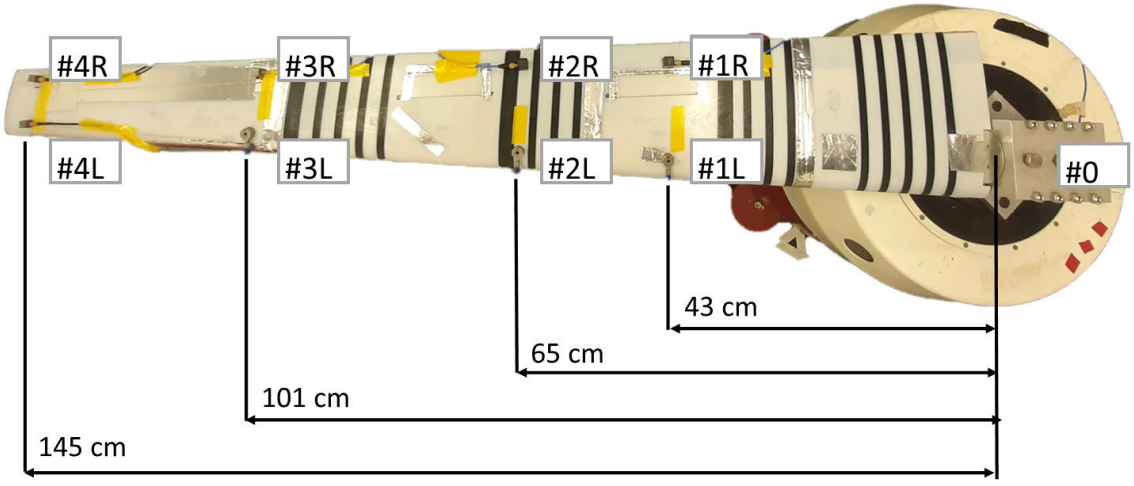

Figure 3.6: Accelerometers locations. The accelerometers do not appear aligned only for the optical effect of the camera lens.

3.2.4 Data Processing and Identification

Accounting for transients and consistency, the signals in the accompanying data [43] lasted 18 min, instead of 20, with a sampling frequency (f_s) of 256 Hz, down-sampled from the original $f_s = 5120$ Hz to smooth out the signal. Only the results for a single realisation of each scenario for each specimen are reported in this study, as the length of the signal and the nature of the input mitigate any possible significant discrepancies with repeated measurements. Since accelerometers #1-3R were tri-axial, the horizontal (Z-axis as per Figure 3.3) accelerations were recorded at those positions. Nevertheless, these analyses focus on the vertical and torsional modes of the specimens; hence, those data were disregarded for

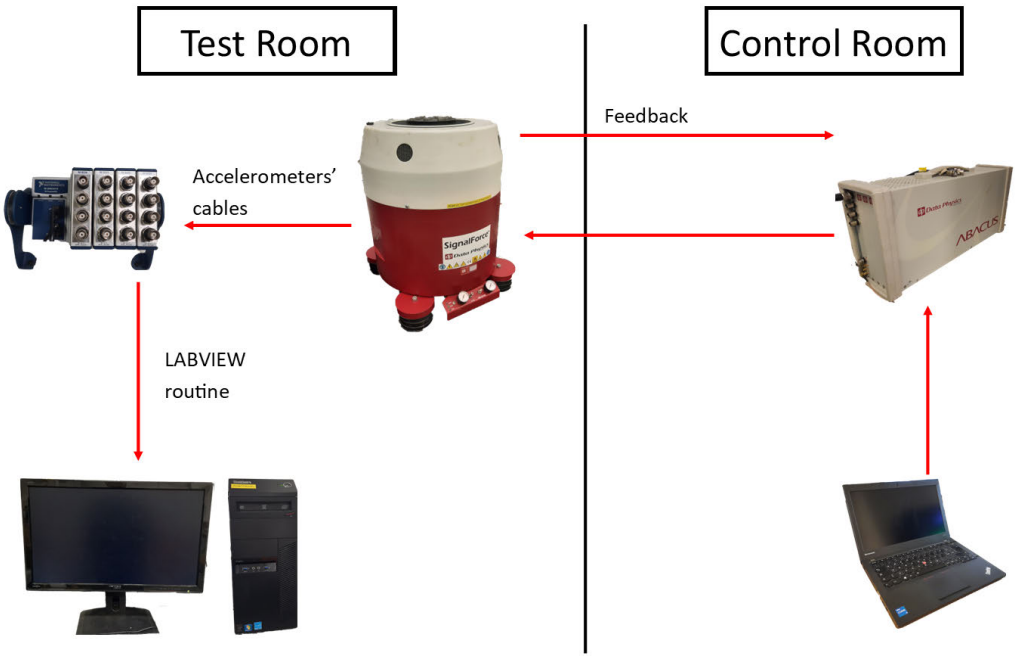

Figure 3.7: Testing setup.

identification. Given the three input amplitudes and the four specimens, twelve different testing cases exist, for which the first three modes' modal parameters, where vertical displacement was dominant, were extracted.

The signal, originally in g, was converted to ms^{-2} for adherence with the SI units, and the band-limited between 2.5 and 98 Hz to exclude the drifts at high and low frequencies. The FRFs were computed in the usual fashion, by element-wise division of the output's FFT with the input's FFT, with channel #0 as the input. A Savitzky–Golay filter of order 3 and length 601 was then applied to smooth out the response. At this point, the LSCE method was employed within a stabilisation diagram to identify the physical modes of all cases. The identification order ranged from 3 to 32 with steps of unity, and the stable modes were identified using the relative frequency (Δf) and damping ($\Delta\zeta$) and the MAC (Modal Assurance Criterion) of order-wise adjacent modes. The results of this procedure are presented in the following section.

3.3 Results

This section introduces the results obtained from the process outlined in the previous section. The results are presented separately for each specimen and input amplitude scenario. The data are presented both visually and numerically, presenting the FRFs computed from the experiment, the stabilisation diagram, a table with the identified modal parameters, the mode shapes diagrams and the FRFs' resonances comparisons. The results are then analysed and discussed in Section 3.4.

3.3.1 Twin Spar

Figure 3.8 shows the magnitude and phase for the FRFs of the high- and low-input scenarios. The first three resonance frequencies are clearly visible in both the magnitude and phase plot, where they are identified by, respectively, the peaks and phase change. The stabilisation diagram for the low-input scenario is shown in Figure 3.9. The identified ω_n and ζ_n for the three input cases are reported in Table 3.8 for the first three modes identified, which are all bending modes. Additionally, Table B.1 reports the raw identification data. Figure 3.10 compares the first three identified mode shapes for the three-input scenario with the baseline shape. The three $\boldsymbol{\phi}_{1-3}$ are pure bending modes and feature the expected shape from theory. Lastly for the twin spar, Figure 3.11 compares the FRF magnitude of the outermost left channel near the first three resonances.

Table 3.8: Twin spar: Natural frequency and damping ratio parameters.

Bending Mode	**Input**					
	Low		**Medium**		**High**	
	ω_n **[Hz]**	ζ_n **[-]**	ω_n **[Hz]**	ζ_n **[-]**	ω_n **[Hz]**	ζ_n **[-]**
1st	4.731	0.013	4.742	0.027	4.738	0.029
2nd	24.732	0.010	25.021	0.021	25.087	0.016
3rd	75.939	0.017	75.124	0.021	75.016	0.022

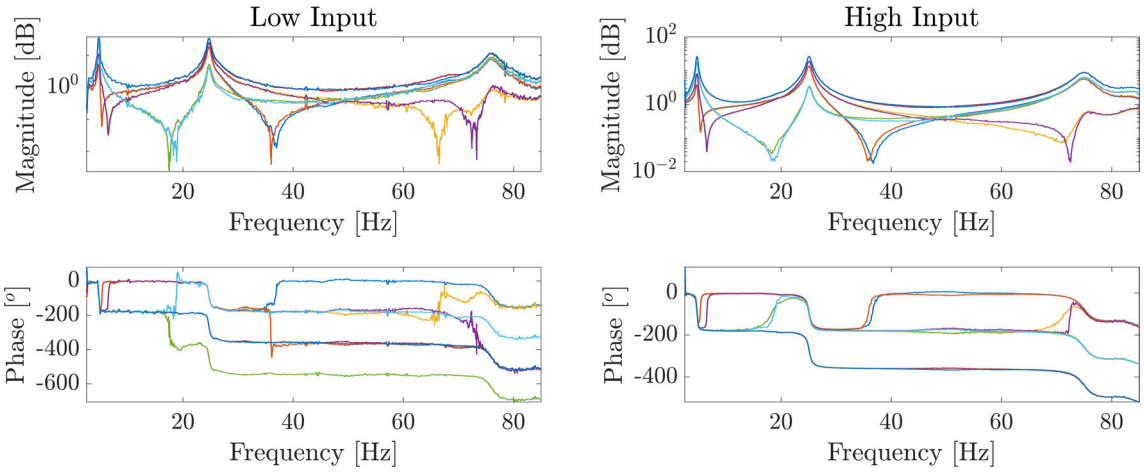

Figure 3.8: Twin spar: FRFs of the low and high input scenarios. All channels are superimposed for conciseness.

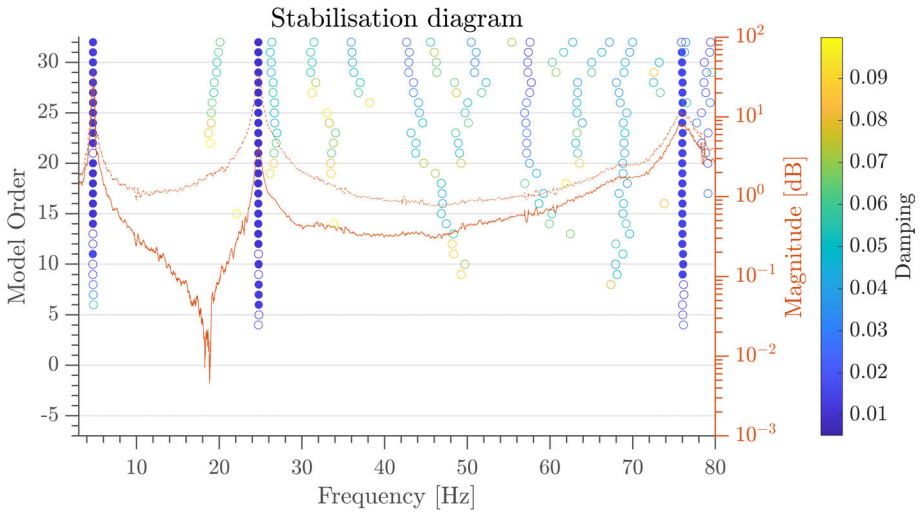

Figure 3.9: Twin spar: stabilisation diagram of the low-input scenario computed with the following parameters: $\Delta f = 1\%$, $\Delta\zeta = 5\%$ and MAC $= 0.95$. The FRF of channels # 3L and 4L are superimposed for further mode visualisation.

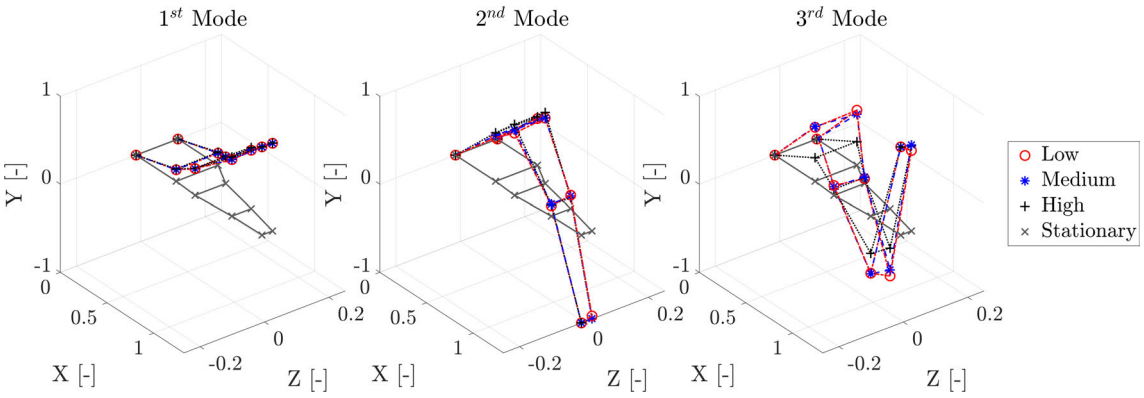

Figure 3.10: Twin spar: mode shapes of the first three vertically dominant modes.

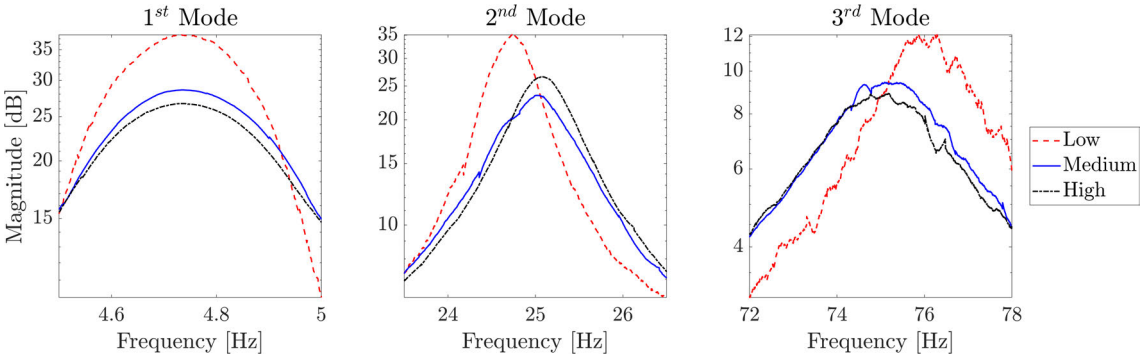

Figure 3.11: Twin spar: comparison of the FRFs of channel #4L for the three input scenarios near resonances.

The following subsections' content is presented in the same manner, and remarks are made only when necessary or when results need further insight.

3.3.2 Main Spar

As per Section 3.3.1, the FRFs of the low-, medium-, and high-input scenarios are presented in Figure 3.12, Figure 3.13 shows the stabilisation diagram for the low input case, while Table 3.9 presents the identified natural frequencies and damping ratios and Figure 3.14 displays the comparison between the mode shapes of the two input cases. Finally, Figure 3.15 compares the near-resonance region of the FRFs computed from channel #4L for the three input scenarios. The raw identification data are reported in Table B.2.

Table 3.9: Main Spar: natural frequency and damping ratio parameters.

Bending Mode	**Input**					
	Low		**Medium**		**High**	
	ω_n **[Hz]**	ζ_n **[-]**	ω_n **[Hz]**	ζ_n **[-]**	ω_n **[Hz]**	ζ_n **[-]**
1st	4.855	0.033	4.866	0.029	4.876	0.029
2nd	26.966	0.010	27.050	0.016	27.057	0.014
3rd	76.851	0.014	76.195	0.020	75.805	0.022

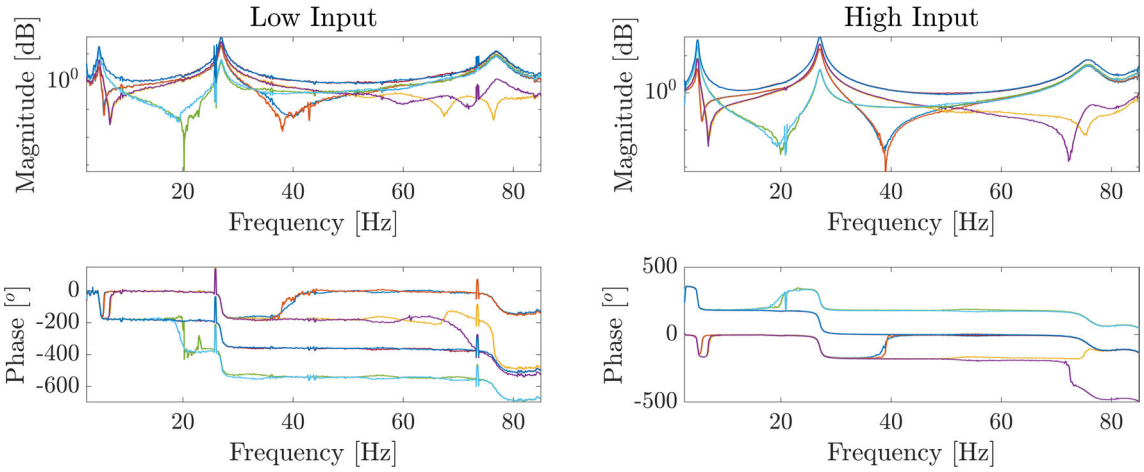

Figure 3.12: Main spar: FRFs of the low- and high-input scenarios. All channels are superimposed for conciseness.

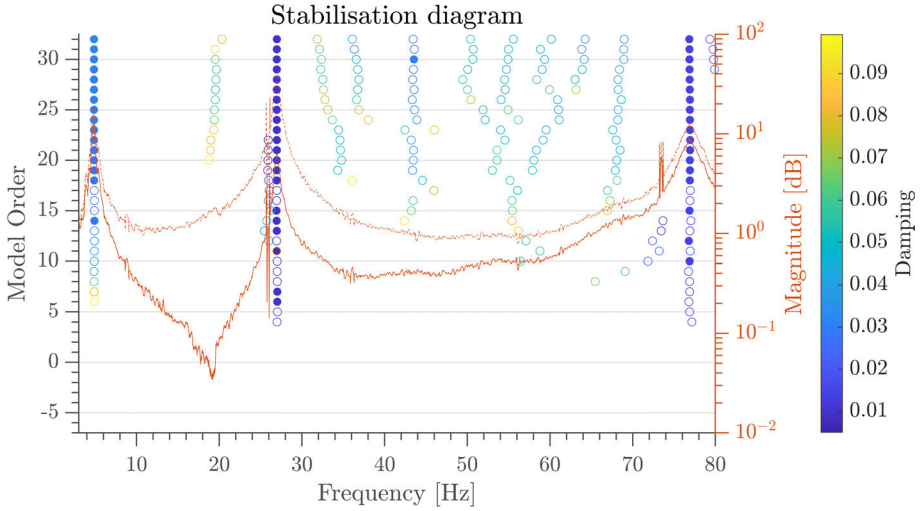

Figure 3.13: Main spar: Stabilisation diagrams showing the low-input scenario computed with the following parameters: $\Delta f = 1\%$, $\Delta \zeta = 5\%$ and MAC $= 0.95$. The FRF of channels # 3L and 4L are superimposed for further mode visualisation.

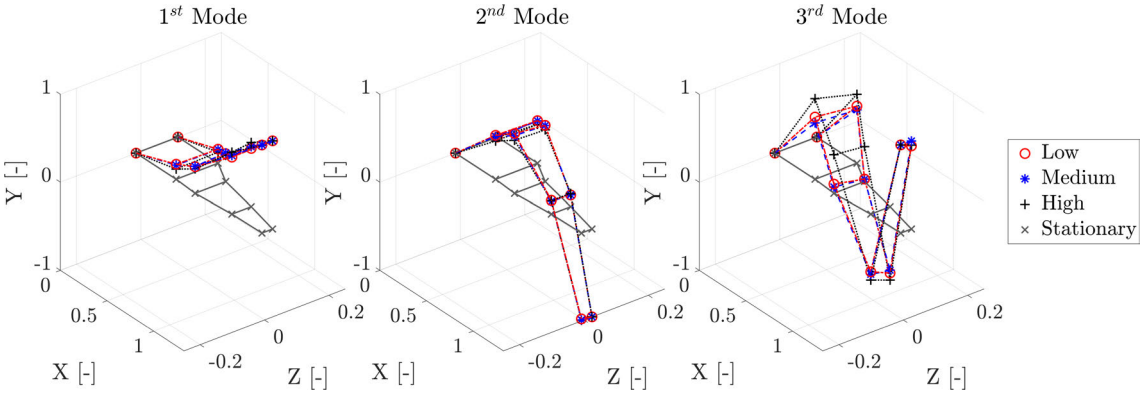

Figure 3.14: Main spar: mode shapes of the first three vertically dominant modes.

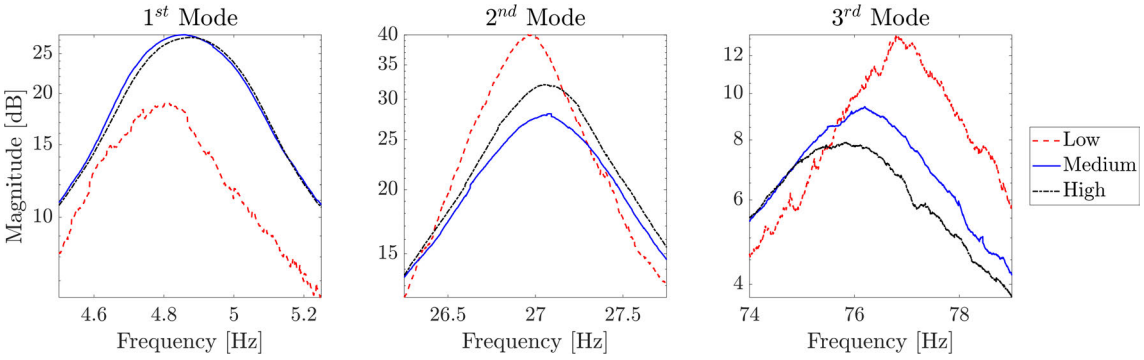

Figure 3.15: Main spar: comparison of the FRFs of channel #4L for the two input scenarios near resonances.

3.3.3 Spar and Tube

The spar and tube results are reported in the same fashion as in Sections 3.3.1 and 3.3.2. Figure 3.16 shows the superimposed FRFs channels, Figure 3.17 shows the stabilisation diagrams for the low- and high-input scenarios, Table 3.10 reports the identified natural frequencies and damping ratios, Figure 3.18 shows the first three vertical dominant modes and, finally, Figure 3.19 shows the comparison of the FRFs of the outermost left channel. In Table B.3, the raw identification data are reported.

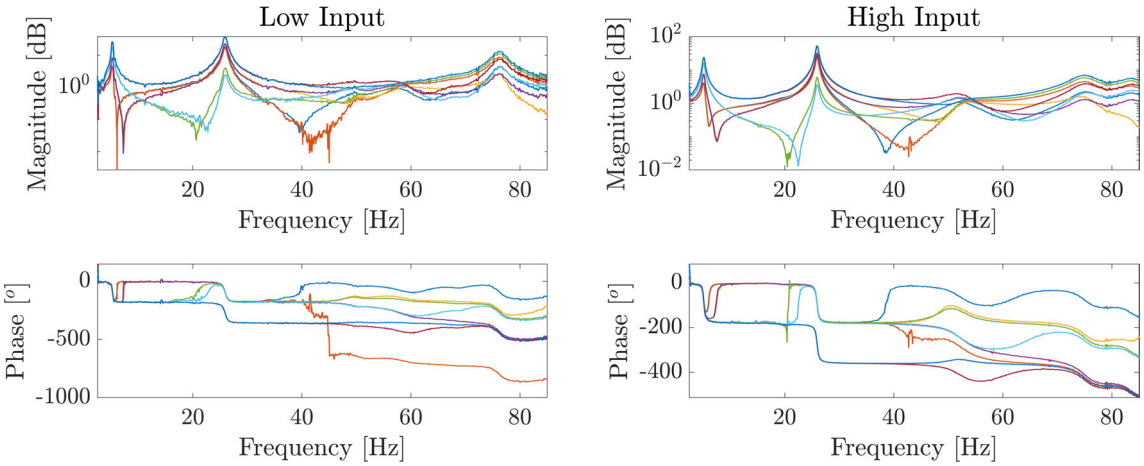

Figure 3.16: Spar and tube: FRFs of the low- and high-input scenarios. All channels are superimposed for conciseness.

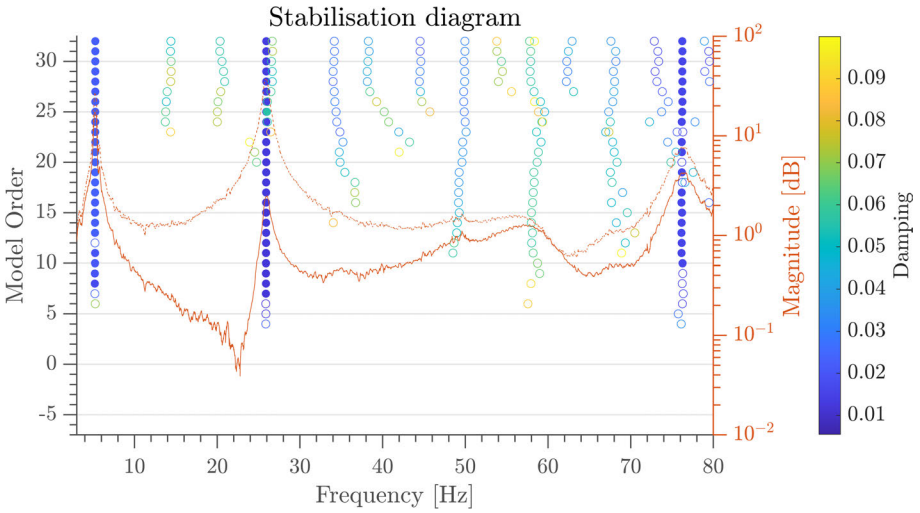

Figure 3.17: Spar and tube: Stabilisation diagrams the low-input scenario computed with the following parameters: $\Delta f = 1\%$, $\Delta\zeta = 5\%$ and MAC $= 0.95$. The FRF of channels # 3L and 4L are superimposed for further mode visualisation.

Table 3.10: Spar and tube: Natural frequency and damping ratio parameters.

Bending Mode	**Input**					
	Low		**Medium**		**High**	
	ω_n **[Hz]**	ζ_n **[-]**	ω_n **[Hz]**	ζ_n **[-]**	ω_n **[Hz]**	ζ_n **[-]**
1st Bending	5.252	0.022	5.151	0.030	5.163	0.036
2nd Bending	25.933	0.014	25.958	0.011	25.941	.010
3rd Coupled	76.242	0.017	75.770	0.034	75.135	0.034

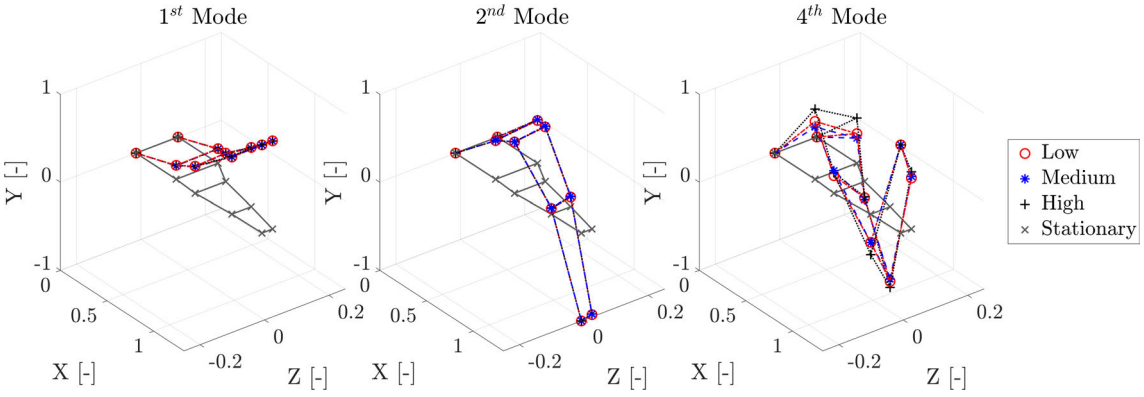

Figure 3.18: Spar and tube: Mode shapes of the first three vertically dominant modes.

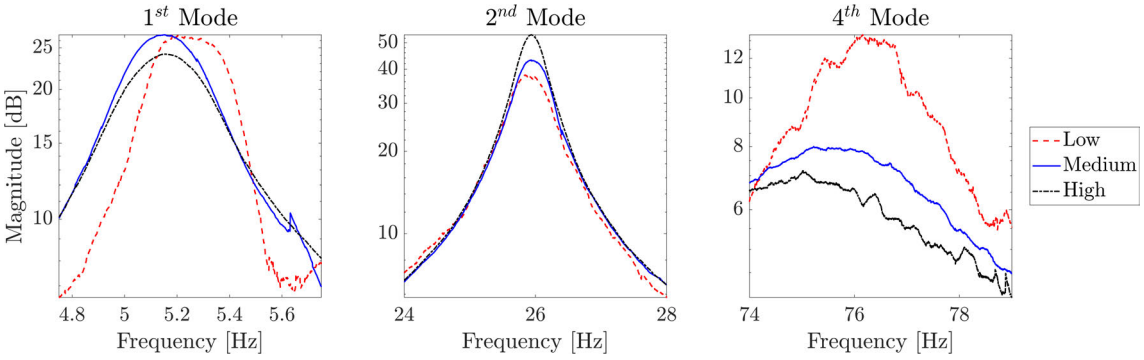

Figure 3.19: Spar and tube: Comparison of the FRFs of channel #4L for the two input scenarios near resonances.

3.3.4 Full Wing

The results for the full wing are reported in the same fashion as in previous sections. Figure 3.20 shows the FRFs, superimposed for conciseness, of the low- and high-input scenario, Table 3.11 reports the identified natural frequencies and damping ratios, Figure 3.22 shows the identified $\boldsymbol{\phi}_{1-2,4}$. Table B.4 shows the raw identification data.

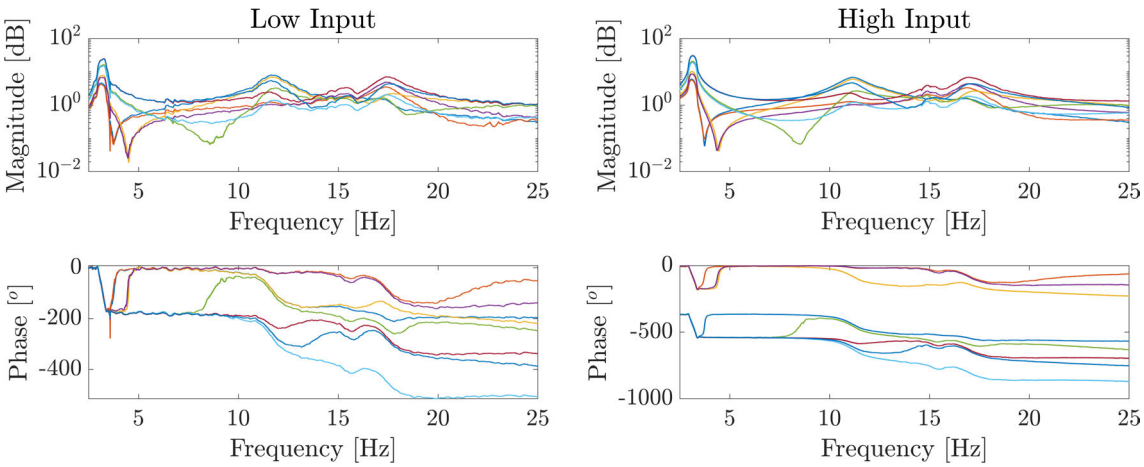

Figure 3.20: Full Wing: FRFs of the low- and high-input scenarios. All channels are superimposed for conciseness.

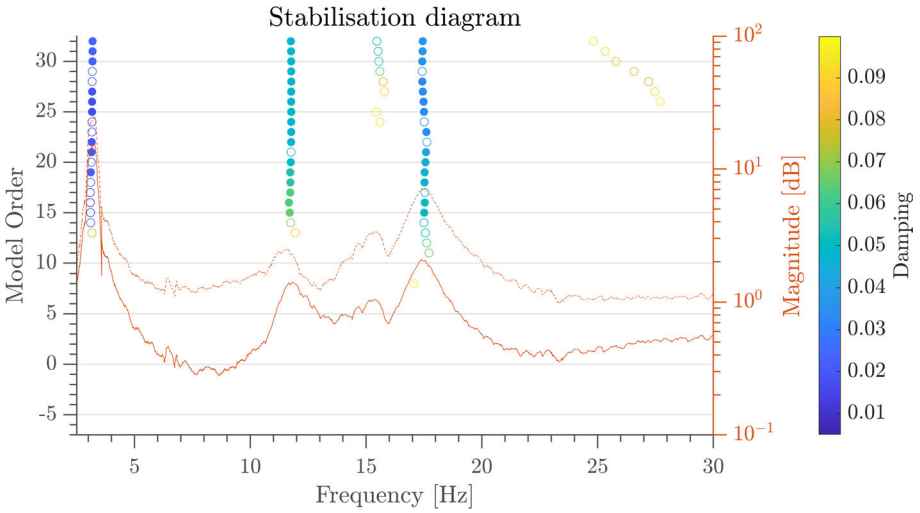

Figure 3.21: Full wing: stabilisation diagrams the low-input scenario computed with the following parameters: $\Delta f = 1\%$, $\Delta\zeta = 5\%$ and MAC $= 0.95$. The FRF of channels # 3L and 4L are superimposed for further mode visualisation.

Table 3.11: Full wing: natural frequency and damping ratio parameters.

Bending Mode	**Input**					
	Low		**Medium**		**High**	
	ω_n **[Hz]**	ζ_n **[-]**	ω_n **[Hz]**	ζ_n **[-]**	ω_n **[Hz]**	ζ_n **[-]**
1st Bending	3.187	0.024	3.164	0.018	3.139	0.018
2nd Coupled	11.752	0.047	11.267	0.060	11.196	0.065
4th Coupled	17.447	0.037	17.070	0.041	16.988	0.042

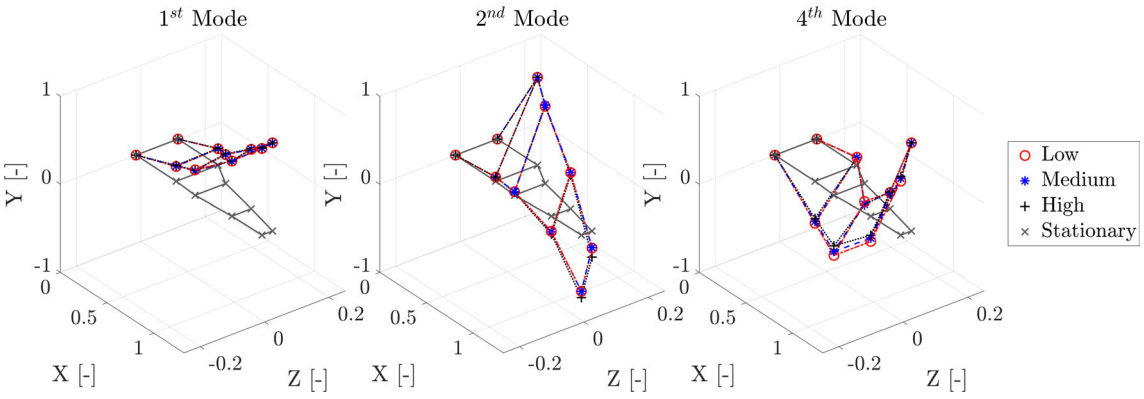

Figure 3.22: Full wing: mode shapes of the first three vertically dominant modes.

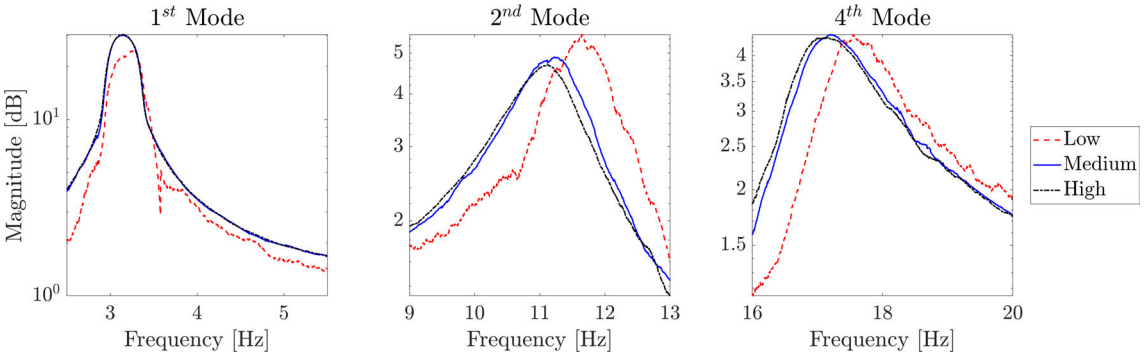

Figure 3.23: Full wing: comparison of the FRFs of channel #4L for the two input scenarios near resonances.

3.4 Discussion

This section deals with the discussion of the results introduced in the previous section and is organised as follows: the discussion is carried out separately for each part or sub-assembly.

3.4.1 Twin Spar

The twin spar results are coherent with the previous campaign results and predictions. The data in Table 3.5 are used as a source of comparison with the theoretical, numerical predictions and previous testing for the identified data in Equation (3.1) and Table 3.8. Nevertheless, a small difference can be identified, but it should be noted that the previous testing campaign used a stinger shaker, rather than a shaker table, hence influencing the identified modal parameters. However, as expected from [41], the ω_n identified in this test are lower than those from [3]. It should be noted that $\boldsymbol{\phi}_3$, while conserving the overall shape, deviates from the trajectory of the same mode shape for lower amplitudes. The comparison within the three input scenarios shows that the modal parameters are influenced by the input strength. However, a clear overall relationship cannot be assessed. The variations are most evident for the second and third mode, for which, respectively, hardening and softening behaviour are observed. Nonethe-

less, the same does not hold for ζ_{1-3} and $\boldsymbol{\phi}_{1-2}$. From the results in Table 3.8 and Figure 3.10, the damping is not dependent on the input scenario and likewise for the mode shapes.

3.4.2 Main Spar

The main spar's modal parameters estimation is closely comparable to the numerical predictions and previous testing campaign results presented in Section 3.2.2. The same argument relating to the shaker type mentioned for the twin spar is valid when the identified data are compared with the testing campaign in [3]. Despite the similar geometry to the twin spar, the identified natural frequencies are higher. The main cause of this discrepancy is to be attributed to the more robust bridge used in the latter, and to its deformed shape. Additionally, the effect of the different input scenarios is different on the main spar. The first and second modes show, in Figure 3.15 and Table 3.9, slight hardening behaviour and more pronounced softening behaviour on the third mode. Once again, the change in ω_{1-3} is not reflected in ζ_{1-3} and $\boldsymbol{\phi}_{1-2}$; for the former, the input scenario seems uncorrelated, while for the latter, it has no influence. Even so, for the medium-input scenario, a slight difference is noticed, but the difference itself does not create a variance in the overall shape, but the amplitude only. As already seen in the twin spar, $\boldsymbol{\phi}_3$ deviates from the trajectory of the same mode shape for lower amplitudes in positions 1R, 1L, 2L and 2R.

3.4.3 Spar and Tube

A numerical prediction for the spar and tube case was not performed in Section 3.2.2, but results similar to the main spar were expected and, indeed, obtained. For the first time in this work, a coupled mode—the third reported—is identified. This is most likely due to the effect of the tube on the dynamics of the

structure and elastic axis position. As clearly shown in Figure 3.18, the mode in question is coupled between bending and torsion. However, that mode is the fourth overall mode of the specimen, as a mode is also present between 50 and 60 Hz, but it was disregarded as its displacement was dominated by the horizontal component. For this case, the influence of the input amplitude is not evident, but for the third mode, the softening behaviour can be identified from Table 3.8 and Figure 3.11. Once again, ζ_{1-3} seems to be unrelated to the input amplitude and $\boldsymbol{\phi}_{1-3}$ to remain constant.

3.4.4 Full Wing

As for the spar and tube, a prediction was not available in Section 3.2.2. The full-wing modal survey detected the first three vertically dominant modes, as it is clear in Figures 3.20 and 3.21 that there are four modes in the scrutinised interval, but only the first and the last two were found to be vertically dominant. In this case, the relationship between the input amplitude and the modes is unambiguous. In fact, all the modes show a clear softening behaviour. The identified ω_n decrease is clearly inverse to the input amplitude. This is a clear indication of some sort of breathing crack phenomenon somewhere in the wing's span [44], or, as pointed out in [45], it can depend on the asymmetry of the loading, which induces a twisting moment, since the exciting force may not be applied in the shear centre. However, without further localised testing or inspections, this is not certain, and its characterisation is left to future works. Even in this case, no relation was found between the change in ζ_{1-3} and the input amplitude, while the $\boldsymbol{\phi}_{1-3}$ remain constant for all cases.

3.4.5 Overall Considerations

It is possible, and beneficial, to compare the result of the analyses across all specimens to develop a greater understanding of the structures themselves.

The first mode, for all specimens and cases, is always found to be a true bending mode. The second and third modes for the two spars are also considered bending modes. However, these change with the spar and tube, where the third mode is now coupled with bending and torsion. In the full-wing case, only the first mode is still pure bending. Considering the first mode, it can be seen that the addition of the stiffening tube and of the skin changes the structure. When the tube is added, ω_1 increases, while with the further addition of the skin, ω_1 decreases. The tube effectively stiffens the structure, while the skin, designed to only transfer and not carry any loads [3], effectively can be seen as an added mass on the structure. A comparison of the different structures based on ζ_n is not possible, as its changes do not follow any pattern, probably due to its intrinsic nature [46]. Concerning $\boldsymbol{\phi}_n$, it can be seen that $\boldsymbol{\phi}_1$ stays consistent throughout all specimens. This does not hold for $\boldsymbol{\phi}_2$, where differences can be assessed graphically (Figures 3.10, 3.14 and 3.18), particularly in channels #1-2LR, between the spars and the spar and tube assembly. The global considerations, focusing on the first mode, are that the different specimens behaved as expected, showing stiffening for the addition of the stiffening tube and, later, a decrease, when compared to the spar and tube, in stiffness for the full-wing scenario.

3.5 Conclusions

The high-aspect-ratio wing, its sub-assembly and its parts, totalling four specimens, are verified via Ground Vibration Testing on a shaker table by the means of random vibration at three different amplitudes. The signals recorded from the experiments are used to retrieve the modal parameters of the structures via the

Least Squares Complex Exponential. Only the modal parameters of the first three modes dominated by vertical displacement are obtained, due to equipment constraints which allow only the recording of vertical accelerations for all nodes. The modal parameters, and the near-resonance regions of the Frequency Response Functions, are then used for non-linearity detection. Finally, the experimental data are shared with the scientific community in an open repository, linked in the Data Availability Statement. Non-linearities, in the form of softening, are detected for the full-wing case. Additionally, the modal results of the different specimens are compared, assessing that the addition of the stiffening tube raises the bending stiffness and that the further addition of the skin increases the structure's mass, reducing the corresponding resonance frequency. This work serves as the first extensive modal survey carried out on the flexible wing under scrutiny and tuning of the numerical predictions' Finite Element Model, using the modal data from this study, remains an objective of future work.

References

[1] M. Civera, L. Zanotti Fragonara, and C. Surace, "Using video processing for the full-field identification of backbone curves in case of large vibrations," *Sensors*, vol. 19, no. 10, p. 2345, 2019, ISSN: 1424-8220, DOI: 10.3390/s19102345 (cit. on p. 59).

[2] A. Pontillo *et al.*, "Flexible high aspect ratio wing: low cost experimental model and computational framework," in *2018 AIAA Atmospheric Flight Mechanics Conference*, Kissimmee, FL: American Institute of Aeronautics and Astronautics, 2018, pp. 1–15, ISBN: 978-1-62410-525-8, DOI: 10.2514/6.2018-1014 (cit. on pp. 59, 63).

[3] S. Y. Yusuf, D. Hayes, A. Pontillo, M. A. Carrizales, G. X. Dussart, and M. M. Lone, "Aeroelastic Scaling for Flexible High Aspect Ratio Wings," in

AIAA Scitech 2019 Forum, Reston, Virginia: American Institute of Aeronautics and Astronautics, 2019, pp. 1–14, ISBN: 978-1-62410-578-4, DOI: 10.2514/6.2019-1594 (cit. on pp. 59, 63, 65, 67, 69, 81, 82, 84).

[4] D. Hayes, A. Pontillo, S. Y. Yusuf, M. M. Lone, and J. Whidborne, "High aspect ratio wing design using the minimum energy destruction principle," in *AIAA Scitech 2019 Forum*, Kissimmee, FL: American Institute of Aeronautics and Astronautics, 2019, ISBN: 978-1-62410-578-4, DOI: 10.2514/6.2019-1592 (cit. on pp. 59, 63).

[5] A. Pontillo, "High Aspect Ratio Wings on Commercial Aircraft: a Numerical and Experimental approach," PhD Thesis, Cranfield University, 2020 (cit. on pp. 59, 63).

[6] F. R. Spitznogle and A. H. Quazi, "Representation and analysis of time-limited signals using a Complex Exponential algorithm," *The Journal of The Acoustical Society of America*, vol. 47, no. 5 (Part I), pp. 1150–1155, 1970 (cit. on pp. 60, 62).

[7] F. R. Spitznogle, J. M. Barrett, C. I. Black, T. W. Ellis, and W. L. LaFuze, "Representation and analysis of sonar signals. Volume I. Improvements in the Complex Exponential signal analysis computational algorithm.," Office of Naval Research- Contract No. NOOO14-69-C0315,1971, Tech. Rep., 1971, p. 47 (cit. on pp. 60, 62).

[8] T. Verhulst, D. Judt, C. Lawson, Y. Chung, O. Al-Tayawe, and G. Ward, "Review for State-of-the-Art Health Monitoring Technologies on Airframe Fuel Pumps," *International Journal of Prognostics and Health Management*, vol. 13, no. 1, pp. 1–20, 2022, ISSN: 2153-2648, DOI: 10.36001/ijphm.2022.v13i1.3134 (cit. on p. 60).

[9] P. Rizzo and A. Enshaeian, "Challenges in bridge health monitoring: a review," *Sensors*, vol. 21, no. 13, p. 4336, 2021, ISSN: 1424-8220, DOI: 10.3390/s21134336 (cit. on p. 60).

[10] G. Dessena, M. Civera, L. Zanotti Fragonara, D. I. Ignatyev, and J. F. Whidborne, "A Loewner-based system identification and structural health monitoring approach for mechanical systems," *Structural Control and Health Monitoring [Accepted]*, p. 17, 2023 (cit. on p. 60).

[11] M. Civera, V. Mugnaini, and L. Zanotti Fragonara, "Machine learning-based automatic operational modal analysis: A structural health monitoring application to masonry arch bridges," *Structural Control and Health Monitoring*, no. May, pp. 1–23, 2022, ISSN: 1545-2255, DOI: 10.1002/stc.3028 (cit. on p. 60).

[12] G. Dessena, D. I. Ignatyev, J. F. Whidborne, and L. Zanotti Fragonara, "A Kriging Approach to Model Updating for Damage Detection," in *EWSHM 2022*, P. Rizzo and A. Milazzo, Eds., LNCE 254, Singapore: Springer, 2023, ch. 26, pp. 245–255, DOI: 10.1007/978-3-031-07258-1_26 (cit. on p. 60).

[13] F. De Florio, *Airworthiness*. Elsevier, 2011, ISBN: 9780080968025, DOI: 10.1016/C2010-0-65567-2 (cit. on p. 60).

[14] A. J. Keane, A. Sóbester, and J. P. Scanlan, *Small Unmanned Fixed-wing Aircraft Design*. Chichester, UK: John Wiley & Sons, 2017, ISBN: 9781119406303, DOI: 10.1002/9781119406303 (cit. on pp. 60, 64).

[15] J. P. Nöel, L. Renson, G. Kerschen, B. Peeters, S. Manzato, and J. Debille, "Nonlinear dynamic analysis of an F-16 aircraft using GVT data," in *IFASD 2013 - International Forum on Aeroelasticity and Structural Dynamics*, 2013, pp. 1–13 (cit. on pp. 60, 62).

[16] P. Lubrina, S. Giclais, C. Stephan, M. Boeswald, Y. Govers, and N. Botargues, "AIRBUS A350 XWB GVT: State-of-the-Art Techniques to Perform a Faster and Better GVT Campaign," in *Topics in Modal Analysis II, Volume 8. Conference Proceedings of the Society for Experimental Mechanics Series*, R. Allemang, Ed., vol. 45, Orlando, FL.: Springer, Cham, 2014, pp. 243–256, DOI: 10.1007/978-3-319-04774-4_24 (cit. on p. 60).

[17] K. J. Lemler and W. H. Semke, "Application of modal testing and analysis techniques on a sUAV," in *Conference Proceedings of the Society for Experimental Mechanics Series*, vol. 6, 2013, pp. 47–57, ISBN: 9781461465454, DOI: 10.1007/978-1-4614-6546-1_5 (cit. on p. 60).

[18] S. Weber *et al.*, "Application of fibre optic sensing systems to measure rotor blade structural dynamics," *Mechanical Systems and Signal Processing*, vol. 158, p. 107 758, 2021, ISSN: 08883270, DOI: 10.1016/j.ymssp.2021.107758 (cit. on p. 60).

[19] D. Göge, "Automatic updating of large aircraft models using experimental data from ground vibration testing," *Aerospace Science and Technology*, vol. 7, no. 1, pp. 33–45, 2003, ISSN: 12709638, DOI: 10.1016/S1270-9638(02)01184-7 (cit. on p. 60).

[20] W. Zhang, Z. Lv, Q. Diwu, and H. Zhong, "A flutter prediction method with low cost and low risk from test data," *Aerospace Science and Technology*, vol. 86, pp. 542–557, 2019, ISSN: 12709638, DOI: 10.1016/j.ast.2019.01.043 (cit. on p. 60).

[21] R. Pecora, F. Amoroso, R. Palumbo, M. Arena, G. Amendola, and I. Dimino, "Preliminary aeroelastic assessment of a large aeroplane equipped with a camber-morphing aileron," in *Industrial and Commercial Applications of Smart Structures Technologies 2017*, D. J. Clingman, Ed., vol. 10166,

2017, 101660E, ISBN: 9781510608177, DOI: 10.1117/12.2260008 (cit. on p. 61).

[22] G. Dessena, M. Civera, A. Pontillo, D. I. Ignatyev, J. F. Whidborne, and L. Zanotti Fragonara, "Comparative Study on Novel Modal Parameters Extraction Methods for Aeronautical Structures," *in preparation*, 2023 (cit. on p. 61).

[23] V. Mugnaini, L. Zanotti Fragonara, and M. Civera, "A machine learning approach for automatic operational modal analysis," *Mechanical Systems and Signal Processing*, vol. 170, no. February, p. 108 813, 2022, ISSN: 08883270, DOI: 10.1016/j.ymssp.2022.108813 (cit. on p. 61).

[24] I. Tsatsas, A. Pontillo, and M. Lone, "Aeroelastic damping estimation for a flexible high-aspect-ratio wing," *Journal of Aerospace Engineering*, vol. 35, no. 2, pp. 1–27, 2022, ISSN: 0893-1321, DOI: 10.1061/(ASCE)AS.1943-5525.0001390 (cit. on pp. 61, 62).

[25] Noviello, Dimino, Concilio, Amoroso, and Pecora, "Aeroelastic Assessments and Functional Hazard Analysis of a Regional Aircraft Equipped with Morphing Winglets," *Aerospace*, vol. 6, no. 10, p. 104, 2019, ISSN: 2226-4310, DOI: 10.3390/aerospace6100104 (cit. on p. 61).

[26] D. J. Ewins, *Modal Testing Theory, Practice and Application*, 2nd. Baldock, UK: Research Studies Press, 2000, p. 562, ISBN: 978-0-863-80218-4 (cit. on p. 61).

[27] K. Worden and G. R. Tomlinson, *Nonlinearity in Structural Dynamics Detection, Identification and Modelling*. Bristol, UK: Institute of Physics Publishing, 2001, ISBN: 0750303565 (cit. on p. 61).

[28] G. Kerschen, K. Worden, A. F. Vakakis, and J.-C. Golinval, "Past, present and future of nonlinear system identification in structural dynamics," *Mechanical Systems and Signal Processing*, vol. 20, no. 3, pp. 505–592,

2006, ISSN: 08883270, DOI: 10.1016/j.ymssp.2005.04.008 (cit. on p. 61).

[29] T. Dossogne *et al.*, "Nonlinear ground vibration identification of an F-16 aircraft - Part II: Understanding nonlinear behaviour in aerospace structures using sine-sweep testing," *International Forum on Aeroelasticity and Structural Dynamics, IFASD 2015*, pp. 1–19, 2015 (cit. on p. 61).

[30] G. Kerschen, L. Soula, J. B. Vergniaud, and A. Newerla, "Assessment of Nonlinear System Identification Methods using the SmallSat Spacecraft Structure," in *Conference Proceedings of the Society for Experimental Mechanics Series*, vol. 1, 2011, pp. 203–219, ISBN: 9781441993014, DOI: 10.1007/978-1-4419-9302-1_18 (cit. on p. 61).

[31] J. Noël and G. Kerschen, "Nonlinear system identification in structural dynamics: 10 more years of progress," *Mechanical Systems and Signal Processing*, vol. 83, pp. 2–35, 2017, ISSN: 08883270, DOI: 10.1016/j.ymssp.2016.07.020 (cit. on p. 61).

[32] M. Civera, S. Grivet-Talocia, C. Surace, and L. Zanotti Fragonara, "A generalised power-law formulation for the modelling of damping and stiffness nonlinearities," *Mechanical Systems and Signal Processing*, vol. 153, p. 107 531, 2021, ISSN: 10961216, DOI: 10.1016/j.ymssp.2020.107531 (cit. on p. 62).

[33] G. Kerschen, M. Peeters, J. C. Golinval, and C. Stéphan, "Nonlinear modal analysis of a full-scale aircraft," *Journal of Aircraft*, vol. 50, no. 5, pp. 1409–1419, 2013, ISSN: 0021-8669, DOI: 10.2514/1.C031918 (cit. on p. 62).

[34] L. Zanotti Fragonara *et al.*, "Dynamic investigation on the Mirandola bell tower in post-earthquake scenarios," *Bulletin of Earthquake Engineering*, vol. 15, no. 1, pp. 313–337, 2017, ISSN: 1570-761X, DOI: 10.1007/s10518-016-9970-z (cit. on p. 62).

[35] F. Dezi, F. Gara, and D. Roia, "Dynamic Characterization of Open-ended Pipe Piles in Marine Environment," in *Applied Studies of Coastal and Marine Environments*, InTech, 2016, pp. 169–204, DOI: 10.5772/62055 (cit. on p. 62).

[36] D. L. Brown, R. J. Allemang, R. Zimmerman, and M. Mergeay, "Parameter estimation techniques for modal analysis," in *1979 Automotive Engineering Congress and Exposition*, Univ.of Cincinnati, 1979, p. 19, DOI: 10.4271/790221 (cit. on p. 62).

[37] N. M. M. Maia, "Extraction of valid modal properties from measured data in structural vibrations," PhD Thesis, Imperial College London, 1988, p. 380 (cit. on p. 62).

[38] Stratasys, *Digital ABS plus*, 2021, [Online]. Available: https://www.stratasys.com/it/materials/search/digital-abs-plus (visited on 2021) (cit. on p. 63).

[39] Stratasys, *Agilus 30*, 2021, [Online]. Available: https://www.stratasys.com/materials/search/agilus30 (cit. on p. 63).

[40] R. D. Blevins, "Formulas for Dynamics, Acoustics and Vibration," *Formulas for Dynamics, Acoustics and Vibration*, pp. 1–448, 2015, DOI: 10.1002/9781119038122 (cit. on p. 68).

[41] X. Hu, "Effects of stinger axial dynamics and mass compensation methods on experimental modal analysis," PhD Thesis, Iowa State University, Digital Repository, Ames, 1992, DOI: 10.31274/rtd-180813-9382 (cit. on pp. 69, 81).

[42] A. Schulze, J. Zierath, S.-E. Rosenow, R. Bockhahn, R. Rachholz, and C. Woernle, "Optimal sensor placement for modal testing on wind turbines," *Journal of Physics: Conference Series*, vol. 753, no. 7, p. 072 031, 2016, ISSN: 1742-6588, DOI: 10.1088/1742-6596/753/7/072031 (cit. on p. 70).

[43] G. Dessena, *Data supporting: Ground Vibration Testing of a Flexible Wing: A Benchmark and Case Study*, 2022, DOI: 10.17862/cranfield.rd.19077023 (cit. on p. 71).

[44] L. Yang, Z. Mao, S. Wu, X. Chen, and R. Yan, "Nonlinear dynamic behavior of rotating blade with breathing crack," *Frontiers of Mechanical Engineering*, vol. 16, no. 1, pp. 196–220, 2021, ISSN: 20950241, DOI: 10.1007/s11465-020-0609-z (cit. on p. 83).

[45] A. Pagani and E. Carrera, "Unified formulation of geometrically nonlinear refined beam theories," *Mechanics of Advanced Materials and Structures*, vol. 25, no. 1, pp. 15–31, 2018, ISSN: 15376532, DOI: 10.1080/15376494.2016.1232458 (cit. on p. 83).

[46] M. Civera, G. Calamai, and L. Zanotti Fragonara, "System identification via Fast Relaxed Vector Fitting for the Structural Health Monitoring of masonry bridges," *Structures*, vol. 30, no. January, pp. 277–293, 2021, ISSN: 23520124, DOI: 10.1016/j.istruc.2020.12.073 (cit. on p. 84).

Chapter 4

Comparative study on novel modal parameters extraction methods for aeronautical structures[1]

Abstract

Experimental Modal Analysis in general, and Ground Vibration Testing in particular for Aerospace applications, are a vital part of the design and certification process for civil and military aircraft. Two recently developed system identification techniques in the frequency domain, Fast Relaxed Vector Fitting and Loewner Framework, have been successfully applied to civil and mechanical systems for the extraction of modal parameters. In this work, both are used for the extraction of the modal parameters in aeronautically relevant structures for damage detection and aeroelastic modelling; respectively, a numerical model of a small fixed-wing unmanned aerial system spar and an experimental case study of a high aspect ratio flexible wing. The signal from different damage and loading scenar-

[1] This is an adapted version of the following preprint in preparation for submission to *Aerospace Science and Technology*: Dessena, G., Civera, M., Ignatyev, D. I., Whidborne, J., Zanotti Fragonara, L. (2023). Comparative study on novel modal parameters extraction methods for aeronautical structures

ios for the numerical system is corrupted with different levels of noise to assess the sensitivity, to changes in the structure, and the robustness to noise of the modal parameters obtained from the methods. Results are benchmarked against the known exact values. Then, the modal parameters identified from the experimental data are used to build a reduced-order model to characterise aeroelastic phenomena onset speeds. The modal parameters identified by the techniques are compared to those derived from a well-established method: Numerical algorithms for subspace state space system identification (N4SID). In addition, the experimental data from the ground vibration testing of the high aspect ratio wing is made available in an open repository.

4.1 Introduction

System Identification (SI) is an important and mature field [1] and finds application in many engineering domains, including aerodynamics [2] and structures [3]. Its main application in structural dynamics is for the modelling of systems from experimental, or operational, data to characterise its modal parameters [4]. The characterisation of a system's modal parameters is known as modal analysis [5] and it can be divided in two subdomains: Experimental Modal Analysis (EMA) [6] and Operational Modal Analysis (OMA) [7]. The former takes into consideration input and output data for the parameters extraction, while the latter only the output [8]. The identified modal parameters, such as natural frequencies (ω_n), damping ratios (ζ_n), and mode shapes ($\boldsymbol{\phi}_n$), can have two main applications: vibration-based damage detection [9] and model updating [10].

In aeronautics, a particular kind of EMA, very commonly used, is known as Ground Vibration Testing (GVT) and it is a vital part of the design and certification process of civil aircraft [11] and a customary procedure for small Unmanned Aerial Systems (UAS) [12]. In particular, GVT can be carried out on the whole vehicle

[13], or on components, such wings or helicopter blades [14]. In particular, GVT is fundamental to validate the Finite Element Models (FEMs) developed during the design process and used for the estimation of the maximum static deflection and aeroelastic phenomena onset speeds [15]. This work aims to compare, on Aeronautical structures, two recently developed SI methods for the extraction of modal parameters in mechanical systems from frequency domain data: the Loewner Framework (LF) [16] and Fast Relaxed Vector Fitting (FRVF) [17]. The two methods' performance is weighted against two test cases: (i) the numerical simulation of a small fixed-wing UAS wing spar modelled in three different damaged scenarios and one loaded case, and (ii) the Numerical algorithms for subspace state space System IDentification (N4SID) [18], considered an industry standard [19], applied to an experimental case study concerning a High Aspect Ratio (HAR) flexible wing with four loaded cases. The comparison between LF and FRVF has the goal to assess the methods' robustness to noise, sensitivity to changes in the target system and their computational performance.

The results of the modal identification are then employed to build a two degrees of freedom (DoF) - flapping and pitching - reduced order model (ROM) for the characterisation of aeroelastic phenomena onset speeds. The modal data from each respective method (N4SID, LF, and FRVF) and scenario are used to build twelve independent models, where the N4SID-derived models are taken as the benchmark. The goal of this comparison is to assess the sensitivity of the methods to small changes in the structure by employing the results for the modelling of aeroelastic phenomena. Ultimately, the methods should obtain an aeroelastic onset speed close to the one derived from the N4SID models and also respect their trends, such as a decrease or increase in the onset speed between two given scenarios. For this method, a 20 % underestimation is expected [12], so the error should be within this limit. The experimental data for the GVT of the HAR flexible wing is made available to interested readers in a Cranfield Online

Research Data entry.

The remainder of this article is organised as follows. Section 4.2 recalls the theoretical backbone of the identification methods used and the use of modal parameters in damage detection and aeroelastic reduced order modelling. In Section 4.3 the numerical case study is introduced and its results are discussed. Following, Section 4.4 deals with the experimental case study of the HAR wing. The specimen and the experimental setup are introduced prior to outlining the modal characterisation results, which leads to the aeroelastic analysis. The paper is closed by a concluding section.

4.2 Methods

A thorough review of the SI discipline, or of its use for modal analysis, is not within the scope of this work and the interested reader is referred to the books [20, 21], for SI, and to the classical work [22], for the SI role in modal analysis. Nevertheless, an introduction to the three SI methods used within this work is necessary. This is followed by their application for damage detection and a description of the aeroelastic ROM used in this work.

4.2.1 Numerical algorithms for(4) subspace state space System IDentification

N4SID is regarded as a state-of-the-art method for *linear* EMA in industrial and civil engineering [16]. Its main aim is to define a system, under known excitation, as a linear time-invariant (LTI) system in state space form [18]:

$$\begin{aligned} \boldsymbol{x}_{k+1} &= \boldsymbol{A}\boldsymbol{x}_k + \boldsymbol{B}\boldsymbol{u}_k + \boldsymbol{w}_k \\ \boldsymbol{y}_k &= \boldsymbol{C}\boldsymbol{x}_k + \boldsymbol{D}\boldsymbol{u}_k + \boldsymbol{v}_k \end{aligned} \tag{4.1}$$

with

$$\hat{\boldsymbol{E}}\left[\begin{pmatrix}\boldsymbol{w}_p\\ \boldsymbol{v}_p\end{pmatrix}(\boldsymbol{w}_q^T \boldsymbol{v}_q^T)\right]=\begin{pmatrix}\boldsymbol{Q} & \boldsymbol{S}\\ \boldsymbol{S}^T & \boldsymbol{R}\end{pmatrix}\delta_{pq}\geq 0 \tag{4.2}$$

where $\boldsymbol{A}\in\mathbb{R}^{n\times n}$ is the system matrix, $\boldsymbol{B}\in\mathbb{R}^{n\times m}$ is the input matrix, $\boldsymbol{C}\in\mathbb{R}^{l\times n}$ is the output matrix, $\boldsymbol{D}\in\mathbb{R}^{l\times m}$ direct feed-through matrix, m is the number of inputs, l is the number of outputs and n is the order of the unknown system. The vectors $\boldsymbol{u}_k\in\mathbb{R}^{m\times 1}$ and $\boldsymbol{y}_k\in\mathbb{R}^{l\times 1}$ are the measurements of, respectively, the inputs and outputs of the process at a time instant k. The $\boldsymbol{x}_k$ vector is the process' state vector at a discrete time instant k, $\boldsymbol{v}_k\in\mathbb{R}^{l\times 1}$ is the measurement noise vector and $\boldsymbol{w}_k\in\mathbb{R}^{n\times 1}$ is the process noise vector. Vectors $\boldsymbol{v}_k$ and $\boldsymbol{w}_k$ are assumed to be zero mean stationary white noise vectors sequences and uncorrelated with the inputs $\boldsymbol{u}_k$. The matrices $\boldsymbol{Q}\in\mathbb{R}^{n\times n}$, $\boldsymbol{S}\in\mathbb{R}^{n\times l}$, and $\boldsymbol{R}\in\mathbb{R}^{l\times l}$ are the covariance matrices of $\boldsymbol{v}_k$ and $\boldsymbol{w}_k$, while $\hat{\boldsymbol{E}}$ is the expected value operator and δ_{pq} is the Kronecker delta. The N4SID identification procedure can be divided in two subsequent parts:

1. the extended observability matrix, $\boldsymbol{\Gamma}_j$, and the estimate of the state sequence X_i , $\tilde{\boldsymbol{X}}_i$, are developed from the input-output data via projection and singular value decompositions;

2. A simple set of overdetermined equations, in the least squares sense, is solved using $\tilde{\boldsymbol{X}}_i$, with a given set of weights specific to N4SID, to obtain the state space matrices and noise model.

The full theoretical background of N4SID can be found in [18].

4.2.2 Fast and Relaxed Vector Fitting

The FRVF, firstly documented in its current and complete form in [23], originated as an improved version of the standard VF algorithm, proposed by Gustavsen & Semlyen in 1999 for the modelling of large multiport electrical circuits [24]. With respect to the Vector Fitting (VF) algorithm, the FRVF adds a relaxed non-trivial

constraint in the pole identification step [25, 26] and exploits the matrix form of the linear problem and QR decomposition, such that a matrix $\boldsymbol{A} = \boldsymbol{QR}$, for fast computation. In its current form, as also applied here, the FRVF procedure was tested and applied for the first time for the SI of simple mechanical systems in [27] and to large civil structures and infrastructures in [17].

The functioning principles of FRVF can be briefly recalled as follows. It is an iterative process, where – for an arbitrary number of iterations, set by the user a priori – an initial set of poles is relocated according to a linear least-squares problem, aiming at reducing the divergence between the estimated transfer function and the experimentally-recorded input-output data. That is to say, the complex-valued data $\boldsymbol{f}(s) \in \mathbb{C}^{p \times k}$ (for k frequency samples, defined over $s = j\omega$, and for p Frequency Response Functions (FRFs) are approximated (for a generic single input-multiple outputs configuration) by the rational function:

$$\boldsymbol{f}(s) \approx \sum_{m=1}^{N_p} \frac{\boldsymbol{c}_m}{s - a_m} + \boldsymbol{d} + s\boldsymbol{e} \tag{4.3}$$

where N_p is the pre-set number of poles to be identified, a_m is the m-th pole (at any given iteration), and $\boldsymbol{c}_m$ is the corresponding vector of residues. The poles are all complex conjugates, thus they come in pairs as $a_m = -\alpha + j\beta$, $a_{(m+1)} = -\alpha - i\beta$, where the real part is strictly negative (i.e. they all lie in the left half of the complex plane) to ensure the stability of the dynamic system. For the first set of poles, β is linearly spaced over the frequency range of interest and $\alpha = \beta/100$. These represent the departing points for the iterative, deterministic optimisation procedure. The components of the rational model described in Equation (4.3) can then be seen as the parameters of the state-space model, such:

$$\boldsymbol{f}(s) \approx \boldsymbol{C}(s\boldsymbol{I} - \boldsymbol{A})^{-1}\boldsymbol{b} + \boldsymbol{d} + s\boldsymbol{e} \tag{4.4}$$

where, according to the common terminology of state-space modelling, $\boldsymbol{A} \in$

$\mathbb{C}^{k\times k}$ is the system matrix, $\boldsymbol{b} \in \mathbb{R}^{k\times 1}$ is the input matrix (which, for this application, is reduced to a column vector of ones), $\boldsymbol{C} \in \mathbb{C}^{p\times k}$ is the output matrix, $\boldsymbol{d} \in \mathbb{R}^{p\times 1}$ is the feedthrough matrix (again, reduced to a column vector for a single input scenario), and $\boldsymbol{e} \in \mathbb{R}^{p\times 1}$ contains the terms proportional to s (generally all zeroed and included here for completeness only). The VF identifies the poles of $\boldsymbol{f}(s)$ by solving (in the least-square sense) the following linear problem.

$$\boldsymbol{\sigma}(s)\boldsymbol{f}(s) = \boldsymbol{p}(s) \tag{4.5}$$

where $\boldsymbol{\sigma}(s) = \sum_{m=1}^{k} \tilde{\boldsymbol{c}}_m/(s-q_m) + 1$ and $\boldsymbol{p}(s) = \sum_{m=1}^{k} \tilde{\boldsymbol{c}}_m/(s-q_m) + \boldsymbol{d} + s\boldsymbol{e}$; q_m indicates the m-th tentative pole. In the FRVF variant, the definition of $\boldsymbol{\sigma}(s)$ is slightly changed; specifically, it is relaxed as

$$\boldsymbol{\sigma}(s) = \sum_{m=1}^{k} \frac{\tilde{\boldsymbol{c}}_m}{s-q_m} + \tilde{\boldsymbol{d}} \tag{4.6}$$

where $\tilde{\boldsymbol{d}}$ is real but not necessarily unity (even if it is expected to approach 1 as the procedure converges throughout the subsequent iterations).

Thus, the pole relocation procedure aims at achieving the terms p_m that most closely resemble their (unknown) counterparts (a_m), such that the root-mean-square error of approximation for $\boldsymbol{f}(s)$, i.e. the error of the fitting, is minimised.

More details concerning the implementation and the several technical aspects can be found in the book of Grivet-Talocia & Gustavsen [26].

4.2.3 Loewner Framework

The LF was first introduced as a single-input multi-output system identification (SI) for the extraction of modal parameters (natural frequencies, ω_n, damping ratios, ζ_n, and mode shapes $\boldsymbol{\phi}_n$) for vibration-based SHM [28] of mechanical systems in the frequency domain. The LF was notably proposed in [29] as a model order reduction (MOR) technique for large dynamical systems, but its origins can

be traced back to the 1930s, when the Loewner interpolation matrix ($\mathbb{L}$), was introduced by Charles Loewner [30]. Antoulas et al. [31, 32] have developed the LF for the MOR of dynamical systems by considering tangential interpolation, or rational interpolation along tangential directions [33]. Later, they have applied it to the SI of electronic systems in [34, 35] to relax the the severely ill-conditioning of current fitting processes[35].

Given an LTI dynamical system $\boldsymbol{\Sigma}$ with k internal variables in descriptor-form representation, m inputs and p outputs:

$$\begin{aligned} \boldsymbol{\Sigma}: \ \boldsymbol{E}\frac{d}{dt}\boldsymbol{x}(t) &= \boldsymbol{A}\boldsymbol{x}(t) + \boldsymbol{B}\boldsymbol{u}(t) \\ \boldsymbol{y}(t) &= \boldsymbol{C}\boldsymbol{x}(t) + \boldsymbol{D}\boldsymbol{u}(t) \end{aligned} \tag{4.7}$$

where $\boldsymbol{x}(t) \in \mathbb{R}^k$ is the internal variable, $\boldsymbol{u}(t) \in \mathbb{R}^m$ is the function's input and $\boldsymbol{y}(t) \in \mathbb{R}^p$ is the output. The constant matrices are:

$$\boldsymbol{E}, \boldsymbol{A} \in \mathbb{R}^{k\times k}, \ \boldsymbol{B} \in \mathbb{R}^{k\times m} \ \boldsymbol{C} \in \mathbb{R}^{p\times k} \ \boldsymbol{D} \in \mathbb{R}^{p\times m} \tag{4.8}$$

When, for a given finite value λ, the matrix $\boldsymbol{A} - \lambda\boldsymbol{E}$ is non singular, such that $\lambda \in \mathbb{C}$, a Laplace transfer function, $\boldsymbol{H}(s)$, of $\boldsymbol{\Sigma}$ can be defined in the form of a $p \times m$ rational matrix function:

$$\boldsymbol{H}(s) = \boldsymbol{C}(s\boldsymbol{E} - \boldsymbol{A})^{-1}\boldsymbol{B} + \boldsymbol{D} \tag{4.9}$$

The LF, via tangential interpolation, actively fits the frequency response functions (FRFs) data to $H(s)$. The aim does not differ from more established techniques, such as rational fraction polynomial. A theoretical exposition of the LF is found in [31], while the authors' contributions to the implementation of the LF is outlined in full detail in [16], a comparison on its computational performance is found in [36] and a MATLAB tutorial is given in [37].

4.2.4 Uses for Damage Detection

A change in a system which undermines or affects its operational capability is defined as damage [38]. For this reason, reliability and safety concerns are a main driver in engineering [39] and it is the duty of operators and regulators to oversee this process [40] to avoid distressing and catastrophic events [41]. The statistical pattern recognition strategy of damage detection in aeronautical [42], civil [43] and mechanical engineering [44] systems is known as Structural Health Monitoring (SHM) [38]. The said procedure can be condensed in four steps:

1. operational evaluation: the system specific damage is postulated, constraints are identified and operation conditions are evaluated;

2. data acquisition: comprising, for vibration-based SHM, OMA or EMA, and its post-processing

3. features selection: the damage relevant features are identified;

4. damage assessment: the developed statistical model is used to assess the presence, extent, location, type, and severity of the damage.

As mentioned, the modal parameters, predominantly ω_n and $\boldsymbol{\phi}_n$, obtained from SI of vibration data are used for damage detection. Modal parameters are a common choice for SHM [45] since a direct relationship between them and a system's mass and stiffness exists [28]. Within this work, ω_n are used mainly for damage severity assessment, rather than localisation, since the small changes in ω_n can easily be buried by environmental and operational variations [46]. $\boldsymbol{\phi}_n$ are more suited for localisation than ω_n as its trajectory variate locally where damage is present. Also damage severity can be inferred from $\boldsymbol{\phi}_n$ as the trajectory change gets more pronounced as the damage increases [16]. Hence, a combination of the two is used for damage severity and localisation. Severity assessment is carried by comparing the changes in ω_n values and the relative changes in

$\boldsymbol{\phi}_n$ trajectories, while localisation is obtained from the local changes in trajectory from an undamaged scenario. Damage quantification is out of the scope of this work as the damage scenarios are known a priori. ζ_n is not used as a damage indicator due to its nature, since it has a strong dependence on non-structural factors, and can lead to misleading results [17]. However, ζ_n is considered for comparison purposes to assess the sensitivity and precision of LF and FRVF versus numerical and benchmark, N4SID, results.

The reader interested in a general overview of SHM can consult [47], a specialised review on vibration-based SHM that employ modal data is found in [28] and a summary on the state of industry implementation for SHM is found in [48].

4.2.5 Aeroelastic Reduced Order Model

Aeroelasticity is concerned with the interaction between aerodynamic, elastic and inertia loads. This interaction can arise in an unstable manner; hence, generating the so called aeroelastic phenomena [49]. In general, aeroelasticity can be divided into two sub groups: static and dynamic [11]. The former includes divergence and aileron reversal, while the latter's main concern is flutter. The division arises from the fact that static phenomena can depend solely on quasi-static behaviours, while flutter has a harmonic dependence:

- *Divergence* happens when the moments due to aerodynamic loads overcome the restoring moments of the wing's structure resulting in structural failure.

- *Aileron*, or control, *reversal* is the phenomenon for which as the flight speed increases, the effectiveness is reduced until some critical speed when there is opposite, or no, response from the inputs.

- *Flutter* occurs at some critical speed where the structure sustains oscillations following an initial disturbance. When the oscillations happen below

the flutter speed they are sufficiently damped, but, near the said speed, unstable oscillations occur when damping reaches zero.

The reader interested in a more profound review on the subject is referred to [50, 51] and to [52, 53] for some practical applications to flexible wings.

In this work, an aeroelastic model is developed to assess, respectively, static and dynamic aeroelasticity phenomena of the different experimental configurations. The main focus is to detect divergence and flutter onset speeds, control reversal is ignored as the specimen does not feature moving control surfaces. The model proposed is based on the first assumed flapping (bending) and pitching (torsion) modes only. For simplicity, an aeroelastic model for a rectangular flexible wing is used; so, a 2 DoF (degrees of freedom) model based on oscillatory aerodynamics, an extension for flexible wings of the classic binary aeroelastic model [11, 54], is selected.

First, let us define the deflection, z, of a point (x, y) on the wing such as:

$$z = y^2 q_1 + y(x - x_f) q_2) \tag{4.10}$$

where q_1 and q_2 are the generalised coordinates and, for each chordwise strip, $q_1 y^2$ and $q_2 y$ are, respectively, the flapping deflection and the pitch angle. Then, by determining the kinetic and potential energy and the incremental work from Equation (4.10) the following equations are obtained:

$$m\begin{bmatrix} \frac{cs^5}{5} & \frac{s^4}{4}\left(\frac{c^2}{2}-cx_f\right) \\ \frac{s^4}{4}\left(\frac{c^2}{2}-cx_f\right) & \frac{s^3}{3}\left(\frac{c^3}{3}-c^2x_f+cx_f^2\right) \end{bmatrix}\begin{Bmatrix}\ddot{q}_1\\ \ddot{q}_2\end{Bmatrix}+ \\ +\rho V\begin{bmatrix} \frac{ca_ws^5}{10} & 0 \\ -\frac{c^2ea_ws^4}{8} & -\frac{c^3s^3M_{\dot{\theta}}}{24} \end{bmatrix}\begin{Bmatrix}\dot{q}_1\\ \dot{q}_2\end{Bmatrix}+ \\ +\left(\rho V\begin{bmatrix} 0 & \frac{ca_ws^4}{8} \\ 0 & -\frac{c^2ea_ws^3}{6} \end{bmatrix}+\begin{bmatrix} 4EIs & 0 \\ 0 & GJs \end{bmatrix}\right)\begin{Bmatrix}q_1\\ q_2\end{Bmatrix}=\begin{Bmatrix}0\\ 0\end{Bmatrix} \quad (4.11)$$

where m is mass per unit area in kgm^{-2}, c is the wing's chord in m, s is the wing's span in m, x_f is the flexural axis position with respect to c, ρ is the air density in kgm^{-3}, V is the air speed in ms^{-1}, a_w is the lift curve slope, $M_{\dot{\theta}}$ is the non-dimensional pitch damping derivative, EI is the bending, or flapping, stiffness, and GJ is the torsional, or pitching, stiffness. Figure 4.1 shows the schematic for the wing's ROM.

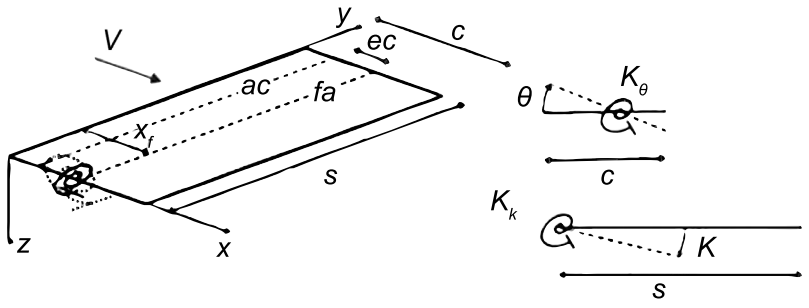

Figure 4.1: Flexible wing 2 DoF model schematic (adapted from [11]).

Equation (4.11) is a special form, for the zero structural damping case $\boldsymbol{D}=0$, of the following:

$$\boldsymbol{A}\ddot{\boldsymbol{q}}+(\rho V\boldsymbol{B}+\boldsymbol{D})\dot{\boldsymbol{q}}+\left(\rho V^2\boldsymbol{C}+\boldsymbol{E}\right)\dot{\boldsymbol{q}}=\boldsymbol{0} \quad (4.12)$$

where $\boldsymbol{A}$ is the mass, or inertia, matrix, $\boldsymbol{B}$ is the aerodynamic damping matrix, $\boldsymbol{C}$ is the aerodynamic stiffness matrix, $\boldsymbol{D}$ is the structural damping and $\boldsymbol{E}$ is the

stiffness matrix. Now, considering the availability of modal data and assuming that the measured damping is dependent solely on the structure itself. $\boldsymbol{D}$ can be built from the uncoupled modal damping assumption in [55]:

$$\boldsymbol{D} = \boldsymbol{\phi}^{-T}\boldsymbol{D}_n\boldsymbol{\phi}^{-1} \text{ for } \boldsymbol{D}_n = 2\zeta_n\omega_n A_n \tag{4.13}$$

where the subscript n identifies the uncoupled matrix, ω_n the natural frequency, ζ_n the damping ratio and $\boldsymbol{\phi}_n$ the mode shape. Hence, Equations (4.11) and (4.13) can be combined to assemble Equation (4.12). Given full knowledge of the wing's geometric characteristics, three properties remain to be defined: $M_{\dot{\theta}}$, EI, and GJ. $M_{\dot{\theta}}$ is the unsteady aerodynamics term and it is defined from oscillatory aerodynamics [11]:

$$\begin{aligned} M_{\dot{\theta}} = 2\pi\Bigg[&-\frac{k}{2}\left(\frac{1}{2}-a\right) + kF\left(a+\frac{1}{2}\right)\left(\frac{1}{2}-a\right) + \\ &+\frac{G}{k}\left(\frac{1}{2}+a\right)\Bigg] \end{aligned} \tag{4.14}$$

where k is the reduced frequency, a is the ratio between c and the flexural axis position, and F and G are, respectively, the real and imaginary part of the Theodorsen's function, $C(k)$, such that:

$$C(k) = F(k) + jG(k) = \frac{H_1^{(2)}(k)}{H_1^{(2)}(k) + jH_1^{(2)}(k)} \tag{4.15}$$

where $H_n^{(2)}(k)$ are Hankel functions of the second kind and j is the imaginary number. The explanation of the concepts of unsteady aerodynamics, $C(k)$, and reduced frequency k are beyond the scope of this work and the interested reader is referred to [11, 56] for a thorough review.

Concerning the flapping and pitching stiffness, EI and GJ, let us consider the still air case where $\boldsymbol{B}$ and $\boldsymbol{C}$ are zero. Equation (4.12) then becomes a simple mass-spring-damper system:

$$\boldsymbol{A}\ddot{\boldsymbol{q}} + \boldsymbol{D}\dot{\boldsymbol{q}} + \boldsymbol{E}\dot{\boldsymbol{q}} = \boldsymbol{0} \tag{4.16}$$

The natural frequencies can then be easily extracted through eigenanalysis. Hence, by having a set of experimental ω_n it is possible to define the EI and GJ of the equivalent system by minimising its squared difference to the experimental ω_n. In order to obtain a stable result the eigenanalysis can be solved iteratively with the well-known p-k method [57] to find the divergence and flutter onset speeds. The p-k method is based on the hypothesis that pure harmonic aerodynamics stands as a good approximation for lightly damped harmonic motions. This allows the computation of the aerodynamic transfer matrix at a complex frequency $p = \delta \pm jk$, such that $p \approx jk$. In simple terms, the real part, the damping, is neglected. A widely accepted workflow of the p-k [11] method can be summarised as follow:

1. Initiate an estimation, usually the still air value, of p, said $p_0 = \delta \pm jk_0$
2. Evaluate the aerodynamics, in our case $M_{\dot{\theta}}$
3. Solve the eigenvalue (λ) problem for Equation (4.12) and obtain a new set of λ, $p_1 = \delta \pm jk_1$
4. Iterate between 2 and 3 until $k_n \approx k_{n-1}$

From the λ obtained after convergence, it is possible to build ω_n, ζ_n, real(λ) and imag(λ) vs air-speed (U_∞) plots, which can be used to graphically obtain divergence and flutter speed. Particularly, critical speeds are identified for ζ_n approaching zero or for real(λ) zero crossings, since both cases are interpreted as instability in the system. Particularly, for flutter only the real(λ) zero crossing condition needs to be satisfied, while for divergence also imag(λ) must be zero.

4.3 Numerical Case Study

For the aim of comparing the resilience to noise of the LF and FRVF SI methods, a numerical case study is set. The selected system mimics a structure of interest in Aeronautical Engineering: the wing spar of a small (MTOW $<$ 7 kg) fixed-wing UAS.

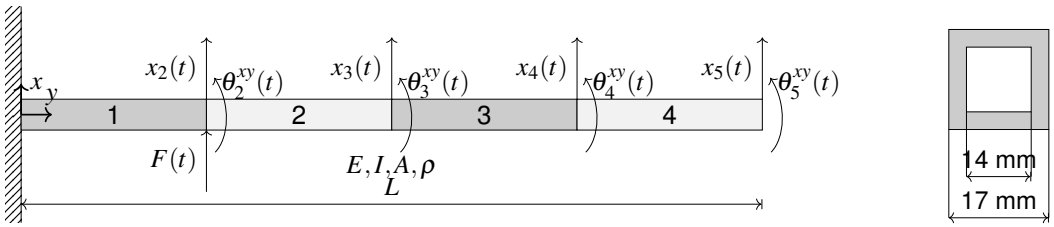

(a) (b)

Figure 4.2: 4-element beam: Figure 4.2a is the schematic drawing of the 4-element Euler-Bernoulli beam and Figure 4.2b is the schematic of the beam's square box cross-section with the relative dimensions.

The spar is discretised as a 4-element 2-D Euler-Bernoulli cantilever beam, where the DoF are rotations (θ_n^{xy}) and vertical displacement (x_n), as shown in Figure 4.2a. The spar's square box cross section is shown in Figure 4.2b. The

Table 4.1: 4-element beam: Physical properties.

Property	**Value**	**Units**
Material	6061-T6 Aluminium	-
Elastic modulus - E	70	GPa
Second moment of area - I_{zz}	$3.759e^{-9}$	m^4
Area - A	$9.3e^{-5}$	m^2
Density - ρ	2700	kgm^{-3}
Span - L	1.1	m

physical properties of the beam in Figure 4.2 are portrayed in Table 4.1, except for ζ_n, which is set to 3% for all modes. Five different scenarios, summarised in Table 4.2, exist for the spar. The ζ_n stays constant in all cases as they are the parameter most heavily influenced by noise; hence, comparison based on ζ_n is deferred to experimental examples in the following section. The five scenarios serve also as a benchmark for the SHM capabilities of LF and FRVF.

Table 4.2: 4-element beam: damage and mass addition scenarios.

Scenario	Characteristics
1	Baseline
2	5% stiffness reduction in the third element.
3	10% stiffness reduction in the third element.
4	30% stiffness reduction in the third element.
5	pylon and engine at the spar's midpoint, discretised as a 0.3 kg lumped mass.

For all scenarios, the numerical system is excited with a unit (1 N) impulse force at the second vertical node (x_2 in Figure 4.2a), the data is recorded at a sampling frequency $f_s = 2^{14}$Hz. Hence, according to Nyquist sampling criterion only the frequencies up to 8192 Hz are inspectable, allowing for the detection of all the eight (known to be upper limited to circa 4000 Hz) modes available. The FFT of the vertical displacements, in m, and of the rotations, in rad, are divided by the FFT of the input force, in N, to obtain the receptance FRFs. Since both LF and FRVF can be applied to SIMO systems, only the case with all output channels available are considered. Table 4.3 lists the ω_n for the five cases of the numerical case. The expected [28] decrease in ω_n is clearly visible and serves as a further ground of comparison for the investigation in Section 4.3.1.

4.3.1 Investigation of Noise Effects

To test the resilience of the LF and FRVF to noise, both input and output channels are, respectively, corrupted with an additive white Gaussian noise at 0, 0.1, 0.2, 0.5, 1, 1.5, 2, 3, 4, and 5%, totalling ten independent cases per scenario. Input-only and output-only noise are not taken into consideration as the input-only noise has negligible effect and the output-only noise has a comparable effect to output-input noise, as shown in [16] for LF and in [27] for FRVF. The noise percentage was defined as a fraction of the signal's standard deviation (σ). Since LF is a numerical method primed by random starting points, defining the tangential directions, a numerical study over the ten noise cases for the five scenarios was

Table 4.3: Natural Frequencies of the numerical models of all scenarios.

	Natural Frequency [Hz]				
Case	1	2	3	4	5
Mode	Baseline	5% damage (%)	10% damage (%)	30% damage (%)	Add mass (%)
1	14.964	14.944 (-0.13)	14.924 (-0.27)	14.211 (-5.04)	5.896 (-60.60)
2	93.885	92.916 (-1.03)	91.874 (-2.25)	89.096 (-5.10)	45.180 (-51.88)
3	264.607	262.353 (-0.85)	260.002 (-1.74)	253.123 (-4.34)	95.389 (-63.95)
4	522.013	518.853 (-0.61)	515.414 (-1.26)	499.181 (-4.37)	383.078 (-26.61)
5	970.919	965.534 (-0.55)	960.097 (-1.12)	936.212 (-3.58)	522.125 (-46.22)
6	1559.300	1545.990 (-0.85)	1531.896 (-1.76)	1485.550 (-4.73)	1320.226 (-15.33)
7	2472.008	2454.272 (-0.72)	2436.426 (-1.44)	2294.185 (-7.19)	1583.006 (-35.96)
8	4056.045	4041.186 (-0.37)	4026.559 (-0.73)	4039.617 (-0.41)	3778.317 (-6.85)

carried by running the identification 100 times at the minimum order. On the other hand, FRVF is a fully deterministic method and such a study is not needed; nevertheless, FRVF is an iterative process and for the scope of this work the number of iterations was set to 5 at its minimum order. The minimum order k for detecting 8 modes for both LF and FRVF is 16.

Figure 4.3 shows the comparison between the identified ω_n from LF and FRVF and the numerical values. Since the LF has a random starting condition, the LF frequencies are labelled as identifications if they satisfy two stability requirements: (i) a maximum 10% deviation from the expected numerical result and (ii) should appear at least in 90 realisations out of 100. In this case, the results reported here correspond to the mean over all such realisations. Conversely, for the FRVF, the initial set of poles is uniformly spaced in the frequency range of interest; hence, for the values identified via FRVF, only the first requirement is considered.

The results of the identified ζ_n, shown in percentage, are presented in Fig-

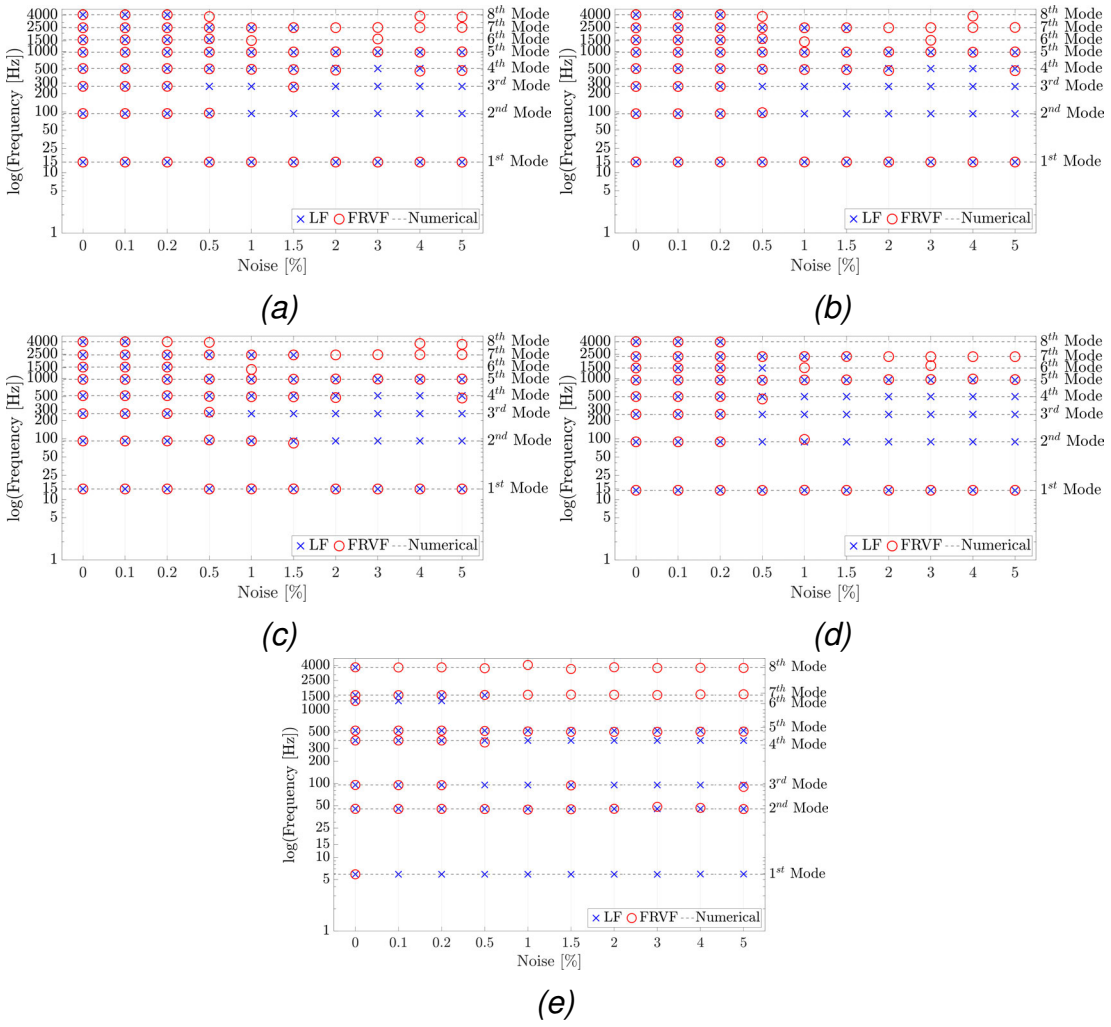

Figure 4.3: 4-element beam: Stable natural frequencies identified via LF and FRVF. Figure 4.3a deals with the baseline scenario, Figure 4.3b with scenario 2, Figure 4.3c with scenario 3, Figure 4.3d with scenario 4, and Figure 4.3e with scenario 5.

ure 4.4 using the average value of the stable ω_n for the LF (as described above) and the nominal value for the FRVF. Each line, consisting of two adjacent plots shows the results for a single scenario, such as Figures 4.4c and 4.4d show the results for scenario 2.

As per Figure 4.3, in Figure 4.5 the stable $\boldsymbol{\phi}_n$ identified via LF (left column) and FRVF (right column) are compared to numerical results using the traditional formulation of the Modal Assurance Criterion (MAC) [58]:

$$\text{MAC}(\boldsymbol{\phi}_b, \boldsymbol{\phi}_e) = \frac{\left(\boldsymbol{\phi}_b \cdot \boldsymbol{\phi}_e\right)^2}{\left(\boldsymbol{\phi}_b \cdot \boldsymbol{\phi}_b\right)\left(\boldsymbol{\phi}_e \cdot \boldsymbol{\phi}_e\right)} \tag{4.17}$$

where the b and e subscripts respectively represent the baseline and the mode shape to be compared. Literature and good practice [5] define two mode shapes to be correlated when their MAC value exceeds 0.8. The MAC value for each stable mode is plotted against noise to verify its effect on LF and FRFVF. Each subfigure line in the plot is respectively linked to a scenario, such as Figures 4.4e and 4.4f show the results for scenario 3.

At first glance in Figure 4.3 it is clear that the LF (note that this value is the average over its 100 realisations) is able to correctly identify a wider range of modes if compared with FRVF. For all cases, as the noise increases the LF is not able to correctly detect the higher modes. Notably, this is not the case with FRVF, which, while always identifying the first mode, struggles more with modes two to five. Generally, the LF identifies correctly the natural frequencies of the first five modes for all noise cases and for the noiseless case and the 0.1% noise case all the ω_n are correctly identified. The same can be said for FRVF, which accurately identifies all the modes for the first three noise cases, except for the fifth scenario. As shown in Figure 4.3 the first mode's ω_n is correctly addressed only for the noise-free case. In summary, it can be said that the LF struggles to identify higher modes with increasing noise, while FRVF is better at identifying those higher modes, but it performs less efficiently than LF with the lower ones.

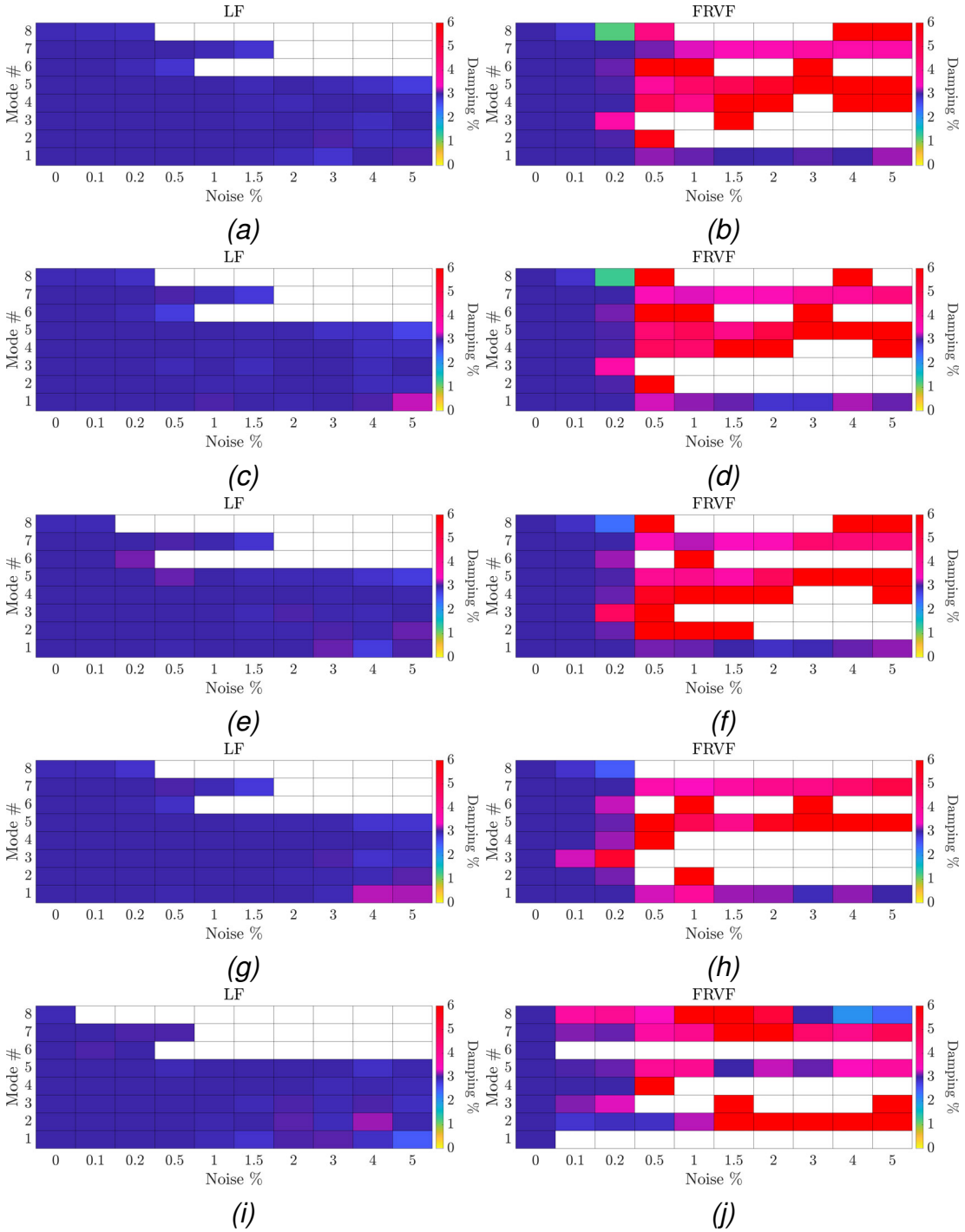

Figure 4.4: 4-element beam: stable damping ratios as identified via LF and FRVF. Figures 4.4a, 4.4c, 4.4e, 4.4g and 4.4i show, respectively, the results of the LF identification for Scenarios #1, #2, #3, #4, and #5. Figures 4.4b, 4.4d, 4.4f, 4.4h and 4.4j show the results of the FRVF identification for the same Scenarios. Please note: ζ_n is 3% for all cases and scenarios.

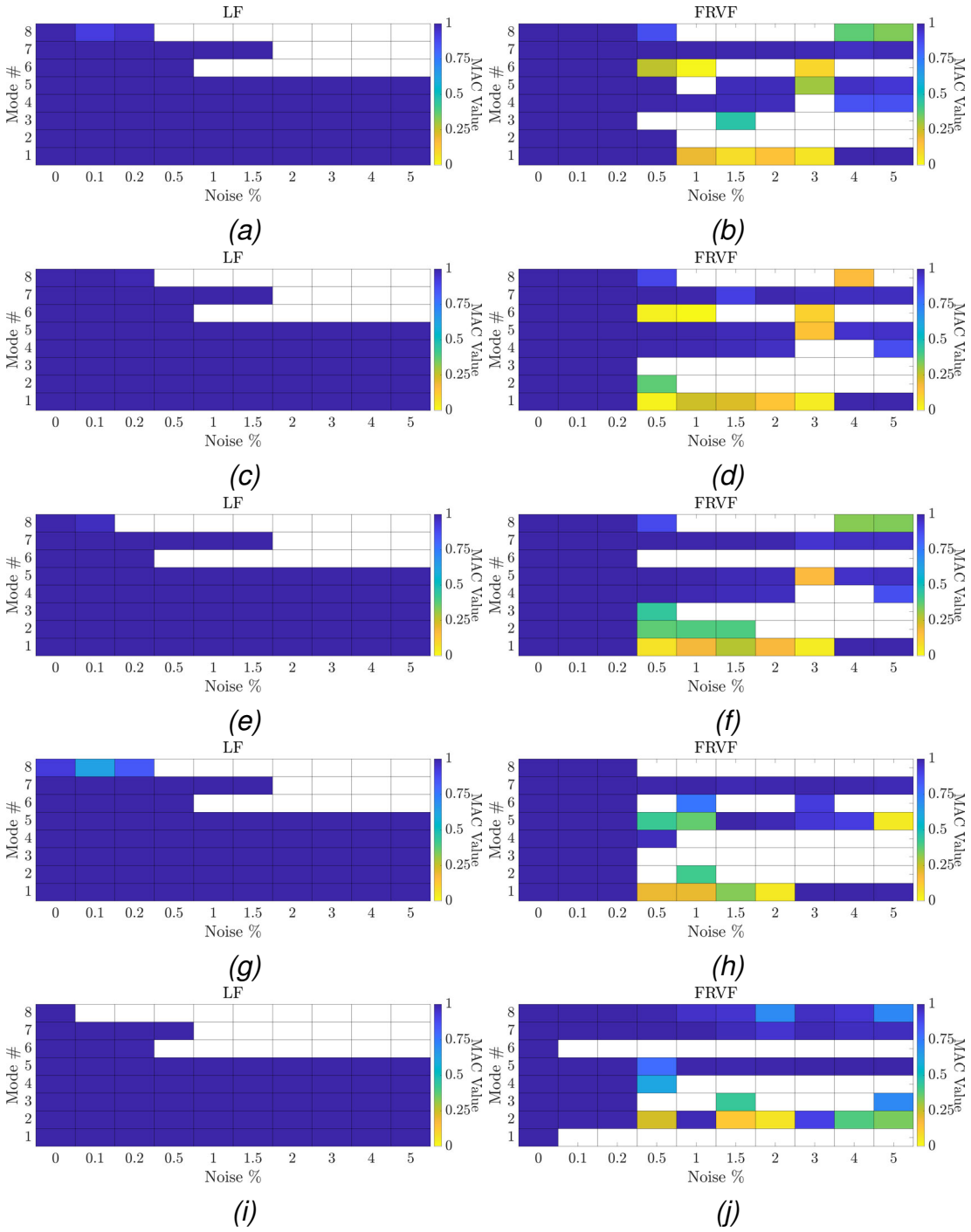

Figure 4.5: 4-element beam: stable MAC values of the mode shapes as identified via LF and FRVF. The scenarios and noise cases are presented as per Figure 4.4.

Particular care should be paid to Figure 4.3e, which refers to scenario 5. As noise increases, FRVF is unable to identify the first mode. This is most likely due to the fact that FRVF is an iterative and deterministic method, whose initial poles struggle to converge at lower frequencies (it does not happen for the other scenarios) when noise arises.

In Figure 4.4, the ζ_n of the stable modes are compared to the numerical value, 3%. The colour bar in the plots identifies the range of values under scrutiny and if the value is, or close to, 3% the cell's colour tends to be blue. At first sight, the left column (LF) appears more coherently populated by values equal to or larger than 75%, if compared to the right column (FRVF). In fact, for the first four scenarios, as shown in Figures 4.4b, 4.4d, 4.4f and 4.4h, the ζ_n identified via FRVF are fully consistent only for the noiseless and the 0.1% noise cases and partly coherent for the 0.2% case. However, the first mode in the remaining noise cases is somewhat consistent with the expected value. Considering the last scenario in Figure 4.4j, only the ω_n of the noiseless case are correctly identified for all modes. This is due to the lump mass influence, which lowers the separation between the ω_n. Nevertheless, few sparse modes are consistently extracted at different noise levels. In summary, it can be said that if a mode is considered stable for the LF, its identified ω_n is most likely consistent with the expected value, while this does not hold for FRVF. In fact, the latter seems more severely influenced by noise than LF. However, it must be kept in mind that LF results are subject to statistical fluctuations (here, averaged over 100 realisations), while FRVF results are deterministic and obtained directly from one identification.

The MAC value between the identified modes and the expected numerical results is shown in Figure 4.5. The results are organised likewise Figure 4.4. The MAC values between the $\boldsymbol{\phi}_n$ identified via LF and the expected numerical value is largely consistent for all stable modes, except for the eighth mode at 0.1% noise in the fourth scenario. Concerning the FRVF identification, the modes of the first

three noise levels are correctly identified for scenarios 1-4, but this does not hold for scenario 5. Generally, the identified $\boldsymbol{\phi}_n$ are more coherent with the expected numerical ones than ω_n as it is clearly shown by the prevailing presence of values equal or larger than 75% in Figure 4.5, when compared to Figure 4.4.

In conclusion, at the minimum order k, the LF is more resilient to noise than FRF. This is testified by the results in Figures 4.3 to 4.5 and the aforementioned discussion, such as that LF has more stable modes in all cases and generally obtains modal parameters closer to the expected numerical value than FRVF. These can traced back to the nature of the two methods. LF is focused on the interpolation of the available data, while the FRVF on the iterative fitting problem, notoriously less resilient to noise.

4.3.2 Investigation of Damage Effects

The aim of this section is twofold, not only to investigate the effect of noise, but also to compare the damage detection capability of LF and FRVF. For this goal, the modal parameters identified from the noiseless data are used. In particular, ω_n and $\boldsymbol{\phi}_n$ are the parameters of interest, since ζ_n is the same for all scenarios.

Figure 4.6 shows the comparison between the absolute value of the relative difference, in percentage, between the ω_{1-3} identified with LF and FRVF of the damaged, or altered, cases and those of the baseline case. As expected from [28], the difference increases with the damage. This is proof that LF and FRVF are, as SI methods, sensitive enough to detect even small damage, such as for the 5% damage scenario. The value in the plots are reported as positive in a log scale only for convenience and the frequencies decreased for increasing mass and damage (i.e. decreasing stiffness). Only the first three modes are taken in consideration for conciseness and clarity, but a similar behaviour is found for all modes. In addition, Figure 4.6 shows that the LF and FRVF computed difference in ω_n is very close with the numerical values.

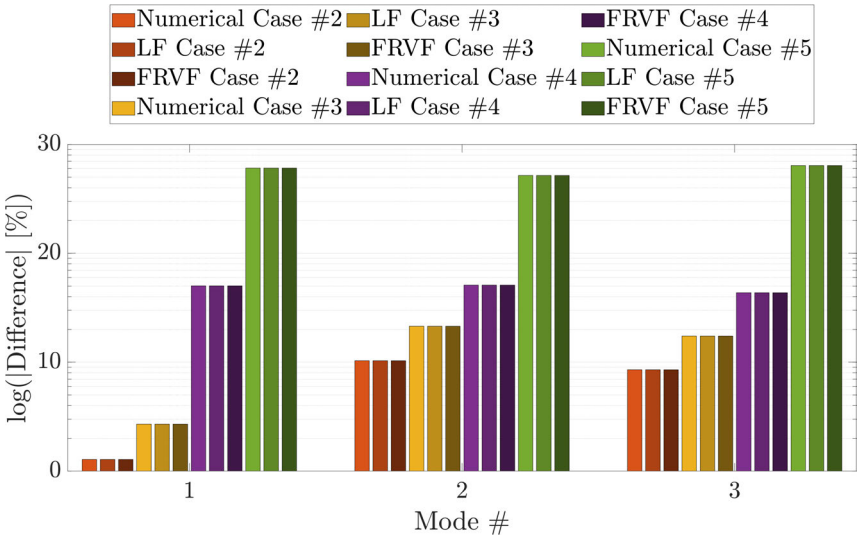

Figure 4.6: 4-element beam: Relative difference of the natural frequencies identified via LF and FRVF between the three damaged and added masses scenarios and the baseline configuration.

According to literature [28], not only the ω_n are influenced by damage and structural changes, but so are the $\boldsymbol{\phi}_n$. In particular, $\boldsymbol{\phi}_n$ are preferred for damage localisation. In Figure 4.7, $\boldsymbol{\phi}_1$ identified via LF (Figure 4.7a) and FRVF (Figure 4.7b) are shown to demonstrate that the methods' sensitivity is sufficient to detect such changes. As clearly shown in Detail A and Detail B the deviation from the baseline $\boldsymbol{\phi}_1$ increases with damage and mass addition. In particular, for both methods, the largest deviation is evident between nodes 3 and 4, the third element, where damage is simulated. Similar behaviour is seen in the remaining modes, but for the sake of clarity and conciseness only the $\boldsymbol{\phi}_1$ of the noiseless case are shown. Concisely, these assess the suitability of the proposed methods for SHM.

With regards to the time to identification, the performance of the two methods, for the minimum order $k = 16$, is showed in Table 4.4, where the mean (μ) and standard deviation (σ) for the time to identification, in s, of the LF and FRVF are compared. For the LF a total of 5000 data points is taken into consideration for computing μ and σ, while they are 50 for FRVF. The difference in realisations is justified by the different nature of the two methods: the LF is stochastic and FRVF

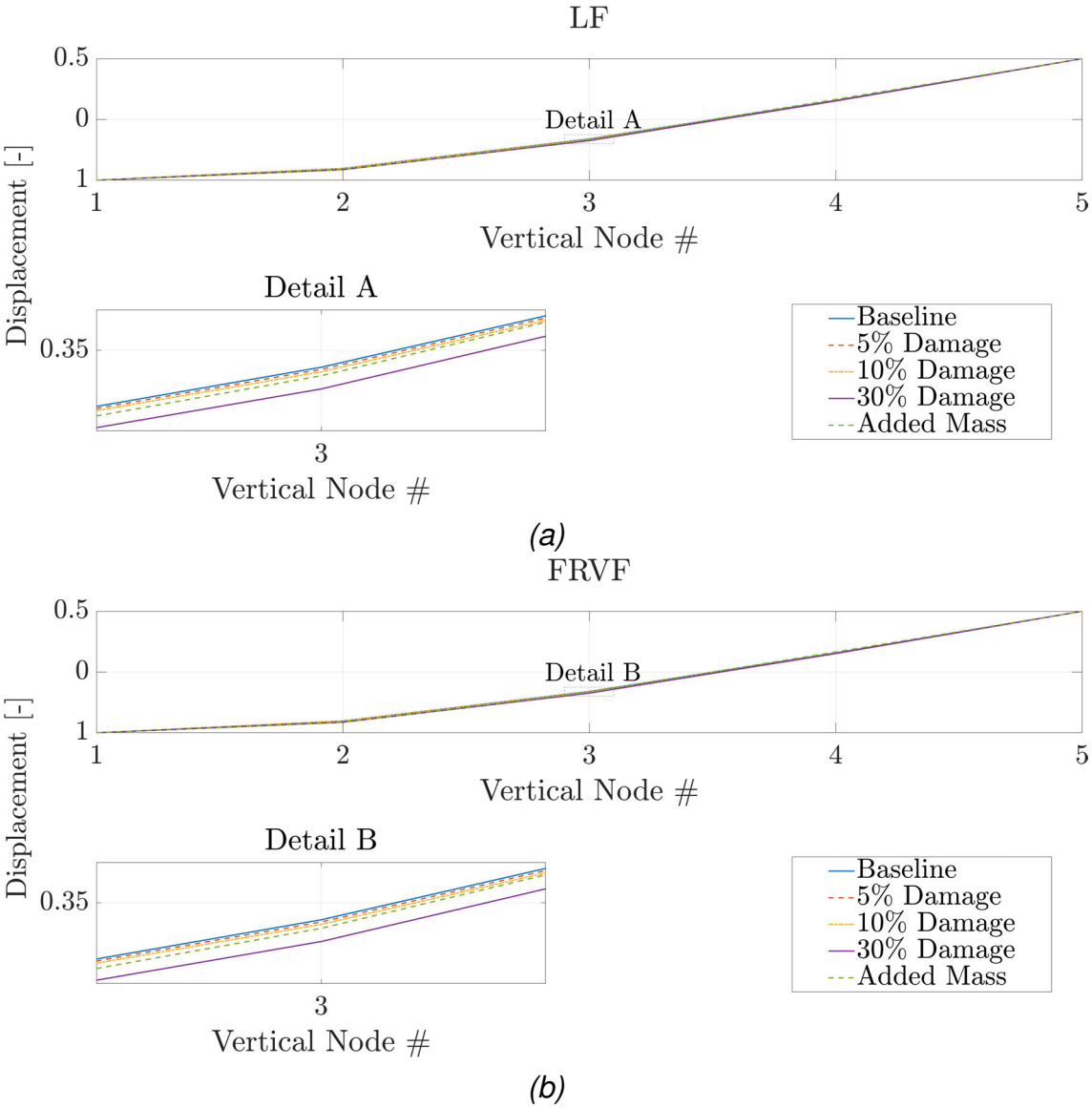

Figure 4.7: 4-element beam: First mode shape of for the vertical component of all cases identified by LF (Figure 4.7a) and FRVF (Figure 4.7b for the noiseless cases. The detailed views (Detail A and B) show a zoomed in view of the mode shape.

is deterministic. Hence, the LF identification is repeated 100 times at each noise and damage scenario. From the results, FRVF is both the least computationally demanding method and the most stable in time, because its σ is smaller than that from LF.

Table 4.4: Mean (μ) and standard deviation (σ) for the time to identification, in s, of the LF and FRVF for the identified data.

Time to identification [s]		
	LF	FRVF
μ	4.170	0.375
σ	0.381	0.264

4.3.3 Discussion

In conclusion, this numerical study outlines that for no-noise or low noise cases the LF and FRVF perform well for the identification of modal parameters and their results are comparable. However, with higher noise levels raises LF is more resilient than FRVF. LF predicts better frequency of low and medium-frequency modes, with the FRVF identifying frequency of high-frequency modes more precisely. Taking into account that LF overperformes FRVF in identifying modes, it can be concluded that LF is more robust to sensors noise. This is a significant advantage of the method that makes it efficient in real-world applications. The methods' accuracy for low level of noise also allows them to detect changes in the structure's modal response linked to a change in its properties, such as damage or added mass. On the computational aspect, FRVF performs better than LF in both average time-to-identification and stability, identified as the standard deviation. Particularly, the FRVF average time to identification is an order of magnitude smaller than that of the LF. However, LF, globally, identifies more stable modes than FRVF for all scenarios.

4.4 Ground Vibration Testing of a Flexible Wing

Having compared the performance of the LF and FRVF methods for their robustness to artificially added noise with a numerical system for damage detection, an experimental case is introduced, such that their performance can be compared with real data. The chosen experimental case study is the eXperimental

BeaRDS-2 (XB-2) HAR wing (Figure 4.8a), developed within the BeaRDS project at Cranfield university [59–62]. The XB-2 wing was conceived as a dynamically scaled example of a civil jet airliner wing to be tested in the University's wind tunnel. The wing is made of three components: the spar, the stiffening tube and the skin. Originally, additional brass masses were used to aid the scaling of mass properties; however, for the purpose of this work the masses are removed in the baseline scenario and are used to create three loaded cases to simulate different loading conditions for the wing, such as under-wing payloads or winglets.

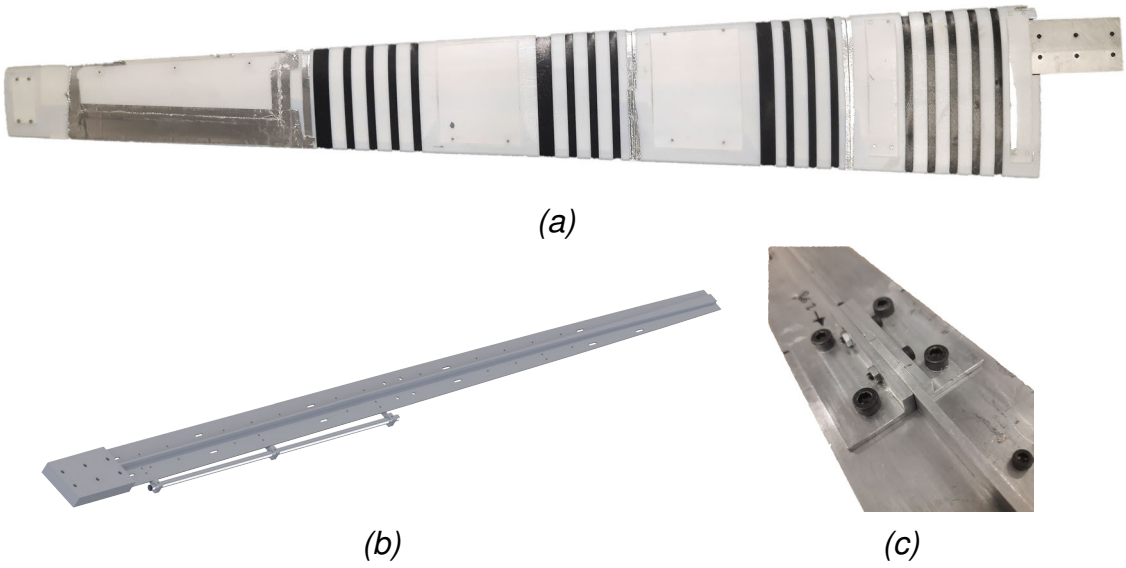

(a)

(b) *(c)*

Figure 4.8: XB-2 wing top view (Retrieved from [6]) in Figure 4.8a, Figure 4.8b shows a CAD rendering of the spar and tube assembly, the wing's torque box, and Figure 4.8c is a close up shot of the spar's bridge (retrieved from [6]).

The aerodynamic surface of the wing, outlined by a NACA 23015 aerofoil, spans for 1.5 m, with a mean aerodynamic chord ($\bar{c}$) of 0.172 m, a taper ratio (λ) of 0.35 and a leading edge (LE) sweep of 1.49^{o} and weighs 3.024 kg. The wing has neutral twist and dihedral. The skin is responsible for transferring the aerodynamic loads to the underlying structure and is made of two 3D printed plastics: rigid Digital ABS [63] and rubber-like compound Agilus 30 [64], shown as white and black section respectively in Figure 4.8a. The combination of a rigid and a rubber-like material allows the skin to be flexible and preserves structural

integrity. Notably, even if the wing is made of 47 alternating (material-wise) strips, it is constituted of 3 parts, thanks to the PolyJet technology that allowed seamless printing from different materials.

The wing's torque box consists of the spar and tube assembly, Figure 4.8b. The spar was machined from two 6082-T6 Aluminium blocks which were welded together and secured with four bolted L-profile plates, Figure 4.8c. The main spar features a Saint George's cross-shaped cross section and a variable taper along its span, while the tube is a simple stainless steel tube with a 10 mm diameter and 1 mm thickness. Overall, the main spar spans for 1.45 m, where the clamping root (0.125 m long) is taken into consideration, while the tube is 0.55 m long and it is linked to the main spar at three different locations. Table 4.5 summarises XB-2's and its materials properties.

Table 4.5: XB-2: Physical characteristics and materials properties.

Property	Details	Unit	**Material**	Young Modulus [GPa]	Poisson Ratio [-]	Density [kgm^{-3}]
Semi span	1.5	m	6082-T6 Aluminium	70	0.33	2700
$\bar{c}$	172	mm	Stainless Steel	193	0.33	8000
λ	0.35	-	Digital ABS	2.8	0.33[12]	1175
LE sweep	14.9	^{o}	Agilus 30	NA	NA	1140
Aerofoil	NACA 23015	-				
Mass	3.024	kg				

For the scope of this work, four scenarios are considered. The specimen described above is considered the baseline and three loaded scenarios are introduced, as per Table 4.6.

The three loaded scenarios are added to assess the ability of LF and FRVF to be adopted for SI of aeronautical structures. In addition, the LF and FRVF results are compared with modal parameters extracted with the well-established method

Table 4.6: XB-2: Specimen scenarios. Distances, in mm, are from the wing root.

Scenario	Characteristics	Mass [kg]
1	Baseline	3.024
2	Added masses: 75 g at 1010 mm, 12 g at 1050 mm and 61 g at 1365 mm.	3.172
3	Added masses: 88 g at 1010 mm, 51 g at 1050 mm, 83 g at 1205 mm and 61 g at 1365 mm.	3.307
4	Added masses: same as Scenario 2 plus 181 g at 570 mm and 170 g at 665 mm.	3.658

N4SID, before their results are used to characterise the aeroelastic models. From a previous modal survey [6] involving the baseline wing, the first three dominant modes in the vertical direction were identified between 3 and 20 Hz. Hence, for this work the frequency band for the linear sine sweep excitation was set between between 2 and 25 Hz and spanned across 20 min. The specimen is clamped to a Data Physics Signal Force modal shaker controlled by the its DP760 close-loop control software running on a consumer grade laptop. The vertical acceleration data is collected via nine accelerometers, eight spread along the wing's span and one used for shaker feedback, as per Table 4.7 and Figure 4.9.

Table 4.7: Accelerometers specifications.

Accelerometers			
ID #	**Model**	**Sensitivity [mVg^{-1}]**	**Mass [g]**
0	PCB Piezotronics model: 352C23	4.88	0.2
1R	PCB Piezotronics model: 356A16	96.50	7.4
1L	Isotron accelerometer model: 7251A	10.30	10.5
2R	PCB Piezotronics model: 356A16	97.20	7.4
2L	Isotron accelerometer model: 7251A	10.08	10.5
3R	PCB Piezotronics model: 356A45	100.20	4.2
3L	Isotron accelerometer model: 7251A	10.34	10.5
4R	Brüel & Kjær accelerometer type: 4507-002	94.12	4.8
4L	Brüel & Kjær accelerometer type: 4507-002	95.52	4.8

After collection, a median filter with a window length of 60 is applied to the data, which is then desampled from 5120 to 128 Hz. Then, the data is filtered with a bandpass filter between 2 and 20 Hz prior to detrending. At this point, N4SID

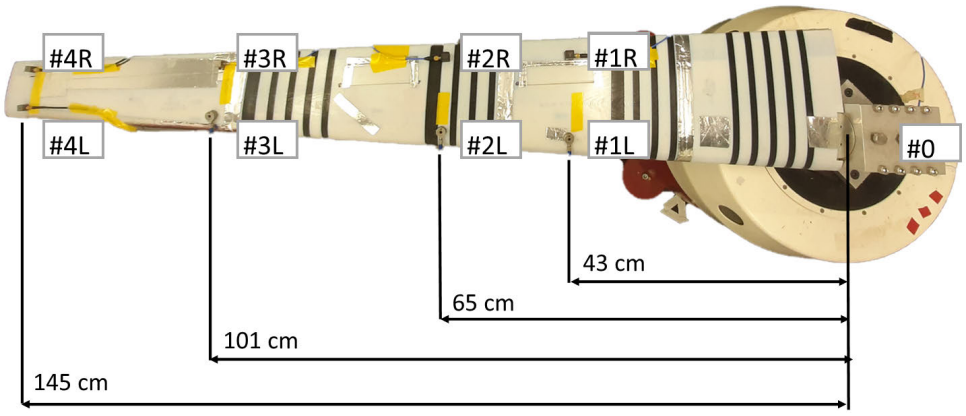

Figure 4.9: XB-2: Accelerometers locations. The accelerometers do not appear aligned only for the optical effect of the camera lens (retrieved from [6]).

is fed directly with the obtained time histories (THs), while these are converted in the frequency domain for LF and FRVF. A further post-processing step is then taken by applying a Savitzky-Golay filter of order 3 and window length 101 to smooth the FRFs.

4.4.1 Identification Results

The identification of modal parameters from the experimental data is carried out with the aid of stabilisation diagrams, where relative differences $\Delta\omega$ and $\Delta\zeta$ are, respectively, employed for ω_n and ζ_n, and MAC is used for $\boldsymbol{\phi}_n$. These ensure the stability of the identified modes along the order range. For all identification methods the following values are used: $\Delta\omega = 1\%$, $\Delta\zeta = 10\%$ and MAC $= 0.95$. The stabilisation diagrams for the baseline scenario for LF, FRVF, and N4SID are shown, respectively, in Figures 4.10a to 4.10c. Please note that the order ranges between 6 and 200 for the newly introduced methods. However, the benchmark identification, carried with N4SID, order ranges between 6 and 50. The difference in the orders between the methods is only to be directed to the computational burden of N4SID. As discussed in [36], N4SID is much slower, by orders of magnitude, than LF, even when an higher order identification is set.

It is clear from Figure 4.10 that the modes are consistently identified through-

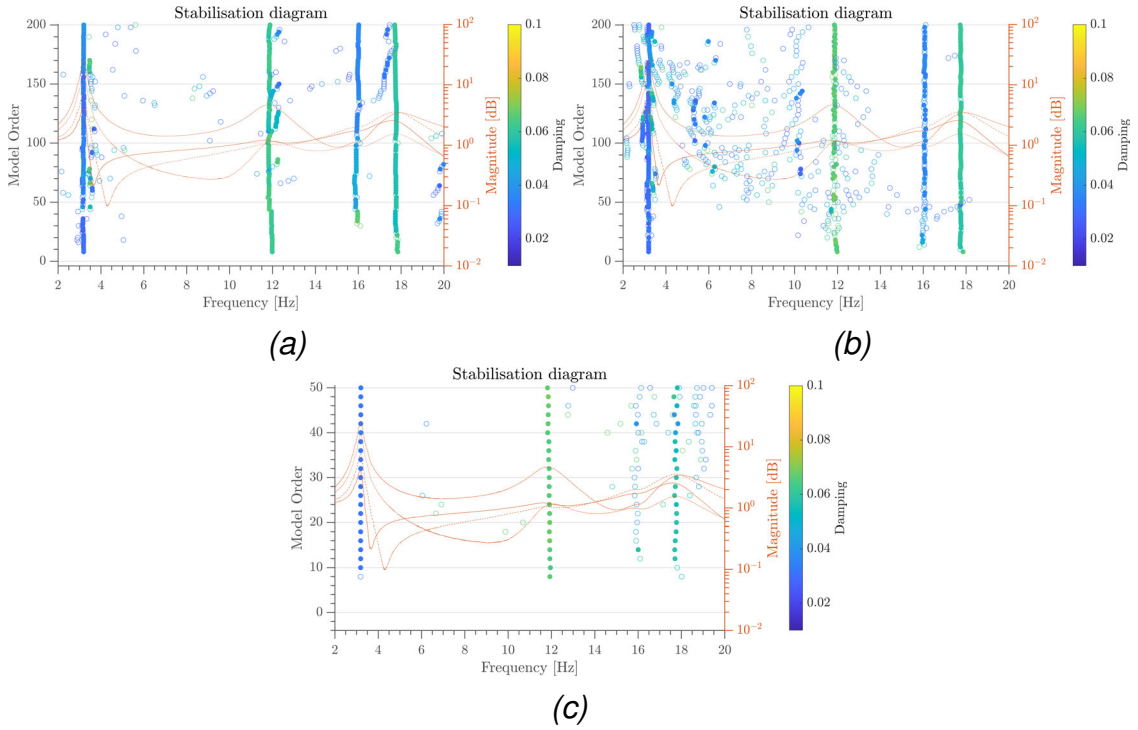

Figure 4.10: XB-2: Stabilisation diagrams of Scenario #1 computed with LF (Figure 4.10a), FRVF (Figure 4.10b), and N4SID (Figure 4.10c) at maximum order $k = 200$, $\Delta f = 1\%$, $\Delta\zeta = 10\%$ and MAC $= 0.95$.

out. However, the stabilisation diagram of FRVF reports more spurious stable points; nevertheless, it is still clear where the physically meaningful stable poles lie. Another interesting fact, is the presence of the third mode (circa 16 Hz), which however is disregarded (not of interest for the aeroelastic ROM) in the study of the modal parameters, as it was previously found to be mainly a lagging mode [6]. Furthermore, the benchmark method, N4SID, cannot detect this mode. Only the stabilisation diagrams for the baseline scenario are reported for brevity, but similar results are found for the other scenarios.

In Table 4.8, the stable ω_n and ζ_n identified with N4SID, LF, and FRVF are presented. The identification with LF and FRVF are mostly consistent with the N4SID benchmark results. In fact, the relative difference between the ω_n of LF and FRVF and those from N4SID never exceeds 1%, while the ζ_n is mostly under 10% and on rare occasions between 10 and 15%. However, this is expected due to the intrinsic nature of damping [16]. In Figure 4.11, the $\boldsymbol{\phi}_n$ of the baselines

Table 4.8: Natural frequencies and damping ratios identified by LF and FRVF for all scenarios.

Natural Frequency [Hz]									
Mode	1st Bending			1st Coupled			2nd Coupled		
Scenario	N4SID	LF	FRVF	N4SID	LF	FRVF	N4SID	LF	FRVF
1	3.190	3.202	3.203	11.896	11.886	11.858	17.763	17.703	17.725
2	2.957	2.958	2.945	12.096	12.134	12.083	17.350	17.302	17.294
3	2.775	2.769	2.788	12.002	12.025	12.014	17.079	17.101	17.023
4	2.729	2.725	2.727	11.970	11.965	11.938	15.067	15.052	15.004
Damping Ratio [-]									
Mode	1st Bending			1st Coupled			2nd Coupled		
Scenario	N4SID	LF	FRVF	N4SID	LF	FRVF	N4SID	LF	FRVF
1	0.032	0.040	0.028	0.066	0.063	0.065	0.058	0.061	0.062
2	0.021	0.024	0.025	0.060	0.057	0.058	0.061	0.056	0.060
3	0.019	0.022	0.021	0.058	0.055	0.057	0.050	0.050	0.057
4	0.019	0.021	0.019	0.050	0.048	0.052	0.046	0.039	0.038

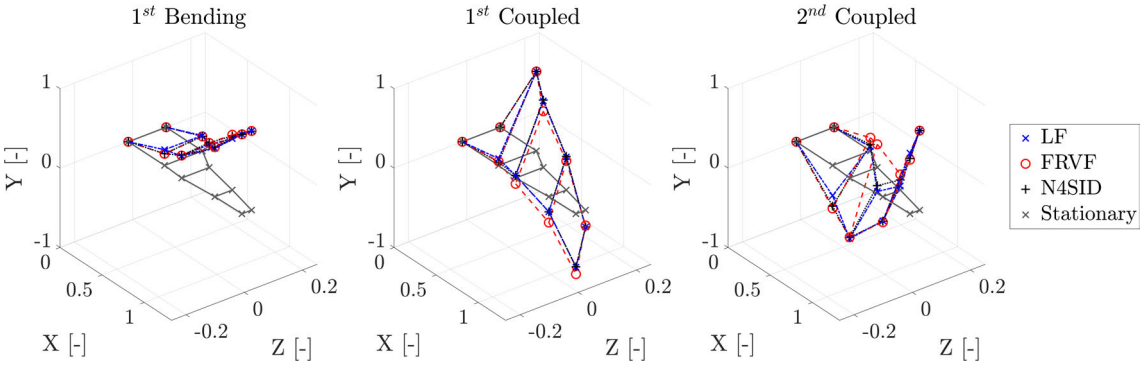

Figure 4.11: XB-2: Mode shapes of the baseline scenario.

scenario are displayed.

The $\boldsymbol{\phi}_n$ in Figure 4.11 are coherent for all scenarios, except for a slight difference for the FRVF in the fourth mode at channels #2-3L. This is also testified by Table 4.9, where the diagonal value of the MAC matrices between LF, or FRVF, and N4SID are reported. Only the diagonal values are reported as the off-diagonal terms have a negligible value. In all cases, apart from $\boldsymbol{\phi}_4$ in the baseline scenario for FRVF, the MAC values exceed 0.95, which means almost perfect correlation between the modes. Even the $\boldsymbol{\phi}_4$ in scenario 2 for FRVF MAC value is 0.89, which means good correlation with its N4SID counterpart.

Concluding on the identification results, it is clear that both LF and FRVF per-

Table 4.9: XB-2: MAC (main diagonal) Value of the mode shapes identified via LF and FRVF vs N4SID.

MAC values on the main diagonal [-]								
Scenario	Baseline		2		3		4	
Mode	LF	FRVF	LF	FRVF	LF	FRVF	LF	FRVF
1st	1	1	1	1	1	1	1	1
2nd	1	0.97	1	1	1	1	1	1
4th	0.97	0.89	0.98	0.99	1	0.99	0.95	0.97

form satisfactorily, when compared to N4SID, for the identification of the XB-2's scenarios, with LF being more consistent with the benchmark for $\boldsymbol{\phi}_n$ identifications.

4.4.2 Aeroelastic Investigation

Having demonstrated the goodness and coherence in the results of the modal parameters identified via N4SID, LF, and FRVF, it is beneficial to assess this in light of a classic aeronautical problem. The flutter speed prediction using a model, introduced in Section 4.2.5, informed by the identified modal parameters. The comparison assumes the N4SID parameters as the benchmark values to assess the LF and FRVF performance.

Given the aeroelastic model developed in Section 4.2.5, a few assumptions to simplify the model need to be made:

- The wing's shape is assumed to be rectangular;
- The EI, GJ and mass are assumed to be constant along the span;
- The identified ζ_n are assumed to be dependent only on structural effects in the wind-off results;
- The second mode is assumed to be a pure pitching mode.

In order to accommodate the assumptions, the mean aerodynamic chord is taken under consideration and, since the wing is assumed to be rectangular, also the

stiffness, Ei and GJ, are assumed constant along the span. The ζ_n assumption stands as a good approximation for small vibrations [65]. Lastly, the proposed model is based on uncoupled modes and the first mode to show pitching motion is considered to be a pitching-only mode for the sake of this analysis. The strong assumptions are motivated by the fact that the main goal of the aeroelastic investigation is to compare the LF and FRVF, rather than a full aeroelastic assessment. Nevertheless, similar approaches still give reasonable estimates, usually underestimating flutter onset speed by around 20% [12].

According to the wing's geometry and physical properties, Equations (4.11) and (4.12) are populated with the values in Table 4.10.

Table 4.10: XB-2: Properties values for the aeroelastic model.

Property	**Value**
m	mass divided by area
c	172 mm
s	1.5 m
s_f	0.25 $\times$ c
ρ	1.225 kgm^{-3}
a_w	7.143 (NACA 23015)
e	0

The aeroelastic system is evaluated between 0 and 50 ms^{-1} U_∞, EI and GJ are derived from still air results (the GVT results) and $M_{\dot{\theta}}$ is a function of the reduced frequency k.

Figure 4.12 show the results, in terms of ω_n, ζ_n and λ vs U_∞ of the linear eigenvalue analysis of the aeroelastic model, respectively from the LF, FRVF and N4SID identified data, for the baseline case. In particular, Figure 4.12a shows results for ω_n vs U_∞, Figure 4.12b plots the ζ_n vs U_∞ curves, Figure 4.12c displays the relation between the λs' real parts and U_∞ and Figure 4.12d plots the λs' imaginary parts vs U_∞. To get an insight on the stability of the λ, their real part is plotted in Figure 4.13 against the respective imaginary part for the baseline scenario for the results obtained from LF, FRVF. and N4SID.

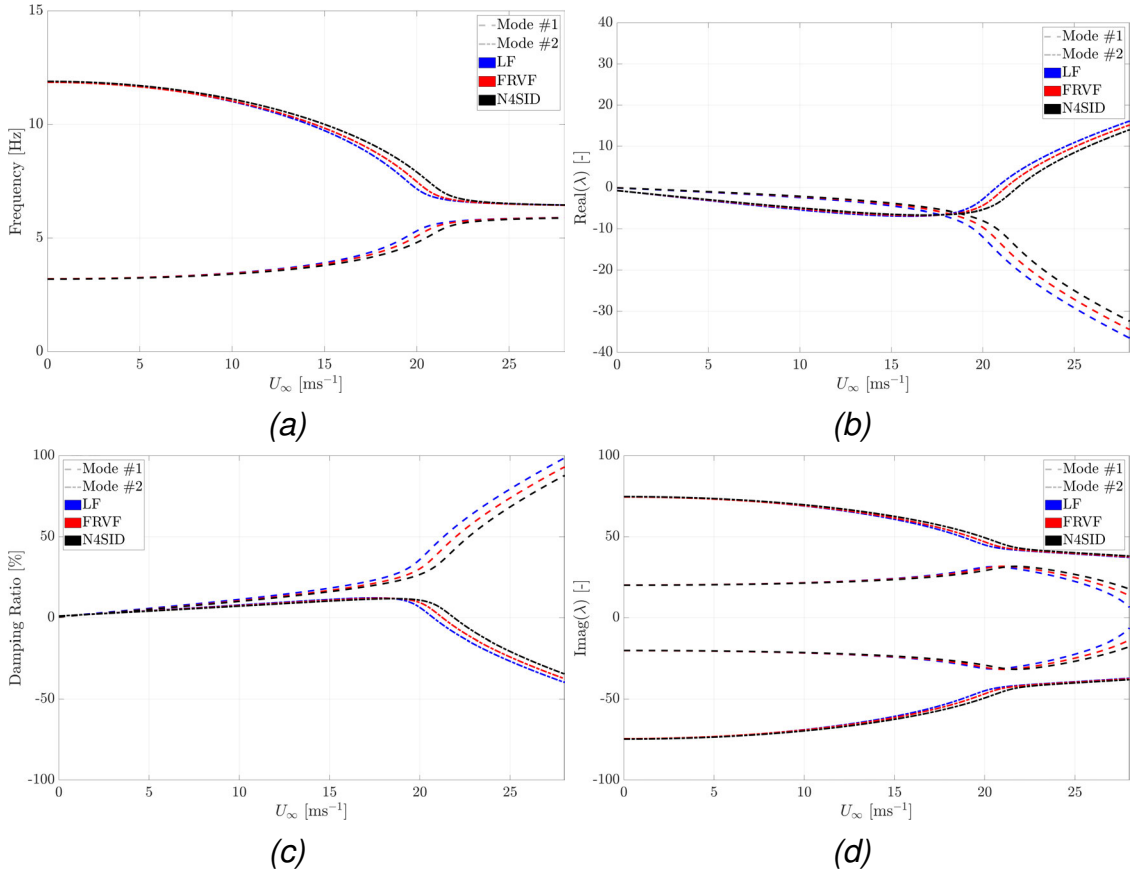

Figure 4.12: XB-2: Frequency (Figure 4.12a), damping ratio (Figure 4.12c), eigenvalues' real part (Figure 4.12b), and eigenvalues' imaginary part (Figure 4.12d) vs U_∞, for the aeroelastic model computed from data obtained via LF, FRVF, and N4SID for the baseline scenario.

Only the results for the baseline scenario results obtained from LF, FRVF, and N4SID are presented graphically, since the results are similar for all other cases. Only flutter is detected for all scenarios in the chosen speed range. However, this is not an issue as flutter usually precedes the insurgence of divergence [11]. The stability behaviour in Figure 4.12 is similar and it is as expected from similar implementations [66]. For the two cases reported in Figure 4.12, flutter, as expected, is related to ζ_n approaching zero; hence, real(λ) crossing the zero line. These phenomena can also be appreciated in Figure 4.13, where the zero line of the imaginary axis is crossed by λ, pointing to the occurrence of an aeroelastic instability. These behaviours are also found in the other cases for which plots are not presented.

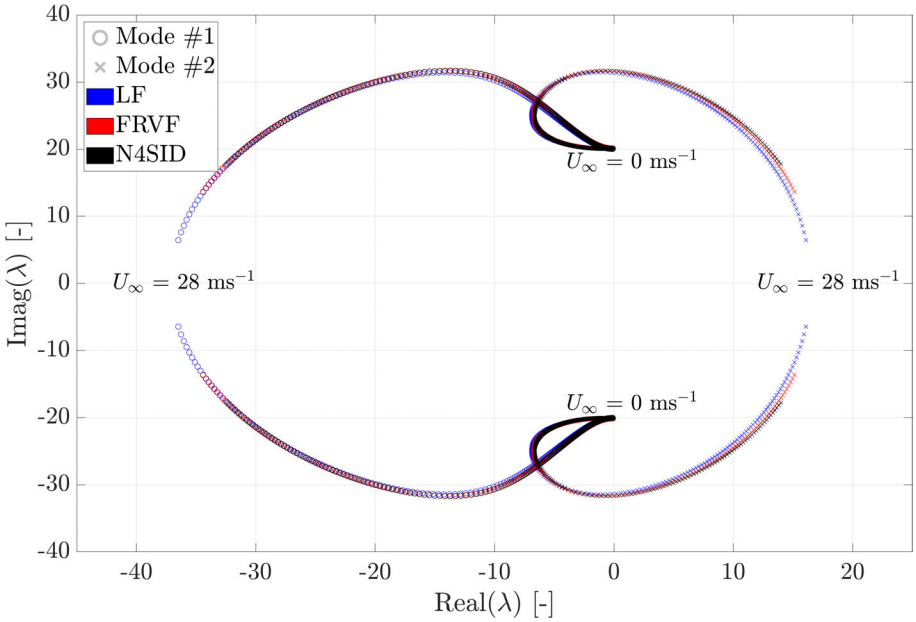

Figure 4.13: XB-2: Polar plot of the eigenvalues obtained from the LF, FRVF, and N4SID data for the baseline scenario.

Table 4.11: XB-2: Aeroelastic phenomena onset speeds.

	Flutter onset speed [ms^{-1}]			
Scenario	Baseline	2	3	4
	(%)	(%)	(%)	(%)
N4SID	21.882	22.778	22.890	22.872
LF	20.730	21.719	21.783	21.706
	(-5.26)	(-4.64)	(-4.84)	(-5.10)
FRVF	21.245	22.239	22.347	22.264
	(-2.91)	(-2.37)	(-2.37)	(-2.66)

The actual values for flutter onset speeds, reported in Table 4.11, show that, when compared with the N4SID-derived model, the FRVF-derived models predicted onset speeds are much closer than the LF-derived models. Particularly, the difference between the FRVF-derived models and those from N4SID never exceed 2.91%. However, even in the worst case, the error of the LF-derived model does not exceed 5.26%. The minimum deviations is also different; FRVF-derived models have a minimum error of 2.37%, while for LF models it is 4.64%. It can be said that LF modal identification performs worse than that for FRVF for the creation of a 2 DoF ROM for aeroelastic phenomena onset speed predictions.

However, the LF-derived models are still able to translate the small changes in modal properties to changes in the predicted flutter speeds, as the expected error is 20% [12]. In conclusion, it can be said that the LF identification is usually more stable, as shown in Figure 4.10, than FRVF identification; however, FRVF-identified modal properties values, in particular ω_n and ζ_n, are closer to those from N4SID, as demonstrated in Table 4.8.

4.5 Conclusions

In this work, the sensitivity, robustness, and performance of the Loewner Framework and Fast Relaxed Vector Fitting are assessed and compared for the extraction of modal parameters from numerical and experimental vibration data in the frequency domain. The main findings of this study can be condensed in the following points:

- The Fast Relaxed Vector Fitting method is more adversely affected than Loewner Framework by measurement noise. However, it is at least one order of magnitude faster to run than Loewner Framework;
- From a System Identification perspective, Fast Relaxed Vector Fitting better detects the higher order modes, while Loewner Framework correctly identifies more modes overall and with more precision for the estimation of damping;
- Both Fast Relaxed Vector Fitting and Loewner Framework returned consistent stabilisation diagrams for experimental signals, with the Loewner Framework being more stable and less affected by spurious identifications than the Fast Relaxed Vector Fitting;
- The identified modal parameters are consistent with the current state-of-the-art (N4SID), with the Fast Relaxed Vector Fitting results being slightly more

accurate and the Loewner Framework values being more stable;

- For damage assessment uses, both Fast Relaxed Vector Fitting and Loewner Framework are capable of detecting occurring damage (modelled as a stiffness reduction) and changing structural configuration (added mass). This was verified both numerically and experimentally;
- From a ROM point of view, both Fast Relaxed Vector Fitting and Loewner Framework data produced efficient and reliable aeroelastic models for the prediction of flutter onset speed, with Fast Relaxed Vector Fitting results matching the benchmark slightly better.

In summary, it can be asserted that the Loewner Framework is more stable, from a results point of view, but, generally, slightly less precise, than Fast Relaxed Vector Fitting. The authors suggest the use of the Loewner Framework over Fast Relaxed Vector Fitting in the case of noisy or disturbed measurement, but advise the implementation of Fast Relaxed Vector Fitting in all other cases.

References

[1] L. Ljung, T. Chen, and B. Mu, "A shift in paradigm for system identification," *International Journal of Control*, vol. 93, no. 2, pp. 173–180, 2020, ISSN: 13665820, DOI: 10.1080/00207179.2019.1578407 (cit. on p. 94).

[2] D. Quero, P. Vuillemin, and C. Poussot-Vassal, "A generalized state-space aeroservoelastic model based on tangential interpolation," *Aerospace*, vol. 6, no. 1, p. 9, 2019, ISSN: 2226-4310, DOI: 10.3390/aerospace6010009 (cit. on p. 94).

[3] L. Zanotti Fragonara *et al.*, "Dynamic investigation on the Mirandola bell tower in post-earthquake scenarios," *Bulletin of Earthquake Engineering*, vol. 15, no. 1, pp. 313–337, 2017, ISSN: 1570-761X, DOI: 10.1007/s10518-016-9970-z (cit. on p. 94).

[4] V. Mugnaini, L. Zanotti Fragonara, and M. Civera, "A machine learning approach for automatic operational modal analysis," *Mechanical Systems and Signal Processing*, vol. 170, no. February, p. 108 813, 2022, ISSN: 08883270, DOI: 10.1016/j.ymssp.2022.108813 (cit. on p. 94).

[5] D. J. Ewins, *Modal Testing Theory, Practice and Application*, 2nd. Baldock, UK: Research Studies Press, 2000, p. 562, ISBN: 978-0-863-80218-4 (cit. on pp. 94, 111).

[6] G. Dessena, D. I. Ignatyev, J. F. Whidborne, A. Pontillo, and L. Zanotti Fragonara, "Ground vibration testing of a flexible wing: a benchmark and case study," *Aerospace*, vol. 9, no. 8, p. 438, 2022, ISSN: 2226-4310, DOI: 10.3390/aerospace9080438 (cit. on pp. 94, 119, 121–123).

[7] E. Neu, F. Janser, A. A. Khatibi, C. Braun, and A. C. Orifici, "Operational Modal Analysis of a wing excited by transonic flow," *Aerospace Science and Technology*, vol. 49, pp. 73–79, 2016, ISSN: 12709638, DOI: 10.1016/j.ast.2015.11.032 (cit. on p. 94).

[8] A. Pagani, R. Azzara, E. Carrera, and E. Zappino, "Static and dynamic testing of a full-composite VLA by using digital image correlation and output-only ground vibration testing," *Aerospace Science and Technology*, vol. 112, p. 106 632, 2021, ISSN: 12709638, DOI: 10.1016/j.ast.2021.106632 (cit. on p. 94).

[9] M. Civera, V. Mugnaini, and L. Zanotti Fragonara, "Machine learning-based automatic operational modal analysis: A structural health monitoring application to masonry arch bridges," *Structural Control and Health Monitoring*,

no. May, pp. 1–23, 2022, ISSN: 1545-2255, DOI: 10.1002/stc.3028 (cit. on p. 94).

[10] G. Dessena, D. I. Ignatyev, J. F. Whidborne, and L. Zanotti Fragonara, "A global-local meta-modelling technique for model updating," *[Submitted to] Computer Methods in Applied Mechanics and Engineering*, 2023 (cit. on p. 94).

[11] J. R. Wright and J. E. Cooper, *Introduction to Aircraft Aeroelasticity and Loads*. Chichester, UK: John Wiley & Sons, 2014, ISBN: 9781118700440, DOI: 10.1002/9781118700440 (cit. on pp. 94, 102–106, 127).

[12] A. J. Keane, A. Sóbester, and J. P. Scanlan, *Small Unmanned Fixed-wing Aircraft Design*. Chichester, UK: John Wiley & Sons, 2017, ISBN: 9781119406303, DOI: 10.1002/9781119406303 (cit. on pp. 94, 95, 120, 126, 129).

[13] P. Lubrina, S. Giclais, C. Stephan, M. Boeswald, Y. Govers, and N. Botargues, "AIRBUS A350 XWB GVT: State-of-the-Art Techniques to Perform a Faster and Better GVT Campaign," in *Topics in Modal Analysis II, Volume 8. Conference Proceedings of the Society for Experimental Mechanics Series*, R. Allemang, Ed., vol. 45, Orlando, FL.: Springer, Cham, 2014, pp. 243–256, DOI: 10.1007/978-3-319-04774-4_24 (cit. on p. 95).

[14] S. Weber *et al.*, "Application of fibre optic sensing systems to measure rotor blade structural dynamics," *Mechanical Systems and Signal Processing*, vol. 158, p. 107 758, 2021, ISSN: 08883270, DOI: 10.1016/j.ymssp.2021.107758 (cit. on p. 95).

[15] N. Tsushima, M. Tamayama, H. Arizono, and K. Makihara, "Geometrically nonlinear aeroelastic characteristics of highly flexible wing fabricated by additive manufacturing," *Aerospace Science and Technology*, vol. 117,

p. 106 923, 2021, ISSN: 12709638, DOI: 10.1016/j.ast.2021.106923 (cit. on p. 95).

[16] G. Dessena, M. Civera, L. Zanotti Fragonara, D. I. Ignatyev, and J. F. Whidborne, "A Loewner-based system identification and structural health monitoring approach for mechanical systems," *Structural Control and Health Monitoring [Accepted]*, p. 17, 2023 (cit. on pp. 95, 96, 100, 101, 108, 123).

[17] M. Civera, G. Calamai, and L. Zanotti Fragonara, "System identification via Fast Relaxed Vector Fitting for the Structural Health Monitoring of masonry bridges," *Structures*, vol. 30, no. January, pp. 277–293, 2021, ISSN: 23520124, DOI: 10.1016/j.istruc.2020.12.073 (cit. on pp. 95, 98, 102).

[18] P. Van Overschee and B. De Moor, "N4SID: Subspace algorithms for the identification of combined deterministic-stochastic systems," *Automatica*, vol. 30, no. 1, pp. 75–93, 1994, ISSN: 00051098, DOI: 10.1016/0005-1098(94)90230-5 (cit. on pp. 95–97).

[19] F. Dezi, F. Gara, and D. Roia, "Dynamic Characterization of Open-ended Pipe Piles in Marine Environment," in *Applied Studies of Coastal and Marine Environments*, InTech, 2016, pp. 169–204, DOI: 10.5772/62055 (cit. on p. 95).

[20] L. Ljung, *System Identification: Theory for the User*, First. Englewood Cliffs, NJ: P T R Prentice Hall, 1987 (cit. on p. 96).

[21] R. Pintelon and J. Schoukens, *System Identification : A Frequency Domain Approach*, 2nd. Hoboken, NJ: John Wiley, 2012 (cit. on p. 96).

[22] N. M. M. Maia, "Extraction of valid modal properties from measured data in structural vibrations," PhD Thesis, Imperial College London, 1988, p. 380 (cit. on p. 96).

[23] D. Deschrijver, M. Mrozowski, T. Dhaene, and D. De Zutter, "Macromodeling of Multiport Systems Using a Fast Implementation of the Vector Fitting Method," *IEEE Microwave and Wireless Components Letters*, vol. 18, no. 6, pp. 383–385, 2008, ISSN: 1531-1309, DOI: 10.1109/LMWC.2008.922585 (cit. on p. 97).

[24] B. Gustavsen and A. Semlyen, "Rational approximation of frequency domain responses by vector fitting," *IEEE Transactions on Power Delivery*, vol. 14, no. 3, pp. 1052–1061, 1999, ISSN: 08858977, DOI: 10.1109/61.772353 (cit. on p. 97).

[25] B. Gustavsen, "Relaxed Vector Fitting Algorithm for Rational Approximation of Frequency Domain Responses," in *2006 IEEE Workship on Signal Propagation on Interconnects*, IEEE, 2006, pp. 97–100, ISBN: 1-4244-0454-1, DOI: 10.1109/SPI.2006.289202 (cit. on p. 98).

[26] S. Grivet-Talocia and B. Gustavsen, *Passive Macromodeling: Theory and Applications*. Wiley, 2016, p. 869 (cit. on pp. 98, 99).

[27] M. Civera, G. Calamai, and L. Zanotti Fragonara, "Experimental modal analysis of structural systems by using the fast relaxed vector fitting method," *Structural Control and Health Monitoring*, vol. 28, no. 4, pp. 1–23, 2021, ISSN: 1545-2255, DOI: 10.1002/stc.2695 (cit. on pp. 98, 108).

[28] A. Rytter, "Vibrational based inspection of civil engineering structures," Ph.D. dissertation, Aalborg University, 1993 (cit. on pp. 99, 101, 102, 108, 115, 116).

[29] I. V. Gosea and A. C. Antoulas, "Model reduction of linear and nonlinear systems in the Loewner framework: A summary," in *2015 European Control Conference (ECC)*, IEEE, 2015, pp. 345–349, ISBN: 978-3-9524-2693-7, DOI: 10.1109/ECC.2015.7330568 (cit. on p. 99).

[30] K. Löwner, "Über monotone matrixfunktionen," *Mathematische Zeitschrift*, vol. 38, no. 1, pp. 177–216, 1934, ISSN: 0025-5874, DOI: 10.1007/BF01170633 (cit. on p. 100).

[31] A. Mayo and A. Antoulas, "A framework for the solution of the generalized realization problem," *Linear Algebra and its Applications*, vol. 425, no. 2-3, pp. 634–662, 2007, ISSN: 00243795, DOI: 10.1016/j.laa.2007.03.008 (cit. on p. 100).

[32] A. C. Antoulas, S. Lefteriu, and A. C. Ionita, "A Tutorial Introduction to the Loewner Framework for Model Reduction," in *Model Reduction and Approximation*, Philadelphia, PA: Society for Industrial and Applied Mathematics, 2017, ch. 8, pp. 335–376, DOI: 10.1137/1.9781611974829.ch8 (cit. on p. 100).

[33] B. Kramer and S. Gugercin, "Tangential interpolation-based eigensystem realization algorithm for MIMO systems," *Mathematical and Computer Modelling of Dynamical Systems*, vol. 22, no. 4, pp. 282–306, 2016, ISSN: 1387-3954, DOI: 10.1080/13873954.2016.1198389 (cit. on p. 100).

[34] S. Lefteriu and A. C. Antoulas, "Modeling multi-port systems from frequency response data via tangential interpolation," in *2009 IEEE Workshop on Signal Propagation on Interconnects*, IEEE, 2009, pp. 1–4, ISBN: 978-1-4244-4490-8, DOI: 10.1109/SPI.2009.5089847 (cit. on p. 100).

[35] S. Lefteriu and A. C. Antoulas, "A new approach to modeling multiport systems from frequency-fomain data," *IEEE Transactions on Computer-Aided Design of Integrated Circuits and Systems*, vol. 29, no. 1, pp. 14–27, 2010, ISSN: 0278-0070, DOI: 10.1109/TCAD.2009.2034500 (cit. on p. 100).

[36] G. Dessena, M. Civera, D. I. Ignatyev, J. F. Whidborne, and L. Zanotti Fragonara, "On the accuracy and computational efficiency of the Loewner

Framework for mechanical systems," *in preparation*, 2023 (cit. on pp. 100, 122).

[37] G. Dessena, *A tutorial on the Loewner-based system identification and structural health monitoring approach for mechanical systems.* Cranfield, 2022, DOI: 10.17862/cranfield.rd.16636279 (cit. on p. 100).

[38] C. R. Farrar, S. W. Doebling, and D. A. Nix, "Vibration–based structural damage identification," *Philosophical Transactions of the Royal Society of London. Series A: Mathematical, Physical and Engineering Sciences*, vol. 359, no. 1778, N. A. J. Lieven and D. J. Ewins, Eds., pp. 131–149, 2001, ISSN: 1364-503X, DOI: 10.1098/rsta.2000.0717 (cit. on p. 101).

[39] C. S. Wang, F. Wu, and F.-K. Chang, "Structural health monitoring from fiber-reinforced composites to steel-reinforced concrete," *Smart Materials and Structures*, vol. 10, no. 3, pp. 548–552, 2001, ISSN: 0964-1726, DOI: 10.1088/0964-1726/10/3/318 (cit. on p. 101).

[40] F. De Florio, *Airworthiness*. Elsevier, 2011, ISBN: 9780080968025, DOI: 10.1016/C2010-0-65567-2 (cit. on p. 101).

[41] P. Milillo, G. Giardina, D. Perissin, G. Milillo, A. Coletta, and C. Terranova, "Pre-Collapse Space Geodetic Observations of Critical Infrastructure: The Morandi Bridge, Genoa, Italy," *Remote Sensing*, vol. 11, no. 12, p. 1403, 2019, ISSN: 2072-4292, DOI: 10.3390/rs11121403 (cit. on p. 101).

[42] R. Roy, M. Gherlone, and C. Surace, "A shape sensing methodology for beams with generic cross-sections: Application to airfoil beams," *Aerospace Science and Technology*, vol. 110, p. 106 484, 2021, ISSN: 12709638, DOI: 10.1016/j.ast.2020.106484 (cit. on p. 101).

[43] M. Donà, A. Palmeri, M. Lombardo, and A. Cicirello, "An efficient two-node finite element formulation of multi-damaged beams including shear deformation and rotatory inertia," *Computers and Structures*, vol. 147, pp. 96–

106, 2015, ISSN: 00457949, DOI: 10.1016/j.compstruc.2014.10.002 (cit. on p. 101).

[44] F. Hemez and S. W. Doebling, "Review and assessment of model updating for non-linear, transient dynamics," *Mechanical Systems and Signal Processing*, vol. 15, no. 1, pp. 45–74, 2001, ISSN: 08883270, DOI: 10.1006/mssp.2000.1351 (cit. on p. 101).

[45] A. Cancelli, S. Laflamme, A. Alipour, S. Sritharan, and F. Ubertini, "Vibration-based damage localization and quantification in a pretensioned concrete girder using stochastic subspace identification and particle swarm model updating," *Structural Health Monitoring*, vol. 19, no. 2, pp. 587–605, 2020, ISSN: 1475-9217, DOI: 10.1177/1475921718820015 (cit. on p. 101).

[46] Wei Fan and Pizhong Qiao, "Vibration-based damage identification methods: A Review and comparative study," *Structural Health Monitoring*, vol. 10, no. 1, pp. 83–111, 2011, ISSN: 1475-9217, DOI: 10.1177/1475921710365419 (cit. on p. 101).

[47] H. Sohn, C. R. Farrar, D. D. Shunk, D. W. Stinemates, B. R. Nadler, and J. Czarnecki, "A Review of Structural Health Monitoring Literature: 1996–2001," Los Alamos National Laboratory (LANL), Los Alamos, CA, Tech. Rep., 2004 (cit. on p. 102).

[48] P. Cawley, "Structural health monitoring: Closing the gap between research and industrial deployment," *Structural Health Monitoring*, vol. 17, no. 5, pp. 1225–1244, 2018, ISSN: 1475-9217, DOI: 10.1177/1475921717750047 (cit. on p. 102).

[49] M. Bras, S. Warwick, and A. Suleman, "Aeroelastic evaluation of a flexible high aspect ratio wing UAV: Numerical simulation and experimental flight validation," *Aerospace Science and Technology*, vol. 122, p. 107 400, 2022, ISSN: 12709638, DOI: 10.1016/j.ast.2022.107400 (cit. on p. 102).

[50] R. Kamakoti and W. Shyy, "Fluid-structure interaction for aeroelastic applications," *Progress in Aerospace Sciences*, vol. 40, no. 8, pp. 535–558, 2004, ISSN: 03760421, DOI: 10.1016/j.paerosci.2005.01.001 (cit. on p. 103).

[51] R. M. Ajaj, M. S. Parancheerivilakkathil, M. Amoozgar, M. I. Friswell, and W. J. Cantwell, "Recent developments in the aeroelasticity of morphing aircraft," *Progress in Aerospace Sciences*, vol. 120, no. February, p. 100 682, 2021, ISSN: 03760421, DOI: 10.1016/j.paerosci.2020.100682 (cit. on p. 103).

[52] W. Su and C. E. Cesnik, "Dynamic response of highly flexible flying wings," *Collection of Technical Papers - AIAA/ASME/ASCE/AHS/ASC Structures, Structural Dynamics and Materials Conference*, vol. 1, no. May, pp. 412–435, 2006, ISSN: 02734508, DOI: 10.2514/6.2006-1636 (cit. on p. 103).

[53] W. Su and C. E. Cesnik, "Nonlinear aeroelasticity of a very flexible blended-wing-body aircraft," *Journal of Aircraft*, vol. 47, no. 5, pp. 1539–1553, 2010, ISSN: 15333868, DOI: 10.2514/1.47317 (cit. on p. 103).

[54] G. J. Hancock, J. R. Wright, and A. Simpson, "On the teaching of the principles of wing flexure-torsion flutter," *Aeronautical Journal*, pp. 285–305, 89 1985, DOI: 10.1017/S0001924000015050 (cit. on p. 103).

[55] F. Naeim and J. M. Kelly, *Design of Seismic Isolated Structures*. Hoboken, NJ, USA: John Wiley & Sons, Inc., 1999, p. 304, ISBN: 9780470172742, DOI: 10.1002/9780470172742 (cit. on p. 105).

[56] R. L. Bisplinghoff, H. Ashley, and R. L. Halfman, *Aeroelasticity*. 1996, p. 860, ISBN: 9780486691893 (cit. on p. 105).

[57] L. Colo, G. Broux, and E. Garrigues, "A new flutter prediction algorithm to avoid P-K method shortcomings," in *International Forum on Aeroelasticity*

and Structural Dynamics 2019, IFASD 2019, Savannah, Georgia, 2019, pp. 1–19 (cit. on p. 106).

[58] R. J. Allemang and D. L. Brown, "A correlation coefficient for modal vector analysis," in *Proceedings of the 1st International Modal Analysis Conference*, Orlando: Union Coll, 1982, pp. 110–116 (cit. on p. 111).

[59] A. Pontillo *et al.*, "Flexible high aspect ratio wing: low cost experimental model and computational framework," in *2018 AIAA Atmospheric Flight Mechanics Conference*, Kissimmee, FL: American Institute of Aeronautics and Astronautics, 2018, pp. 1–15, ISBN: 978-1-62410-525-8, DOI: 10.2514/6.2018-1014 (cit. on p. 119).

[60] S. Y. Yusuf, D. Hayes, A. Pontillo, M. A. Carrizales, G. X. Dussart, and M. M. Lone, "Aeroelastic Scaling for Flexible High Aspect Ratio Wings," in *AIAA Scitech 2019 Forum*, Reston, Virginia: American Institute of Aeronautics and Astronautics, 2019, pp. 1–14, ISBN: 978-1-62410-578-4, DOI: 10.2514/6.2019-1594 (cit. on p. 119).

[61] D. Hayes, A. Pontillo, S. Y. Yusuf, M. M. Lone, and J. Whidborne, "High aspect ratio wing design using the minimum energy destruction principle," in *AIAA Scitech 2019 Forum*, Kissimmee, FL: American Institute of Aeronautics and Astronautics, 2019, ISBN: 978-1-62410-578-4, DOI: 10.2514/6.2019-1592 (cit. on p. 119).

[62] A. Pontillo, "High Aspect Ratio Wings on Commercial Aircraft: a Numerical and Experimental approach," PhD Thesis, Cranfield University, 2020 (cit. on p. 119).

[63] Stratasys, *Digital ABS plus*, 2021, [Online]. Available: https://www.stratasys.com/it/materials/search/digital-abs-plus (visited on 2021) (cit. on p. 119).

[64] Stratasys, *Agilus 30*, 2021, [Online]. Available: https://www.stratasys.com/materials/search/agilus30 (cit. on p. 119).

[65] M. Civera, S. Grivet-Talocia, C. Surace, and L. Zanotti Fragonara, "A generalised power-law formulation for the modelling of damping and stiffness nonlinearities," *Mechanical Systems and Signal Processing*, vol. 153, p. 107 531, 2021, ISSN: 10961216, DOI: 10.1016/j.ymssp.2020.107531 (cit. on p. 126).

[66] J. Zhang *et al.*, "Aeroelastic model and analysis of an active camber morphing wing," *Aerospace Science and Technology*, vol. 111, p. 106 534, 2021, ISSN: 12709638, DOI: 10.1016/j.ast.2021.106534 (cit. on p. 127).

Chapter 5

Identification of Nonlinearity Sources in a Flexible Wing: a Case Study[1]

Abstract

Nonlinearities exist, to different extents, in all real systems. In aeronautics, flexible high aspect ratio wings have become the new state-of-the-art in wing design, pushed by the pursuit of greater aerodynamic efficiency, by decreasing drag, and lighter aircraft, thanks to the use of composite materials. Nevertheless, accounting for nonlinearities in the design and testing phase of aeronautical product development is still a challenge. In this work, a flexible wing that showed unusual, softening, behaviour during two previous ground vibration testing campaigns is considered. In order to determine the nature of the nonlinearity, the wing backbone curve is extracted from the free-decay from resonance data, along with the time-frequency spectrogram and the Hilbert spectrum. The softening behaviour

[1]This is an adapted version of the following preprint in preparation for submission to *Journal of Aerospace Engineering*: Dessena, G., Pontillo A., Ignatyev, D. I., Whidborne, J.F., Zanotti Fragonara, L. (2023). Identification of Nonlinearity Sources in a Flexible Wing: a Case Study

is confirmed and further testing and visual inspections on the sub-assemblies and components are carried out to pinpoint the main sources of nonlinearity.

5.1 Introduction

Linear behaviour is a common assumption for engineering design and testing, but for some products and applications, such as automotive shock absorbers [1] and flexible wings [2], nonlinear effects cannot be neglected. This is particularly true within aeronautics, where structures, controls and aerodynamics interact closely [3]. Lately, nonlinear identification [4] and reduced order modelling [5] have been of great interest for slender wing structures, due to the shift in wing design paradigm, driven by the search for more efficient designs [6]. Research has focused on nonlinear modelling of structural components interaction, such as wing-pylon interaction [7] and morphing structures [8] for the characterisation of aeroelastic behaviour.

The aeroelastic behaviour characterisation is the main motivation for the ever-growing interest of the aeronautic community in nonlinearity. The search for more efficient designs has increased the amount of composite materials and has made the wings lighter and slenderer than ever before [9]. Two prime examples in civil aviation are the Airbus A350 and the Boeing 787 Dreamliner. For these new and challenging structures, classical linear, experimental or operational, modal analysis (LMA) cannot be applied and new challenges arise. Fortunately, nonlinear modal analysis (NLMA) has been proposed over a decade ago and general reviews are found in [10] and, its recent update, in [11]. The aim of NLMA is to prescribe a universal and immediate tool similar to LMA, but for the nonlinear regime. However, there does not yet exist a clear and widely accepted global theory. It is not the purpose of this work to give an extensive review of NLMA, for which the interested reader is referred to the book of [12], and for this introduction,

priority is given to the widely accepted practices in NLMA.

Nonlinear normal modes (NNMs) have been proposed as an extension of LMA modes. Nevertheless, two different, but not irreconcilable, definitions exist: the Rosenberg NNM [13] and the Shaw and Pierre NNM [14]. The former is defined when synchronous and periodic oscillations approach their respective maxima at the same instant for all modal coordinates, while the latter introduces the concept of invariant manifold, a graph over the two-dimensional modal subspace of the linearised equivalent system. When the synchronous requirement is relaxed, the two definitions can be reconciled. In fact, the Shaw and Pierre NNM can be seen as the surface where the Rosenberg NNM exists in a fixed phase space. Extensive scrutiny of the matter is beyond the scope of this research, but the interested reader is directed to the review by [15].

all masses execute periodic motions of the same period, when all of them pass through the equilibrium position at the same instant

A foundation block in the NNM practical usage is the backbone (BB) curve, which can be defined as the frequency-amplitude projection of NNMs. This projection carries useful information about the system, such as energy dependence and the direction of the stiffness nonlinearity, such as softening and hardening. For flexible wings, geometric nonlinearities dominate the spectrum causing hardening effects. Notably, in [16, 17] a methodology for extracting the NNM BB curve is outlined by considering the free-decay from resonance excited via a stepped sine and subsequent time-frequency analysis on the results. This approach is also used in [9] for the validation of a vision-based measurement system and in [5] for the model order reduction of a flexible beam, with a single degree of freedom (SDOF) oscillator based on the Duffing model. Also, control-based continuation through phase resonance testing can be used to extract BB curves [18], but it requires ad hoc control software and adds to the overall complexity of the test. Hence, only the former approach is considered in this work.

SDOF oscillators are commonly used for identifying and reducing the order of a nonlinear system. The most popular model used for these tasks is the Duffing oscillator [19], which adds a cubic stiffness term to a linear SDOF oscillator. Numerous other modified formulations and models have been proposed for specific problems [5, 20, 21]; however, the state-of-the-art for the modelling of slender structures, such as flexible wings, considers an added quadratic damping coefficient [22]. The latter formulation, the Duffing oscillator with the quadratic damping term, is considered for the remainder of this work.

In this work, a flexible wing that had previously undergone Ground Vibration Testing (GVT) at different amplitudes [23, 24] is considered. Two GVT testing campaigns with different input excitations and identification methods returned a surprising result: the geometric nonlinearities were not dominant and the wing showed softening behaviour across the input amplitude range. Hence, further testing is required to investigate this nonlinearity. The aims of this work are threefold: (i) investigating the detected softening behaviour by extracting the BB curve of the wing's first mode, (ii) fitting the free-decay time series with a Duffing model to characterise the nonlinearity and (iii) assess the nature of the nonlinearity, which is suspected to be either damage [25] or load misalignment [26].

The remaining of this work is organised as follows. The flexible wing used as the specimen for this study is introduced in Section 5.2, with previous test results that justify this research. In Section 5.3, the nonlinear experimental test, their results and the identification procedure are presented. Following, Section 5.4 deals with the process of identifying the main source of nonlinearity and Section 5.5 discusses the results in a global manner. The article is closed by concluding remarks in Section 5.6.

5.2 The Flexible Wing

The flexible wing specimen used in this work is the eXperimental BeaRDS 2 (XB2) High Aspect Ratio (HAR) wing from the Beam Reduction Dynamic Scaling (BeaRDS) project [27–30]. The project aimed to establish a workflow for the design, manufacture and testing of dynamically scaled HAR wings for use in the Cranfield University 8'×6' wind tunnel. For this reason, the XB-2 is a dynamically scaled prototype of an alternative design, for drag minimisation, for a high-wing version of an A320-like airframe.

The XB-2 wing (Figure 5.1a) defining characteristic is its skin, which was additive manufactured using two different materials within the same print. The PolyJet technology [31] allowed for using alternating strips of Digital ABS [32] and Agilus 30 [33]. The former is a type of 3D printable ABS and the latter is a rubber-like material. In Figure 5.1a the black strips are made of Agilus 30 and the white strips of Digital ABS. The Agilus 30 strips allow the wing to be extremely flexible without compromising the integrity of the skin and, according to [28], it does not allow the skin to have a stiffening effect on the wing. Under XB-2's skin, the wing's torque box can be found and it is shown in Figure 5.1b. The torque box is made up of two main components: (i) a 6082-T6 Aluminium spar and (ii) a Stainless Steel tube. The former is machined out of two Aluminum blocks and joined at mid-span with a weld reinforced by four reinforcement plates. The latter is a stiffening tube that was added aft of the spar to allow for higher aeroelastic phenomena onset speed for wind tunnel testing [34]. The tube has a 10 mm diameter and a 1 mm thickness. In Figure 5.1b, the spar's sections and taper are shown on the torque box assembly.

The wing's geometrical and material properties, including aerofoil profile, semi span, mean aerodynamic chord ($\bar{c}$), taper ratio (λ), leading edge (LE) sweep (Λ_{LE}), quarter chord sweep ($\Lambda_{\text{c/4}}$) and mass are reported in Table 5.1.

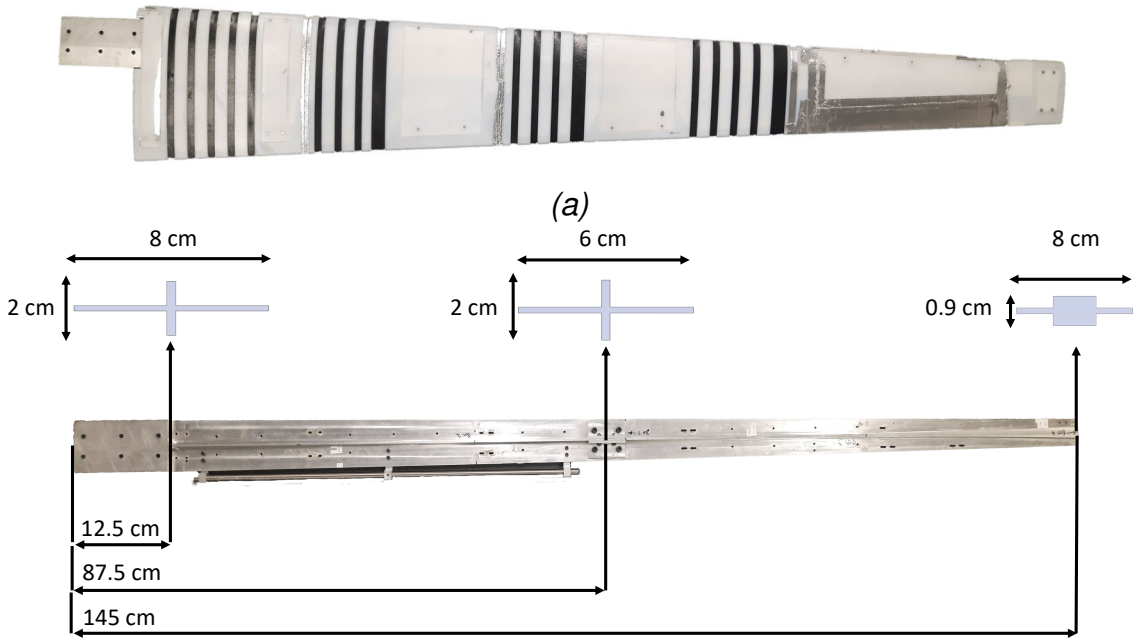

(a)

(b)

Figure 5.1: XB-2 HAR wing top view (retrieved from [23]) in Figure 5.1a, Figure 5.1b shows the torque box assembly (adapted from [23]).

Table 5.1: Materials and physical properties.

Material	**Young Modulus [GPa]**	**Poisson Ratio [-]**	**Density [kgm^{-3}]**
6082-T6 Aluminium	70	0.33	2700
Stainless Steel	193	0.33	8000
Digital ABS	2.6–3.0	0.33 [35]	1170–1180
Agilus 30	NA	NA	1140
Property	**Details**	**Unit**	
Semi span	1.5	m	
AR	18.8	-	
$\bar{c}$	172	mm	
λ	0.35	-	
Λ_{LE}	14.9	$^\circ$	
$\Lambda_{c/4}$	0	$^\circ$	
Aerofoil	NACA 23015	-	
Mass	3.024	kg	

The readers interested in a more profound review of the XB-2 wing are referred to [23, 24, 28, 30, 36, 37].

5.2.1 Previous Experimental Results

As mentioned in Section 5.1, the motivation of this work is to investigate the nature and origin of the nonlinearities detected in of two previous testing campaigns [23, 24] on the XB-2 wing. The first involved the extensive GVT of the XB-2 wing and its sub-assemblies and components, the latter investigated the effect of different setting angles on modal parameters within the GVT of XB-2. In both instances, the test are carried on a table shaker, where the wing is secured with a clamp (more information about the clamp itself are available in [24]). The table shaker is a Data Physics Signal Force modal shaker, which is controlled by its DP760 closed-loop control software running on a consumer-grade laptop.

For the first testing campaign, only the data regarding the full wing is reported, while for the second only the cases at the neutral setting angle are. It should be noted that the excitation inputs of the two tests are slightly different: in the first instance, a bandwidth-limited random vibration between 2 and 400 Hz is used, while in the second the bandwidth is between 2 and 100 Hz. In both instances, three different input amplitudes are used and are referred as ”low”, ”medium”, and ”high” input. These, respectively, correspond to an input amplitude of 0.305, 1.034 and 1.712 g RMS (root mean square) for the first set of tests and to 0.649, 0.919 and 1.590 g RMS for the second set.

In order to obtain useful results, a set of sensors (accelerometers) were placed on the wing. A sensor placement strategy based on the minimisation of the cross-correlation between adjacent modes via a genetic algorithm [38] is selected. The optimisation routine is run to choose the position of four rows of accelerometers, allowing for the detection of bending and torsional modes. Hence, eight accelerometers are positioned along the wing’s span and one on the clamp, to provide feedback to the table shaker controller, as per Figure 5.2.

The accelerometers properties are listed in Table 5.2 and their recorded acceleration data is recorded by a National Instruments cDAQ-9178 and saved on

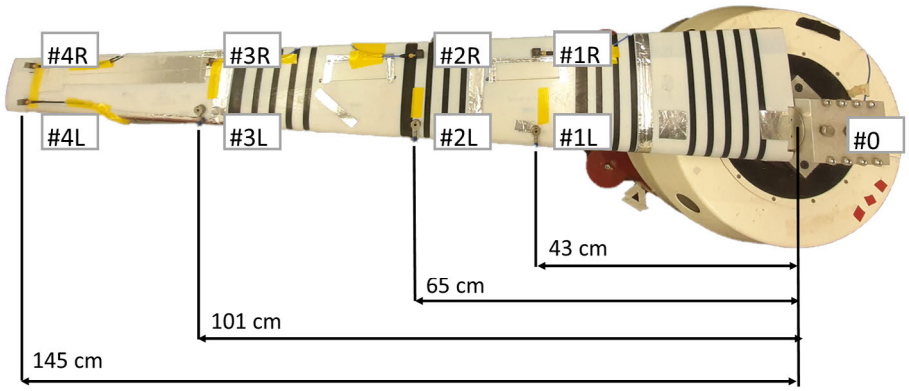

Figure 5.2: XB-2: Accelerometers locations. The accelerometers do not appear aligned only for the optical effect of the camera lens (retrieved from [23]).

a desktop machine via a LABVIEW routine.

Table 5.2: Accelerometers specifications.

Accelerometers			
ID #	**Model**	**Sensitivity [mVg^{-1}]**	**Mass [g]**
0	PCB Piezotronics model: 352C23	4.88	0.2
1R	PCB Piezotronics model: 356A16	96.50	7.4
1L	Isotron accelerometer model: 7251A	10.30	10.5
2R	PCB Piezotronics model: 356A16	97.20	7.4
2L	Isotron accelerometer model: 7251A	10.08	10.5
3R	PCB Piezotronics model: 356A45	100.20	4.2
3L	Isotron accelerometer model: 7251A	10.34	10.5
4R	Brüel & Kjær accelerometer type: 4507-002	94.12	4.8
4L	Brüel & Kjær accelerometer type: 4507-002	95.52	4.8

In the first test case the modal parameters are identified using the well-known [39] Least Squares Complex Exponenetial (LSCE) method [40, 41] and in the second instance a technique introduced for mechanical systems by some of the authors, the Loewner Framework (LF) [36, 42, 43], is used. Both techniques are input-output techniques in the frequency domain with, at least, Single-Input-Multiple-Output capabilities. In Table 5.3 and Figure 5.3, the modal parameters (natural frequencies - ω_n -, damping ratios - ζ_n - and mode shapes - $\boldsymbol{\phi}_n$ -) extracted from the two campaigns are reported.

From Table 5.3, it is clear that a relationship between the excitation amplitude and the identified modal parameters exists. More importantly, this relation

Table 5.3: Natural frequencies and damping ratios identified in [23, 24].

	Input	**Mode**	1st	2nd	4th
Natural Frequencies [Hz]	Low	LSCE	3.187	11.752	17.447
		LF	3.210	12.500	17.360
	Medium	LSCE	3.164	11.267	17.070
		LF	3.200	11.920	17.150
	High	LSCE	3.139	11.196	16.988
		LF	3.170	11.760	17.050
Damping Ratios [-]	Low	LSCE	0.024	0.047	0.037
		LF	0.035	0.053	0.045
	Medium	LSCE	0.018	0.060	0.041
		LF	0.023	0.053	0.045
	High	LSCE	0.018	0.065	0.042
		LF	0.018	0.055	0.057

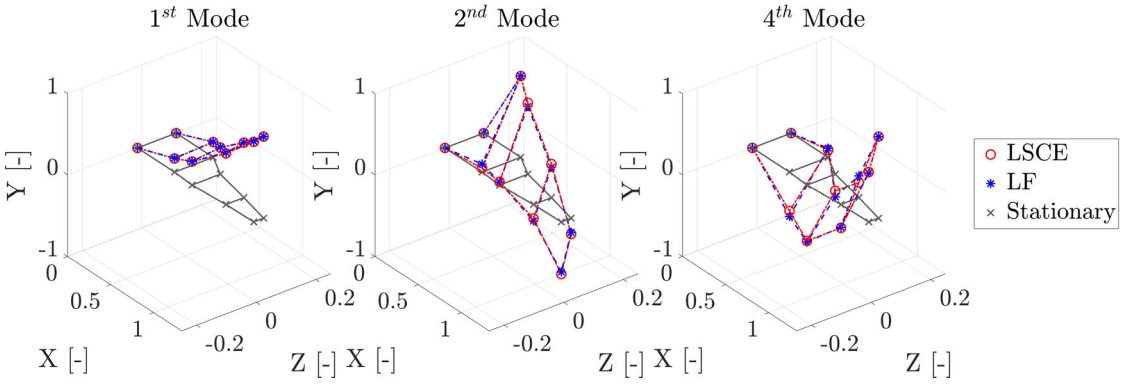

Figure 5.3: Mode shapes identified in [23, 24], respectively, by LSCE and LF for the low input cases.

holds for different excitation signals and identification methods and, so, cannot be classified as a casuality. In Figure 5.3 the $\boldsymbol{\phi}_n$ identified in the two testing campaigns, respectively with LSCE and LF are shown. For clarity and conciseness, only those from the low input cases are reported, as the correlation, calculated with the modal assurance criterion [44], between the $\boldsymbol{\phi}_n$ obtained from the different input signals is well over 90%. The first mode is found to be a bending mode and the second and the fourth are found to be coupled, bending and torsion, modes. The third mode is not investigated in [23, 24] as it was found to be lagging dominant and so outside of the scope of those studies.

In Table 5.3 for both the testing campaigns, the ω_n decrease as the input

excitation amplitude increases. This behaviour is not what is expected for a HAR wing under large deflections. In fact, geometric nonlinearities should dominate delivering a hardening effect [5], which should result in the ω_n raising with the input. However, for XB-2 a decrease in the resonance frequencies is shown. This phenomenon is known as nonlinear softening. Nevertheless, this effect is not major and it can be defined as slight nonlinear softening behaviour. This is also shown by the fact that ζ_n are virtually independent of the input and $\boldsymbol{\phi}_n$ are basically unchanged.

5.3 NNM free-decay identification

Random vibration tests alone are only good to pinpoint a nonlinearity and not to properly characterise it [12]. Further testing is designed in order to extract the BB curves relevant to the first NNM from free-decay data and model the nonlinearity using an SDOF oscillator.

The baseline experimental setup and sensor position are left unchanged from the previous GVTs. The difference lies in the input signal and the data of interest. A stepped sine excitation ($p(t) = F\sin(\omega t)$ - F is the amplitude) is used to excite the structure to resonance [16]. This process can be laborious because the frequency step has to be sufficiently small [9]. A 0.01 Hz step is used in this work, to step up the frequency when the balance is reached. For this test, the RMS amplitude (F) in g of the stepped sine is set to 1. From previous testing, it is clear that the first linear mode lived around 3.2 Hz. Hence, the stepped sine is initiated at 2.5 Hz. At quadrature, the input from the shaker is stopped and the free-decay is recorded. In this section, the results from accelerometer channel #4L (as per Figure 5.2 and Table 5.2) are reported and discussed.

Figure 5.4a shows the free-decay from resonance for the first mode of accelerometer channel #4L. The time series data is recorded at 5120 Hz, converted

from g to ms^{-2}, down-sampled to 512 Hz and de-trended. In Figure 5.4b, the BB curve is extracted using the zero-crossing technique, which gives enhanced performance and precision over the Hilbert Transform approach [9]. In this approach, the zero-crossing points are recorded and the frequency between the full cycle of the sinusoidal free-decay is recorded to obtain the frequency and the maximum peak, within that interval, sets the amplitude, outlining the points of the BB curve. In the case of interest, a moving average with a window length of 20 is applied to smooth out the response. The circles in Figure 5.4b mark the query points.

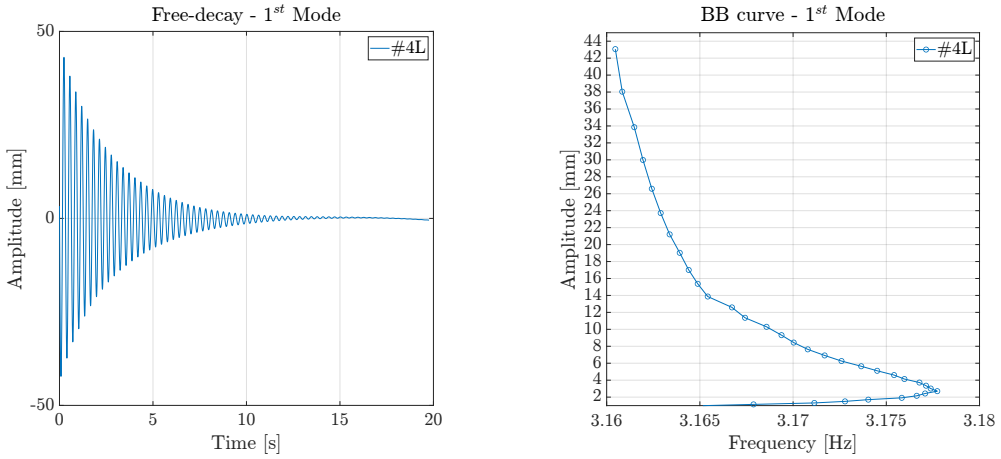

(a) *(b)*

Figure 5.4: Figure 5.4a shows the free-decay, measured from accelerometer channels #4L, from resonance for the first mode of the XB-2 wing and Figure 5.4b shows the linked BB curve.

From the BB curve in Figure 5.4b it is clear that the softening trend is confirmed even from the free-decay from resonance data. As a further sanity check, the time-frequency analysis of the free-decay is carried out with a modified version of the continuous wavelet transform (CWT), known as superlet [45]. The superlet allows for custom resolution in both time and frequency, instead of what happens with normal CWT and short-time Fourier transform. To the knowledge of the authors, this is the first instance in the literature that the superlet is applied to mechanical systems. The resulting spectrogram is found in Figure 5.5a, where the black dashed line shows the ridge of the log(Energy). Figure 5.5b shows

the Hilbert spectrum of the free-decay signal under scrutiny. The time-frequency analysis of the Hilbert-Huang transform [46, 47] is used to cross-check if any of the signals was influenced by lower or higher harmonics.

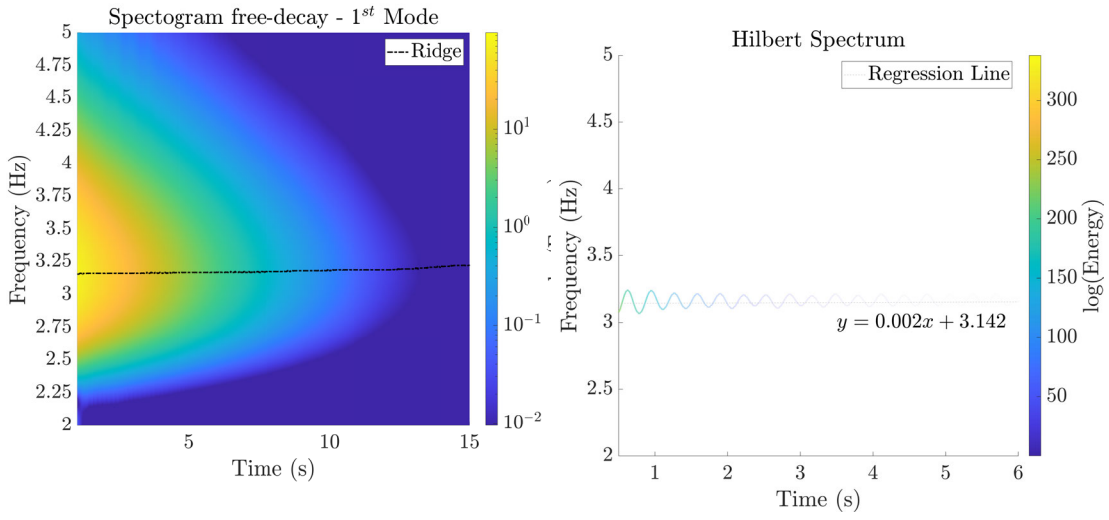

(a) *(b)*

Figure 5.5: Figure 5.5a shows the spectogram obtained via superlet of the free-decay signal and in Figure 5.4b its Hilbert spectrum is shown.

In Figure 5.5a, the spectrogram of the free-decay for the first mode of the XB-2 wing is shown. As expected the energy decreases as time goes, on due to the signal amplitude decreasing. Notably, the dashed black line shows the energy ridge, or crest. This line clearly has a positive slope. Hence, the results from the spectrogram confirm the results from the GVTs and the BB curve extraction: a softening nonlinearity is present in the wing. Nevertheless, Figure 5.5b shows the Hilbert spectrum of the signal. Clearly, only one signal component is found; hence, the nonlinearity is not caused by other external phenomena, but by the structure's harmonic motion itself. In addition, a regression line, taking the form of a grey dashed line, is plotted, once again confirming the softening nature of the nonlinearity.

At this stage, the numerical quantification of the nonlinearity is carried out before investigating its nature. According to [5, 20], a linear SDOF oscillator can

be used, as a preliminary step, to fit a system's free-decay. For a time series, the SDOF takes the form of:

$$m\ddot{x} + c\dot{x} + kx = 0 \tag{5.1}$$

where m, c and k are, respectively, the equivalent mass, damping and stiffness coefficients. The SDOF in Equation (5.1) has an analytical solution when the critical damping ratio (c_c) is larger than c such that:

$$\ddot{x} = A\cos(2\pi\omega_d t + \varphi)\ \exp(-\zeta 2\pi\omega t) \tag{5.2}$$

where $\ddot{x}$ is the acceleration time history, A is the acceleration amplitude, ω_d is the damped natural frequency, φ is the phase angle in radians, ζ is the damping ratio and ω is the natural frequency. For these the usual relationships hold:

$$\omega = \frac{\sqrt{km^{-1}}}{2\pi} \qquad \zeta = \frac{c}{4\pi\omega_n m} \qquad \omega_d = \omega\sqrt{1-\zeta^2} \tag{5.3}$$

Given the free-decay acceleration time series in Figure 5.4b, Equation (5.2)'s parameters can be fitted via the least squares method. First the modal parameters, from the GVT in [24] (Table 5.3) are used as starting point. In particular ω_1 is set as ω_d and ζ_1 as ζ. Then, ω can be extracted as per Equation (5.3). These defines a starting acceleration time series from Equation (5.2) to be fitted to the free-decay data. A random value is taken for the initiation of φ. The least squares problem is solved in MATLAB via the `fit` function. According to [20], m can be fixed to the overall mass of the tested specimen. In this case this results in $m =$ 3.024 kg. Subsequently, the damping and stiffness coefficients are also defined, such that $c =$ 2.115 Nsm^{-1} and $k =$ 1.195 kNm^{-1}.

For systems like flexible wings, the dominant nonlinear terms lie in the damping and stiffness terms [9]. The state-of-the-art formulation is a modified SDOF Duffing oscillator with quadratic damping, which takes this form when considering

free-decay:

$$m\ddot{x} + c\dot{x} + c_2\dot{x}^2 \sin\dot{x} + kx + k_3x^3 = 0 \tag{5.4}$$

where k_3 is the cubic stiffness coefficient (or Duffing term) and c_2 is the quadratic damping coefficient. Now, the coefficient identified for the linear model can be used to reduce the number of unknowns to only the nonlinear parameters. The fitting problem is defined between the free-decay time series acceleration and Equation (5.4)'s parameters. In order to solve the nonlinear least squares fitting problem, the MATLAB `lsqnonlin` function is used. The coefficient m, c and k are assumed constant from the linear system and the starting points for c_2 anf k_3 are set to 0. After the computation, c_2 is found to be 7.275 Ns^2m^{-2} and k_3 is -1081.7 kNm^{-3}. Furthermore, the process is repeated, but using all parameters (m, c, k, c_2 and k_3) for tuning. The starting points for the linear coefficients are the values identified with the linear SDOF and those for the nonlinear coefficients are zero. The results of this further fitting are reported in Table 5.4, alongside the parameters identified in the other two fitting problems. Column-wise, from left to right, the parameters extracted from the linear fitting, nonlinear fitting for only c_2 anf k_3 and nonlinear fitting for all parameters are presented. Also the error, as the root mean square error (RMSE) between the scaled acceleration time series, is presented in Table 5.4, while the scaled time series are presented in Figure 5.6.

Table 5.4: Model parameters identified via the linear and nonlinear SDOF oscillators.

Parameter	**Linear**	**Nonlinear**	**Nonlinear-2**
m **[kg]**	3.024	3.024	3.059
c **[Nsm^{-1}]**	2.116	2.116	2.146
k **[kNm^{-1}]**	1.195	1.195	1.205
c_2 **[Ns^{2}m^{-2}]**	-	7.275	7.107
k_3 **[kNm^{-3}]**	-	-6.861	-6.488
RMSE	0.01062	0.01058	0.01052

In Table 5.4, the results between the two nonlinear identification strategies

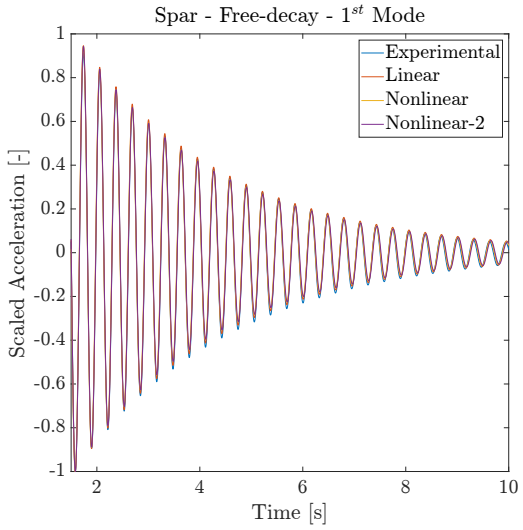

Figure 5.6: Scaled acceleration time series of the experimental and fitted data.

are slightly different. The linear terms are within a 2% difference and the nonlinear terms are less than 6%. The low sensitivity at convergence shows that the identified parameters can be trusted as a suitable solution. On the other hand, Figure 5.6 shows the three scaled acceleration free-decay time series between 1 and 10 s from the onset. The RMSE values presented in Table 5.4 are relative to the time series presented in Figure 5.6 and the metric is used to rank the data fitting models. As aforementioned, the XB-2 wing shows a slight nonlinear softening behaviour, hence the improvement of the nonlinear models over the linear SDOF is small, but still significant when the identified nonlinear parameters in Table 5.4 are assessed. The identification results clearly confirm what was already assessed from the time-frequency analysis in Figures 5.4 and 5.5a and in the previous GVTs [23, 24]: the XB-2 wing exhibits a slight nonlinear softening behaviour.

5.4 Nonlinearity source identification

Having assessed that the XB-2 wing shows a weak softening behaviour; hence; the source of this particular nonlinearity needs to be investigated. Usually, for

such slender structures geometric stiffening nonlinearities are dominant, but this is not the case. The main hypotheses are two:

- Damage in the structure:
  - breathing cracks are known to give this behaviour [25];
- A misalignment between the loading force (from the shaker table) and the shear centre (located between the spar section centroid and tube) and centre of mass exist:
  - a torsional motion is induced to the wing simulating the softening behaviour [26];

In order to assess these, the wing is first visually inspected for any apparent damage. No relevant damage is found in the wing skin, even if it would be unlikely for damage on the skin to majorly influence the stiffness of the structure as it was designed to be stiffness-free [28]. Finally, no damage is identified, by visual inspection, in the torque box. The only possible source of damage not inspected is the weld between the two halves of the main spar. Hence, the four reinforcement plates (Figure 5.7) are removed. Figure 5.8 shows the spar middle section without the reinforcement plates for the top (Figure 5.8a) and bottom surfaces (Figure 5.8b).

It is clear from Figure 5.8 that cracks exist in the top and bottom surfaces of the spar at the weld at mid-span. Each crack is 8 mm deep and constitutes a double (top and bottom) breathing crack mechanism. The two cracks would explain the nonlinearity in the structure. However, it should be considered that two halves of the spar are heavily constrained by the reinforcement plates and the problem is now to determine how these cracks actually influence the overall response of the wing. As for the GVTs in [23], nonlinear testing by the means of free-decay from resonance is performed also on the sub-assemblies and components of XB-2. In

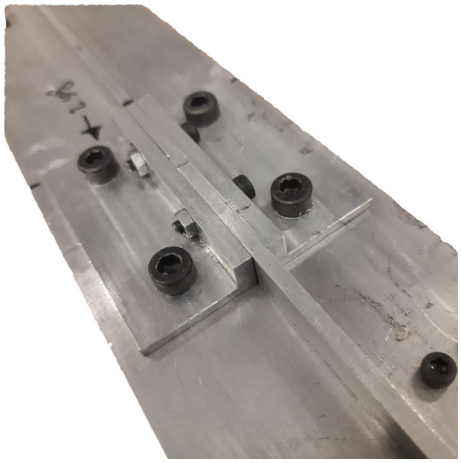

Figure 5.7: Reinforcement plates at mid-span of the spar.

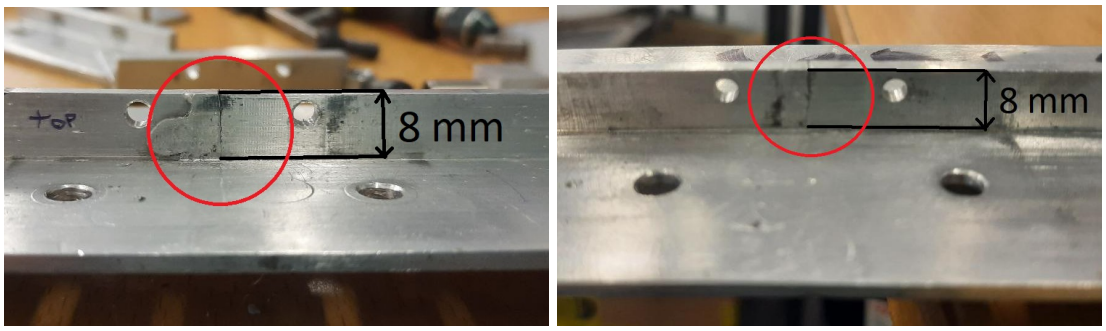

(a) *(b)*

Figure 5.8: The crack on the top surface is shown in Figure 5.8a and thatin the bottom surface in Figure 5.8b.

particular, the analysis of the nonlinear regime for the wing's spar should determine the nature of the nonlinearity of the structure. The main hypothesis is that if the spar shows a softening behaviour the breathing cracks are the main source of nonlinearity in the structure; otherwise, if the spar shows either a linear or stiffening behaviour, the wing's softening behaviour can be explained by an imbalance between the loading and inertial forces. These also need to be checked against the torque box nonlinear response.

5.4.1 Free-decay response of the spar and torque box

The spar and torque box are subjected to the same testing routine used for the XB-2 wing in Section 5.3. The goal of this further testing is to assess the be-

haviour of the wing's spar and torque box in terms of nonlinearity. This information would allow for determining the dominant source of nonlinearity of the wing within the testing regime. For this scope, in Figure 5.9 the free-decay acceleration time series, BB curves and spectrograms of the spar (Figures 5.9a, 5.9c and 5.9e) and torque box (Figures 5.9b, 5.9d and 5.9f) are presented.

The BB curves in Figures 5.9c and 5.9d are obtained via the zero-crossing technique and the spectrograms Figures 5.9e and 5.9f by employing the superlet, as per the full wing scenario in Section 5.3. From Figures 5.9a, 5.9c and 5.9e it is clear that the spar does not show a softening behaviour, on the contrary, it shows hardening. This is particularly visible in the backbone curve presented in Figure 5.9c and to a lesser extent in Figure 5.9e. The issue that makes the hardening less visible in the spectrogram has to do with the instabilities at amplitudes lower than 1.5 ms^{-2}.

The same can be said for the torque box, which, again, shows nonlinear hardening. However, the torque box behaviour at lower amplitudes, less than 7 ms^{-2}, is unstable. This is clearly seen in the BB curve in Figure 5.9d and in the spectrogram in Figure 5.9f. However, this is not a major concern as for nonlinearities in slender structures high amplitudes are the regions where most phenomena manifest.

After having identified that the XB-2 wing shows nonlinear softening and that its subpart show varying levels of nonlinear hardening, the effect of the cracks in the span can be ruled out as a potential contributor to the softening behaviour shown in the full wing. Rather, this shows that the reinforcements plates perform exactly the task they were designed for, ensuring continuity in the structure. The hardening behaviour shown by the spar and torque box is typical for such beam-like slender structures under large excitations (geometric nonlinearity) [48].

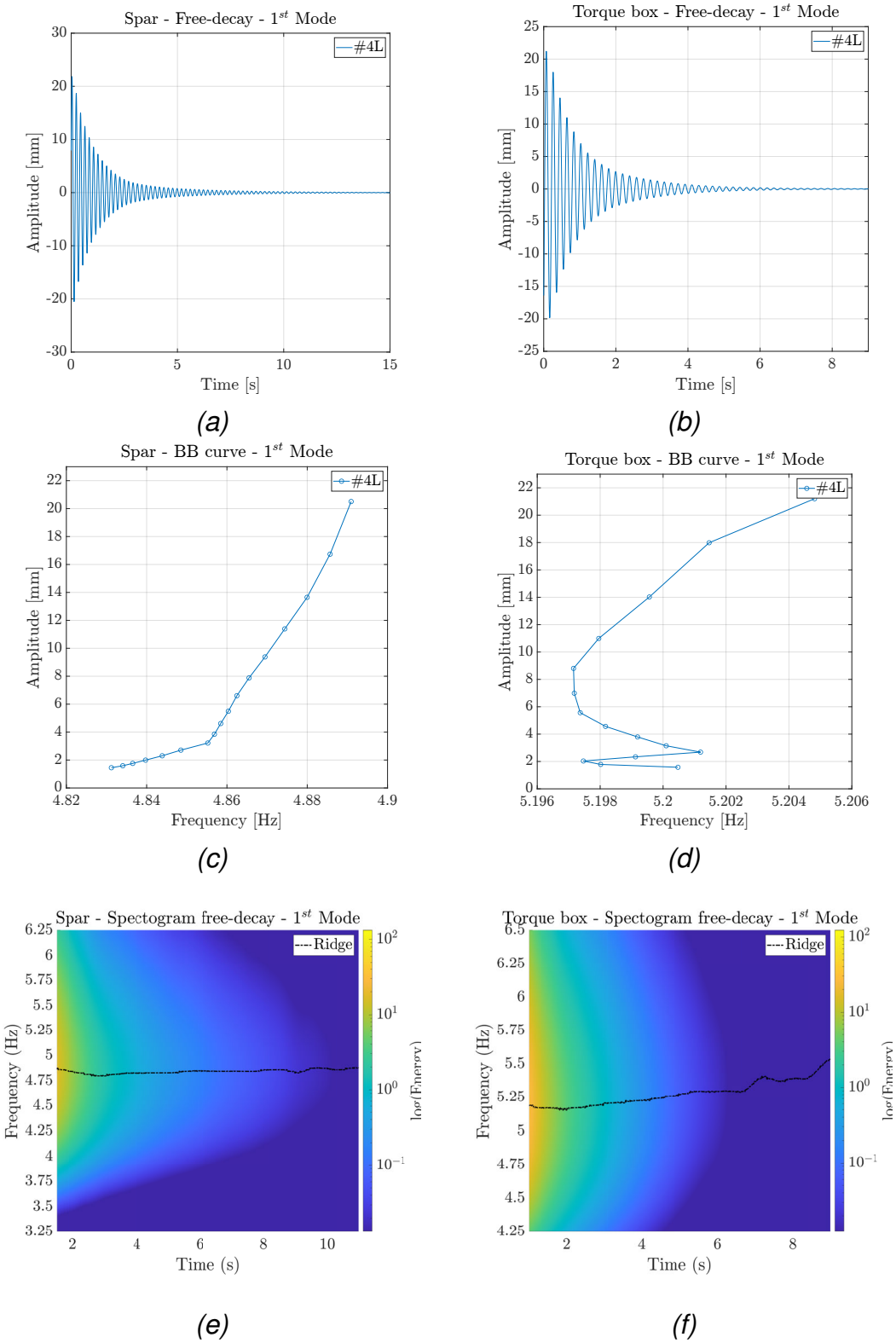

Figure 5.9: Free-decay time series and BB curves of the spar (left column - Figures 5.9a, 5.9c and 5.9e) and the torque box (right column - Figures 5.9b, 5.9d and 5.9f)

5.4.2 Mass distribution considerations

Having excluded damage as the potential main source of nonlinearity for the XB-2 wing, the second hypothesis is to be investigated: load, inertia and shear centre misalignment. First, the reference system should be considered. In Figure 5.10 a CAD model of the testing setup is shown with the reference axes. From now on the span-wise direction is identified with direction x and the chord-wise with y.

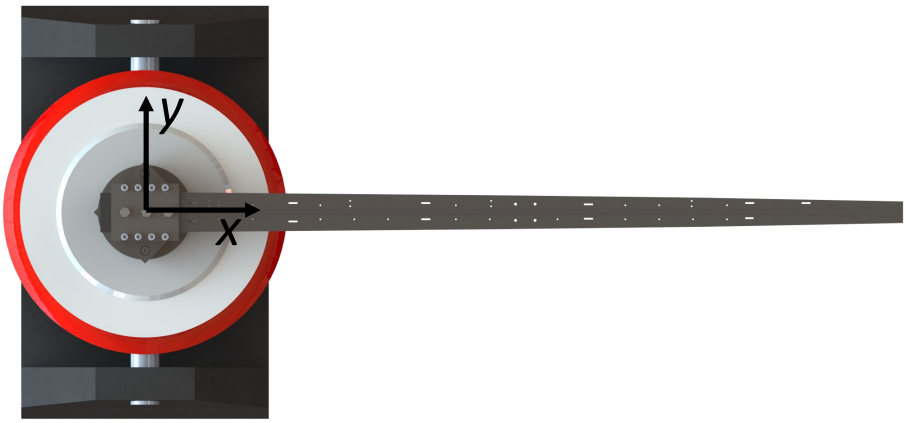

Figure 5.10: Reference axes for the mass distribution analysis.

The underlying assumption of the second hypothesis is that a chord-wise misalignment exists between the centre of mass of the full wing and the shaker excitation, such as to induce a torsional moment between the two. Hence, the centre of mass positions of the spar, torque box and XB-2 wing are studied in this section to investigate the nonlinearity.

Next, the spar centre of mass is investigated. The spar is symmetric in the chord-wise direction, so the centre of mass lies at $y = 0$ mm and span-wise at $x = 423$ mm. Hence, no torsional moment in the span-wise direction exists due to inertia effects.

The torque box is not symmetric, so some sort of imbalance is expected. It is found that the centre of mass for the torque box lies at $x = 418$ mm and $y =$ -3.6 mm. This means that a very small moment exists between the inertial forces and the shaker's excitation.

Finally, the XB-2 centre of mass is investigated. The centre of mass of XB-2 is found at $x =$ 529 mm and $y =$ -35 mm. This means that the wing's centre of mass is misaligned with the shaker's excitation. The moment relative to the location of the centre of mass of the wing can be estimated, in stationary conditions, to be a moment of 1 Nm.

In Figure 5.11 the centre of mass positions are presented with the nominal mass in kg. The origin in the plot is the same as per Figure 5.10, the centroid of the shaker table. Figure 5.11 summarises the findings of the mass distribution study: (i) the spar centre of mass lies in the centerline (x axis), (ii) the torque box centre of mass is slightly behind the centerline and (iii) the wing's centre of mass is decisively (35 mm) behind the centerline.

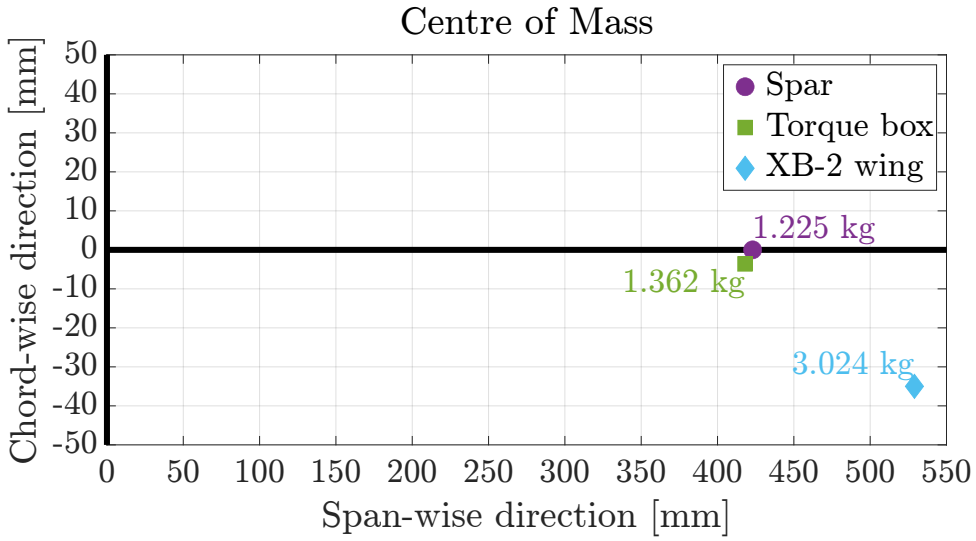

Figure 5.11: Centre of mass positions, relative to the origin in Figure 5.10, of the spar, torque box and XB-2 wing.

5.4.3 Shear centre considerations

When a load is not applied on a section's shear centre a torsional moment is generated. A torsion moment is not generated in the spar tests, due to its symmetric section; hence, the load is applied at the shear centre. However, this does not happen for the torque box and the XB-2 wing, because the stiffening tube is

placed aft of the main spar. This translates to the creation of a torsional moment between the structure and the load. This event usually develops to nonlinear softening behaviour [26]. However, the softening behaviour is not found in the nonlinear analysis of the torque box, but rather a nonlinear hardening is found at amplitudes above 7 ms^{-2}. Since the wing skin is designed to have the least possible effect on the structure's stiffness [28] (Agilus 30 strips), this means that the shear centre location is not too distant from its original position and its softening effects are dominated by nonlinear geometric hardening at higher amplitudes. However, this does not happen for the XB-2 wing, which experiences nonlinear softening. Hence, it can be considered that the shear centre location is only a contributor to the nonlinear behaviour rather than a decisive component within this testing regime.

5.5 Discussion

In Section 5.2 the XB-2 wing is introduced and the motivation for this investigation is presented. The results of two previous GVT campaigns [23, 24], where the wing is excited via a random vibration input at three different amplitudes, are shown. The ω_n extracted via LSCE and LF show that as the amplitude of the excitation increases their value decreases. Hence, a nonlinear behaviour is detected in the wing [12].

Section 5.3 investigates the nonlinearity found in the previous GVTs using the free-decay from resonance method [16]. The free-decay acceleration time series from the outermost accelerometer (channel #4 as per Figure 5.2) are isolated and the BB curve is extracted. From the BB curve, a slight softening nonlinearity is highlighted after some instability at low (less than 1 ms^{-2}) amplitudes. Further time-frequency analysis, via spectrogram and Hilbert spectrum, is carried out to verify these results. The spectrogram highlights the nonlinearity and the Hilbert

spectrum shows that the signal is not influenced by external components. After the nonlinear softening confirmation, the model is identified. First, a linear SDOF oscillator is used to identify the underlying linear system, then the identified parameters are used for the nonlinear identification. As expected from the analysis, a small negative cubic stiffness is found.

Two main hypotheses are then brought forward to identify the main source of nonlinearity in the system: (i) damage or (ii) load misalignment. The former is investigated by visual inspection and breathing cracks are found at mid-span, under the reinforcement plates, in the spar. Breathing cracks [25] would explain the softening phenomena. However, further nonlinear testing, in Section 5.4.1, on the spar and torque box shows that they are, as expected, subject to nonlinear hardening, rather than softening.

In Sections 5.4.2 and 5.4.3 the positions of the centres of mass and shear centres are considered. As expected, as parts are added to the spar, the centre of mass moves further inboard and aft of the centerline (linear extension of the excitation point of the shaker). The same happens for the shear centre when the stiffening tube is added to constitute the torque box assembly. The underlying assumption is that the shear centre does not move when the skin is added, as the latter is designed to make the least possible influence on the stiffness properties [28]. These mean that there are two, inertia and load misalignment, moments acting on the XB-2 wing. These asymmetries result in a twisting moment on the wing, which in turn decreases its bending stiffness, prompting the softening nonlinear behaviour.

Further evidence of this can be found in [37], where the time histories recorded from a disturbance in the wind tunnel for the XB-2 wing are used to identify damping for the first two modes. In fact, at the large displacements experienced in the wind tunnel test, the first mode is found to be coupled between bending and torsion. This means that, as input and displacement increase, so do the torsional

moments from inertia and load misalignment. Nevertheless, these tests were carried out on a slightly different configuration of the wing, including ballast masses, so the results cannot be directly compared.

5.6 Conclusions

In this work, high aspect ratio flexible wing nonlinearities detected in two ground vibration testing campaigns are investigated. The flexible wing shows a nonlinear softening behaviour, which is driven by inertial effects and load misalignment. This is demonstrated with nonlinear experimental testing, via the free-decay from resonance technique, backbone curve extraction, time-frequency analysis via superlets and identification of the nonlinear parameters with a Duffing oscillator with quadratic damping on the flexible wing. In addition, for the nonlinearity source identification, visual inspections, for damage assessment, and further testing on the components, such as the spar and torque box, are used to determine the source of the nonlinearity. Coincidentally, this is the first time that the superlets are used for the time-frequency analysis of experimental mechanical systems.

References

[1] C. Surace, K. Worden, and G. R. Tomlinson, “An improved nonlinear model for an automotive shock absorber,” *Nonlinear Dynamics*, vol. 3, no. 6, pp. 413–429, 1992, ISSN: 0924-090X, DOI: 10.1007/BF00045646 (cit. on p. 142).

[2] F. Mastroddi, L. M. Travaglini, and S. Gemma, “Multi-objective Optimization for the Design of an Unconventional Sun-Powered High-Altitude-Long-Endurance Unmanned Vehicle,” *Aerotecnica Missili & Spazio*, vol. 97, no. 2,

pp. 68–84, 2018, ISSN: 0365-7442, DOI: 10.1007/BF03405802 (cit. on p. 142).

[3] A. Da Ronch, K. Badcock, Y. Wang, A. Wynn, and R. Palacios, "Nonlinear Model Reduction for Flexible Aircraft Control Design," in *AIAA Atmospheric Flight Mechanics Conference*, Minneapolis, Minnesota: American Institute of Aeronautics and Astronautics, 2012, pp. 1–23, ISBN: 978-1-62410-184-7, DOI: 10.2514/6.2012-4404 (cit. on p. 142).

[4] J. M. Londoño, J. E. Cooper, and S. A. Neild, "Identification of systems containing nonlinear stiffnesses using backbone curves," *Mechanical Systems and Signal Processing*, vol. 84, pp. 116–135, 2017, ISSN: 10961216, DOI: 10.1016/j.ymssp.2016.02.008 (cit. on p. 142).

[5] M. Civera, S. Grivet-Talocia, C. Surace, and L. Zanotti Fragonara, "A generalised power-law formulation for the modelling of damping and stiffness nonlinearities," *Mechanical Systems and Signal Processing*, vol. 153, p. 107 531, 2021, ISSN: 10961216, DOI: 10.1016/j.ymssp.2020.107531 (cit. on pp. 142–144, 150, 152).

[6] S. Malik, S. Ricci, and L. Riccobene, "Aeroelastic analysis of a slender wing," *CEAS Aeronautical Journal*, vol. 11, no. 4, pp. 917–927, 2020, ISSN: 1869-5582, DOI: 10.1007/s13272-020-00459-6 (cit. on p. 142).

[7] Y. Xu, D. Cao, C. Shao, and H. Lin, "Effects of the pylon–store system on the nonlinear aeroelastic responses of a slender wing," *Nonlinear Dynamics*, vol. 95, no. 2, pp. 1471–1494, 2019, ISSN: 0924-090X, DOI: 10.1007/s11071-018-4639-6 (cit. on p. 142).

[8] X. Zhou and R. Huang, "Efficient nonlinear aeroelastic analysis of a morphing wing via parameterized fictitious mode method," *Nonlinear Dynamics*, vol. 105, no. 1, pp. 1–23, 2021, ISSN: 0924-090X, DOI: 10.1007/s11071-021-06577-y (cit. on p. 142).

[9] M. Civera, L. Zanotti Fragonara, and C. Surace, "Using video processing for the full-field identification of backbone curves in case of large vibrations," *Sensors*, vol. 19, no. 10, p. 2345, 2019, ISSN: 1424-8220, DOI: 10.3390/s19102345 (cit. on pp. 142, 143, 150, 151, 153).

[10] G. Kerschen, K. Worden, A. F. Vakakis, and J.-C. Golinval, "Past, present and future of nonlinear system identification in structural dynamics," *Mechanical Systems and Signal Processing*, vol. 20, no. 3, pp. 505–592, 2006, ISSN: 08883270, DOI: 10.1016/j.ymssp.2005.04.008 (cit. on p. 142).

[11] J. Noël and G. Kerschen, "Nonlinear system identification in structural dynamics: 10 more years of progress," *Mechanical Systems and Signal Processing*, vol. 83, pp. 2–35, 2017, ISSN: 08883270, DOI: 10.1016/j.ymssp.2016.07.020 (cit. on p. 142).

[12] K. Worden and G. R. Tomlinson, *Nonlinearity in Structural Dynamics Detection, Identification and Modelling*. Bristol, UK: Institute of Physics Publishing, 2001, ISBN: 0750303565 (cit. on pp. 142, 150, 162).

[13] R. M. Rosenberg, "The Normal Modes of Nonlinear n-Degree-of-Freedom Systems," *Journal of Applied Mechanics*, vol. 29, no. 1, pp. 7–14, 1962, ISSN: 0021-8936, DOI: 10.1115/1.3636501 (cit. on p. 143).

[14] S. Shaw and C. Pierre, "Non-linear normal modes and invariant manifolds," *Journal of Sound and Vibration*, vol. 150, no. 1, pp. 170–173, 1991, ISSN: 0022460X, DOI: 10.1016/0022-460X(91)90412-D (cit. on p. 143).

[15] G. Haller and S. Ponsioen, "Nonlinear normal modes and spectral submanifolds: existence, uniqueness and use in model reduction," *Nonlinear Dynamics*, vol. 86, no. 3, pp. 1493–1534, 2016, ISSN: 0924-090X, DOI: 10.1007/s11071-016-2974-z (cit. on p. 143).

[16] M. Peeters, G. Kerschen, and J. Golinval, "Dynamic testing of nonlinear vibrating structures using nonlinear normal modes," *Journal of Sound and Vibration*, vol. 330, no. 3, pp. 486–509, 2011, ISSN: 0022460X, DOI: 10.1016/j.jsv.2010.08.028 (cit. on pp. 143, 150, 162).

[17] M. Peeters, G. Kerschen, and J. C. Golinval, "Modal testing of nonlinear vibrating structures based on nonlinear normal modes: Experimental demonstration," *Mechanical Systems and Signal Processing*, vol. 25, no. 4, pp. 1227–1247, 2011, ISSN: 08883270, DOI: 10.1016/j.ymssp.2010.11.006 (cit. on p. 143).

[18] M. Song, L. Renson, B. Moaveni, and G. Kerschen, "Bayesian model updating and class selection of a wing-engine structure with nonlinear connections using nonlinear normal modes," *Mechanical Systems and Signal Processing*, vol. 165, no. December 2020, p. 108 337, 2022, ISSN: 10961216, DOI: 10.1016/j.ymssp.2021.108337 (cit. on p. 143).

[19] A. H. Nayfeh and D. T. Mook, *Nonlinear Oscillations*. Wiley, 1995, ISBN: 9780471121428, DOI: 10.1002/9783527617586 (cit. on p. 144).

[20] F. Cao and Y. Ge, "Air-induced nonlinear damping and added mass of vertically vibrating bridge deck section models under zero wind speed," *Journal of Wind Engineering and Industrial Aerodynamics*, vol. 169, no. June, pp. 217–231, 2017, ISSN: 01676105, DOI: 10.1016/j.jweia.2017.07.022 (cit. on pp. 144, 152, 153).

[21] S. Urasaki and H. Yabuno, "Identification method for backbone curve of cantilever beam using van der Pol-type self-excited oscillation," *Nonlinear Dynamics*, vol. 103, no. 4, pp. 3429–3442, 2021, ISSN: 0924-090X, DOI: 10.1007/s11071-020-05945-4 (cit. on p. 144).

[22] B. R. Smith, "The quadratically damped oscillator: A case study of a nonlinear equation of motion," *American Journal of Physics*, vol. 80, no. 9,

pp. 816–824, 2012, ISSN: 0002-9505, DOI: 10.1119/1.4729440 (cit. on p. 144).

[23] G. Dessena, D. I. Ignatyev, J. F. Whidborne, A. Pontillo, and L. Zanotti Fragonara, "Ground vibration testing of a flexible wing: a benchmark and case study," *Aerospace*, vol. 9, no. 8, p. 438, 2022, ISSN: 2226-4310, DOI: 10.3390/aerospace9080438 (cit. on pp. 144, 146–149, 155, 156, 162).

[24] G. Dessena, D. I. Ignatyev, J. F. Whidborne, A. Pontillo, and L. Zanotti Fragonara, "Ground vibration testing of a high aspect ratio wing with revolving clamp," in *33rd Congress of the International Council of the Aeronautical Sciences*, Stockholm, Sweden, 2022, DOI: 10.17862/cranfield.rd.20486229 (cit. on pp. 144, 146, 147, 149, 153, 155, 162).

[25] L. Yang, Z. Mao, S. Wu, X. Chen, and R. Yan, "Nonlinear dynamic behavior of rotating blade with breathing crack," *Frontiers of Mechanical Engineering*, vol. 16, no. 1, pp. 196–220, 2021, ISSN: 20950241, DOI: 10.1007/s11465-020-0609-z (cit. on pp. 144, 156, 163).

[26] A. Pagani and E. Carrera, "Unified formulation of geometrically nonlinear refined beam theories," *Mechanics of Advanced Materials and Structures*, vol. 25, no. 1, pp. 15–31, 2018, ISSN: 15376532, DOI: 10.1080/15376494.2016.1232458 (cit. on pp. 144, 156, 162).

[27] A. Pontillo *et al.*, "Flexible high aspect ratio wing: low cost experimental model and computational framework," in *2018 AIAA Atmospheric Flight Mechanics Conference*, Kissimmee, FL: American Institute of Aeronautics and Astronautics, 2018, pp. 1–15, ISBN: 978-1-62410-525-8, DOI: 10.2514/6.2018-1014 (cit. on p. 145).

[28] S. Y. Yusuf, D. Hayes, A. Pontillo, M. A. Carrizales, G. X. Dussart, and M. M. Lone, "Aeroelastic Scaling for Flexible High Aspect Ratio Wings," in *AIAA Scitech 2019 Forum*, Reston, Virginia: American Institute of Aero-

nautics and Astronautics, 2019, pp. 1–14, ISBN: 978-1-62410-578-4, DOI: 10.2514/6.2019-1594 (cit. on pp. 145, 146, 156, 162, 163).

[29] D. Hayes, A. Pontillo, S. Y. Yusuf, M. M. Lone, and J. Whidborne, "High aspect ratio wing design using the minimum energy destruction principle," in *AIAA Scitech 2019 Forum*, Kissimmee, FL: American Institute of Aeronautics and Astronautics, 2019, ISBN: 978-1-62410-578-4, DOI: 10.2514/6.2019-1592 (cit. on p. 145).

[30] A. Pontillo, "High Aspect Ratio Wings on Commercial Aircraft: a Numerical and Experimental approach," PhD Thesis, Cranfield University, 2020 (cit. on pp. 145, 146).

[31] N. P. Macdonald, J. M. Cabot, P. Smejkal, R. M. Guijt, B. Paull, and M. C. Breadmore, "Comparing Microfluidic Performance of Three-Dimensional (3D) Printing Platforms," *Analytical Chemistry*, vol. 89, no. 7, pp. 3858–3866, 2017, ISSN: 15206882, DOI: 10.1021/acs.analchem.7b00136 (cit. on p. 145).

[32] Stratasys, *Digital ABS plus*, 2021, [Online]. Available: https://www.stratasys.com/it/materials/search/digital-abs-plus (visited on 2021) (cit. on p. 145).

[33] Stratasys, *Agilus 30*, 2021, [Online]. Available: https://www.stratasys.com/materials/search/agilus30 (cit. on p. 145).

[34] S. Y. Yusuf, "On System Identification and Dynamic Scaling of a Flexible Aircraft," PhD Thesis, Cranfield University, 2019 (cit. on p. 145).

[35] A. J. Keane, A. Sóbester, and J. P. Scanlan, *Small Unmanned Fixed-wing Aircraft Design*. Chichester, UK: John Wiley & Sons, 2017, ISBN: 9781119406303, DOI: 10.1002/9781119406303 (cit. on p. 146).

[36] G. Dessena, M. Civera, A. Pontillo, D. I. Ignatyev, J. F. Whidborne, and L. Zanotti Fragonara, "Comparative Study on Novel Modal Parameters Extraction Methods for Aeronautical Structures," *in preparation*, 2023 (cit. on pp. 146, 148).

[37] I. Tsatsas, A. Pontillo, and M. Lone, "Aeroelastic damping estimation for a flexible high-aspect-ratio wing," *Journal of Aerospace Engineering*, vol. 35, no. 2, pp. 1–27, 2022, ISSN: 0893-1321, DOI: 10.1061/(ASCE)AS.1943-5525.0001390 (cit. on pp. 146, 163).

[38] A. Schulze, J. Zierath, S.-E. Rosenow, R. Bockhahn, R. Rachholz, and C. Woernle, "Optimal sensor placement for modal testing on wind turbines," *Journal of Physics: Conference Series*, vol. 753, no. 7, p. 072 031, 2016, ISSN: 1742-6588, DOI: 10.1088/1742-6596/753/7/072031 (cit. on p. 147).

[39] F. Dezi, F. Gara, and D. Roia, "Dynamic Characterization of Open-ended Pipe Piles in Marine Environment," in *Applied Studies of Coastal and Marine Environments*, InTech, 2016, pp. 169–204, DOI: 10.5772/62055 (cit. on p. 148).

[40] F. R. Spitznogle and A. H. Quazi, "Representation and analysis of time-limited signals using a Complex Exponential algorithm," *The Journal of The Acoustical Society of America*, vol. 47, no. 5 (Part I), pp. 1150–1155, 1970 (cit. on p. 148).

[41] F. R. Spitznogle, J. M. Barrett, C. I. Black, T. W. Ellis, and W. L. LaFuze, "Representation and analysis of sonar signals. Volume I. Improvements in the Complex Exponential signal analysis computational algorithm.," Office of Naval Research- Contract No. NOOO14-69-C0315,1971, Tech. Rep., 1971, p. 47 (cit. on p. 148).

[42] G. Dessena, *A tutorial on the Loewner-based system identification and structural health monitoring approach for mechanical systems.* Cranfield, 2022, DOI: 10.17862/cranfield.rd.16636279 (cit. on p. 148).

[43] G. Dessena, M. Civera, D. I. Ignatyev, J. F. Whidborne, and L. Zanotti Fragonara, "On the accuracy and computational efficiency of the Loewner Framework for mechanical systems," *in preparation*, 2023 (cit. on p. 148).

[44] R. J. Allemang and D. L. Brown, "A correlation coefficient for modal vector analysis," in *Proceedings of the 1st International Modal Analysis Conference*, Orlando: Union Coll, 1982, pp. 110–116 (cit. on p. 149).

[45] V. V. Moca, H. Bârzan, A. Nagy-Dăbâcan, and R. C. Mureșan, "Time-frequency super-resolution with superlets," *Nature Communications*, vol. 12, no. 1, pp. 1–18, 2021, ISSN: 20411723, DOI: 10.1038/s41467-020-20539-9 (cit. on p. 151).

[46] N. E. Huang *et al.*, "The empirical mode decomposition and the Hilbert spectrum for nonlinear and non-stationary time series analysis," *Proceedings of the Royal Society of London. Series A: Mathematical, Physical and Engineering Sciences*, vol. 454, no. 1971, pp. 903–995, 1998, ISSN: 1364-5021, DOI: 10.1098/rspa.1998.0193 (cit. on p. 152).

[47] N. E. Huang and N. O. Attoh-Okine, *The Hilbert-Huang Transform in Engineering*, 1st Editio, N. E. Huang and N. O. Attoh-Okine, Eds. Boca Raton, FL: CRC Press, 2005, p. 328, ISBN: 9780429114311, DOI: 10.1201/9781420027532 (cit. on p. 152).

[48] J. Taghipour, M. Dardel, and M. H. Pashaei, *Nonlinear vibration mitigation of a flexible rotor shaft carrying a longitudinally dispositioned unbalanced rigid disc*. Springer Netherlands, 2021, vol. 104, pp. 2145–2184, ISBN: 0123456789, DOI: 10.1007/s11071-021-06428-w (cit. on p. 158).

Chapter 6

A Global-local Meta-modelling Technique for Model Updating[1]

Abstract

The finite element model updating procedure of large or complex structures is a challenge for engineering practitioners and researchers. Iterative methods, such as genetic algorithms and response surface models, have a high computational burden for these problems. In this work, an enhanced version of the well-known Efficient Global Optimisation technique is introduced to address this issue. The enhanced method, refined Efficient Global Optimisation or rEGO, exploits a two-step refinement and selection technique to expand the global search capability of the original method to a global-local, or hybrid, search capability. rEGO is tested and validated on four optimisation test functions against the original methods and genetic algorithms with different settings. Good results in terms of precision and computational performance are achieved, so an application to model updating is sought. A penalty function for the finite element model updating is identified in

[1] This is an adapted version of the article submitted to *Computer Methods in Applied Mechanics and Engineering* on the 20th February 2023: Dessena, G., Ignatyev, D. I., Whidborne, J. F., Zanotti Fragonara, L. (2023). A global-local meta-modelling technique for model updating

residuals of the modified total modal assurance criterion, which uses the modal parameters from an existing structure and compares them to those of the model. The choice process is carried out using a numerical system and comparing five suitable penalty functions as candidates. Finally, rEGO for finite element model updating is implemented on a hybrid, numerical and experimental, case study based on a well-known experimental dataset. A finite element model of the structure is built and then tuned to the experimental data, then a numerical study, based on the numerical model, is carried out for damage detection and lastly the same task is done for experimental data. Satisfactory results in terms of precision and computational performance are achieved when compared to the original methods and genetic algorithms.

6.1 Introduction

Finite Element Models (FEMs) are a fundamental tool for the design and analysis of engineering structures. However, out-of-the-box FEMs rarely match the behaviour of a system without tuning. The process of tuning a model to data obtained from an existing structure is known as FEM updating (FEMU) and for large, or complex structures the process can become lengthy and convoluted. Particularly, iterative processes driven by Evolutionary Algorithms (EAs) suffer this drawback. In this work, a novel global-local optimisation routine based on the Efficient Global Optimization (EGO) [1] and Kriging [2] is introduced to address this problem. The new techniques draw on the advantages of meta-modelling to create an iterative routine for FEMU, which, in particular, can be applied for damage detection of mechanical systems. The method is first outlined, and then validated against existing optimisation techniques on a selection of well-known test functions. Subsequently, a suitable goal function for FEMU is identified and, lastly, the method is used for the model updating and damage detection on the

well-know three storey frame structure from the Engineering Institute (EI) at the Los Alamos National Laboratory (LANL) [3]. The goal of this paper is to introduce and validate a new surrogate-based optimisation technique which broadens the scope of EGO to global-local optimisation. The new technique needs to improve the precision and computational performance, particularly in the applications of interest: FEMU and damage detection.

A brief review on the application of meta-modelling-based FEMU for damage detection is given in Section 6.2. The newly developed technique, refined Efficient Global Optimisation (rEGO), is introduced in Section 6.3, its application to model updating in Section 6.4 and a hybrid, numerical and experimental, case study on the three storey frame structure from the Engineering Institute at LANL in Section 6.5.

6.2 Methods

In this section the applications of FEMU for damage detection are recalled before introducing Kriging and EGO.

6.2.1 Model Updating for Damage Detection

Model updating, intended as the calibration of FEMs using experimental data, is an established strategy within structural engineering [4]. Hence, the main goal of model updating is to establish a FEM which is representative, as much as possible, of the actual system. In fact, due to manufacturing, materials or modelling assumptions an out-of-the-box FEM is rarely adequately coherent with its real counterpart [5]; for this reason, a growing interest in model updating is registered over the last three decades [6–9].

Apart from matching the behaviour of a model to a real structure, model updating can be used for damage detection, commonly referred to as Structural Health

Monitoring (SHM) [10]. SHM is defined as the statistical pattern recognition strategy of damage in a system, by which operational capability or functionality is influenced. According to [11] this can be summarised in a four-point procedure:

1. Operational evaluation: such as a testing campaign;
2. Data acquisition and cleansing: data collection and processing from the test data;
3. Feature selection: defining what parameters or values are going to be employed for the SHM task;
4. Statistical model development: assessing the structure by comparing the undamaged and current state.

A considerable number of methods for SHM have been developed [12]; however, the most prominent are the vibration-based approaches [13], which, in turn, can be divided in direct [14] and indirect [15] methods. The former involves data obtained directly from tests, such as modal parameters or frequency response functions (FRFs), while the latter, involving model-oriented approaches known as model-based SHM, is the focus of this work. The underlying assumption of this approach is that a change in the parameters of the model between a baseline and a damaged scenario returns information on the presence, location, and severity of the damage [16]. Giving a thorough review of SHM is beyond the scope of this paper and the interested reader is referred to [17] for a general overview, to [12] for a summary of the state of industry implementation for SHM and to [16] for a review on iterative methods for SHM.

Model updating techniques can be divided into direct and indirect methods [16]. The former use modal characteristics to update the FEMs and are regarded as efficient and accurate methods. *Direct* methods include matrix updates [18], optimal matrix [19], error matrix [20] and eigenstructure assignment [21]. How-

ever, these methods are not particularly appealing for engineering practice, particularly damage detection, as they present several critical drawbacks: (i) they require very precise measurement of the structural vibration response, (ii) the sensitivity to noise, (iii) the impossibility of using truncated data and (iv) the possibility of losing symmetry in the FEM matrix. With these preconditions, *indirect*, or iterative, methods are introduced. Firstly, it is beneficial to make a distinction based on the information used for the FEMU, which can be modal data (ω_n, ζ_n, and $\boldsymbol{\phi}_n$) or directly the structure response, either in time or frequency domain. Most commonly, modal parameters and frequency domain data are used. This work focuses on modal data-based FEMU.

The *indirect* FEMU methods can be divided into five subcategories: (i) sensitivity-based methods, (ii) response surface methods (RSMs), (iii) Bayesian and Monte Carlo methods, (iv) computational intelligence techniques, and (v) Evolutionary Algorithms (EAs) methods. The general rule for indirect methods is that there is a penalty, or goal, function to be minimised in order to update the model, generally based on frequency response [22] or modal parameters [23]. The distinction within the methods lies in the way this is obtained.

Sensitivity-based methods consider a system's measured response as a change in the initial FEM parameters and the aim is to minimise this difference with a penalty function. The main limitation of this approach is its constraint in detecting small-scale damage. Nevertheless, the method is widely employed in literature, e.g the work of [24] for heritage structures.

Bayesian–Monte Carlo methods are based on the probability distribution function built on a set of data, such as defined by Bayes' theorem. These methods have the drawbacks of high computational cost, due to the requirement of solving complex integrals, and of the prior knowledge of interval distributions of updating parameters [25]. Nevertheless, fruitful implementations are available in the literature, such as the work of [26].

Computational intelligence, or machine learning, model updating techniques take advantage of the fact that FEM model updating is an optimisation problem. The requirement for a large amount of data, as for any other machine learning problem, is the main drawback of this method. However, researchers have successfully applied the method in many instances. A prominent example is the work of [27], which treats on-line model updating for structural health monitoring.

Sometimes classified with the computational intelligence methods, EAs are regarded as an efficient method to solve highly nonlinear and multimodal problems [16]. This allows them to be accurate instruments for dealing with optimisation-driven FEMU. As stated in [28], the most prominent and employed EA technique is the genetic algorithm (GA) [29], which, however, was shown to have a major drawback for model updating [30]: the number of iterations needed is relatively high, when compared to other techniques. This poses a problem when employing this methodology with complex or very large structures. Nevertheless, many applications of FEMU with EAs exist, such as the work of [31], which employed GAs to tune a FEM from modal data.

Lastly, the RSM is a statistical driven approach where a correlation is built between the input variables and response. The response is driven by a predefined goal or penalty function. While simple methods like polynomial functions can be used to draw the RSM, more advanced techniques are available, such as Kriging [2] and its RSM implementation, the Efficient Global Optimisation (EGO) [1]. A slightly modified version of EGO is used in [30] for FEMU, while [7] usees classical polynomial regression for the same scope. The main drawback of RSM for FEM is the application of statistical approximations with unknown parameters which may result in the ill-conditioning of the final model [25].

The reader interested in a more comprehensive review can refer to the book by [32] and the work by [6]. The reader particularly interested in *indirect* methods can refer to works of [25] and [16].

6.2.2 Kriging and the Efficient Global Optimisation

The idea behind meta-modelling is to create a response surface which mimics the relationship between a function, or problem, input variables and its output. RSMs obtain this goal by replacing the underlying implicit function of the original problem with an approximation model, traditionally a polynomial; hence, a computationally inexpensive function to evaluate [25]. However, more involved approaches exist which offer models with higher fidelity. One of these approaches, Kriging, is used in this work. The reader interested in a review and implementation of classical techniques is referred to the book in [25] and the work in [7].

Kriging originated in geostatistics, in the 1950s [2]; however, more recently it has seen multiple applications within engineering, particularly in design [33, 34]. Nevertheless, applications for FEM model updating are scarce [30, 35–37] and mostly do not take full advantage of surrogate-based optimisation, being mostly limited to response surface fitting. The main reason for the lack of applications in FEMU is because there is no real proof of convergence, in the sense that the obtained minimum could be far from the actual minimum [38]. However, this has longly [1] been deemed to be irrelevant when the meta-model is built *strategically*, such as for EGO. EGO can be defined as the strategic RSM implementation of Kriging. EGO can be outlined as follows:

1. The design of experiment (DoE) is drawn to collect a number of samples from the goal, or penalty, function in a strategic manner (usually LH);

2. Kriging is fitted to the data obtained through the DoE and a predictor is established;

3. The RSM can be updated with new results *strategically*, such as computing the value of the expected minimum;

4. Iterating between points 2 and 3 until convergence is reached.

In fairness, the procedure could stop after point 2 is cleared. However, the approximated response at that stage is most likely not going to be accurate enough for exploiting it, which is what EGO aims to do. The procedure starts with the DoE, which aims to evaluate the original function, or problem, at well-distributed points in the search space. The most prominent technique to obtain this is the Morris–Mitchell optimal Latin Hypercube (LH) [39, 40], which minimises the largest distance between any pair of points within the sample through an iterative procedure. This technique is considered to create the initial population, the DoE, within this work. General consensus [41] is that the initial sample should contain a number of points ten times the number of variables in the problem. The interested reader can refer to the work by [42] for a more broader review of sampling strategies.

As a stochastic-based meta-modelling technique, Kriging is based on the relationship between the sample data (input) $\boldsymbol{X}$ and the observed response (output) $\boldsymbol{Y}$ which is defined as follows:

$$\begin{aligned} & y_i(\boldsymbol{x}) = \boldsymbol{f}^T(\boldsymbol{x}_i)\boldsymbol{\beta} + z(\boldsymbol{x}_i), \text{ for } i = 1,2,...,n \\ & \text{with} \\ & \boldsymbol{X} = \{\boldsymbol{x}_1, \boldsymbol{x}_2, ..., \boldsymbol{x}_n\}^T, \ \boldsymbol{Y} = \{y_1, y_2, ..., y_n\}^T \end{aligned} \tag{6.1}$$

where $\boldsymbol{f}(\boldsymbol{x})$ is the polynomial vector of $\boldsymbol{x}$, $\boldsymbol{\beta}$ is the linear regression vector of the coefficients to be estimated and $z(\boldsymbol{x})$ represents the error as a stochastic process following a normal distribution, such as $N(0, \sigma^2)$ with a zero mean (μ) and standard deviation (σ). In order to estimate $z(\boldsymbol{x})$, a correlation model needs to be set. The most common model is Gaussian correlation [30]; hence the entries of the correlation matrix $\boldsymbol{R}$ can be built accordingly:

$$\boldsymbol{R}_{ij}(z(\boldsymbol{x}_i), z(\boldsymbol{x}_j)) = \exp\left(-\sum_{k=1}^{m} \theta_k \left| x_i^k - x_j^k \right|^2 \right) \tag{6.2}$$

where x_i^k are x_j^k the ith and jth elements of, respectively, $\boldsymbol{x}_i$ and $\boldsymbol{x}_j$, m is the number of variables and θ_k is the decay rate of correlation between the different variables. At this point the likelihood function can be defined as:

$$L = \frac{1}{(2\pi\sigma^2)^{m/2}|\boldsymbol{R}|^{1/2})} \exp\left[-\frac{(\boldsymbol{Y}-\boldsymbol{F}\boldsymbol{\beta})^T\boldsymbol{R}^{-1}(\boldsymbol{Y}-\boldsymbol{F}\boldsymbol{\beta})}{2\sigma^2} \right] \tag{6.3}$$

where $\boldsymbol{F}$ represents the matrix of $\boldsymbol{f}(\boldsymbol{x})$ for each point. If the maximum likelihood is considered [33], the following are defined:

$$\begin{aligned} \hat{\boldsymbol{\beta}} &= (\boldsymbol{F}^T\boldsymbol{R}^{-1}\boldsymbol{F})^{-1}\boldsymbol{F}^T\boldsymbol{R}^{-1}\boldsymbol{Y} \\ \hat{\sigma}^2 &= \frac{(\boldsymbol{Y}-\boldsymbol{F}\boldsymbol{\beta})^T\boldsymbol{R}^{-1}(\boldsymbol{Y}-\boldsymbol{F}\boldsymbol{\beta})}{n} \end{aligned} \tag{6.4}$$

The maximum likelihood can be expressed in a logarithmic way:

$$\ln(L) \approx -\frac{m}{2}\ln(\hat{\sigma}^2) - \frac{1}{2}\ln|\boldsymbol{R}| \tag{6.5}$$

At this stage, Equation (6.5) is maximised via a GA to obtain the value of θ_k for the different variables.

The Kriging model is now built and the predictor for any point $\boldsymbol{x}_0$ can be defined as follows:

$$\hat{y}(\boldsymbol{x}_0) = \boldsymbol{f}^T(\boldsymbol{x}_0)\hat{\boldsymbol{\beta}} + \boldsymbol{r}^T(\boldsymbol{x}_0)\boldsymbol{R}^{-1}(\boldsymbol{Y}-\boldsymbol{F}\hat{\boldsymbol{\beta}}) \tag{6.6}$$

with $\boldsymbol{r}$ denoting the n-vector of correlations between the error term, $z(\boldsymbol{x}_0)$, at $\boldsymbol{x}_0$ and the error terms $z(\boldsymbol{x}_{0-n})$ at the previously sampled points.

After generating the initial model, an updating strategy has to be considered to increase the model's precision. Traditionally, the quantities such as the minimum of the model error are infilled (data points added to model); however, EGO [1] introduced the expected improvement (EI), which can be intuitively defined as the measure of how much the minimum of the goal function can be improved if a point at a given location is infilled. Also, it is, graphically, defined as the first moment of

the area under the Gaussian distribution of the best-observed value [33]:

$$\begin{aligned} \text{EI} = E[I(x)] = (y_{min} - \hat{y}(\boldsymbol{x})) \left[\frac{1}{2} + \frac{1}{2} \text{erf} \left(\frac{y_{min} - \hat{y}(\boldsymbol{x})}{\hat{s}\sqrt{2}} \right) \right] + \\ + \hat{s} \frac{1}{\sqrt{2\pi}} \exp \left[\frac{-(y_{min} - \hat{y}(\boldsymbol{x}))^2}{2\hat{s}^2} \right] \end{aligned} \tag{6.7}$$

where $\hat{y}(\boldsymbol{x})$ is the model predicted value at $\boldsymbol{x}$, erf is the error function and $\hat{s}$ is the standard deviation.

For deeper insight into the EI the interested reader is referred to [1, 33]. The graphical definition of EI in Equation (6.7) is considered within this work.

Summarising, *direct* methods for FEMU are not feasible in real operations; hence, resorting to *indirect* methods is imperative. Within this realm, drawbacks exist for all four subcategories. Moreover, the good track record of RSM in engineering design [34, 43] makes them a suitable candidate to solve, with a novel implementation, its modest drawbacks. Given the aforementioned introduction of FEMU methods, SHM and meta-modelling, the aim of this work is to exploit the capabilities of RSM FEMU by introducing a new RSM, based on Kriging and EI, to improve the search performance in a global-local, or hybrid, sense for FEMU and damage detection applications.

6.3 The refined Efficient Global Optimisation

This section deals with the introduction of the newly developed meta-modelling technique, the rEGO, and with its numerical validation. First, the rEGO workflow and foundations are described, then a numerical study, of four test functions, has the goal of establishing a general rule for the quantification of the first stopping criterion (ε_1) and comparing rEGO to the well-established EGO and GA for optimisation purposes.

6.3.1 Workflow

The main goal of rEGO is to enhance the search capability given by the standard EGO by implementing a global-local search capability,a partly successful attempt is found in [44]. The enhancement is achieved in two ways: refinement and selection. First of all, refinement is achieved at a global scale, by halving the search space, when good knowledge of the response surface is achieved. Then, at a local level, with a local convergence criterion, the second stopping criterion (ε_2), which is based on the Euclidean distance between the variables of proposed minima (x_{dist}). The former is inspired by the design domain reduction method in [45, 46], which aims to halve the search space near the known minimum after some condition is met, in a similar fashion to multi-objective optimisation [47] and Pareto fronts dominance [48]. In the application under scrutiny, the condition is related to the exploration of the response surface and, hence, to the ε_1 and the EI. Moreover, the latter is a common feature of optimisation algorithms and it is set as 10^{-4}, such that $\varepsilon_2 = 10^{-4}$.

The refinement technique can be split in two separate tasks: exclusion and de-clustering. Exclusion is a direct consequence of the search space halving and consists in eliminating from the data pool the points which do not lie in the new search space. However, this is not sufficient in ensuring an efficient computation, as a cluster of points might have formed within the data pool. At this stage, de-clustering enters into action by ensuring points within the same cluster are excluded and only the middle point, in terms of variables' position in space, is left. This ensures the most efficient possible computation of the updated Kriging meta-model.

In order to avoid convergence to local minima with few data points, a minimum requirement for the size of the data pool is created, in such a way that the ε_1 cannot be satisfied if the number of points is less than ten times the number of variables, which is the same principle driving initial sampling. In addition, two

stopping criteria are defined. The first prescribes a refinement if, after 100 times the number of variables ($m \times 100$) iterations, there has not been another refinement (ε_1 not reached), while the second criterion stops the optimisation when the minimum of the function has not improved (stall) after 100 times the number of variables ($m \times 100$) iterations.

The above-mentioned techniques allow rEGo to become a global-local optimisation technique and improve the global-only capability of EGO. Now, the running algorithm if rEGO is outlined:

1. The initial population of size 10 $\times m$, m is the number of variables, is computed using an LH for ;
2. The initial Kriging model is built as per Equation (6.6);
3. The point where the maximum EI is found is computed and the Kriging model is updated. This process is known as infill;
4. The ε_1 is verified. If the condition is not met the process goes back to step 2;
5. The minimum location, with a GA, found from the predictor is computed;
6. If ε_2 is verified the algorithm terminates. Otherwise, the number of points is evaluated and if less than 10 $\times m$, the process goes back to point 2.
7. The search space is refined and the dominant points are selected, declustering, and the algorithm iterates from step 2.

Steps 1 to 3 represent the left column of the rEGO diagram in Figure 6.1 and frame the EGO algorithm first introduced in [1].

The critical part of the workflow is the definition of ε_1, linked to the EI. In theory, perfect convergence can be reached when $\hat{s} = 0$ of Equation (6.7); nevertheless, when dealing with real data this is highly impracticable. However, in practice [1]

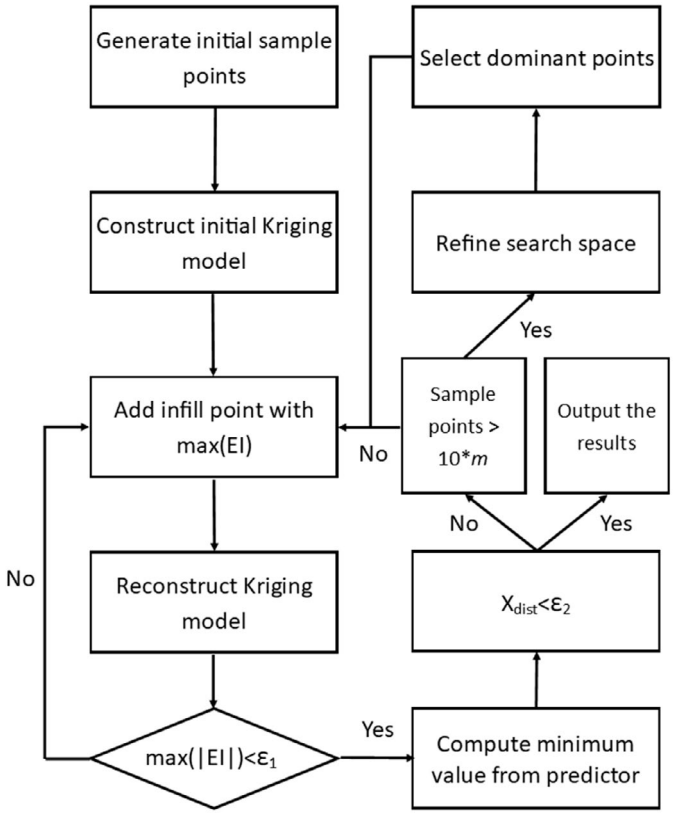

Figure 6.1: rEGO workflow. m stands for the number of variables.

suggests that a good convergence condition can be achieved for EI $= 1\%$ of the minimum of the function that is searched. If the condition is not satisfied, then the point with the maximum EI is infilled and the process iterates until convergence. The impracticability of the $\hat{s} = 0$ condition makes EGO less reliable in global search because an amount of uncertainty is postulated with the stopping criterion. In fact, in rEGO ε_1, as per EGO, is the measure of the global exploration of the response surface and, since a new method is proposed, it is improper to retain the value suggested in [1]. Hence, a numerical study, in the following subsection, investigates the relationship between EI and the algorithm's precision.

Within this work, the Design and Analysis of Computer Experiments (DACE) toolbox [49] is used to create the Kriging model and for de-clustering the data pool, with the `dsmerge` function, and the EI function is retrieved from [50, 51], while the optimal LH code is native of MATLAB, the `lhdesign` function. The authors'

complete implementation and an introductory tutorial of rEGO can be found in a Cranfield Online Research Data entry.

6.3.2 Numerical Validation

In order to investigate the relationship between the EI and the precision of the algorithm, four optimisation test functions, presented in Table 6.1, have been selected and their inputs and outputs scaled between 0 and 1. The functions implementations are adapted from [52].

Table 6.1: Test functions.

Function	Number of Variables
Modified Branin [33]	2
Hartmann 4-D Function [53]	4
Rastrigin [54]	6
Styblinski–Tang [55]	8

The ε_1 taken into consideration within this numerical study are EI = [1 %, 0.1 %, 0.01 %, 0.001 %]. Since the original EGO implementation considered 1 % to be a suitable stopping criterion, only smaller values are considered. This study's main goal is to select a suitable EI value to be used as ε_1 within rEGO. The decision is based on the compromise between precision and computational effort, the number of functions evaluations to convergence. The results of this survey for the functions in Table 6.1 are presented in Figure 6.2. The plots' ellipses represent the 95 % Confidence Interval (CI) and the markers show the mean values, both over 100 realisations.

The statistical study is necessary for the random nature of the Kriging modelling. In all cases, the largest intervals for CI are observed for the highest EI value, 1 %. This is somewhat expected as for a higher EI the knowledge of the response surface is more uncertain than smaller EIs. Nevertheless, this general rule does not apply for the number of evaluations. In fact, as clearly shown in Fig-

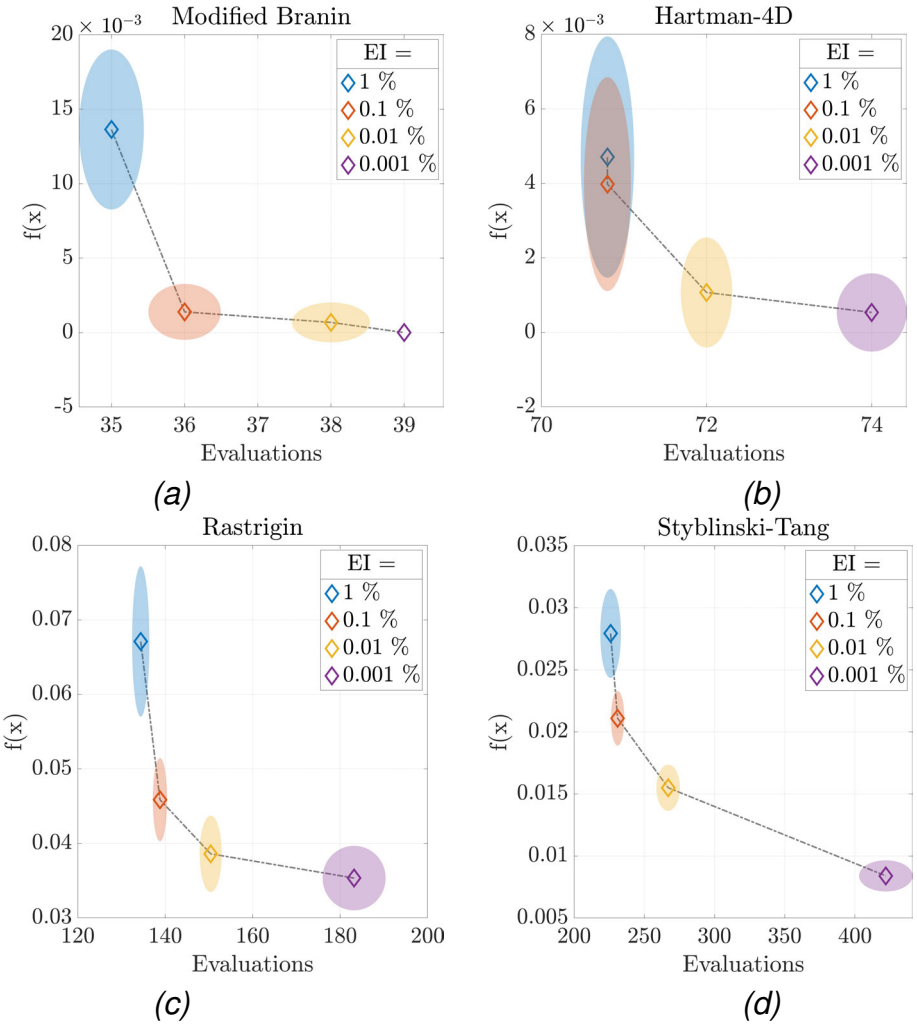

Figure 6.2: Results of the numerical study concerning ε_1 and computational efficiency. The ellipses represent the uncertainty in therms of 95 % Confidence Interval (CI) over 100 realisations.

ures 6.2b to 6.2d, for the smallest EI value (EI=0.001%) the largest uncertainty, in terms of computational effort, is found.

The highest and lowest proposed EI have two major drawbacks: the former's precision is notably worse than the others and the latter is the worst computationally; hence, they are excluded, leaving two potentially suitable values. Apart from the Modified Branin, the 0.01 % value always offer a steep improvement in precision, in terms of both the average value and smaller CI, than its larger counterpart. Even if the computational effort is larger for EI = 0.01 %, when compared to EI = 0.1 %, the difference is small, always within 10 %. Finally, from a graphical

consideration, only the EI = 0.01 % value lies in what is called the knee of the Pareto front, which, for a two-objective problem like this, indicates a good compromise between the two objectives. Hence, the value of EI = 0.01 % is selected as the ε_1 within this work and as the standard value for the rEGO algorithm. For the EI=0.001% the 95% CI of $f(x)$ is very small. Hence the ellipse looks more like a horizontal line.

After having established the two stopping criteria driving the rEGO search, it is pivotal to validate the new algorithm against existing techniques. The same test functions are evaluated by rEGO, EGO and GA 100 times for statistical relevance. For rEGO, ε_1 is 0.01 % and ε_1 is 10^{-4}, while for EGO two implementations are considered. One takes into consideration EI = 0.01 % as the stopping criterion (EGO_EI) and the other with a maximum number of function evaluations equal to the average of rEGO's evaluations to convergence (EGO_n). This means that the evaluation budget for the four functions is set, respectively to 39, 75, 176, and 265. With respect to GAs, two sets of GAs are considered. One with a number of generations of 10 (GA_10) and the other of 100 (GA_100). All the other parameters are standard as per its MATLAB implementation in the `ga` function. For all strategies, the starting population is defined by an LH generating a number of points ten times the number of variables.

In Figure 6.3 the results of this numerical study are presented. Figure 6.3a compared the mean of the minima of the functions, and their 95 % CI, found over 100 realisations with the said techniques. As expected, GA_100 generally identified the lowest values. However, as shown in Figure 6.3b, which deals with the number of evaluations to convergence, the price is that many more iterations, two orders of magnitudes more, are needed. The CI is not represented due to its negligible magnitude when compared to the number of evaluations. In terms of precision, rEGO outperformed EGO_EI, GA_10, and GA_100 for the Modified Branin Function, same for the Hartman-4D. However, for the Rastrigin function

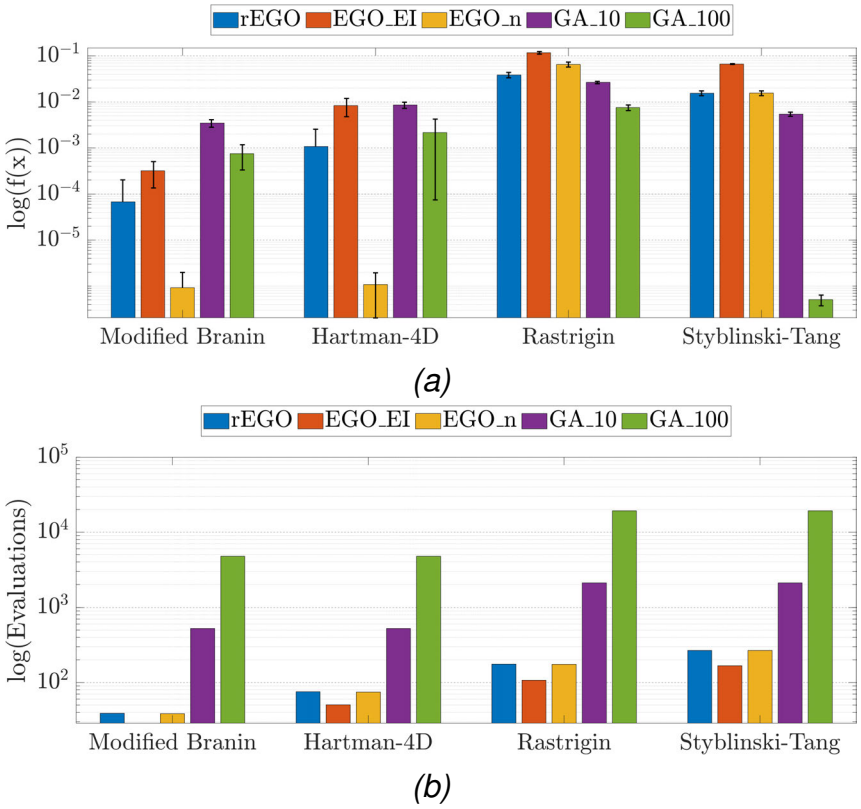

Figure 6.3: Results of the numerical study concerning the objective, f(x), and computational efficiency, number of evaluations. The plots' error bars are represent the 95 % Confidence Interval (CI) over 100 realisations.

rEGO outperformed all the surrogate-based techniques, but not the two GAs. Finally, for the Styblinkski-Tang function rEGO outperforms EGO_EI, lays in the CI of EGO_n and falls short of the two GAs. Unsurprisingly, the GAs are able to obtain better minimums as they use many more function evaluations when compared to rEGO and EGO. On the other hand, the baseline EGO is less precise for all functions, while the iteration-limited implementation reaches better performance, due to having more function evaluations. This proves that the preliminary study for the ε_1 is justified as the baseline EI value of 1 % would have brought much worse results. The performance of rEGO and EGO_n are comparable, with the latter, resulting slightly worse for the Modified Branin function and the Rastrigin. rEGO is more computationally efficient.

In Figure 6.4 the elapsed time for each iteration of 100 realisations of rEGO

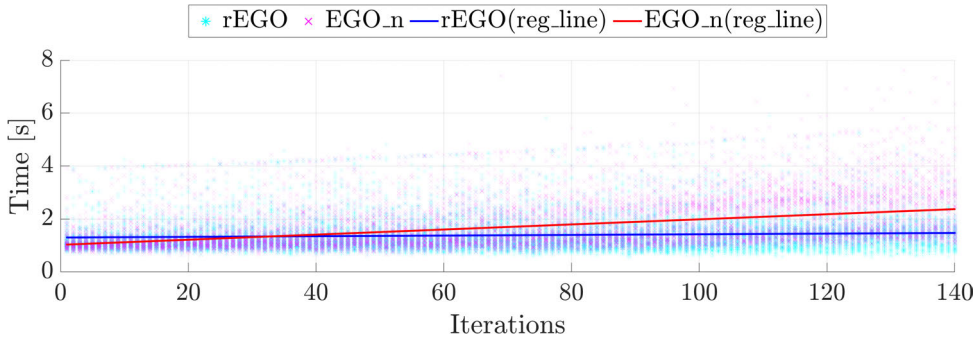

Figure 6.4: Elapsed time for each iteration of rEGO and EGO_n for the Styblinkski-Tang function. The scatter represents the actual measurements and solid lines are the regression lines (reg_line).

and EGO_n for the Styblinkski-Tang function is presented. The scatter represents the time measured for each iteration and the solid lines are the regression lines, respectively rEGO(reg_line) and EGO_n(reg_line) for rEGO and EGO_n. Clearly, the slope of EGO_n(reg_line) is much steeper than its rEGO counterpart. This is only presented for one function as results are similar for any possible function since the speed of the computation depends mainly on the amount of data. This has to do with the way EGO, and Kriging, work. In fact, if refinement and selection are not implemented the data matrix of the model keeps growing and slows down the computation. However, if the refinement and selection are implemented, the computational time remains more stable. Consequently, it can be said that rEGO's computational performance is more efficient than EGO_n. Hence, justifying its implementation.

6.4 Model updating via rEGO

After having benchmarked rEGO against existing methods, practical implementation is taken under scrutiny. Within this section, rEGO is used for the FEMU of numerical and experimental systems. However, prior to diving into the FEM application, a suitable goal function needs to be defined. In fact, rEGO clearly works as an optimisation technique and it needs a function to search. Most commonly

in FEMU, modal parameters are sought as the driving force of model updating. Hence, a set of five functions are selected for the preliminary study and are shown in Table 6.2.

Table 6.2: Preliminary study: Potential goal functions for FEMU.

Function	Formula
Residuals of the mean of the MAC diagonal	$1-\mu(\text{MAC}(\boldsymbol{\phi}_i^E,\boldsymbol{\phi}_i^N))$
Total modal assurance citerion (TMAC) [56]	1- $\prod_{i=1}^{m}\text{MAC}(\boldsymbol{\phi}_i^E,\boldsymbol{\phi}_i^N)$
Modified total modal assurance criterion (MTMAC) [31]	$1-\prod_{i=1}^{n}\frac{\text{MAC}(\boldsymbol{\phi}_i^E,\boldsymbol{\phi}_i^N)}{\left(1+\frac{\lvert\omega_i^N-\omega_i^E\rvert}{\lvert\omega_i^N+\omega_i^E\rvert}\right)}$
Root mean square error (RMSE) of the natural frequencies	$\text{RMSE}(fi_i^E,fi_i^N)$
RMSE of the natural frequencies and mode shapes	$\text{RMSE}(fi_i^E,fi_i^N)+\text{RMSE}(\boldsymbol{\phi}_i^E,\boldsymbol{\phi}_i^N)$

The five functions are used to update the FEM of a numerical case study: a 5-element Euler-Bernoulli cantilever beam, as shown in Figure 6.5.

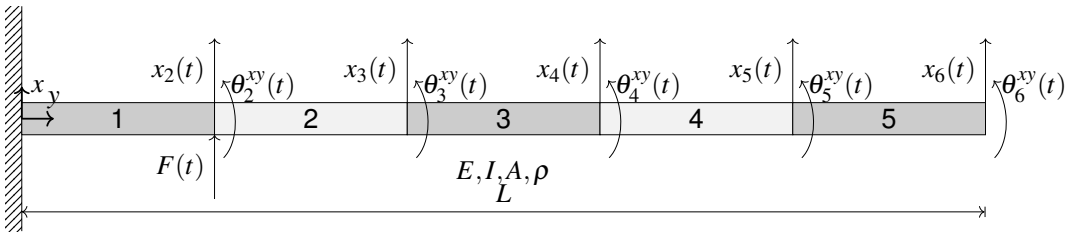

Figure 6.5: Preliminary study: 5-element Euler-Bernoulli encastre beam

The beam is made of Aluminium, resulting in the following properties: Young modulus, E, is 70 GPa and the density, ρ, is 2700 kg/m^{-3}. The beam is 1 m long, L, and its cross-section is a square with 20 mm sides, resulting in a second moment of area, I, of 1.33×10^{-8} mm^4 and an area, A, of 4×10^{-4} mm^2. The beam mass and stiffness matrices are modelled as per theory with vertical displacement and curvature degrees of freedom (DoF). The said properties define the beam's

baseline scenario, while a 10% reduction of stiffness in elements 2 and 3 and a 5% reduction of stiffness in elements 4 and 5 characterise the second scenario. For the purpose of this study, the former is known as baseline, and the latter as pseudo-experimental. Table 6.3 summarises the beam model scenarios and Table 6.4 shows the first five, for conciseness, natural frequencies of the baseline and pseudo-experimental system.

Table 6.3: Preliminary study: Beam model scenarios.

Scenarios	Description
Baseline	baseline configuration as described above
Pseudo-experimental	10% reduction of stiffness in elements 2 and 3 and a 5% reduction of stiffness in elements 4 and 5

Table 6.4: Preliminary study: First five natural frequencies of the baseline and pseudo-experimental beam model.

	Natural frequency [Hz]	
Mode #	Baseline	Experimental
1	16.443	16.098
2	103.098	99.928
3	289.570	280.946
4	572.042	553.945
5	949.446	920.842

This example mimics the mismatch between real structures and preliminary FEMs. In order to tune the beam model from the baseline to the pseudo-experimental results, a GA, such as the one previously defined as GA_100, is used in 100 independent realisations. The objective of this analysis is to find the function which offers the best compromise in terms of computational effort, number of evaluations, and precision, which is a two-fold objective as it considers both objective minimisation and parameters evaluation, the latter being critical for SHM applications.

In order to tune the model, a parameter, x_i, is used to scale a beam's element

stiffness,k_i^e in such a fashion:

$$k_n^e(x_i) = k_i^e \times x_i \tag{6.8}$$

The beam stiffness elements are then assembled as usual and the system's modal properties are obtained through eigenanalysis. Hence, the optimisation problem is to minimise the functions in Table 6.2 by changing the ratios x_i and so tweaking the model's stiffness. The parameters search bound is set between 0.7 and 1.

The results of this study are reported in Figure 6.6, where Figure 6.6a compares the numbers of average evaluations to convergence and the mean values of the minimised objectives ($f(x)$). In Figure 6.6b the evaluations are compared with the mean euclidean distance between the parameters ($\sqrt[5]{x}$, because the number of variables is five). Only the mean values (μ) are reported as the standard deviation (σ) is found to be of at least two order of magnitude less than the μ.

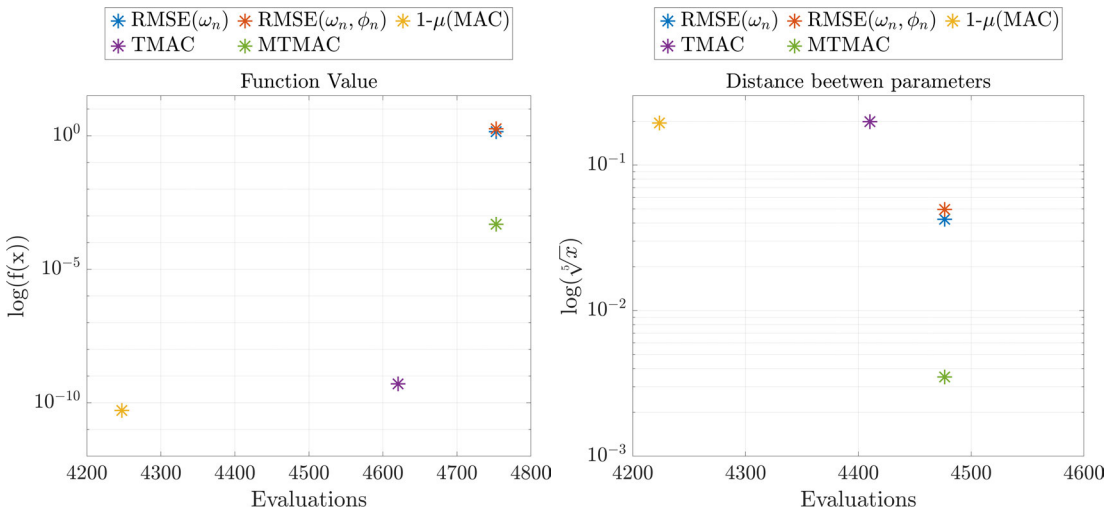

Figure 6.6: Preliminary study: Results of the numerical study concerning the goal function selection. Figure 6.6a shows the average objective over 100 realisations for the five functions, while Figure 6.6b shows the precision of the estimation of the parameters as the average Euclidean distance between the expected and the computed value.

Figure 6.6a shows that the MAC-based functions obtain the smallest $f(x)$ values and the RMSE based ones the highest values. This is somewhat expected as the RMSE-based functions are not scaled between 0 and 1 as the other three. Nevertheless, this outcome is reverted in Figure 6.6b, which shows that the parameters are massively misidentified by the MAC-based goal functions. The best goal function for parameters identification is the MTMAC. In fact, it has better results, both in terms of objective and parameters, than the RMSE techniques for a comparable number of iterations. The MAC-only techniques are discarded because they do not offer a real correlation between the minimised model and the real structure, as shown by the parameters mismatch. Hence, the MTMAC is selected as the objective function for the FEMU via rEGO.

6.5 Numerical and Experimental Case Study

After having established the rEGO theoretical and practical backbone for FEMU, a hybrid, numerical and experimental, case study is selected. The system is a three-storey frame structure, as shown in Figure 6.7 developed at the Engineering Institute at LANL as a benchmark for SHM [3].

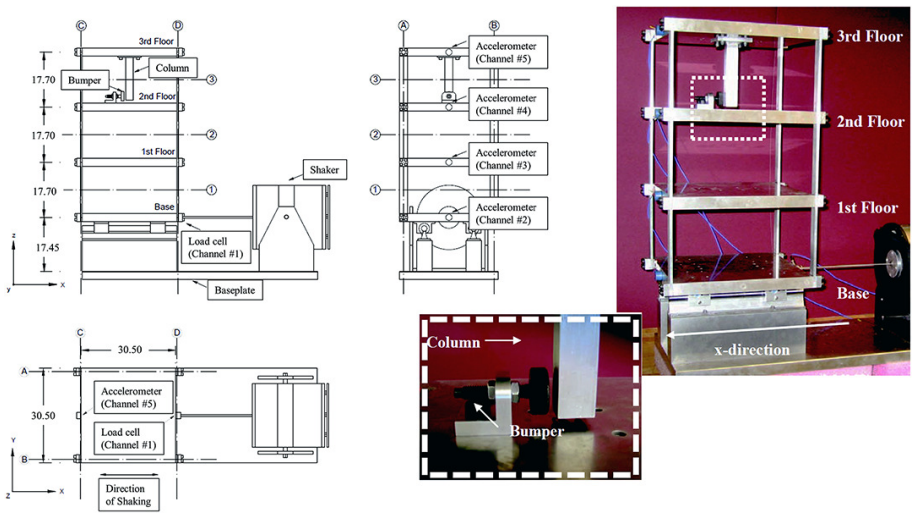

Figure 6.7: Three-storey frame structure: Experimental test set-up and schematic diagrams of the three-storey frame structure. (Adapted from [3, 57]).

The three-storey frame structure is made of four Aluminium plates (30.5 × 30.5 × 2.5 cm) stacked over four, twelve total, Aluminium columns (17.7 × 2.5 × 0.6 cm) at each floor. The columns connect the adjacent corners of the plate to constitute a frame-like structure. An additional Aluminium column (15.0 × 2.5 × 2.5 cm) hangs from the top plate and it is used to simulate the nonlinear behaviour induced by its interaction with a bumper placed on the second floor (see the zoomed-in particular in Figure 6.7), which can be considered as a breathing crack mechanism [58]. The frame is excited in the transverse direction at the base plate, which is also constrained on rails to allow displacements only in that direction. The data collected refer to four accelerometers, respectively placed at the centerline of each floor and to a load cell attached between the base and the stinger. The accelerometers have a nominal sensitivity of 1,000 mVg^{-1} and the load cell of 2.2 mVN^{-1}. The structure is excited with a 2.6 V RMS in the Dactron system, which equals to approximately 20 N RMS measured at the input load cell. The selected excitation signal is a band-limited random excitation between 20 and 150 Hz, where the lower bound is selected to avoid a rigid body mode, and lasting 25.6 s. The testbed includes 17 independent cases; however, for the scope of this work, only cases # 1-5 are considered. These cases include damage and changes in environmental conditions by the means of mass addition scenarios. Respectively, case 1 is treated as the baseline, used for the preliminary model updating, as a benchmark for cases # 2-5, and as a starting point for the numerical study. Table 6.5 summarises the pertinent cases.

Table 6.5: Three-storey frame structure: damage and nonlinear scenarios.

Case #	Description
1	Linear, baseline
2	Linear, added mass of 1.2 kg at the base
3	Linear, added mass of 1.2 kg at the first floor
4	Linear, 87.5% stiffness reduction in one column of the first inter-storey
5	Linear, 87.5% stiffness reduction in two columns of the first inter-storey

Fifty realisations for each case exist, with each instance including time histories recording for the input force, in N, and accelerations, in g. The focus of this work is model updating via modal parameters. Benchmark data for the system under scrutiny is only available in terms of ω_n and ζ_n, since $\boldsymbol{\phi}_n$ values are not quantitatively given in [3]. Hence, ω_n and ζ_n are retrieved from the benchmark data, while $\boldsymbol{\phi}_n$ are retrieved from [59], where they are identified with the Loewner Framework, a modal parameters extraction method introduced by the authors [59–61]. These data are considered as the average over fifty realisations of the same case. The reader interested in a more detailed description of the experimental system is referred to [3].

6.5.1 Model Updating

According to [3], the frame can be represented as a 4 DoF system, with each DoF corresponding to a floor, or plate. These take the form of a classic mass-spring-damper system:

$$\boldsymbol{M}\ddot{\boldsymbol{x}} + \boldsymbol{C}\dot{\boldsymbol{x}} + \boldsymbol{K}x = \boldsymbol{F}(t) \tag{6.9}$$

where $\boldsymbol{M}$, $\boldsymbol{C}$, and $\boldsymbol{K}$ are respectively the mass, damping, and stiffness matrices, $\boldsymbol{F}(t)$ is the input force vector and x is the displacements vector. $\boldsymbol{M}$ and $\boldsymbol{K}$ are built accordingly to usual practice for such systems, while $\boldsymbol{C}$ is built by considering the uncoupled modal damping assumption in [62]:

$$\boldsymbol{C} = \boldsymbol{\phi}^{-T}\boldsymbol{C}_n\boldsymbol{\phi}^{-1} \text{ for } \boldsymbol{C}_n = 2\zeta_n\omega_n M_n \tag{6.10}$$

$\boldsymbol{\phi}$ are the eigenvectors from the eigenanalysis involving $\boldsymbol{M}$ and $\boldsymbol{K}$, $\boldsymbol{C_n}$ is the uncoupled modal damping matrix, ζ_n is the n^{th} damping ratio, ω_n is the n^{th} natural frequency and M_n is the uncoupled modal mass matrix.

$\boldsymbol{M}$ can be assembled considering the structure mass:

$$\boldsymbol{M} = \text{diag}\{m_1, m_2, m_3, m_4\} \tag{6.11}$$

where m_n corresponds to the mass of the corresponding floor. Since real mass values are not specified in [3], by assuming the density of Aluminium to be 2700 kgm^{-3} and considering the above-mentioned dimensions for the plates and columns it can be estimated that:

$$\begin{aligned} m_1 &= 6.442 \text{ kg} \\ m_2 = m_3 &= 6.565 \text{ kg} \\ m_4 &= 6.750 \text{ kg} \end{aligned} \tag{6.12}$$

Also for $\boldsymbol{K}$, no information about the actual stiffness is supplied in [3]. However, given the material properties of Aluminium and the geometric dimensions of the columns the stiffness of a single column, k_c can be derived [63]:

$$k_c = \frac{12\,\text{E}\text{I}_{zz}}{h^3} \tag{6.13}$$

where E is the Young's modulus, I_{zz} is the second moment of area of the column, and h is the column height. For this formulation, the discretisation in a mass-spring-damper system means that the stiffness of the equivalent spring is equal to the sum of the columns' stiffness on that floor. Given these information, it is possible to compute the stiffness of the three inter-storey column arrangements: $k_{2-4} = 68.167 \times 10^3$ Nm^{-1}. In accordance with [3], k_1 is modelled to simulate the friction between the rails and the structure and for this use is set 1 Nm^{-1}. For the same argument, also ζ_1 is set to zero. For modelling the shear frame structure under scrutiny several implications and simplifications are made. In particular, axial deformation of columns and floors is neglected and so it's the effect of axial forces.

Having defined $\boldsymbol{M}$ and $\boldsymbol{K}$, and using the benchmark values for ζ_{2-4} it is pos-

sible to extract the modal parameters of the system via eigenanalysis of Equation (6.9) (by setting $\boldsymbol{F}$ to zero). This allows to update the developed model using the benchmark and experimental data described above. The updating is carried out as described for the beam model, with the difference that this time rEGO's performance is going to be compared with EGO_EI, EGO with a number of function evaluations equals to the mean over 100 iterations of rEGO (EGO_n) and three GAs with, respectively, 10 (GA_10), 100 (GA_100), and 1000 (GA_1000) generations. For all scenarios and methods, the FEMU is run 100 times to obtain statistically significant results. The optimisation techniques are summarised in Table 6.6.

Table 6.6: Optimisation techniques summary.

Optimisation technique	**Description**
EGO_EI	Standard EGO
EGO_n	Iterations-limited EGO. The limit comes from the average number of iterations for 100 realisations of rEGO
GA_10	GA with 10 generations
GA_100	GA with 100 generations
GA_1000	GA with 1000 generation

Results of the updating procedures are presented in Table 6.7. Experimental refers to the data reported in [3] (for ω_n) and those from LF (for $\boldsymbol{\phi}_n$), FEM_model identifies the data, only ω_n is quantitatively available, from the FEM developed in [3], FEM_base indicates the results from the baseline model developed in this section and the others identify the results, obtained from the input parameters average over 100 realisations, for rEGO and the comparative techniques. Also, Table 6.8 reports the number of required functions evaluations, in terms of mean (to the nearest integer), minimum and maximum over 100 realisations.

The model developed for the frame structure in this section (FEM_base) clearly underestimates ω_{2-4} of the real frame, but it still coherently matches $\boldsymbol{\phi}_{2-4}$. However, a ω_{2-4} relative error exceeding 15% is not acceptable in a FEM model, so

Table 6.7: Three-storey frame structure: Natural frequencies, in Hz, and MAC values between the experimental $\boldsymbol{\phi}_n$ and those derived from the models.

Natural frequency [Hz]			
Model	Mode # 2 (%)	Mode # 3 (%)	Mode # 4 (%)
Experimental	30.7	54.2	70.7
FEM_model [3]	29.8 (-2.9)	54.0 (-0.4)	71.6 (1.3)
FEM_base	24.852 (-19.050)	45.813 (-15.475)	59.947 (-15.210)
EGO_EI	30.537 (-0.531)	54.132 (-0.125)	71.234 (0.756)
EGO_n	30.639 (-0.198)	54.181 (-0.035)	70.916 (0.306)
GA_10	30.586 (-0.370)	54.165 (-0.064)	71.073 (0.527)
GA_100	30.699 (-0.004)	54.001 (0.002)	70.729 (0.041)
GA_1000	30.700 (-0.002)	54.200 (0.001)	70.718 (0.026)
rEGO	30.696 (-0.012)	54.200 (0)	70.751 (0.072)
MAC Value [-] wrt Experimental			
Model	Mode # 2	Mode # 3	Mode # 4
FEM_model [3]	NA	NA	NA
FEM_base	0.983	0.999	0.997
EGO_EI	0.991	0.997	0.997
EGO_n	0.990	0.997	0.997
GA_10	0.991	0.997	0.997
GA_100	0.990	0.996	0.996
GA_1000	0.990	0.996	0.996
rEGO	0.990	0.996	0.996

tuning is required. This is carried out via rEGO and can be compared with the said comparative techniques results. The rEGO updated FEM has ω_{2-4} closer to the experimental value than those obtained from EGO_EI, EGO_n and GA_10 models, while GA_100 results are on par with rEGO. Only GA_1000 derived models outperform rEGO in terms of identified ω_n. On the $\boldsymbol{\phi}_n$ side, the identified $\boldsymbol{\phi}_n$ are all very consistent with those from experimental data and their MAC values are at least 0.99, showing almost perfect correlation. The only exception is FEM_base,

where the MAC value is slightly lower for $\boldsymbol{\phi}_1$, being 0.983, which however still shows great coherence.

Table 6.8: Three-storey frame structure: Functions evaluations needed for convergence for the model updating case. Mean (to the nearest integer), maximum (Max), and minimum (Min) values of 100 realisations are presented.

Evaluations [-]			
Model	Mean	Max	Min
EGO_EI	128	233	83
EGO_n	427	427	427
GA_10	2110	2110	2110
GA_100	19210	19210	19210
GA_1000	116669	190210	22630
rEGO	427	655	280

In terms of evaluations, as shown in Table 6.8, EGO_EI needs the least function evaluations to converge and GA_1000 the most. rEGO, on average, requires 3.3 times the number of iterations than EGO_EI, but the relative difference, between experimental and identified, of ω_{2-4} obtained through rEGO is at least an order of magnitude less than EGO_EI. Hence, rEGO offers performance on par with the more computationally intensive GAs, but requires a number of function evaluations orders of magnitude less than them. On the other hand, it requires more evaluations than EGO_EI, but it offers a more coherent model, particularly in terms of ω_{2-4}.

For validation purposes, the Experimental, FEM_base, and rEGO $\boldsymbol{\phi}_{2-4}$ are plotted for comparison in Figure 6.8.

Notably, the $\boldsymbol{\phi}_{2-4}$ computed from the FEM model have, graphically, a very similar trajectory than those, model-derived, presented in [3].

From now on the FEM updated via rEGO is known as FEM_rEGO and it represents the baseline condition for the numerical and experimental study. The new

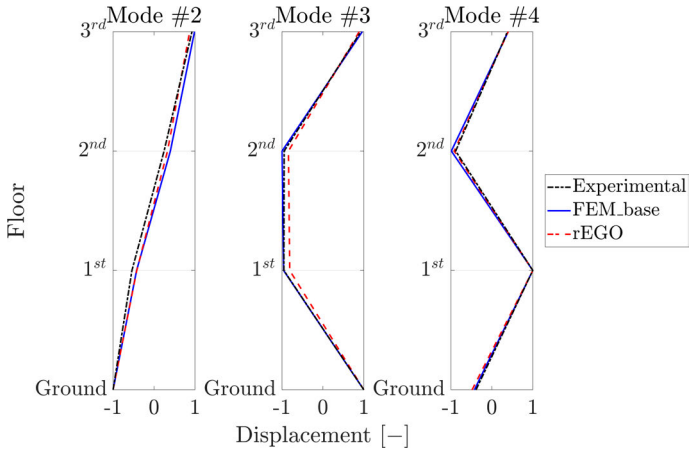

Figure 6.8: Three-storey frame structure: Comparison of the $\boldsymbol{\phi}_{2-4}$ identified from Experimental data and computed from FEM_base and rEGO.

parameters, in terms of m_n and k_n, of the new model are:

$$m_1 = 6.202 \text{ kg} \quad k_1 = 1 \text{ Nm}^{-1}$$

$$m_2 = 7.504 \text{ kg} \quad k_2 = 398.93 \text{ kNm}^{-1}$$

$$m_3 = 8.225 \text{ kg} \quad k_3 = 464.36 \text{ kNm}^{-1}$$

$$m_4 = 7.656 \text{ kg} \quad k_4 = 457.67 \text{ kNm}^{-1}$$

6.5.2 Numerical Case Study

After having successfully updated FEM_base to FEM_rEGO improving the model's fidelity to experimental data, a numerical study is defined. The main goal of the numerical study is to preliminarily assess the capability of rEGO-based model updating to detect damage, modelled as a decrease in stiffness, in optimal scenarios and in environmentally challenging scenarios, simulated by the addition of masses. For these reasons four damage scenarios are postulated: two in optimal conditions and two featuring the addition of masses. Table 6.9 defines the damage scenarios characteristics.

The assumption at the base of this approach is that the change in the updated parameters matches the change in the conditions, mass or stiffness, of the structure. This allows the detection of a stiffness decrease and, hence, damage.

Table 6.9: Three-storey frame structure: Numerically damaged scenarios.

Scenario #	Description
1	Baseline scenario. Mass and stiffness properties as defined for FEM_rEGO.
2	15% stiffness reduction in the first inter-storey and 10% in the third inter-storey.
3	15% stiffness reduction in the first inter-storey and 20% in the third inter-storey.
4	15% stiffness reduction in the second inter-storey and 10% in the third inter-storey and 1.2 kg mass addition on the first floor.
5	15% stiffness reduction in the second inter-storey and 20% in the third inter-storey and 1.2 kg mass addition on the first floor.

As previously for the model updating, rEGO is compared with the other methods to assess its precision and performance over 100 realisations, for statistical significance. For the scope of this study ζ_n stay constant for all scenarios, such that $\zeta_{2-4} = [0.06.\, 0.02,\, 0.008]$. In scenarios # 2 and 3 only the stiffness values are updated, giving three variables, while for the remaining seven, four masses and three stiffness, are considered variables. The search bounds for the stiffness values are $[0.7,\, 1.02]$ and for the mass values $[0.98,\, 1.3]$.

The results, in terms of identified change in the parameters, are presented in Figure 6.9, where a boxplot is used to condense the results for the 100 realisations. The central mark in the boxes indicates the median, while the bottom and top edges of the box, respectively, indicate the 25$^{\text{th}}$ and 75$^{\text{th}}$ percentiles. The most extreme data points not considered outliers are comprised within the whiskers. Figures 6.9a and 6.9b, respectively showing the results for scenarios # 2 and 3, only present the results for the three variables updated, while Figures 6.9c and 6.9d show results for all the seven variables.

Table 6.10 shows the required number of function evaluations for convergence for all scenarios and models used within the numerical case study. The results are presented in terms of mean (to the nearest integer), minimum and maximum over 100 realisations.

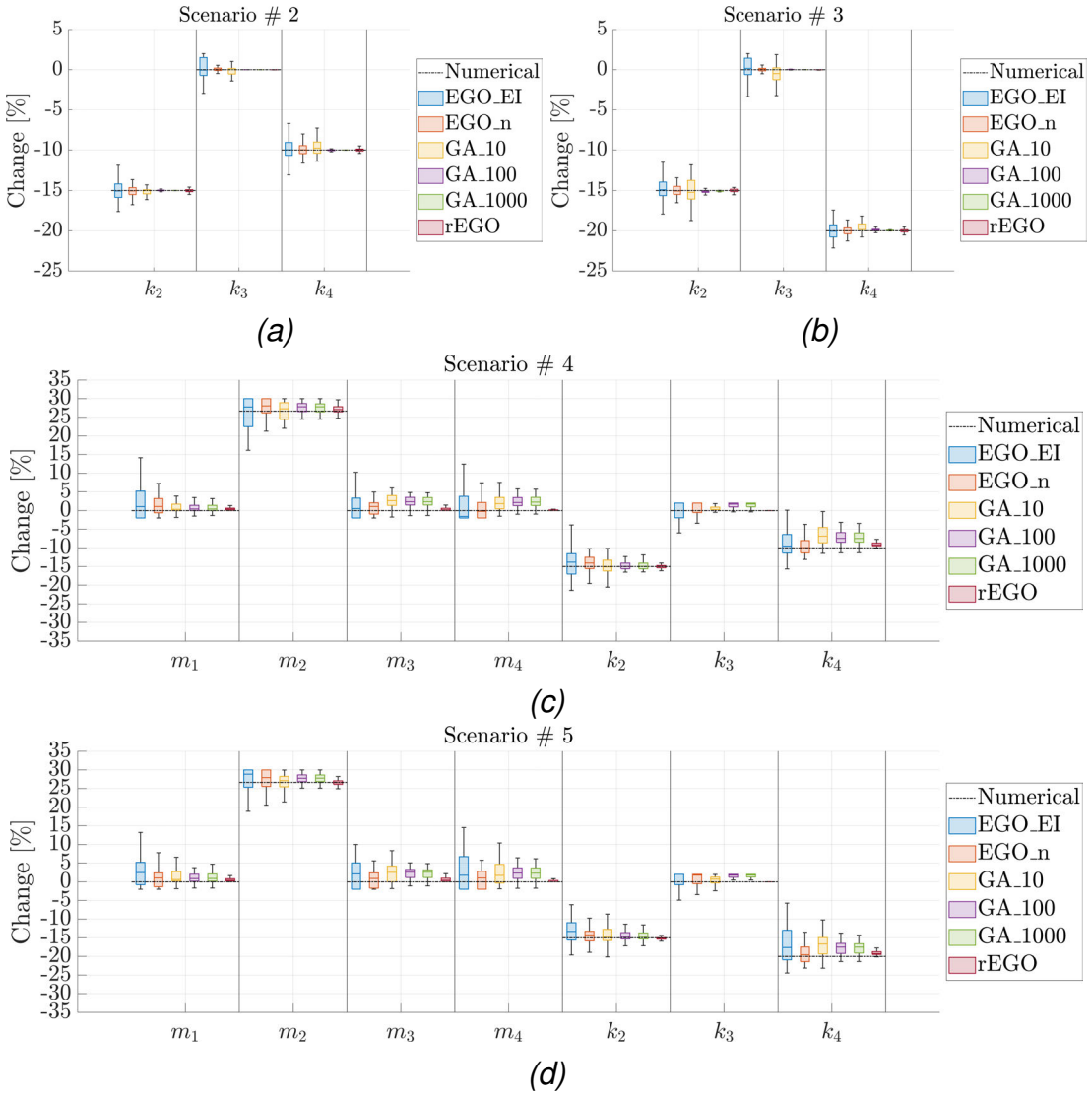

Figure 6.9: Three-storey frame structure: Results, in terms of identified change in the parameters, of the numerical study for the four damaged scenarios. Scenario # 2 is shown in Figure 6.9a, Scenario # 3 in Figure 6.9b, Scenario # 4 in Figure 6.9c, and Scenario # 5 in Figure 6.9d.

Table 6.10: Three-storey frame structure: Functions evaluations needed for convergence for the numerical case study. Mean (to the nearest integer), maximum (Max), and minimum (Min) values of 100 realisations are presented.

Numerical Case Study - **Evaluations** [-]												
Scenario	# 2			# 3			# 4			# 5		
Model	Mean	Max	Min	Mean	Max	Min	Mean	Max	Min	Mean	Max	Min
EGO_EI	37	69	32	37	68	32	90	163	75	92	127	76
EGO_n	112	112	112	111	111	111	314	314	314	329	329	329
GA_10	523	523	523	523	523	523	2110	2110	2110	2110	2110	2110
GA_100	4753	4753	4753	4751	4753	4565	19210	19210	19210	19210	19210	19210
GA_1000	13515	34316	5270	12601	32013	4565	66302	190210	22630	69676	176910	22630
rEGO	112	159	60	111	172	67	314	461	172	329	523	188

For all scenarios analysed, Figure 6.9 shows that all methods, apart from EGO_EI, give somewhat satisfactory results. However, rEGO outperforms, for nearly all variables in all scenarios and for all comparative methods. In Figure 6.9a, for scenario # 2 the higher generations GA and rEGO perform very similarly, while EGO_n performs slightly worse. EGO_EI and GA_10 are well behind. Nevertheless, all the methods are somewhat consistent such that their median line overlaps, or it is close to overlap, the numerical damage line. The same can be said for scenario # 3 in Figure 6.9b. Things start to change for the more complex scenarios, # 4 and 5, where also the mass values are considered. In Figure 6.9c, the results for the variable changes for scenario # 4 are presented and rEGO-derived parameters are the most accurate, in terms of median and 23$^{\text{th}}$ to 75$^{\text{th}}$ percentile. However, for one instance, k_4, rEGO slightly overestimates the stiffness value. EGO_n's median line seems to perfectly match the numerical value, but at the cost of more uncertainty, a bigger box. Hence, rEGO is still the best compromise, precision-wise, even for its least-performing value. An identical occurrence is identified in Figure 6.9d, but the same conclusion can be drawn in favour of rEGO. Notably, the maximum difference from the numerical value for rEGO computed variables never exceeds 1%, for all cases and for both mass and stiffness values.

Concerning the required number of function evaluations for convergence, a similar situation to the one presented in Section 6.5.1 is found. From Table 6.10 it is clear that GA_10 and GA_100 struggle to converge before the maximum number of evaluations is reached. This is clear from the fact that the values presented for them are all equal to the maximum values. Once again, EGO_EI requires the least number of evaluations to converge, but, as aforementioned, it is less precise than all methods, and particularly much worse than rEGO. On the other hand, rEGO takes two orders of magnitude fewer evaluations to converge when compared with GA_1000, one to two when compared with GA_100 and at least two-thirds

less than GA_10.

Given these results, it can be asserted that rEGO is suitable for the model updating for damage detection in numerical systems, particularly rEGO is able to both damage localisation and severity assessments.

6.5.3 Experimental Case Study

After having updated the baseline FEM and verified the feasibility of damage detection on a numerically damaged system, model updating for damage detection via rEGO is tested on the experimental case study from Engineering Institute at LANL: the three-storey frame structure. As aforementioned, for the sake of model updating, cases # 2-5 from Table 6.5 are considered. Table 6.11 shows the characteristics of cases # 1-5 in terms of decrease, or increase, of parameters relative to the updated baseline model in Section 6.5.1.

Table 6.11: Three-storey frame structure: cases under scrutiny.

Case #	Description
1	Baseline
2	19.35 % mass addition at the base
3	15.99 % mass addition at the first floor
4	21.88% stiffness reduction in the first inter-storey
5	43.75% stiffness reduction in the first inter-storey

Notably, cases # 2-3 deal with a mass addition and # 4-5 with a stiffness reduction in the first inter-storey. There are no experimental cases where mass and stiffness values are changed at the same time. Hence, for cases # 2-3 only the mass values are tuned, and, likewise, for cases # 4-5, only the stiffness values are. The procedure is the same as followed for the previous case study: rEGO and the comparative methods are used to match FEM_rEGO to experimental data for detecting damage, or changes, in the structure via its modal parameters. The procedure is repeated 100 times for each method and case for statistical significance. The search bounds for the mass values are $[0.98,\ 1.5]$ and for the stiffness

values are $[0.5,\ 1.02]$.

In Figure 6.10, the results for the changes in parameters are presented in a boxplot, as in the numerical case study, that allows understanding the stability, as in the 25th and 75th percentiles, and precision, median value, of each method.

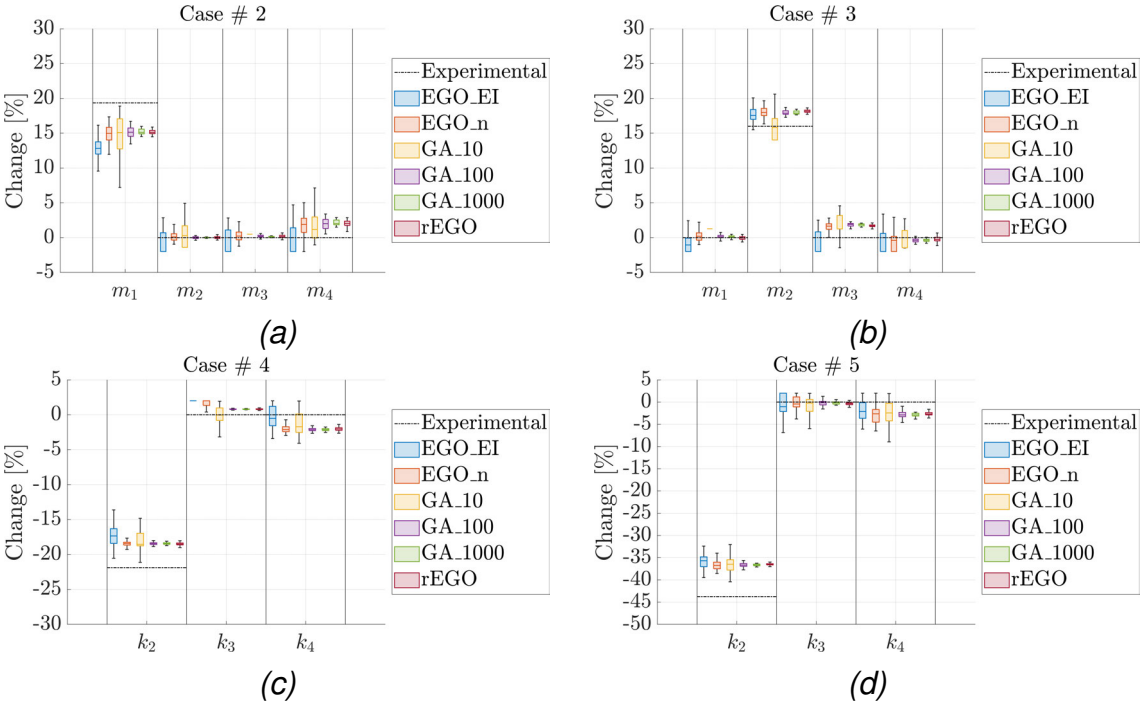

Figure 6.10: Three-storey frame structure: Results, in terms of identified change in the parameters, for the experimental case study. Case # 2 is shown in Figure 6.10a, case # 3 in Figure 6.10b, case # 4 in Figure 6.10c, and case # 5 in Figure 6.10d.

Table 6.12: Three-storey frame structure: Functions evaluations needed for convergence for the experimental case study. Mean (to the nearest integer), maximum (Max), and minimum (Min) values of 100 realisations are presented.

Experimental Case Study - **Evaluations** [-]												
Case #	2			3			4			5		
Model	Mean	Max	Min	Mean	Max	Min	Mean	Max	Min	Mean	Max	Min
EGO_EI	46	51	44	46	54	43	36	42	33	37	49	33
EGO_n	185	185	185	174	174	174	133	133	133	132	132	132
GA_10	523	523	523	523	523	523	523	523	523	523	523	523
GA_100	4753	4753	4753	4753	4753	4753	4725	4753	4142	4746	4753	4048
GA_1000	28952	47053	5646	12727	39110	4753	8865	27689	4142	23938	47053	4048
rEGO	185	247	131	174	277	105	133	195	88	132	204	84

For case #2 (Figure 6.10a) m_2 amd m_3 are well identified by all methods apart EGO_EI and GA_10, particularly for m_2. On the other hand, m_4 is slightly overes-

timated by the more precise methods, GA_1000 and rEGO, and unstable results, in terms of 25th and 75th percentiles, are reported for the remaining. However, all methods clearly identify a prominent mass change in the base floor with rEGO and GA_1000 showing the best compromise between stability and precision. In fact, GA_10 upper whisker is closer to the expected value, but its lower bound falls much lower, between 5 and 10 % when the expected value is 19.35 %. A similar situation can be seen for case # 3 in Figure 6.10b, where, however, the slightly overestimated mass is m_3 and m_2, the increased mass, is actually overestimated rather than underestimated. Notably, the absolute maximum difference between the rEGO-identified parameters and the actual values never exceeds 4.3 % for the mass values of case # 2 and 2.2 % for those of case # 3.

Cases # 4 and 5 deal with the damage, by stiffness reduction, cases. In Figure 6.10c the results for the computed parameters of k_{2-4} are reported. In case # 4 the damage is localised in the first inter-storey for a stiffness reduction of 21.88 % over FEM_rEGO. Damage is successfully localised, but its severity is slightly underestimated, at k_2, by all methods; however, rEGO is the best performing in terms of precision and stability. The maximum absolute difference between the computed and the expected value is 3.4 % and it is located in the damaged inter-storey. For the remaining stiffness values, k_3 is slightly overestimated ($<$ 1 %) and k_4 is underestimated (2 %). A similar situation is found for case # 5, where the damage located in the first inter-storey is modelled with a stiffness reduction of 43.75 %. Again, the damage is localised accordingly, but it is underestimated (7.2 %). On the other hand, k_3 is perfectly identified and k_4, once again, is underestimated (2.6 %).

In terms of computational performance, rEGO, as per other cases, takes many fewer function evaluations, e.g. 2 orders of magnitude less than GA_1000, for convergence. The only method taking less function evaluations for convergence is EGO_EI, but at the price of precision.

rEGO outperforms all other methods in terms of stability, precision and computational performance. However, all methods seem to be influenced by some sort of bias resulting in over-, or under-, estimation of some values. Since damage is correctly localised and severity reasonably assessed, these differences are to be traced back to the assumptions made in Section 6.5.1 to characterise the three-storey frame structure with a mass-spring-damper model.

6.6 Conclusions

In this work, an enhanced version of the well-known Efficient Global Optimization method is proposed. The optimisation technique is named as rEGO, refined Efficient Global Optimisation, and it extends the global capability of the original method to a global-local, or hybrid, search. This is achieved with the introduction of a refinement and selection technique, implemented in two steps: search domain reduction and sample points de-clustering. The capability and performance of the new method are tested successfully on four test functions, where the method outperforms its predecessor and performs accordingly to genetic algorithms, in terms of precision, but shows a lower computational burden. This successful implementation is then followed by the introduction of a model updating technique based on rEGO. The technique uses modal parameters, extracted from experimental data, to tune a finite element model via a penalty function, the modified total modal assurance criterion. After validation on a numerical system, a five degrees of freedom cantilever beam, the technique is employed on a well-known experimental dataset from the Engineering Institute at the Los Alamos National Laboratory: the three-storey frame structure. First, a baseline model is developed, and then it is tuned to the real experimental case. The tuned model is then numerically damaged, by stiffness reduction in four cases, two considering damage-only and the other damage and mass addition. Finally, rEGO is imple-

mented in four experimental cases for the detection of damage, or mass addition. rEGO is able to detect, localise and quantify damage and mass addition satisfactorily in all cases, numerical and experimental, examined. For these reasons, the authors highly recommend the use of model updating via rEGO for the detection of damage in mechanical and civil structures and the implementation of rEGO as a single-objective optimisation technique over existing ones, such as very computationally heavy genetic algorithms. Also, the authors' implementation of rEGO is made available in an open repository.

References

[1] D. R. Jones, M. Schonlau, and W. J. Welch, "Efficient global optimization of expensive black-box functions," *Journal of Global Optimization*, vol. 13, pp. 455–492, 1998, DOI: 10.1023/A:1008306431147 (cit. on pp. 173, 177, 178, 180, 181, 183, 184).

[2] D. G. Krige, "A statistical approach to some basic mine valuation problems on the Witwatersrand," *Journal of the Chemical, Metallurgical and Mining Society of South Africa*, vol. 52, no. 6, pp. 119–139, 1951 (cit. on pp. 173, 177, 178).

[3] E. Figueiredo, G. Park, J. Figueiras, C. Farrar, and K. Worden, "Structural health monitoring algorithm comparisons using standard data sets," Los Alamos National Laboratory (LANL), Los Alamos, NM (United States), Tech. Rep., 2009, DOI: 10.2172/961604 (cit. on pp. 174, 193, 195–199).

[4] P. Ni, J. Li, H. Hao, Q. Han, and X. Du, "Probabilistic model updating via variational Bayesian inference and adaptive Gaussian process modeling," *Computer Methods in Applied Mechanics and Engineering*, vol. 383, p. 113 915, 2021, ISSN: 00457825, DOI: 10.1016/j.cma.2021.113915 (cit. on p. 174).

[5] H. Moravej, S. Jamali, T. H. Chan, and A. Nguyen, "Finite element model updating of civil engineering infrastructures: A literature review," in *SHMII 2017 - 8th International Conference on Structural Health Monitoring of Intelligient Infrastructure, Proceedings*, 2017, pp. 1139–1150, ISBN: 9781925553055 (cit. on p. 174).

[6] J. Mottershead and M. Friswell, "Model updating in structural dynamics: A survey," *Journal of Sound and Vibration*, vol. 167, no. 2, pp. 347–375, 1993, ISSN: 0022460X, DOI: 10.1006/jsvi.1993.1340 (cit. on pp. 174, 177).

[7] W.-X. Ren and H.-B. Chen, "Finite element model updating in structural dynamics by using the response surface method," *Engineering Structures*, vol. 32, no. 8, pp. 2455–2465, 2010, ISSN: 01410296, DOI: 10.1016/j.engstruct.2010.04.019 (cit. on pp. 174, 177, 178).

[8] L. Zanotti Fragonara *et al.*, "Dynamic investigation on the Mirandola bell tower in post-earthquake scenarios," *Bulletin of Earthquake Engineering*, vol. 15, no. 1, pp. 313–337, 2017, ISSN: 1570-761X, DOI: 10.1007/s10518-016-9970-z (cit. on p. 174).

[9] M. Girardi, C. Padovani, D. Pellegrini, M. Porcelli, and L. Robol, "Finite element model updating for structural applications," *Journal of Computational and Applied Mathematics*, vol. 370, p. 112 675, 2020, ISSN: 03770427, DOI: 10.1016/j.cam.2019.112675, arXiv: 1801.09122 (cit. on p. 174).

[10] C. J. Stull, C. J. Earls, and P.-S. Koutsourelakis, "Model-based structural health monitoring of naval ship hulls," *Computer Methods in Applied Mechanics and Engineering*, vol. 200, no. 9-12, pp. 1137–1149, 2011, ISSN: 00457825, DOI: 10.1016/j.cma.2010.11.018 (cit. on p. 175).

[11] C. R. Farrar, S. W. Doebling, and D. A. Nix, "Vibration–based structural damage identification," *Philosophical Transactions of the Royal Society*

of London. Series A: Mathematical, Physical and Engineering Sciences, vol. 359, no. 1778, N. A. J. Lieven and D. J. Ewins, Eds., pp. 131–149, 2001, ISSN: 1364-503X, DOI: 10.1098/rsta.2000.0717 (cit. on p. 175).

[12] P. Cawley, "Structural health monitoring: Closing the gap between research and industrial deployment," *Structural Health Monitoring*, vol. 17, no. 5, pp. 1225–1244, 2018, ISSN: 1475-9217, DOI: 10.1177/1475921717750047 (cit. on p. 175).

[13] A. Rytter, "Vibrational based inspection of civil engineering structures," Ph.D. dissertation, Aalborg University, 1993 (cit. on p. 175).

[14] M. Civera, G. Calamai, and L. Zanotti Fragonara, "System identification via Fast Relaxed Vector Fitting for the Structural Health Monitoring of masonry bridges," *Structures*, vol. 30, no. January, pp. 277–293, 2021, ISSN: 23520124, DOI: 10.1016/j.istruc.2020.12.073 (cit. on p. 175).

[15] J. Zacharias, C. Hartmann, and A. Delgado, "Damage detection on crates of beverages by artificial neural networks trained with finite-element data," *Computer Methods in Applied Mechanics and Engineering*, vol. 193, no. 6-8, pp. 561–574, 2004, ISSN: 00457825, DOI: 10.1016/j.cma.2003.10.009 (cit. on p. 175).

[16] N. F. Alkayem, M. Cao, Y. Zhang, M. Bayat, and Z. Su, "Structural damage detection using finite element model updating with evolutionary algorithms: a survey," *Neural Computing and Applications*, vol. 30, no. 2, pp. 389–411, 2018, ISSN: 0941-0643, DOI: 10.1007/s00521-017-3284-1 (cit. on pp. 175, 177).

[17] H. Sohn, C. R. Farrar, D. D. Shunk, D. W. Stinemates, B. R. Nadler, and J. Czarnecki, "A Review of Structural Health Monitoring Literature: 1996–2001," Los Alamos National Laboratory (LANL), Los Alamos, CA, Tech. Rep., 2004 (cit. on p. 175).

[18] M. Baruch, "Optimization procedure to correct stiffness and flexibility matrices using vibration tests," *AIAA Journal*, vol. 16, no. 11, pp. 1208–1210, 1978, ISSN: 0001-1452, DOI: 10.2514/3.61032 (cit. on p. 175).

[19] R. G. J. Ross, "Synthesis of stiffness and mass matrices from experimental vibration modes," *SAE Transactions*, vol. 80, no. 4, pp. 2627–2635, 1971, [Online]. Available: https://www.jstor.org/stable/44650348 (cit. on p. 175).

[20] J. Sidhu and D. J. Ewins, "Correlation of finite element and modal test studies of a practical structure," in *Proceedings of the 2nd IMAC*, Orlando, FL, 1984, pp. 756–762 (cit. on p. 175).

[21] D. C. Zimmerman and M. Kaouk, "Eigenstructure assignment approach for structural damage detection," *AIAA Journal*, vol. 30, no. 7, pp. 1848–1855, 1992, ISSN: 0001-1452, DOI: 10.2514/3.11146 (cit. on p. 175).

[22] Z. Wang, R. Lin, and M. Lim, "Structural damage detection using measured FRF data," *Computer Methods in Applied Mechanics and Engineering*, vol. 147, no. 1-2, pp. 187–197, 1997, ISSN: 00457825, DOI: 10.1016/S0045-7825(97)00013-3 (cit. on p. 176).

[23] A. Teughels and G. De Roeck, "Damage detection and parameter identification by finite element model updating," *Archives of Computational Methods in Engineering*, vol. 12, no. 2, pp. 123–164, 2005, ISSN: 1134-3060, DOI: 10.1007/BF03044517 (cit. on p. 176).

[24] G. Boscato, S. Russo, R. Ceravolo, and L. Z. Fragonara, "Global sensitivity-based model updating for heritage structures," *Computer-Aided Civil and Infrastructure Engineering*, vol. 30, no. 8, pp. 620–635, 2015, ISSN: 14678667, DOI: 10.1111/mice.12138 (cit. on p. 176).

[25] T. Marwala, *Finite-element-model Updating Using Computional Intelligence Techniques*. London: Springer London, 2010, ISBN: 978-1-84996-322-0, DOI: 10.1007/978-1-84996-323-7 (cit. on pp. 176–178).

[26] T. Marwala and S. Sibisi, "Finite element model updating using bayesian framework and modal properties," *Journal of Aircraft*, vol. 42, no. 1, pp. 275–278, 2005, ISSN: 0021-8669, DOI: 10.2514/1.11841 (cit. on p. 176).

[27] R. Rocchetta, M. Broggi, Q. Huchet, and E. Patelli, "On-line Bayesian model updating for structural health monitoring," *Mechanical Systems and Signal Processing*, vol. 103, pp. 174–195, 2018, ISSN: 10961216, DOI: 10.1016/j.ymssp.2017.10.015 (cit. on p. 177).

[28] A. Keane and J. Scanlan, "Design search and optimization in aerospace engineering," *Philosophical Transactions of the Royal Society A: Mathematical, Physical and Engineering Sciences*, vol. 365, no. 1859, pp. 2501–2529, 2007, ISSN: 1364-503X, DOI: 10.1098/rsta.2007.2019 (cit. on p. 177).

[29] D. E. Goldberg, *Genetic Algorithms in Search, Optimization and Machine Learning*. Boston, MA: Addison-Wesley Longman, 1989, p. 372, ISBN: 978-0-201-15767-3 (cit. on p. 177).

[30] X. Yang, X. Guo, H. Ouyang, and D. Li, "A Kriging model based finite element model updating method for damage detection," *Applied Sciences*, vol. 7, no. 10, p. 1039, 2017, ISSN: 2076-3417, DOI: 10.3390/app7101039 (cit. on pp. 177–179).

[31] R. Perera and R. Torres, "Structural damage detection via modal data with genetic algorithms," *Journal of Structural Engineering*, vol. 132, no. 9, pp. 1491–1501, 2006, ISSN: 0733-9445, DOI: 10.1061/(ASCE)0733-9445(2006)132:9(1491) (cit. on pp. 177, 190).

[32] M. I. Friswell and J. E. Mottershead, *Finite Element Model Updating in Structural Dynamics* (Solid Mechanics and its Applications). Dordrecht: Springer Netherlands, 1995, vol. 38, ISBN: 978-90-481-4535-5, DOI: 10.1007/978-94-015-8508-8 (cit. on p. 177).

[33] A. I. J. Forrester, A. Sóbester, and A. J. Keane, *Engineering Design via Surrogate Modelling*. Wiley, 2008, ISBN: 9780470060681, DOI: 10.1002/9780470770801 (cit. on pp. 178, 180, 181, 185).

[34] A. Sóbester, A. I. Forrester, D. J. Toal, E. Tresidder, and S. Tucker, "Engineering design applications of surrogate-assisted optimization techniques," *Optimization and Engineering*, vol. 15, no. 1, pp. 243–265, 2014, ISSN: 15732924, DOI: 10.1007/s11081-012-9199-x (cit. on pp. 178, 181).

[35] J. Wang and C. Wang, "Structural model updating of frequency response function based on Kriging model," in *2016 3rd International Conference on Information Science and Control Engineering (ICISCE)*, IEEE, 2016, pp. 640–644, ISBN: 978-1-5090-2535-0, DOI: 10.1109/ICISCE.2016.142 (cit. on p. 178).

[36] J. Wang, C. Wang, and J. Zhao, "Structural dynamic model updating based on kriging model using frequency response data," *Journal of Vibroengineering*, vol. 18, no. 6, pp. 3484–3498, 2016, ISSN: 13928716, DOI: 10.21595/jve.2016.16973 (cit. on p. 178).

[37] H. Yin, J. Ma, K. Dong, Z. Peng, P. Cui, and C. Yang, "Model updating method based on Kriging model for structural dynamics," *Shock and Vibration*, vol. 2019, pp. 1–12, 2019, ISSN: 1070-9622, DOI: 10.1155/2019/8086024 (cit. on p. 178).

[38] G. E. P. Box and K. B. Wilson, "On the Experimental Attainment of Optimum Conditions," *Journal of the Royal Statistical Society. Series B (Method-*

ological), vol. 13, no. 1, pp. 1–45, 1951, ISSN: 00359246, [Online]. Available: http://www.jstor.org/stable/2983966 (cit. on p. 178).

[39] M. D. McKay, R. J. Beckman, and W. J. Conover, "A comparison of three methods for selecting values of input variables in the analysis of output from a computer code," *Technometrics*, vol. 21, no. 2, p. 239, 1979, ISSN: 00401706, DOI: 10.2307/1268522 (cit. on p. 179).

[40] M. D. Morris and T. J. Mitchell, "Exploratory designs for computational experiments," *Journal of Statistical Planning and Inference*, vol. 43, no. 3, pp. 381–402, 1995, ISSN: 03783758, DOI: 10.1016/0378-3758(94)00035-T (cit. on p. 179).

[41] A. I. Forrester, A. Sóbester, and A. J. Keane, "Multi-fidelity optimization via surrogate modelling," *Proceedings of the Royal Society A: Mathematical, Physical and Engineering Sciences*, vol. 463, no. 2088, pp. 3251–3269, 2007, ISSN: 14712946, DOI: 10.1098/rspa.2007.1900 (cit. on p. 179).

[42] A. Lye, A. Cicirello, and E. Patelli, "Sampling methods for solving Bayesian model updating problems: A tutorial," *Mechanical Systems and Signal Processing*, vol. 159, p. 107 760, 2021, ISSN: 08883270, DOI: 10.1016/j.ymssp.2021.107760 (cit. on p. 179).

[43] A. Sóbester and A. I. J. Forrester, *Aircraft Aerodynamic Design: Geometry and Optimization*. Wiley, 2014, p. 264 (cit. on p. 181).

[44] G. Dessena, D. I. Ignatyev, J. F. Whidborne, and L. Zanotti Fragonara, "A Kriging Approach to Model Updating for Damage Detection," in *EWSHM 2022*, P. Rizzo and A. Milazzo, Eds., LNCE 254, Singapore: Springer, 2023, ch. 26, pp. 245–255, DOI: 10.1007/978-3-031-07258-1_26 (cit. on p. 182).

[45] J. Xing, Y. Luo, and Z. Gao, "A global optimization strategy based on the Kriging surrogate model and parallel computing," *Structural and Multidis-*

ciplinary Optimization, vol. 62, no. 1, pp. 405–417, 2020, ISSN: 16151488, DOI: 10.1007/s00158-020-02495-6 (cit. on p. 182).

[46] D. Whitley, "A genetic algorithm tutorial," *Statistics and Computing*, vol. 4, no. 2, 1994, ISSN: 0960-3174, DOI: 10.1007/BF00175354 (cit. on p. 182).

[47] I. Voutchkov and A. Keane, "Multi-Objective Optimization Using Surrogates," in *Computational Intelligence in Optimization*, Y. Tenne and C.-K. Goh, Eds., Berlin: Springer, 2010, ch. 7, pp. 155–175, DOI: 10.1007/978-3-642-12775-5_7 (cit. on p. 182).

[48] K. Deb, A. Pratap, S. Agarwal, and T. Meyarivan, "A fast and elitist multiobjective genetic algorithm: NSGA-II," *IEEE Transactions on Evolutionary Computation*, vol. 6, no. 2, pp. 182–197, 2002, ISSN: 1089778X, DOI: 10.1109/4235.996017 (cit. on p. 182).

[49] H. B. Nielsen, S. N. Lophaven, and J. Søndergaard, "DACE - A MATLAB Kriging Toolbox," Informatics and Mathematical Modelling, Technical University of Denmark, DTU, Tech. Rep., 2002, [Online]. Available: https://orbit.dtu.dk/en/publications/dace-a-matlab-kriging-toolbox (cit. on p. 184).

[50] D. Zhan, *The standard and parallel efficient global optimization (EGO) algorithms*, 2017, [Online]. Available: https://github.com/zhandawei/Single_objective_EGO_algorithms (visited on 2022) (cit. on p. 184).

[51] J. Qian, Y. Cheng, J. Zhang, J. Liu, and D. Zhan, "A parallel constrained efficient global optimization algorithm for expensive constrained optimization problems," *Engineering Optimization*, vol. 53, no. 2, pp. 300–320, 2021, ISSN: 10290273, DOI: 10.1080/0305215X.2020.1722118 (cit. on p. 184).

[52] S. Surjanovic and D. Bingham, *Virtual Library of Simulation Experiments: Test Functions and Dataset*, 2013, [Online]. Available: http://www.sfu.

ca/$%5Csim$ssurjano/optimization.html (visited on 2022) (cit. on p. 185).

[53] V. Picheny, T. Wagner, and D. Ginsbourger, "A benchmark of kriging-based infill criteria for noisy optimization," *Structural and Multidisciplinary Optimization*, vol. 48, no. 3, pp. 607–626, 2013, ISSN: 16151488, DOI: 10.1007/s00158-013-0919-4 (cit. on p. 185).

[54] L. Rastrigin, *Systems of External Control*. Moscow: Mir, 1974 (cit. on p. 185).

[55] M. Jamil and X. S. Yang, "A literature survey of benchmark functions for global optimisation problems," *International Journal of Mathematical Modelling and Numerical Optimisation*, vol. 4, no. 2, p. 150, 2013, ISSN: 2040-3607, DOI: 10.1504/IJMMNO.2013.055204 (cit. on p. 185).

[56] Y. Gao and B. F. Spencer, "Damage localization under ambient vibration using changes in flexibility," *Earthquake Engineering and Engineering Vibration*, vol. 1, no. 1, pp. 136–144, 2002, ISSN: 1671-3664, DOI: 10.1007/s11803-002-0017-x (cit. on p. 190).

[57] M. Civera, G. Calamai, and L. Zanotti Fragonara, "Experimental modal analysis of structural systems by using the fast relaxed vector fitting method," *Structural Control and Health Monitoring*, vol. 28, no. 4, pp. 1–23, 2021, ISSN: 1545-2255, DOI: 10.1002/stc.2695 (cit. on p. 193).

[58] A. Bovsunovsky and C. Surace, "Non-linearities in the vibrations of elastic structures with a closing crack: A state of the art review," *Mechanical Systems and Signal Processing*, vol. 62-63, pp. 129–148, 2015, ISSN: 08883270, DOI: 10.1016/j.ymssp.2015.01.021 (cit. on p. 194).

[59] G. Dessena, M. Civera, L. Zanotti Fragonara, D. I. Ignatyev, and J. F. Whidborne, "A Loewner-based system identification and structural health monitoring approach for mechanical systems," *Structural Control and Health Monitoring [Accepted]*, p. 17, 2023 (cit. on p. 195).

[60] G. Dessena, M. Civera, D. I. Ignatyev, J. F. Whidborne, and L. Zanotti Fragonara, “On the accuracy and computational efficiency of the Loewner Framework for mechanical systems,” *in preparation*, 2023 (cit. on p. 195).

[61] G. Dessena, M. Civera, A. Pontillo, D. I. Ignatyev, J. F. Whidborne, and L. Zanotti Fragonara, “Comparative Study on Novel Modal Parameters Extraction Methods for Aeronautical Structures,” *in preparation*, 2023 (cit. on p. 195).

[62] F. Naeim and J. M. Kelly, *Design of Seismic Isolated Structures*. Hoboken, NJ, USA: John Wiley & Sons, Inc., 1999, p. 304, ISBN: 9780470172742, DOI: 10.1002/9780470172742 (cit. on p. 195).

[63] A. K. Chopra, *Dynamics of Structures: Theory and Applications to Earthquake Engineering*, 4th Editio. Upper Saddle River, NJ: Prentice Hall, 2011, p. 992 (cit. on p. 196).

Chapter 7

An Iterative Approach for the Model Updating of Flexible Wings[1]

Abstract

In general, there is a mismatch between a finite element model of a structure and its real behaviour. In aeronautics, this mismatch must be small as finite element models are a fundamental part of the development of an aircraft. With the advent of flexible wings as the new state-of-the-art, the need for precise modelling to avoid unexpected behaviour is even higher. Finite element model updating can be computationally expensive for complex structures and surrogate models can be employed to reduce the computational burden. In this work, a recently introduced surrogate-based technique, the refined Efficient Global Optimisation, is used for the model updating of a flexible wing. Two approaches, a global and a component-based one, are compared and their merits validated. Good results are achieved in terms of model errors and computational efficiency.

[1]This is an adapted version of the following preprint in preparation for submission to *Chinese Journal of Aeronautics*: Dessena, G., Pontillo A., Ignatyev, D. I., Whidborne, J.F., Zanotti Fragonara, L. (2023). An iterative approach for the model updating of flexible wings.

7.1 Introduction

Over the last three decades, increasing computational power has allowed for the rapid development of finite element model updating (FEMU) methods [1]. This is because a general mismatch between the finite element models (FEMs) and the real systems they are meant to describe usually exists.

In [2], FEMU techniques are divided in two categories: direct and indirect methods. The former is not suitable for practical engineering applications as (i) they require very precise measurements of the structural vibration response, (ii) have a high sensitivity to noise, (iii) cannot be used with truncated data and (iv) are prone to lose symmetry in the FEM matrix. However, indirect, or iterative, methods accommodate these drawbacks. Moreover, iterative methods, driven by the minimisation of penalty functions, can require a heavy computational burden. This happens for evolutionary techniques, such as genetic algorithms (GAs) [3]. Surrogate-based techniques hence can be employed for more efficient use of computational power. This is done in [4] for the FEMU of numerical and benchmark structures using the well-known Efficient Global Optimization (EGO) on frequency domain data. In order to improve the local capabilities of a global algorithm like EGO, an enhanced version of EGO, the refined Efficient Global Optimisation (rEGO) [3, 5] has been proposed. rEGO was successfully applied to numerical and experimental systems for damage detection via FEMU. The reader interested in a more comprehensive review on FEMU can refer to [6] and [7], while for thorough reviews of indirect methods, [2, 8] are suggested.

The FEMU task is fundamental across all fields of engineering, but even more so in aeronautics, where having a reliable FEM is pivotal in meeting certification requirements [9]. Further challenges have recently arisen for FEMU in aeronautics, in particular for aircraft wings, because the design paradigm is shifting towards lightweight materials and slenderer wings, in order to improve their aero-

dynamic efficiency [10]. Hence, developing accurate models is not only necessary for analysing aeroelastic effects, but also for design and controls. In [11] a FEMU technique is implemented for positioning a wing box's composite material layers for passive aeroelastic suppression, while in [12] model updating is used for enhancing the handling qualities of an aircraft with flexible wings. FEMU has also been implemented for other applications, such as reverse engineering of a fighter aircraft internal structure [13]. Nevertheless, FEMU, in aeronautics, is not only carried out in wings but also full aircraft, e.g. [14], and components, e.g. [15].

Experimental data is required to update a FEM and in most cases, results from vibration data are used. The most prominent product of vibration data are modal parameters [16], which can be obtained by experiment, the so-called Experimental Modal Analysis (EMA) [17], and during normal operation, known as Operational Modal Analysis [18]. In fact, modal parameters, in particular, natural frequencies (ω_n) and mode shapes ($\boldsymbol{\phi}_n$) are a common metric for FEMU [19]. Notably, [20] used mode shapes, via the Modal Assurance Criterion (MAC) [21], from operational data for the FEMU of a wing section. Nevertheless, approaches based on the direct use of experimental data are still common, such as in [22] where a flexible wing spar FEM is updated using the near resonance region of the Frequency Response Function (FRF). A particular type of EMA, used in aeronautics, is ground vibration testing (GVT) and in this work, the two terms are used interchangeably as it deals with aeronautical structures.

In [23] a sub-component-based FEMU strategy is applied to a composite wing. Instead of updating the complete structure, the updating is carried out for individual components and assemblies; however, no comparison is given to direct approaches. In this work, the goodness of component-based approaches is assessed against the direct approach on a flexible wing model and the experimental testing in [24], which not only involved the full wing but also its parts and subassemblies. The hypothesis is that there could be an improvement in model ac-

curacy and computational performance. Hence, the aim of this work is threefold: (i) assess the merits of the component-based approach, (ii) employ the rEGO-based FEMU technique on a real structure and (iii) obtain a precise FEM of the flexible wing model.

The remainder of this work is organised as follows. In Section 7.2, rEGO for model updating is introduced, Section 7.3 deals with the flexible wing specimen and its preliminary FEMs and Section 7.4 treats the FEMU process of the flexible wing. The article is closed by concluding remarks in Section 7.6.

7.2 The refined Efficient Global Optimisation for Model Updating

The rEGO is introduced to broaden the search capability of the Efficient Global Optimization (EGO) [25, 26]. The main aim was to establish rEGO as a global-local, in a hybrid sense [27], a technique able to both navigate search spaces globally (avoiding local minima) and landing, not only, in the area of the global minimum but as close as possible to it. The main novelties of EGO were the use of a Kriging surrogate model and the implementation of a new infill metric, the Expected Improvement (EI). The EI can be defined as a measure of how much could the known minimum improve if a given point is added to the data pool. The EGO workflow is similar to other surrogate-based techniques: (i) the design space is searched strategically, usually with Latin Hypercube Sampling (LHS) [28], (ii) the absolute value of the EI is maximised to find the suitable infill point and (iii) the point is infilled. The process is iterated between (ii) and (iii) until convergence is reached. For rEGO, usually, this happens when EI is less than 1% of the objective function minimum [25].

In order to improve this process, rEGO retains the same global structure but introduces two important principles: refinement and selection. In Figure 7.1 the

rEGO workflow is outlined. Notably, the left column reflects the original EGO and the right column the improvements brought by rEGO.

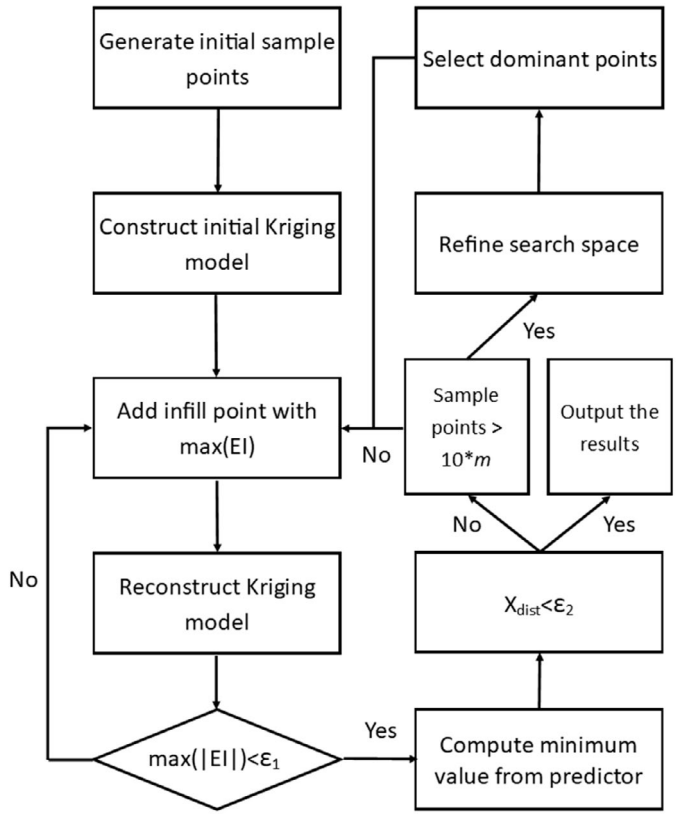

Figure 7.1: rEGO workflow. m stands for the number of variables (retrieved from [5]).

Refinement is first triggered by the first stopping criterion (ε_1), which is directly linked with EI. In this work ε_1 is set to 0.1%. The selection allows for the halving of the search domain and for the de-clustering of points in the search. The two processes are, respectively, inspired by the design domain reduction method in [29, 30] for multi-objective optimisation [31] and Pareto fronts dominance [32]. The main assumption is that given a lower EI value than that originally prescribed in [25] (1%) and ensuring enough data points (10 times the number of variables) [28], the search space can be halved without losing global minima in favour of local minima. Hence, the selection comes into play. The data points outside the newly defined search space are eliminated from the data pool and the remaining are de-clustered, resulting in a better use of computational power as possibly re-

dundant points are excluded. However, refinement is also active on a local scale, linked to the second stopping criterion (ε_2), based on the Euclidean distance between the variables of proposed minima (x_{dist}). ε_2 is a local convergence criterion, which paired with EI makes rEGO, locally, a derivative-free optimiser.

For the scope of this work, the preliminary sampling is carried out via LHS with the number of points ten times the number of variables and the remainder of the process is as outlined in Figure 7.1.

Having outlined the optimisation routine, a suitable goal function for FEMU via rEGO needs to be defined. In [3, 5], the use of the Modified Total Modal Assurance Criterion (MTMAC) [33] is proposed paired with rEGO for FEMU. The MTMAC is found in [5] to perform better than other common choices, such as MAC [21], when used with rEGO. For the sake of minimising the function, the residuals' product of the MTMAC is used in this work and its formulation is presented as:

$$\text{MTMAC} = 1 - \prod_{i=1}^{n} \frac{\text{MAC}(\boldsymbol{\phi}_i^E, \boldsymbol{\phi}_i^N)}{\left(1 + \frac{|\omega_i^N - \omega_i^E|}{|\omega_i^N + \omega_i^E|}\right)} \tag{7.1}$$

where n denotes for the number of modes, superscript E for experimental data and superscript N for numerical data.

In order to minimise the MTMAC, rEGO is meant to tune parameters, which for a complex FEM, can involve materials, such as density and Young Modulus, and geometry, such as moments of inertia, and properties. This will be discussed in depth when dealing with the implementation of the technique on the flexible wing.

The reader interested in a more thorough review of EGO is referred to [25, 26, 28] and to [3, 5] for the introductory work on rEGO. A MATLAB tutorial for rEGO can be found in [34].

7.3 The Flexible Wing Model

The wing model chosen to validate the FEMU technique is a High Aspect Ratio (HAR) flexible wing model developed at Cranfield University for the Beam Reduction Dynamic Scaling (BeaRDS) project [35–38]. The main aim of BeaRDS was to establish a workflow for the design, manufacture and testing of dynamically scaled HAR wings for use in Cranfield University's 8'×6' wind tunnel. Specifically, the wing under scrutiny is the eXperimental BeaRDS-2 (XB-2) model; a dynamically scaled model for an optimised (drag reduction) wing to be used in an A320-like aircraft. The scaled model is made up of four main components: the spar, the stiffening tube, the additional brass ballasts and the skin (Figure 7.2b). The spar and stiffening tube serve as the wing's torque box (Figure 7.2a), the brass ballasts were added for dynamic scaling purposes [39] and the skin was designed in such a way so as to minimise its effect on the wing stiffness [36]. Since dynamic scaling is not the focus of this work, the brass ballasts are removed for the current study.

The spar is machined from two 6082-T6 Aluminium Alloy blocks and joined at mid-span with a weld and reinforced by four bolted L-section plates, as shown in Figure 7.3. Geometrically the spar can be divided into three main sections, according to its profile. The clamping section is rectangular and serves as a clamping point for the wing to the shaker table, the suspended part of the wing sees three different Saint George's cross-shaped cross sections as shown in Figure 7.2a. The spar's section changes linearly across the span following the three profiles. The spar mass is 1.225 kg.

In order to aid the execution of the original experimental campaign, a stiffening tube was introduced aft of the spar. This was done to prevent flutter onset during the wind tunnel test of the BeaRDS project [39]. The tube is linked to the main spar at three points (near each end and in the middle) all within the wing's

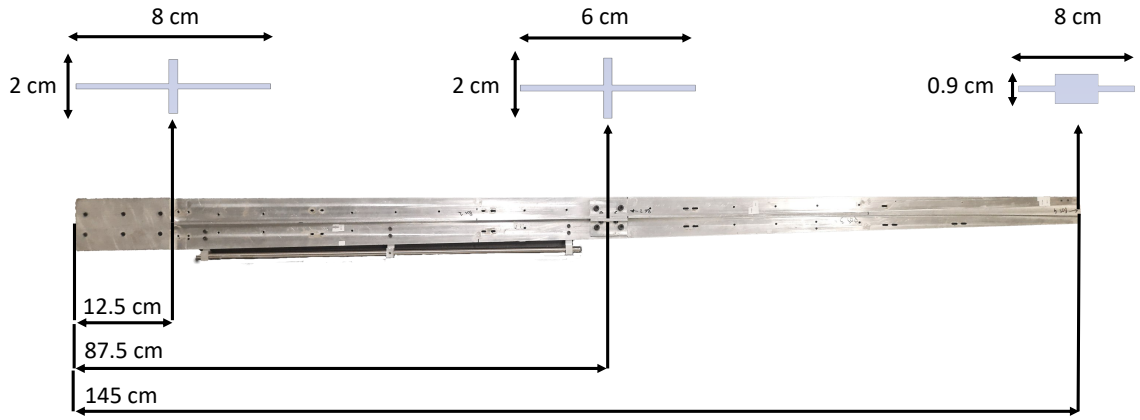

(a)

(b)

Figure 7.2: XB-2: Top views of the torque box (Figure 7.2a) and the full wing (Figure 7.2b). Figure 7.2a also features the spar cross-sections and information about their span-wise position. Not in scale.

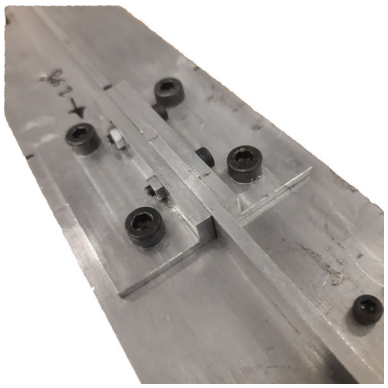

Figure 7.3: XB-2: Reinforcement plates of the wing spar.

inboard half (with regards to the two original material blocks). The tube is made of stainless steel and features an outer diameter of 10 mm, with a thickness of 1 mm and a length of 600 mm. The torque box, the spar and tube assembly, have a combined mass of 1.362 kg.

The outer surface of the wing is defined by the skin. The skin (Figure 7.2b) is made up of 47 different subsections, which are 3D printed in Digital ABS (white)

and Agilus 30 (black), a rubber-like material. Despite the use of different materials for the adjacent strips, the skin is made only of three separate parts, thanks to the PolyJet technology, which allows to 3D print subsequent layers with different materials [40]. This, and the use of a rubber-like material, gives enhanced flexibility to the wing's skin, allowing for large tip displacements. The assembly of the torque box and the skin constitutes the full wing. Table 7.1 introduces the wing's material and physical properties, including aerofoil, aspect ratio (AR), mean aerodynamic chord ($\bar{c}$), taper ratio (λ), Leading Edge sweep (Λ_{LE}) and quarter-chord sweep ($\Lambda_{c/4}$). Please note, the wing has a neutral twist and dihedral angles.

Table 7.1: Materials and physical properties.

Material	**Young Modulus [GPa]**	**Poisson Ratio [-]**	**Density [kgm^{-3}]**
6082-T6 Aluminium	70	0.33	2700
Stainless Steel	193	0.33	8000
Digital ABS	2.6–3.0	0.33 [41]	1170–1180
Agilus 30	NA	NA	1140
Property	**Details**	**Unit**	
Semi span	1.5	m	
AR	18.8	-	
$\bar{c}$	172	mm	
λ	0.35	-	
Λ_{LE}	14.9	$^\circ$	
$\Lambda_{c/4}$	0	$^\circ$	
Aerofoil	NACA 23015	-	
Mass	3.024	kg	

The reader interested a more profound review of the BeaRDS project is referred to [35–39] and further information on the XB-2 wing can be found in [24, 36, 38, 42, 43].

7.3.1 Preliminary Finite Element Models

Having outlined the general geometry, components and properties of the XB-2, three preliminary FEMs are built in ANSYS Mechanical APDL 2021. Respectively, a spar, torque box and full wing are built following an assembly-like approach.

First, the spar model is built, then the tube is added for the torque box model and finally, the wing skin is modelled. This approach is followed because experimental data of each scenario is available in [24].

The first FEM developed is the spar model. The spar is easily discretised as a multi-element beam with 3 different sections. The first section is rectangular and represents the clamped root. Then three sections are defined along the spar to represent the three different section changes and two tapered sections are defined along the span. The reinforcements plates are modelled as a 63 g lumped mass at mid-span. `BEAM188` and `MASS21` elements are used to, respectively, model the spar and the reinforcement plates. 6082-T6 Aluminium is assigned to the three sections. In Figure 7.4a the FEM of the spar is shown with its boundary conditions (BCs). The constrained end of the spar is identified by the yellow arrows and the plates, discretised as a lumped mass, are shown as a cyan asterisk.

Building on the spar model, the torque box FEM is constructed by adding the stiffening tube aft of the existing spar. The tube is discretised with a `BEAM188` element and it is linked to the spar with 3 rigid link constraints (`CERIG`) (near the tube ends and in the middle) for all degrees of freedom (DOF). Stainless steel material properties are assigned to the tube. Figure 7.4b displays the FEM for the torque box. The baseline spar remains unchanged and the tube is added aft of the spar and connected with rigid links, shownin magenta.

The last step is to build the full wing model by adding the skin. According to [36], the skin's only structural contribution is to transmit the aerodynamic load to the torque box, without any further stiffness contribution, as the Agilus 30 strips do not allow the skin to stiffen the structure. Hence, the skin can be suitably discretised as lumped masses, modelling each strip as a separate mass. Fifty-six lumped masses are added to the model as `MASS21` elements with `CERIG` links to the spar. In Figure 7.4c the FEM of the flexible wing is shown. The torque box

FEM is used as a baseline for the addition of the skin as mass elements (MASS21) along the span. The lumped masses are linked to the spar with rigid links.

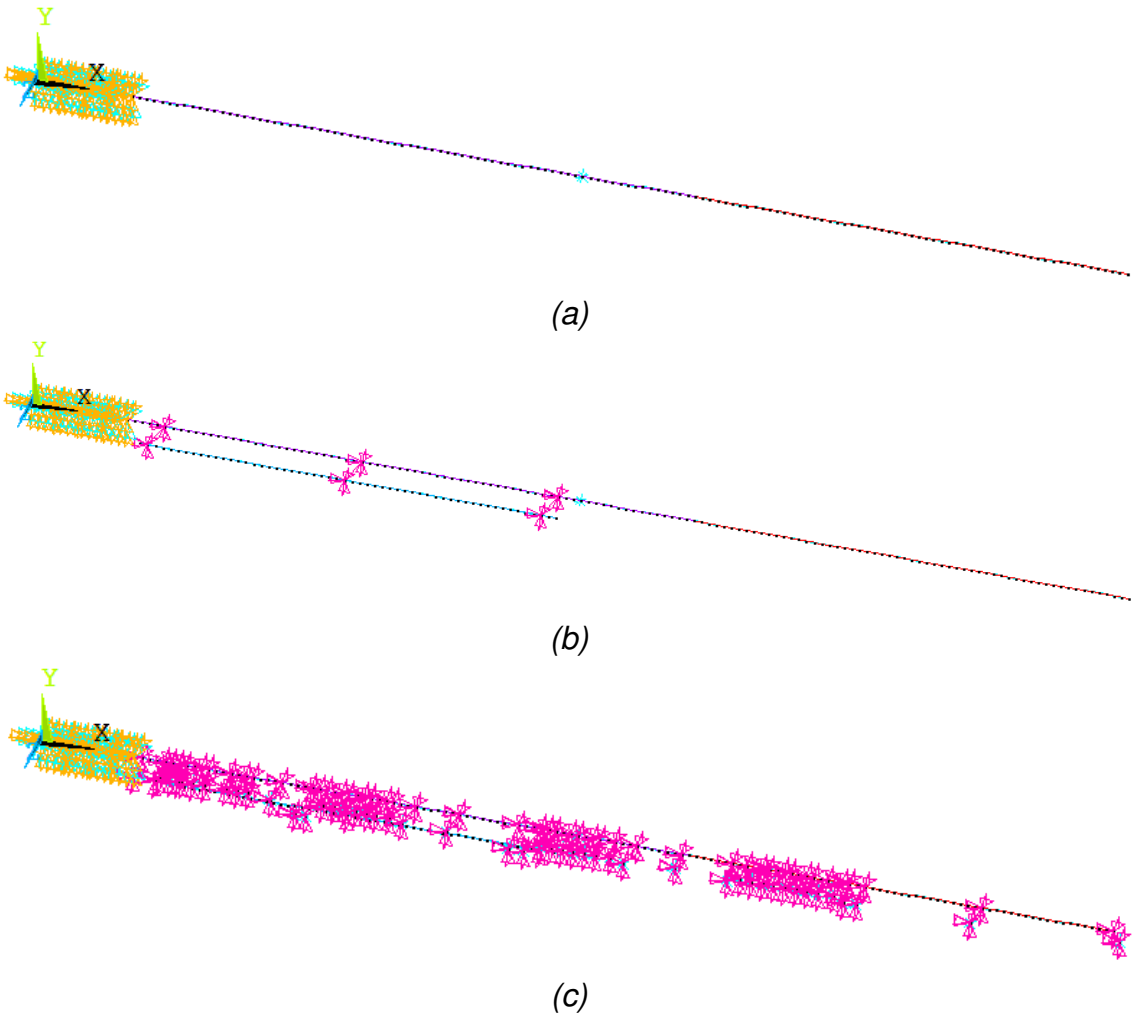

Figure 7.4: FEM of the spar (Figure 7.4a), torque box (Figure 7.4b) and full wing (Figure 7.4c).

For the modelling aspect, five sections of interest can be identified: four related to the spar and one to the tube. The relevant properties used for the creation of the model are listed in Table 7.2. They include moments of inertia (I_{xx} and I_{yy}) in m^4, areas (A) in m^2 and torsion constants (J) in m^4. Please note that for the three spar's suspended sections (these values are marked with * in Table 7.2) the J could not be computed analytically and was derived with a numerical experiment in ANSYS Workbench using SOLID186 elements. The profile was extruded for 1 m (L), clamped at one end and a remote displacement (θ) of 1° applied to the

other end, resulting in a reaction torque (T). Hence, by considering the following formulation:

$$\theta = \frac{TL}{GJ} \tag{7.2}$$

where G is the shear modulus (G$= 26.31$ GPa for 6082-T6 Aluminium), J can be derived.

Table 7.2: Sections properties.

Section			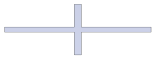		
$\mathbf{I}_{xx}$ [m^4]	5×10^{-8}	6.50×10^{-8}	3.46×10^{-8}	1.29×10^{-8}	1.68×10^{-10}
$\mathbf{I}_{yy}$ [m^4]	6.50×10^{-7}	2.30×10^{-9}	1.90×10^{-9}	1.24×10^{-9}	1.68×10^{-10}
A [m^2]	14.60×10^{-4}	2.07×10^{-4}	1.69×10^{-4}	1.98×10^{-4}	1.49×10^{-11}
J [m^4]	7×10^{-7}	*4.5×10^{-10}	*3.1×10^{-10}	*3×10^{-9}	3.38×10^{-10}

The 44 skin sections are modelled as 47 independent masses. Properties for the masses can be found in Table C.1.

The modal parameters are obtained from the FEMs by clamping the root of the specimens and running a damped modal analysis for extracting the modes between 0 and 150 Hz. Rayleigh damping is used for the definition of the damping coefficients, which were derived from the experimental results in [24]. Details are provided in the following sections. An element size of 0.001 is set, as it is found not to condition results.

7.3.2 Experimental Setup

In order to validate and, if needed, update the models, experimental data is needed. A previous testing campaign on the above-mentioned wings and sub-assemblies is carried out in [24] and the results are used in this work.

A bandwidth limited, between 2 and 400 Hz, random verification at 0.305 g RMS (root mean square) input is carried out for the spar, torque box, and full wing assemblies. The input excitation is obtained with a Data Physics® Signal

Force™ modal shaker controlled by DP760™ closed-loop control software running on a consumer-grade laptop and lasts 20 min. However, for consistency and to avoid transients, only 18 min are used in the identification process. The acceleration input (from the shaker table) and output (along) of the specimens are collected with nine accelerometers. One is positioned on the wing's clamp for the input acceleration and the remaining eight are positioned along the span in four rows. The acceleration data is then transmitted to a desktop machine which saves the data through an in-house LABVIEW routine. According to the available measurement equipment, only vertical accelerations are recorded, so only vertical displacements and rotation can be inspected. Table 7.3 and Figure 7.5 show, respectively, the characteristics and positions of the accelerometers.

Table 7.3: Accelerometers specifications.

ID #	Accelerometers Model	Sensitivity [mVg^{-1}]	Mass [g]
0	PCB Piezotronics® model: 352C23	4.88	0.2
1R	PCB Piezotronics® model: 356A16	96.50	7.4
1L	Isotron® accelerometer model 7251A	10.30	10.5
2R	PCB Piezotronics® model: 356A16	97.20	7.4
2L	Isotron® accelerometer model 7251A	10.08	10.5
3R	PCB Piezotronics® model: 356A45	100.20	4.2
3L	Isotron® accelerometer model 7251A	10.34	10.5
4R	Brüel & Kjær® accelerometer type 4507-002	94.12	4.8
4L	Brüel & Kjær® accelerometer type 4507-002	95.52	4.8

The accelerometers' rows position is selected with a sensor placement technique based on autoMAC (Modal Assurance Criterion between the modes themselves) and GA [44]. A preliminary FEM is used to minimise the cross-correlation between adjacent modes by moving the probe points (accelerometers row positions) along the span.

The first step in post-processing the data is to convert the acceleration from g to ms^{-2} and to resample the signal from 5120 to 256 Hz. The signal is then band

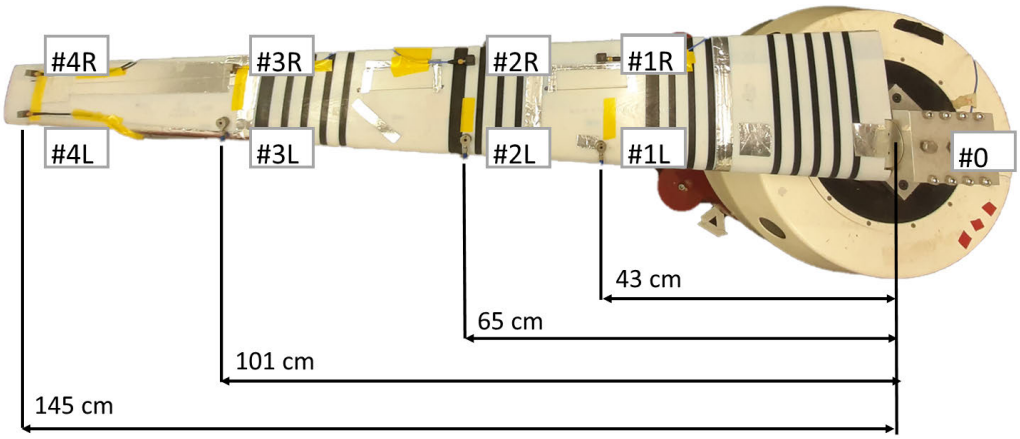

Figure 7.5: Accelerometers locations. The accelerometers do not appear aligned only for the optical effect of the camera lens (retrieved from [24]).

limited between 2.5 and 98 Hz, excluding any drifts at high and low frequencies. Following, the FRFs are computed in the usual fashion. A Fast Fourier Transform (FFT) of the input and output acceleration is taken and FRFs are obtained by the element-wise division between output and input FFTs. Finally, a Savitzky-Golay filter of order 3 and length 601 is applied to the FRF.

The modal parameters of the first three vertically dominant modes are then obtained via the industry-standard method [45] Least Squares Complex Exponential [46, 47]. The identification is obtained by the means of stabilisation diagrams with orders between 3 and 32.

The reader interested in the full experimental work is referred to [24] and to [42, 43, 48] for further experimental work on XB-2.

7.3.3 Experimental Campaign and Preliminary Finite Element Models Results

This subsection reports on the modal parameters extracted from the preliminary FEMs and compares them with those from the GVT campaign in [24]. In particular, the experimental results for the so-called low input scenarios are used. In Table 7.4 the ω_n of the first three vertically dominant modes from the experimen-

tal campaign are compared with those found from the damped modal analysis in Ansys Mechanical APDL 2021 R1.

Table 7.4: Natural frequencies identified from the experimental data and the preliminary FEMs.

Natural Frequencies [Hz]								
	Spar			Torque box			XB-2 wing	
Mode	Exp.	FEM (%)	**Mode**	Exp.	FEM (%)	**Mode**	Exp.	FEM (%)
1st Bending	4.855	5.447 (12.19)	1st Bending	5.252	5.887 (12.10)	1st Bending	3.187	3.539 (11.03)
1st Lagging	-	26.917	2nd Bending	25.933	30.617 (18.07)	1st Coupled	11.752	-
2nd Bending	26.966	30.597 (13.46)	1st Lagging	-	35.080	2nd Coupled	17.447	17.774 (1.88)
1st Torsion	68.049	-	1st Coupled	76.242	85.162 (11.70)	-	-	-
3rd Bending	76.851	88.757 (15.49)	-	-	-	-	-	-

In Table 7.5 the correlation between the experimental and FEM $\boldsymbol{\phi}_n$ is investigated using the MAC value. The values for the spar and torque box are shown for the three modes that have a similar one in the FEM results. For the XB-2 wing, only two modes are shown.

Table 7.5: MAC values (of the diagonal) between the mode shapes identified from the experimental data and the preliminary FEMs.

MAC Value [-]					
Spar		**Torque box**		**XB-2 wing**	
Mode	MAC	**Mode**	MAC	**Mode**	MAC
1st Bending	0.98	1st Bending	0.99	1st Bending	0.98
2nd Bending	0.94	2nd Bending	0.95	1st Coupled	-
3rd Bending	0.90	1st Coupled	0.80	2nd Coupled	0.75

In Table 7.6 the MTMAC residuals values, as in Equation (7.1), between the ω_n and $\boldsymbol{\phi}_n$ from the experimental and the preliminary FEMs.

In Table 7.4 the ω_n identified from the experimental data are compared to those from the preliminary FEMs. Notably, more modes are, generally, identified in the same frequency interval in the FEMs. Table 7.4 shows only the results for the modes identified between the first and last modes that can be found in both

Table 7.6: Residuals of the MTMAC computed between the mode shapes identified from the experimental data and the preliminary FEMs.

	MTMAC Value [-]	
Spar	**Torque box**	**XB-2 wing**
0.30	0.39	0.30

the experimental and FEMs data. At least three coincident modes are found for the spar and torque box; however, this is not the case for the full wing. Only two coherent modes are identified and, thus, they will be used for the FEMU process. However, three modes are going to be considered for the spar and torque box. Namely, the three bending modes for the spar, the first two bending modes and the first coupled for the torque box. In terms of comparison, the FEM modes always overestimate the ω_n identified from the experimental data. In particular, the second bending mode for the torque box is overestimated by over 15%, while the first coupled mode of the XB-2 wing is overestimated by just under 2%.

Table 7.5 reports on the $\boldsymbol{\phi}_n$ correlation between experimental and FEM data. Notably, most modes are well correlated, showing a MAC value over 0.9. Nevertheless, two problematic modes can be identified: the 1st coupled mode for the torque box and the 2nd coupled mode for the XB-2 wing. In particular, the latter is under the minimum of what can be considered sufficient correlation, a MAC value of 0.8 [49].

Table 7.6 shows the values of the MTMAC residuals, the goal function selected for the FEMU process. All three residuals are around 0.3, which, considering that the MTMAC residuals are scaled between 0 and 1, may seem a high value. Nevertheless, by experience [3, 5], it is seen that at residual values around 0.3 the model starts to have a significant correlation with the experimental systems. In simple terms, the FEMU process, using the MTMAC residuals, is feasible for this system as its initial guesses, the preliminary FEMs, have a sufficient correlation with the experimental results.

Given the results outlined for the preliminary FEMs, the FEMU task is fundamental to guarantee a model that represents as closely as possible the real system. Particular attention should be paid to the parameters that are furthest from the experimental values, such as the above-mentioned $\boldsymbol{\phi}_n$ and most of the ω_n.

Damping ratios (ζ_n) are not shown in the results above as the FEMs are built based on those values. The ζ_n from the experimental data are presented in Table 7.7.

Table 7.7: Damping ratios identified from the experimental data.

Damping ratio [-]					
Spar		**Torque box**		**XB-2 wing**	
Mode	ζ_n	**Mode**	ζ_n	**Mode**	ζ_n
1st Bending	0.033	1st Bending	0.022	1st Bending	0.024
2nd Bending	0.010	2nd Bending	0.014	1st Coupled	0.047
3rd Bending	0.014	1st Coupled	0.017	2nd Coupled	0.0375

In order to obtain a damped FEM, the ζ_n from the GVT results is assumed to obey the classical Rayleigh damping formulation, such as:

$$\zeta = \frac{1}{2}\left(\frac{\alpha}{\omega} + \beta\omega\right) \tag{7.3}$$

where ζ is the damping ratio, ω is the frequency in rads^{-1}, α is the mass proportional Rayleigh damping coefficient and β is the stiffness proportional Rayleigh damping coefficient.

In order to obtain the relative α and β values, the curve-fitting to the experimental values is done by minimising the difference at the query points, the three modes, between ζ_n and ζ. Please note, for the XB-2 case only the 1st bending and 2nd coupled modes are used, since no counterpart is found in the respective FEM for the 1st coupled mode. In Figure 7.6 and Table 7.8, the results of the fitting process are shown. Please note, $\zeta(\omega)$ refers as Equation (7.3) with the fitted

values of α and β. Rayleigh damping is chosen as the damping model as it has a good agreement with the experimental data, as shown in Figure 7.6. Note that only the 1st bending and the 2nd coupled modes are considered for the full wing.

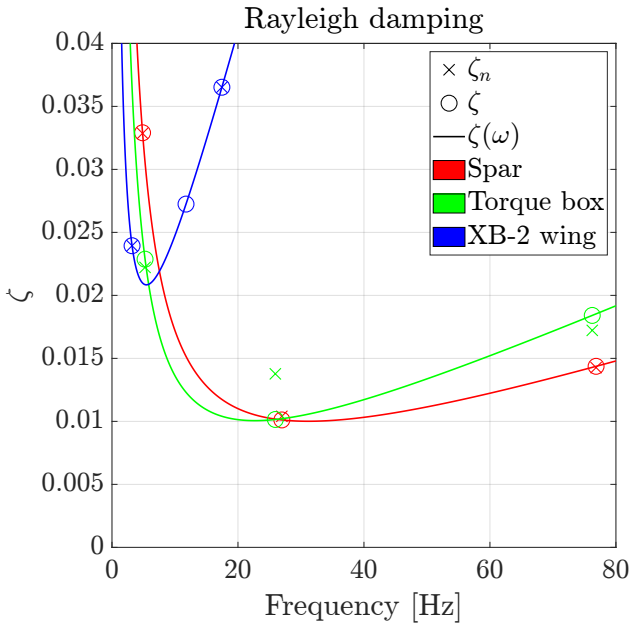

Figure 7.6: Damping ratios from the experimental data and as fitted by the Rayleigh damping.

Table 7.8: Rayleigh damping coefficients.

	α & β		
	Spar	**Torque box**	**XB-2 wing**
α	0.312	0.228	0.114
β	3.21e-4	4.44e-4	3.8e-3

The raw identified data from the preliminary FEMs are available in Table C.2.

7.4 Finite Element Model Updating of the Flexible Wing

In this section, the FEMU process and its results are introduced. The preliminary FEMs presented in Section 7.3 are tuned to match the modal response of the

experimental campaign in [24]. Finally, the results of the component-based and direct approaches are presented and discussed.

7.4.1 Finite Element Model Updating Implementation

The FEMU implementation follows a standard implementation for surrogate-based iterative FEMU methods. In this section, what happens inside the box "Add infill point with max(EI)" in Figure 7.1 is explained in terms of the practical implementation of the MATLAB-based `rEGO` and the Ansys Mechanical APDL model.

First, a baseline FEM is defined as an input file for Ansys Mechanical APDL. The input file takes some parameters, linked to the model's properties. The MATLAB implementation finds the set of parameters from rEGO and modifies the input file accordingly, then, still within MATLAB, ANSYS Mechanical APDL is called for running the input file. After this is complete, another file, with the modal parameters results from the FEM, is generated from ANSYS and imported into MATLAB to calculate the MTMAC and recompute the surrogate model.

7.4.2 Updating Parameters and the Component-based Approach

A set of parameters needs to be defined in order to carry out the FEMU process. It is clear that an idealised model, like those presented in Section 7.3 is influenced by material and geometric properties. In fact, stiffness in these models is a function of geometry and material properties, such as the Young Modulus, E. Hence, materials and geometric properties are considered in this work. In addition, the experimental results can identify both vertical and rotational displacements. Hence, two dimensions of displacement have to be considered. The ρ of all materials, as per Table 7.1, is selected as an updating parameter. The same is done for the E of all materials, apart from the Agilus 30 and the Digital ABS, because the skin is modelled as lumped masses (no stiffness). In addition,

the geometric properties, such as I_{yy} and J are selected as model parameters. The lumped mass used to model the reinforcement plates at the spar's mid-span is employed as updating parameters. Lastly, a conceptual FEMU on the spar showed that the FEM would not converge adequately to the experimental results. Hence, the suspended sections are defined with two different material entries with base values for 6082-T6 aluminium.

A total of fifteen parameters, as shown in Table 7.9, is identified across all the specimens for the FEMU process. For the component-based approach, the parameters are assigned to a given part or sub-assembly. For the spar FEMU, eight parameters are updated, while for the torque box thirteen and for the XB-2 all fifteen are tuned. The parameters specific to the spar model include the two 6082-T6 Aluminium densities and E, the reinforcement plates lumped mass, and the I_{yy} of the three spar sections ($x_{1-4,7-10,12,14}$). The torque box includes all of those from the spar and adds, the ρ and E for the stainless steel tube and the J of the three spar sections ($x_{7,8,11,13,15}$). Finally, the XB-2 wing inherits all the parameters from the torque box plus those relative to the modelling of the skin as lumped masses (($x_{4,5}$)): the densities of Agilus 30 and Digital ABS. The updating parameters lower and bounds are set at 0.6 and 1.4 and they actively scale the baseline value to match the FEM response to the experimental one.

Since the main aim of this work is to investigate the goodness and feasibility of the component-based approach for the FEMU of flexible wings, different updating scenarios have to be defined. Two approaches are determined. The first considers the spar FEM as the base for the component-based approach and the torque box and XB-2 wing models are built from there. This, known as the bottom-up approach, means that the spar model is first updated, then FEMU is carried out on the torque box and the wing, by carrying over the parameters updated in the previous component. A second component-based approach works the other way around, as a top-down approach. First the XB-2 wing model is updated taking

Table 7.9: Properties updated for the FEMU processes.

	Poperty	Description	Model
x_1	6082-T6 aluminium ρ	ρ of the inboard half of the spar.	Spar
x_2	6082-T6 aluminium E	E of the inboard half of the spar.	Spar
x_3	6082-T6 aluminium ρ	ρ of the outboard half of the spar.	Spar
x_4	6082-T6 aluminium E	E of the outboard half of the spar.	Spar
x_5	Digital ABS ρ	ρ of the Digital ABS sections.	XB-2 wing
x_6	Agilus 30 ρ	ρ of the Agilus 30 sections.	XB-2 wing
x_7	Stainless steel ρ	ρ of the stainless steel tube.	Torque box
x_8	Stainless steel E	E of the stainless steel tube.	Torque box
x_9	Reinforcement plates	Lumped mass value for the reinforcement plates discretisation.	Spar
x_{10}	I_{yy} spar (inboard)	Spar inboard cross-section I_{yy}	Spar
x_{11}	J spar (inboard)	Spar inboard cross-section J	Torque box
x_{12}	I_{yy} spar (inboard)	Spar mid-span cross-section I_{yy}	Spar
x_{13}	J spar (inboard)	Spar mid-span cross-section J	Torque box
x_{14}	I_{yy} spar (inboard)	Spar outboard cross-section I_{yy}	Spar
x_{15}	J spar (inboard)	Spar outboard cross-section J	Torque box

into consideration all fifteen parameters and the torque box and spar model are built with the parameters identified in that study. Table 7.10 recaps the phases of the component-based approach.

Table 7.10: Component-based approach schematic.

Component-based Approach		
	Bottom-up	Top-down
Spar	FEMU - 8 parameters	Fetching 8 parameters
Torque box	FEMU - 5 parameters	Fetching 13 parameters
XB-2 wing	FEMU - 2 parameters	FEMU - 15 parameters

7.4.3 The Spar

As outlined above, two FEMU updating strategies using rEGO are compared. The bottom-up and top-down approach results are presented in this subsection. The results are evaluated in terms of ω_n, $\boldsymbol{\phi}_n$, MTMAC and model evaluations.

First, let us consider the results in terms of ω_n for the spar. In Table 7.11 and Figure 7.7 the ω_n obtained from the experimental campaign (Exp.), prelimi-

nary FEM (FEM), FEM updated via bottom-up (FEMU_1) and FEM updated via top-down (FEMU_2) are compared.

Table 7.11: Natural frequencies identified from the experimental data, the preliminary FEM and the updated FEMs for the spar.

	Natural Frequencies [Hz]			
Mode	Exp.	FEM (%)	FEMU - Bottom-up (%)	FEMU - Top-down (%)
1st Bending	4.885	5.447 (12.19)	4.855 (-)	5.062 (4.26)
2nd Bending	26.966	30.597 (13.46)	26.864 (-0.38)	31.775 (17.83)
3rd Bending	76.851	88.757 (15.49)	80.624 (4.91)	95.269 (23.97)

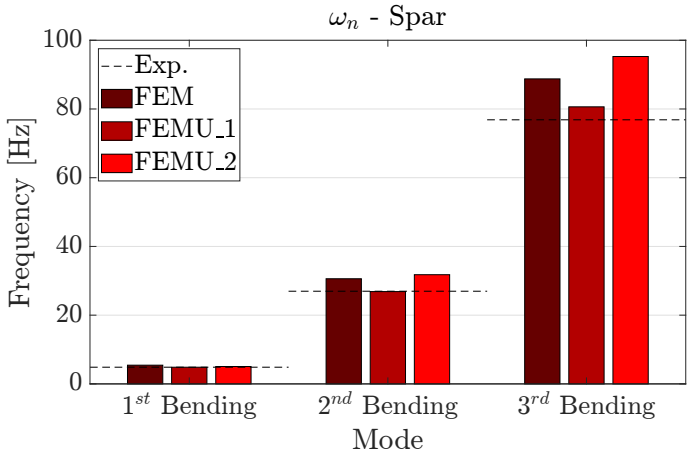

Figure 7.7: Natural frequencies identified from the experimental data (Exp.), the preliminary FEM (FEM) and the updated FEMs (FEMU_1-2) for the spar.

Apart from ω_n, another modal parameter is taken into consideration. The $\boldsymbol{\phi}_n$ identified from the experimental campaign, preliminary FEM, FEM updated via bottom-up and FEM updated via top-down are shown in Figure 7.8. Table 7.12 reports on the MAC values computed between the preliminary and updated FEMs.

Table 7.12: MAC values (of the diagonal) between the spar's mode shapes identified from the experimental data and the preliminary and updated FEMs.

	MAC Values (of the diagonal) [-]		
Mode	FEM (%)	FEMU - Bottom-up (%)	FEMU - Top-down (%)
1st Bending	0.98	0.99	0.99
2nd Bending	0.94	0.98	0.97
3rd Bending	0.90	0.98	0.94

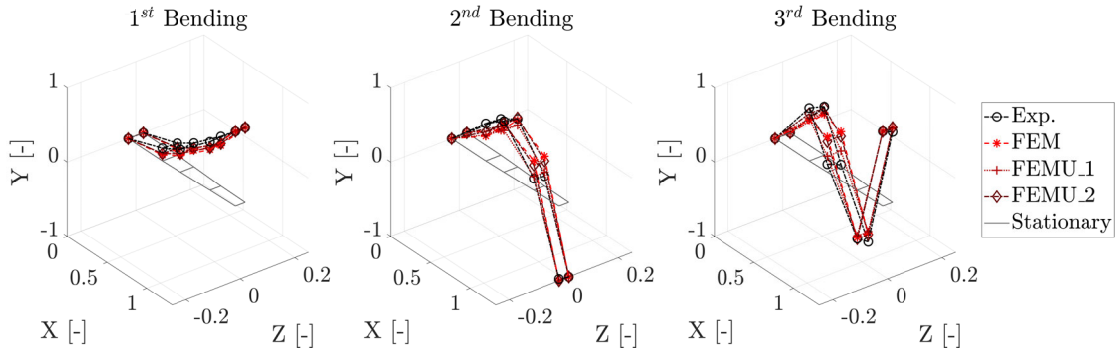

Figure 7.8: Mode shapes identified from the experimental data (Exp.), the preliminary FEM (FEM) and the updated FEMs (FEMU_1-2) for the spar.

In Table 7.11 and Figure 7.7, the results of the top-down (FEMU_2) and bottom-up (FEMU_1) approaches are compared to the preliminary FEM and experimental results. The results for the bottom-up approach are very good, in terms of identifying ω_n. They are better than the preliminary model and the top-down approach, which is the worst. The top-down approach ω_n are higher than those identified by the preliminary FEM, apart from the first bending mode.

The analysis on the identified $\boldsymbol{\phi}_n$ is carried out in Figure 7.8 and Table 7.12. The $\boldsymbol{\phi}_n$ from the experimental data, preliminary FEM and updated FEMs are superimposed for comparison in Figure 7.8, which is further investigated in Table 7.12. There, the diagonal values of the MAC matrix are presented. Please note, the off-diagonal terms are not presented due to their negligible magnitude. Globally, all FEMs offer a good approximation of the spar's $\boldsymbol{\phi}_n$ showing numerical correlation with values above 0.94 in Table 7.12 and graphical correlation in Figure 7.8. Nevertheless, the bottom-up approach performs better than the top-down approach and it is a clear improvement over the preliminary FEM. Notably, all the modes identified from the top-down approach are well correlated to the experimental case; however, they show less improvement than the bottom-up approach.

In order to globally compare the ω_n and $\boldsymbol{\phi}_n$ together, the penalty function of the optimisation routine can be considered, the MTMAC. The MTMAC for the prelimi-

nary FEM is 0.30, for bottom-up is 0.07 and for top-down is 0.26. Clearly, bottom-up, globally, shows an improvement over the preliminary FEM. This means that the small deterioration in the ω_n is counterbalanced by a greater precision in the $\boldsymbol{\phi}_n$ identification, as reported in Table 7.12. In terms of computational power, the preliminary FEM is built just by exploiting engineering practice and knowledge of the structure, while top-down takes the parameters from the FEMU of the XB-2 wing. However, bottom-up FEMU is carried out on the spar itself. The rEGO needs 327 model evaluations to have the solution converge to the presented results.

7.4.4 The Torque Box

The ω_n identified for the torque box from the updated FEMs are compared to those from experimental data and the preliminary FEM in Table 7.13 and Figure 7.9.

Table 7.13: Natural frequencies identified from the experimental data, the preliminary FEM and the updated FEMs for the torque box.

	Natural Frequencies [Hz]			
Mode	Exp.	FEM (%)	FEMU - Bottom-up (%)	FEMU - Top-down (%)
1st Bending	5.252	5.887 (2.76)	5.658 (7.734)	5.354 (1.94)
2nd Bending	25.933	31.452 (21.18)	32.663 (25.95)	31.092 (19.89)
1st Coupled	76.242	86.344 (13.25)	82.992 (8.85)	68.926 (-9.60)

In Figure 7.10 the $\boldsymbol{\phi}_n$ of the torque box identified by the FEMs and the experimental data are superimposed for graphical comparison. A quantitative comparison between the identified $\boldsymbol{\phi}_n$ is found in Table 7.14, where the MAC (diagonal) values with respect to the experimental data are reported.

The ω_n identified from the preliminary FEM seems to be more closely related to those from experimental data. Their maximum error, in Table 7.13, is 21.18%, which is less than the maximum errors for the updated FEMs. Notably, the maximum errors are always found for the second bending mode. On the other hand, the FEM from top-down has the lowest error (1.94%) for ω_1. This is a small im-

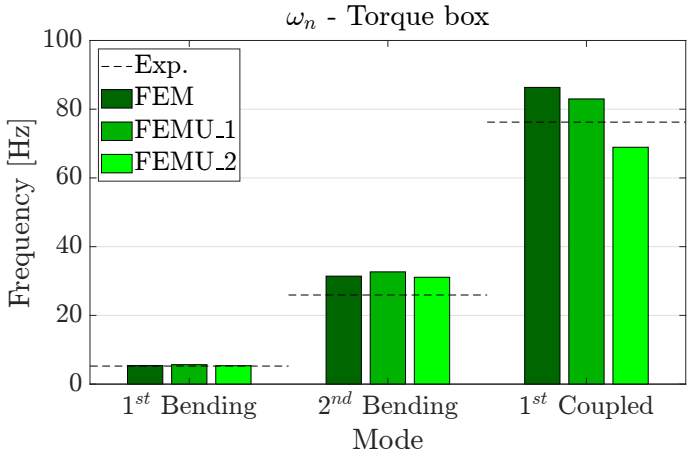

Figure 7.9: Natural frequencies identified from the experimental data (Exp.), the preliminary FEM (FEM) and the updated FEMs (FEMU_1-2) for the torque box.

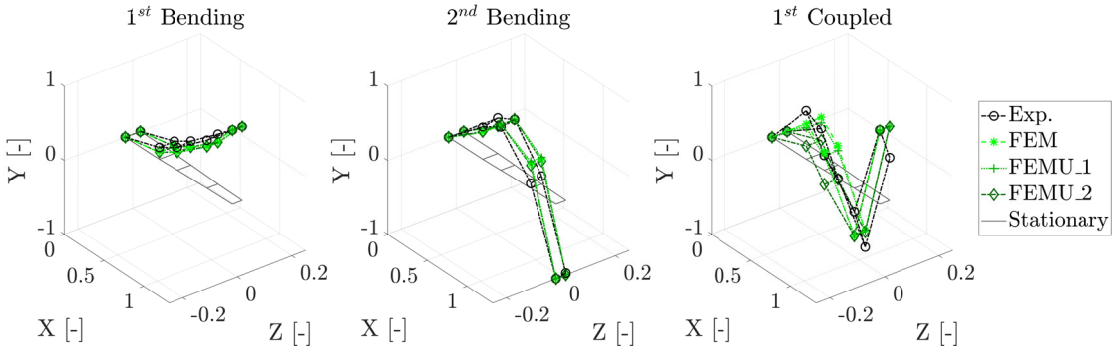

Figure 7.10: Mode shapes identified from the experimental data (Exp.), the preliminary FEM (FEM) and the updated FEMs (FEMU_1-2) for the torque box.

Table 7.14: MAC values (of the diagonal) between the torque box's mode shapes identified from the experimental data and the preliminary and updated FEMs.

	MAC Values (of the diagonal) [-]		
Mode	FEM (%)	FEMU - Bottom-up (%)	FEMU - Top-down (%)
1st Bending	0.99	0.99	0.99
2nd Bending	0.96	0.95	0.96
1st Coupled	0.83	0.84	0.76

provement over the preliminary FEM, but it is much better than the bottom-up FEM (7.734). Until now, all the FEMs have overestimated the ω_n values. However, this changes with the first coupled mode identified by the top-down approach for the torque box, which underestimates the experimental value by 9.6%. Concerning ω_3, the bottom-up FEM shows an improvement over the preliminary FEM

value, but the values for the other modes are overestimated. As it is clear from Figure 7.9, no model can be clearly set as the best, in terms of ω_n identification for the torque box.

The $\boldsymbol{\phi}_n$ extracted from the updated FEMs are compared to those from experimental data and preliminary FEM graphically, in Figure 7.10, and quantitatively in Table 7.14. Already from Figure 7.10, it is clear that the most problematic $\boldsymbol{\phi}_n$ is the first coupled mode. In particular, it seems that the FEMs struggle to mimic the amplitude of the torsional rotation. This impinges on the MAC values. As shown in Table 7.14, the lowest values are found for the first coupled mode, where the highest recorded value is 0.84 for the bottom-up updated FEM. In terms of MAC values, the preliminary FEM and the bottom-up FEM perform similarly. The same could be said about the top-down FEM, but the last mode results are not satisfactory.

In order to consider ω_n and $\boldsymbol{\phi}_n$ simultaneously, the MTMAC values with respect to the experimental data should be examined. The preliminary FEM MTMAC value is 0.34, that of bottom-up FEM is 0.35 and for top-down FEM is 0.37. Now, why are the values of the updated FEM higher than the preliminary FEM? This question should be addressed by examining the nature of these models. First, they are in a way constrained, such that they derive from the FEMU of a previous model (the spar and the XB-2 wing). Here, the bottom-up has an advantage over the top-down model since it is allowed to optimise some relevant parameters. This does not happen for the top-down FEM which has all the parameters pre-set by the FEMU for the XB-2 wing. In fact, the bottom-up model performs better than the top-down model, but still not as well as the preliminary model. In terms of model evaluations to convergence, the bottom-up model took 780 evaluations to be updated starting from the spar model. Notably, the algorithm did not fully converge via the usual route, but stopped at reaching the maximum number of stall iterations.

7.4.5 The XB-2 wing

In Table 7.15 a quantitative report of the ω_n extracted from the updated FEM is given and the values from experimental data and the preliminary FEM are recalled for comparison. A qualitative comparison is given in Figure 7.11.

Table 7.15: Natural frequencies identified from the experimental data, the preliminary FEMs and the updated FEM for the XB-2 wing.

	Natural Frequencies [Hz]			
Mode	Exp.	FEM (%)	FEMU - Bottom-up (%)	FEMU - Top-down (%)
1st Bending	3.187	3.5397 (11.03)	3.187 (-)	3.187 (-)
2nd Coupled	17.447	17.774 (1.88)	17.448 (0.01)	17.447 (-)

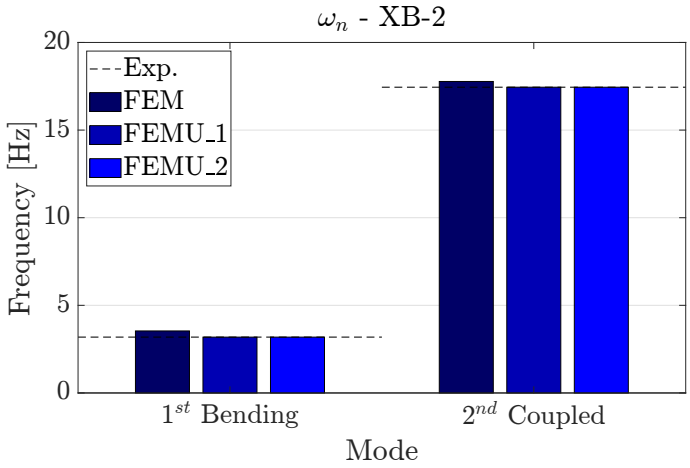

Figure 7.11: Natural frequencies identified from the experimental data (Exp.), the preliminary FEM (FEM) and the updated FEMs (FEMU_1-2) for the XB-2 wing.

In Figure 7.12 and Table 7.16 the $\boldsymbol{\phi}_n$ extracted from the updated FEM are compared to those from the experimental data and the preliminary FEM. Notably, Figure 7.12 shows the $\boldsymbol{\phi}_n$ superimposed for comparison and Table 7.16 gives a quantitative comparison by reporting the MAC values between the FEMs and the experimental data.

Figure 7.11 gives a qualitative overview of the precision, relative to the experimental data, of the parameters extracted via the FEMs. All FEM-extracted parameters are very close to the experimental data. In fact, Table 7.15 shows that the maximum error, relative to the experimental ω_n, for the updated FEMs

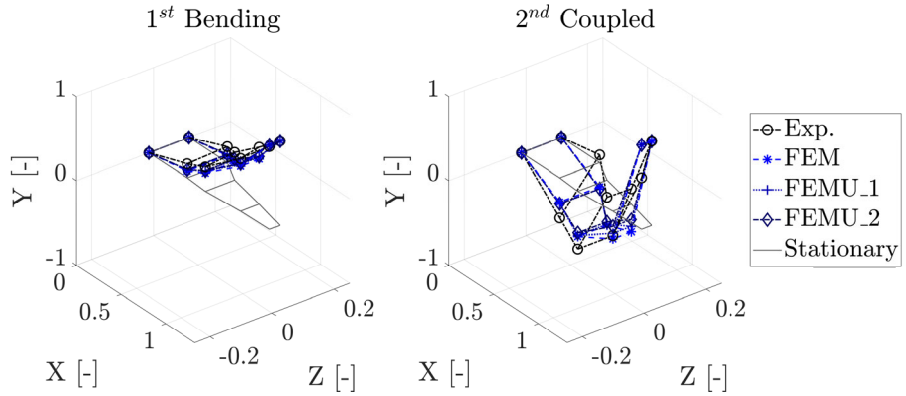

Figure 7.12: Mode shapes identified from the experimental data (Exp.), the preliminary FEM (FEM) and the updated FEMs (FEMU_1-2) for the XB-2 wing.

Table 7.16: MAC values (of the diagonal) between the XB-2 wing's mode shapes identified from the experimental data and the preliminary and updated FEMs.

	MAC Values (of the diagonal) [-]		
Mode	FEM (%)	FEMU - Bottom-up (%)	FEMU - Top-down (%)
1st Bending	0.98	0.99	0.99
2nd Coupled	0.75	0.77	0.78

is 0.01% in the bottom-up FEMU. The updated FEMs show a large if considered error percentage, improvement, in terms of ω_n, over the preliminary FEM.

Figure 7.12 and Table 7.16 report on the identified $\boldsymbol{\phi}_n$ from the updated FEMs and compare them with the experimental and the preliminary FEM data. In Figure 7.12 the first $\boldsymbol{\phi}_n$ is almost a perfect overlap for all FEMs. However, this does not happen for the second coupled mode, where, despite following the vertical deflection, the torsional magnitude is much smaller. These are confirmed in the quantitative analysis in Table 7.16, where the MAC values for the first bending mode are close to 1 for the updated FEMs and 0.98 for the preliminary model, but those for the second coupled mode do not go over 0.78, stopping at 0.75 for the preliminary FEM and 0.77 for the bottom-up FEM. In order to give equal consideration to ω_n and $\boldsymbol{\phi}_n$ the MTMAC is addressed. The starting MTMAC for the XB-2 wing is 0.30, but the updated models are able to reduce to 0.24 (bottom-up) and 0.23 (top-down). Similar results in terms of precision are delivered by the

bottom-up and 2 updated FEMs; however, the use of computational power needs to be taken into account. The top-down optimisation over 15 parameters took 1462 evaluations.

On the other hand to obtain a relevant number the evaluations of all preceding models need to be accounted for. The spar model took 327 evaluations to converge, the torque box model converged after 780 evaluations and, lastly, the final update took 57 evaluations, totalling 1164. Hence making the bottom-up approach more computationally efficient than the bottom-down approach when using rEGO.

The raw identified data from the FEMs updated with both approaches are available in Tables C.3 and C.4, while Table C.5 shows the optimisation parameters (as scaling values from Table 7.9).

7.5 Discussion

In Section 7.2 the surrogate-based optimisation technique, the rEGO, and its FEMU implementation are described. Following, Section 7.4 introduces the flexible wing specimen, the XB-2 wing, the experimental campaign and the preliminary FEM. Then, in Section 7.4 the implementation of the Ansys Mechanical APDL FEM within the rEGO MATLAB program is explained, before introducing the two FEMU processes and the chosen updating parameters, or optimisation variables. The two FEMU processes, bottom-up and top-down, are characterised, respectively, by a bottom-up and a top-down approach. This means that the former updates the FEM's wing's components as they are assembled, while the latter updates the flexible wing model and the parameters are passed to the components.

The top-down approach is found to struggle to identify modes beyond the first bending mode for the wing's component, while the gradual approach of bottom-up

allows for more precise tuning, particularly for $\boldsymbol{\phi}_n$, such as for the torque box. In terms of the main metric used in this work, the MTMAC residual, the bottom-up approach outperforms top-down in all models, apart from the XB-2 wing where top-down performs slightly better. Both methods however struggle to obtain a representation for the torque box better than the preliminary FEM. In fact, they are slightly worse.

Nevertheless, both XB-2 wing models are much better than the preliminary one. However, the top-down model used more total model evaluations than the bottom-up approach, which also computed smaller models. Only 57 evaluations of the full wing model, after 327 of the spar model and 780 of the torque box model, are necessary to obtain an MTMAC residual within 5% that obtained from more, 1462, evaluations of the more computationally expensive model, the XB-2 wing.

7.6 Conclusions

In this work, a flexible wing finite element model is characterised and updated using modal data from an experimental campaign following two component-based, bottom-up and top-down, approaches. The first updates the wing's components models as they are assembled, while the latter updates the final wings and the parameters are passed down to the other components models. It is found that the bottom-up approach works better on the components, while the top-down approach is slightly better for the modelling of the wing. However, it is, considering the modified total modal assurance criterion, only 5% better than the bottom-up, which takes fewer total model evaluations and does so by mainly evaluating the, smaller and computationally cheaper, components models. Notably, this is the first time that the refined Efficient Global Optimisation is used for the model updating of a real, non-benchmark, structure. The authors suggest the use of the

bottom-up approach, in similar problems, when there is a constraint on computational power or the need to develop interim models of the sub-components; otherwise, the top-down, or direct approach, is recommended.

References

[1] C. Fei, H. Liu, S. Li, H. Li, L. An, and C. Lu, "Dynamic parametric modeling-based model updating strategy of aeroengine casings," *Chinese Journal of Aeronautics*, vol. 34, no. 12, pp. 145–157, 2021, ISSN: 10009361, DOI: 10.1016/j.cja.2020.10.036 (cit. on p. 219).

[2] N. F. Alkayem, M. Cao, Y. Zhang, M. Bayat, and Z. Su, "Structural damage detection using finite element model updating with evolutionary algorithms: a survey," *Neural Computing and Applications*, vol. 30, no. 2, pp. 389–411, 2018, ISSN: 0941-0643, DOI: 10.1007/s00521-017-3284-1 (cit. on p. 219).

[3] G. Dessena, D. I. Ignatyev, J. F. Whidborne, and L. Zanotti Fragonara, "A Kriging Approach to Model Updating for Damage Detection," in *EWSHM 2022*, P. Rizzo and A. Milazzo, Eds., LNCE 254, Singapore: Springer, 2023, ch. 26, pp. 245–255, DOI: 10.1007/978-3-031-07258-1_26 (cit. on pp. 219, 223, 233).

[4] X. Yang, X. Guo, H. Ouyang, and D. Li, "A Kriging model based finite element model updating method for damage detection," *Applied Sciences*, vol. 7, no. 10, p. 1039, 2017, ISSN: 2076-3417, DOI: 10.3390/app7101039 (cit. on p. 219).

[5] G. Dessena, D. I. Ignatyev, J. F. Whidborne, and L. Zanotti Fragonara, "A global-local meta-modelling technique for model updating," *[Submitted to]*

Computer Methods in Applied Mechanics and Engineering, 2023 (cit. on pp. 219, 222, 223, 233).

[6] M. I. Friswell and J. E. Mottershead, *Finite Element Model Updating in Structural Dynamics* (Solid Mechanics and its Applications). Dordrecht: Springer Netherlands, 1995, vol. 38, ISBN: 978-90-481-4535-5, DOI: 10.1007/978-94-015-8508-8 (cit. on p. 219).

[7] J. Mottershead and M. Friswell, "Model updating in structural dynamics: A survey," *Journal of Sound and Vibration*, vol. 167, no. 2, pp. 347–375, 1993, ISSN: 0022460X, DOI: 10.1006/jsvi.1993.1340 (cit. on p. 219).

[8] T. Marwala, *Finite-element-model Updating Using Computional Intelligence Techniques*. London: Springer London, 2010, ISBN: 978-1-84996-322-0, DOI: 10.1007/978-1-84996-323-7 (cit. on p. 219).

[9] F. De Florio, *Airworthiness*. Elsevier, 2011, ISBN: 9780080968025, DOI: 10.1016/C2010-0-65567-2 (cit. on p. 219).

[10] S. Malik, S. Ricci, and L. Riccobene, "Aeroelastic analysis of a slender wing," *CEAS Aeronautical Journal*, vol. 11, no. 4, pp. 917–927, 2020, ISSN: 1869-5582, DOI: 10.1007/s13272-020-00459-6 (cit. on p. 220).

[11] M. Mihaila-Andres, P.-V. Rosu, C. Larco, M. Demsa, L. Constantin, and R. Pahonie, "Preliminary design of aeroelastically tailored wing box structures with bend-twist coupling," *ITM Web of Conferences*, vol. 24, N. Bardis, Ed., p. 02 010, 2019, ISSN: 2271-2097, DOI: 10.1051/itmconf/20192402010 (cit. on p. 220).

[12] Y. Wang, A. Wynn, and R. Palacios, "Nonlinear aeroelastic control of very flexible aircraft using model updating," *Journal of Aircraft*, vol. 55, no. 4, pp. 1551–1563, 2018, ISSN: 15333868, DOI: 10.2514/1.C034684 (cit. on p. 220).

[13] C. Chiodi, G. Coppotelli, and J. V. Covioli, "Identification of the static and dynamic numerical model of a jet aircraft wing from experimental tests," *AIAA Scitech 2021 Forum*, no. January, pp. 1–21, 2021, DOI: 10.2514/6.2021-1498 (cit. on p. 220).

[14] J. Cecrdle, "Updating of jet trainer aircraft dynamic model to results of ground vibration test," in *33rd Congress of the International Council of the Aeronautical Sciences*, Stockholm, Sweden, 2022, pp. 1–9 (cit. on p. 220).

[15] W. Wang, X. Zhang, D. Hu, D. Zhang, and P. Allaire, "A novel none once per revolution blade tip timing based blade vibration parameters identification method," *Chinese Journal of Aeronautics*, vol. 33, no. 7, pp. 1953–1968, 2020, ISSN: 10009361, DOI: 10.1016/j.cja.2020.01.014 (cit. on p. 220).

[16] G. Dessena, *A tutorial on the Loewner-based system identification and structural health monitoring approach for mechanical systems.* Cranfield, 2022, DOI: 10.17862/cranfield.rd.16636279 (cit. on p. 220).

[17] M. Civera, G. Calamai, and L. Zanotti Fragonara, "Experimental modal analysis of structural systems by using the fast relaxed vector fitting method," *Structural Control and Health Monitoring*, vol. 28, no. 4, pp. 1–23, 2021, ISSN: 1545-2255, DOI: 10.1002/stc.2695 (cit. on p. 220).

[18] V. Mugnaini, L. Zanotti Fragonara, and M. Civera, "A machine learning approach for automatic operational modal analysis," *Mechanical Systems and Signal Processing*, vol. 170, no. February, p. 108 813, 2022, ISSN: 08883270, DOI: 10.1016/j.ymssp.2022.108813 (cit. on p. 220).

[19] J. Cecrdle, "Updating of aircraft structure dynamic model to ground vibration test results," in *29th Congress of the International Council of the Aeronautical Sciences*, St. Petersburg, Russia, 2014, pp. 1–7, ISBN: 3-932182-80-4 (cit. on p. 220).

[20] G. Coppotelli, F. D. Giandomenico, C. Groth, S. Porziani, A. Chiappa, and M. E. Biancolini, "On the structural updating using operational responses of a realistic wing model: The ribes test article," in *8th IOMAC - International Operational Modal Analysis Conference, Proceedings*, 2019 (cit. on p. 220).

[21] R. J. Allemang and D. L. Brown, "A correlation coefficient for modal vector analysis," in *Proceedings of the 1st International Modal Analysis Conference*, Orlando: Union Coll, 1982, pp. 110–116 (cit. on pp. 220, 223).

[22] M. Civera, L. Z. Fragonara, and C. Surace, "A Computer Vision-Based Approach for Non-contact Modal Analysis and Finite Element Model Updating," in *EWSHM 2020, LNCE 127*, vol. 127, 2021, pp. 481–493, ISBN: 9783030645939, DOI: 10.1007/978-3-030-64594-6_47 (cit. on p. 220).

[23] W. Zhao, N. Muthirevula, R. K. Kapania, A. Gupta, C. D. Regan, and P. J. Seiler, "A Subcomponent-based Finite Element Model Updating for a Composite Flying-wing Aircraft," in *AIAA Atmospheric Flight Mechanics Conference*, Grapevine, Texas: American Institute of Aeronautics and Astronautics, 2017, ISBN: 978-1-62410-448-0, DOI: 10.2514/6.2017-1393 (cit. on p. 220).

[24] G. Dessena, D. I. Ignatyev, J. F. Whidborne, A. Pontillo, and L. Zanotti Fragonara, "Ground vibration testing of a flexible wing: a benchmark and case study," *Aerospace*, vol. 9, no. 8, p. 438, 2022, ISSN: 2226-4310, DOI: 10.3390/aerospace9080438 (cit. on pp. 220, 226, 227, 229, 231, 236).

[25] D. R. Jones, M. Schonlau, and W. J. Welch, "Efficient global optimization of expensive black-box functions," *Journal of Global Optimization*, vol. 13, pp. 455–492, 1998, DOI: 10.1023/A:1008306431147 (cit. on pp. 221–223).

[26] A. I. J. Forrester, A. Sóbester, and A. J. Keane, *Engineering Design via Surrogate Modelling*. Wiley, 2008, ISBN: 9780470060681, DOI: 10.1002/9780470770801 (cit. on pp. 221, 223).

[27] A. Keane and J. Scanlan, "Design search and optimization in aerospace engineering," *Philosophical Transactions of the Royal Society A: Mathematical, Physical and Engineering Sciences*, vol. 365, no. 1859, pp. 2501–2529, 2007, ISSN: 1364-503X, DOI: 10.1098/rsta.2007.2019 (cit. on p. 221).

[28] A. I. Forrester, A. Sóbester, and A. J. Keane, "Multi-fidelity optimization via surrogate modelling," *Proceedings of the Royal Society A: Mathematical, Physical and Engineering Sciences*, vol. 463, no. 2088, pp. 3251–3269, 2007, ISSN: 14712946, DOI: 10.1098/rspa.2007.1900 (cit. on pp. 221–223).

[29] J. Xing, Y. Luo, and Z. Gao, "A global optimization strategy based on the Kriging surrogate model and parallel computing," *Structural and Multidisciplinary Optimization*, vol. 62, no. 1, pp. 405–417, 2020, ISSN: 16151488, DOI: 10.1007/s00158-020-02495-6 (cit. on p. 222).

[30] D. Whitley, "A genetic algorithm tutorial," *Statistics and Computing*, vol. 4, no. 2, 1994, ISSN: 0960-3174, DOI: 10.1007/BF00175354 (cit. on p. 222).

[31] I. Voutchkov and A. Keane, "Multi-Objective Optimization Using Surrogates," in *Computational Intelligence in Optimization*, Y. Tenne and C.-K. Goh, Eds., Berlin: Springer, 2010, ch. 7, pp. 155–175, DOI: 10.1007/978-3-642-12775-5_7 (cit. on p. 222).

[32] K. Deb, A. Pratap, S. Agarwal, and T. Meyarivan, "A fast and elitist multiobjective genetic algorithm: NSGA-II," *IEEE Transactions on Evolutionary Computation*, vol. 6, no. 2, pp. 182–197, 2002, ISSN: 1089778X, DOI: 10.1109/4235.996017 (cit. on p. 222).

[33] R. Perera and R. Torres, "Structural damage detection via modal data with genetic algorithms," *Journal of Structural Engineering*, vol. 132, no. 9, pp. 1491–1501, 2006, ISSN: 0733-9445, DOI: 10.1061/(ASCE)0733-9445(2006)132:9(1491) (cit. on p. 223).

[34] G. Dessena, *A tutorial on the refined Efficient Global Optimisation*, Cranfield, UK, 2022, DOI: 10.17862/cranfield.rd.21163750 (cit. on p. 223).

[35] A. Pontillo *et al.*, "Flexible high aspect ratio wing: low cost experimental model and computational framework," in *2018 AIAA Atmospheric Flight Mechanics Conference*, Kissimmee, FL: American Institute of Aeronautics and Astronautics, 2018, pp. 1–15, ISBN: 978-1-62410-525-8, DOI: 10.2514/6.2018-1014 (cit. on pp. 224, 226).

[36] S. Y. Yusuf, D. Hayes, A. Pontillo, M. A. Carrizales, G. X. Dussart, and M. M. Lone, "Aeroelastic Scaling for Flexible High Aspect Ratio Wings," in *AIAA Scitech 2019 Forum*, Reston, Virginia: American Institute of Aeronautics and Astronautics, 2019, pp. 1–14, ISBN: 978-1-62410-578-4, DOI: 10.2514/6.2019-1594 (cit. on pp. 224, 226, 227).

[37] D. Hayes, A. Pontillo, S. Y. Yusuf, M. M. Lone, and J. Whidborne, "High aspect ratio wing design using the minimum energy destruction principle," in *AIAA Scitech 2019 Forum*, Kissimmee, FL: American Institute of Aeronautics and Astronautics, 2019, ISBN: 978-1-62410-578-4, DOI: 10.2514/6.2019-1592 (cit. on pp. 224, 226).

[38] A. Pontillo, "High Aspect Ratio Wings on Commercial Aircraft: a Numerical and Experimental approach," PhD Thesis, Cranfield University, 2020 (cit. on pp. 224, 226).

[39] S. Y. Yusuf, "On System Identification and Dynamic Scaling of a Flexible Aircraft," PhD Thesis, Cranfield University, 2019 (cit. on pp. 224, 226).

[40] N. P. Macdonald, J. M. Cabot, P. Smejkal, R. M. Guijt, B. Paull, and M. C. Breadmore, "Comparing Microfluidic Performance of Three-Dimensional (3D) Printing Platforms," *Analytical Chemistry*, vol. 89, no. 7, pp. 3858–3866, 2017, ISSN: 15206882, DOI: 10.1021/acs.analchem.7b00136 (cit. on p. 226).

[41] A. J. Keane, A. Sóbester, and J. P. Scanlan, *Small Unmanned Fixed-wing Aircraft Design*. Chichester, UK: John Wiley & Sons, 2017, ISBN: 9781119406303, DOI: 10.1002/9781119406303 (cit. on p. 226).

[42] G. Dessena, D. I. Ignatyev, J. F. Whidborne, A. Pontillo, and L. Zanotti Fragonara, "Ground vibration testing of a high aspect ratio wing with revolving clamp," in *33rd Congress of the International Council of the Aeronautical Sciences*, Stockholm, Sweden, 2022, DOI: 10.17862/cranfield.rd.20486229 (cit. on pp. 226, 231).

[43] G. Dessena, M. Civera, A. Pontillo, D. I. Ignatyev, J. F. Whidborne, and L. Zanotti Fragonara, "Comparative Study on Novel Modal Parameters Extraction Methods for Aeronautical Structures," *in preparation*, 2023 (cit. on pp. 226, 231).

[44] A. Schulze, J. Zierath, S.-E. Rosenow, R. Bockhahn, R. Rachholz, and C. Woernle, "Optimal sensor placement for modal testing on wind turbines," *Journal of Physics: Conference Series*, vol. 753, no. 7, p. 072 031, 2016, ISSN: 1742-6588, DOI: 10.1088/1742-6596/753/7/072031 (cit. on p. 230).

[45] F. Dezi, F. Gara, and D. Roia, "Dynamic Characterization of Open-ended Pipe Piles in Marine Environment," in *Applied Studies of Coastal and Marine Environments*, InTech, 2016, pp. 169–204, DOI: 10.5772/62055 (cit. on p. 231).

[46] F. R. Spitznogle and A. H. Quazi, "Representation and analysis of time-limited signals using a Complex Exponential algorithm," *The Journal of*

The Acoustical Society of America, vol. 47, no. 5 (Part I), pp. 1150–1155, 1970 (cit. on p. 231).

[47] F. R. Spitznogle, J. M. Barrett, C. I. Black, T. W. Ellis, and W. L. LaFuze, "Representation and analysis of sonar signals. Volume I. Improvements in the Complex Exponential signal analysis computational algorithm.," Office of Naval Research- Contract No. NOOO14-69-C0315,1971, Tech. Rep., 1971, p. 47 (cit. on p. 231).

[48] G. Dessena, A. Pontillo, D. I. Ignatyev, J. F. Whidborne, and L. Zanotti Fragonara, "Identification of Nonlinearity Sources in a Flexible Wing: a Case Study," *in preparation*, 2023 (cit. on p. 231).

[49] D. J. Ewins, *Modal Testing Theory, Practice and Application*, 2nd. Baldock, UK: Research Studies Press, 2000, p. 562, ISBN: 978-0-863-80218-4 (cit. on p. 233).

Chapter 8

Conclusions and Suggestions for Future Work

In this chapter, the concluding remarks and future works related to the scientific aim, objectives and content of this thesis are presented. First, in Section 8.1 a brief summary of the research is given, outlining the main findings and contributions of the thesis. Then, the objectives (O1-3) presented in Chapter 1 provide the basis for the discussion of the research's results in terms of academic contributions, in Section 8.2, and potential impact, in Section 8.3. The thesis is closed by the potential extensions of this research in Section 8.4.

8.1 Conclusions

In this thesis, the structural behaviour of a flexible wing model is identified by employing advanced methods and introducing new, computationally efficient, ones.

A System Identification (SI) technique, the Loewner Framework (LF), first introduced in electronics, is pioneeringly used for the extraction of modal parameters in mechanical, numerical and experimental, systems for the scope of Structural Health Monitoring (SHM). The LF introduction as a SI method for mechanical sys-

tems is justified by the ill-conditioning of the fitting process, that occurs for other popular frequency domain techniques incur. In addition, the LF shows a higher resilience to noise than other newly proposed SI methods, such as the Fast Relaxed Vector Fitting (FRVF). Lastly, the LF is successfully applied to the flexible wing model to characterise aeroelastic phenomena. The main limitation of the method is the single-input-multi-output capability, rather than a multi-input-multi-output (MIMO) one. This can be a limitation, particularly for the implementation of the technique for full-scale structures Experimental Modal Analysis (EMA). However, this is not further explored in the work due to the fact that the testing setup does not involve multiple inputs. These are discussed in details in Chapters 2 and 4.

An extensive experimental campaign on the flexible wing model generated two distinct, but linked, case studies. The first deals with extensive ground vibration testing with random excitation at different amplitudes that involved the flexible wing and its sub-assembly and components. In this campaign, a slight nonlinearity is detected in the wing's dynamics. The nonlinearity is then investigated in the second case study. Nonlinear modal analysis (NLMA) is used to determine the source of the nonlinearity on the wing. The backbone curve is extracted from the free-decay from the resonance of the first mode and the signal is then analysed in the time-frequency domain with the superlets, employed for the first time in a mechanical system. Nonlinear softening is identified and, after visual inspections and further testing on the wing's parts, its source is assessed to be a combination of inertia effects and load misalignment with respect to the shear centre. This induces a torsion moment that weakens the bending stiffness. Even if the methods employed are applicable to different systems, the results are representative only of the flexible wing model thoroughly examined in this study and cannot be generalised. Data from all tests are made available to serve as a benchmark to the structural dynamics community. The complete discussions and findings of the

case studies are found in Chapters 4 and 5.

A novel surrogate-based technique, the refined Efficient Global Optimisation (rEGO), is introduced as an improved version of the well-known Efficient Global Optimization (EGO) method. rEGO's main achievements are to complete the global search capabilities of EGO with a local search capability, in a hybrid optimiser fashion, and to give, in the optimisation task, a precision comparable to genetic algorithms (GAs), but with less computational burden. These are achieved with the principles of refinement and selection. rEGO is first introduced, successfully, for damage detection via finite element model updating (FEMU) in numerical and experimental systems. Then, rEGO is applied for the FEMU of flexible wings to validate component-by-component approaches. rEGO successfully updated the flexible wing finite element model (FEM) and it has demonstrated that a bottom-up component-based approach to FEMU can be more computationally efficient than direct methods. The FEM of the flexible is solely updated for the linear regime and has no extension to nonlinear properties. From a technical standpoint, the ANSYS Mechanical ADPL model can be easily adapted for large deflections. However, a change in goal function and metric for the FEMU strategy might be needed to account for nonlinear effects. rEGO is introduced and employed for FEMU in Chapters 6 and 7.

8.2 Academic Contributions

The academic contributions are determined by relating the thesis outcomes with the objectives list in Chapter 1.

A1. Development of a computationally efficient technique for system identification in structural dynamics:

O1a. The LF algorithm is developed in MATLAB to solve the ill-conditioning of current frequency domain methods. (Chapter 2)

O1b. Robustness of the method to noise, while maintaining the required precision, is shown through the numerical and experimental examples.; (Chapters 2 and 4)

O1c. The proposed technique was validated against state-of-the-art SI methods for SHM. The capabilities of prediction of an aeroelastic phenomena onset speed on the flexible wing are demonstrated. The LF is compared to the FRVF against expected results on a numerical system, which are also used for studying the methods' robustness to noise. In addition, experimental data are retrieved for a flexible wing and a 2 degrees-of-freedom (DoF) is built from their identified modal parameters for aeroelastic onset speed prediction. The speeds obtained from LF and FRVF are compared to benchmark values, those identified from N4SID. (Chapter 4)

A2. Generation of an experimental data set of the flexible wing model via vibration testing for experimental validation:

O2a. Linear and nonlinear vibration testing is carried out on the flexible wing. Linear testing is achieved with ground vibration testing on a shaker table at three different input amplitudes of random vibration, while nonlinear testing is executed with the free-decay from resonance of the first mode; (Chapters 3 and 5 and Appendix E)

O2b. EMA of the flexible wing is used to extract modal parameters from the wing and its sub-assembly and parts. Vibration testing with a band-limited random excitation at three increasing amplitudes is carried out on the parts, sub-assembly, and wing, totalling 12 cases. The modal parameters identified via LSCE showed a slight softening nonlinearity for the wing. The study was published as a benchmark and case study; (Chapter 3 and Appendix E)

O2c. Nonlinear characterisation of the flexible wing is carried out with a combination of visual and vibration testing techniques. The characterisation of the nonlinearity is obtained by extracting the backbone curve of the first mode and carrying out the respective time-frequency analysis. This confirms the nonlinearity, but its origin was still uncertain. A duffing oscillator with quadratic damping is used to identify the equivalent 1 DoF system. The nonlinearity origin is investigated by further studying the wing's part via time-frequency analysis and by assessing the mass and stiffness distributions. (Chapters 3 and 5)

O3. Developing a computationally efficient technique for the model updating of flexible wings:

O3a. A novel optimisation algorithm, rEGO, based on EGO, is introduced, giving an enhanced performance, in terms of precision, over EGO and, in terms of computational power required, GAs. The algorithm is implemented in MATLAB; (Chapter 6 and Appendix D);

O2b. A novel FEMU technique is proposed for the damage detection of numerical and experimental systems. A numerical study is carried out to fix the rEGO hyperparameters and a further study to pick the metric used for the model updating process. Finally, rEGO is validated for model updating on a hybrid, numerical and experimental, system from a well-known benchmark; (Chapter 6 and Appendix D);

O2c. The new technique is used to validate the effects of component-to-component FEMU for flexible wings. The model updating via rEGO is used to update the FEM model of the flexible wing with two strategies. The top-down and bottom-up approaches. The latter only updates the full wing and in the former, the spar is updated, then the torque box and finally the wing, in a progressive manner. (Chapter 7).

8.3 Potential Impact

The LF has the potential to establish itself as a reliable and consistent SI input-output frequency-domain technique for mechanical systems. The main merit is the overcoming of the ill-conditioning of the fitting process that happens with the pre-existing methods.

The testing techniques used for the characterisation are, even if some methods can be classified as advanced, standard procedures in experimental dynamics. Nevertheless, the source of the potential impact may lie in the process of implementation rather than in the tests themselves. The workflow followed in the tests of first assessing the structure with random vibration at different inputs and, then, if trends arise, going forward with more specific testing.

rEGO is a suitable alternative to established optimisation routines and can become a staple itself thanks to its enhanced computational efficiency and its global-local capability. Its application to FEMU has proved successful in simulated and experimental systems, which is promising for other domains, such as design.

The important aspects relating to potential impact are accessibility and ease of use. The former is obtained with the open distribution of related programs. The idea is to publish all programmes and datasets in an open repository, such the Cranfield Online Research Data (CORD), all the codes, programmes and dataset developed for the LF, testing and rEGO. To help in the ease of use, the programs are developed in MATLAB, a widely used tool in academia and industry, and the dataset is available in MATLAB's native `.mat` format, which can also be imported in Python through the `scipy.io` library.

8.4 Future Work

In terms of future works, the main aim for the LF should be to expand the identification capability to multi-input-multi-output systems for EMA. This can be achieved by changing the way the state-space matrices are formulated in the MATLAB implementation to allow for the extraction of modal parameters for multi-input-multi-output systems. A further improvement, could be identified in extending the method for operational modal analysis. This can be obtained using the Natural Excitation Technique (NExT), which has already been used successfully in pair with the Eigensystem Realization Algorithm (ERA) in the so-called NExT-ERA. Finally, a further extension to the modelling of nonlinear systems, beyond linearisation, could be attempted as some advancements for the model order reduction of simple nonlinear systems via the LF have already been proposed.

Further experimental work concerning the flexible wing can include the use of the designed and manufactured clamp, which allows different setting angles of the specimen, to simulate MIMO testing from a single excitation point by vector decomposition (horizontal and vertical) of the shaker input. In addition, NLMA can be carried out on the wing set at different setting angles to investigate their effects on nonlinearity, both in terms of direction (hardening or softening) and damping. For the latter, comparisons can be carried out with the recent advancements in the single degree of freedom analytical formulation of flexible slender structures. Concerning the identification of the wing's properties, a nonlinear reduced order model of the flexible wing, which takes into consideration also the data from different setting angles, can be generated to be implemented in real-time or quasi-real-time for SHM and aeroelastic modelling purposes. Also, a second flexible wing specimen, with different characteristics, could be used to validate the specific findings from the first wing and, so, generalise some results.

Lastly, rEGO can be implemented in different areas of engineering, such as

design or manufacturing, for the optimisation of different problems. The main candidate would be topology optimisation for aerodynamic efficiency. However, the application could be even broader, such as multi-objective. In fact, Topology optimisation could be carried out for both minimising the drag and weight of a wing. Hence, a suitable multi-objective implementation of rEGO can also help in its dissemination and impact. The main tasks for the implementation of multi-objective Kriging are to define a suitable surrogate, either multi-dimensional Kriging or multiple models, and the choice of suitable test improvement metrics that take into consideration the Pareto fronts.

A general goal can be to import the MATLAB script for the LF and rEGO into Python to give full open access also on the software side and aid the dissemination of the work.

Appendix A

Authors' Contributions

In this Appendix information about the authors' contributions to the works included in this thesis is given. First, a list of the authors involved in the production of the research outputs is outlined, and then the authors' contributions in the CRediT taxonomy format are given for each chapter\paper.

A.1 Contributing Authors

In this section the authors that contributed to the works included in this thesis are listed:

Gabriele Dessena (G.D.)	Thesis author
Dmitry I. Ignatyev (D.I.)	Supervisor, Senior Research Fellow in Autonomous Systems and Control at Cranfield University
James F. Whidborne (J.W.)	Supervisor, Professor in Control Engineering at Cranfield University
Luca Zanotti Fragonara (L.Z.)	Supervisor, Visiting Fellow at Cranfield University
Marco Civera (M.C.)	Research partner, Assistant Professor at Politecnico di Torino
Alessandro Pontillo (A.P.)	Research partner, Research Associate in Aeroelastic Modelling at University of Bristol

A.2 Authors' Contributions

Chapter 2. A Loewner-based system identification and structural health monitoring approach for mechanical systems

Conceptualisation, G.D., M.C. and L.Z.; methodology, G.D. and M.C.; software, G.D.; validation, G.D. and M.C.; formal analysis, G.D. and M.C.; investigation, G.D.; resources, D.I., J.F. and L.Z.; data curation, G.D.; writing—original draft preparation, G.D.; writing—review and editing, G.D., M.C., D.I., J.F. and L.Z.; visualisation, G.D. and M.C.; supervision, D.I., J.F. and L.Z.; funding acquisition, L.Z..

Chapter 3. Ground vibration testing of a flexible wing: A benchmark and case study

Conceptualisation, G.D., L.Z and A.P.; methodology, G.D., L.Z. and A.P.; software, L.Z and G.D.; validation, G.D.; formal analysis, G.D.; investigation, G.D.; resources, D.I., J.W. and L.Z.; data curation, G.D.; writing—original draft preparation, G.D.; writing—review and editing, G.D., D.I., J.W., L.Z., and A.P.; visualisation, G.D.; supervision, D.I., J.W., and L.Z.; funding acquisition, L.Z..

Chapter 4. Comparative study on novel modal parameters extraction methods for aeronautical structures

Conceptualisation, G.D. and M.C.; methodology, G.D., M.C., and A.P; software, G.D., M.C., and L.Z.; validation, G.D., M.C., A.P., D.I., and J.W.; formal analysis, G.D. and M.C.; investigation, G.D.; resources, A.P., D.I., J.W. and L.Z.; data curation, G.D. and M.C.; writing—original draft preparation, G.D.; writing—review and editing, G.D., M.C., A.P., D.I., J.W., and L.Z.; visualisation, G.D., M.C., and D.I.I.; supervision, D.I., J.W., and L.Z.; funding acquisition, L.Z..

Chapter 5. Identification of nonlinearity sources in a flexible wing: a case study

Conceptualisation, G.D., L.Z and A.P; methodology, G.D.; software, G.D.; valida-

tion, G.D.; formal analysis, G.D.; investigation, G.D.; resources, A.P., D.I., J.W. and L.Z.; data curation, G.D.; writing—original draft preparation, G.D.; writing—review and editing, G.D., D.I., J.W. and L.Z.; visualisation, G.D.; supervision, D.I., J.W., and L.Z.; funding acquisition, L.Z..

Chapter 6. A global-local meta-modelling technique for model updating

Conceptualisation, G.D.; methodology, G.D.; software, G.D.; validation, G.D.; formal analysis, G.D.; investigation, G.D.; resources, D.I., J.W. and L.Z.; data curation, G.D.; writing—original draft preparation, G.D.; writing—review and editing, G.D., D.I., J.W. and L.Z.; visualisation, G.D., D.I. and J.W.; supervision, D.I., J.W., and L.Z.; funding acquisition, L.Z..

Chapter 7. An iterative approach for the model updating of flexible wings

Conceptualisation, G.D.; methodology, G.D.; software, G.D.; validation, G.D.; formal analysis, G.D.; investigation, G.D.; resources, A.P., D.I., J.W. and L.Z.; data curation, G.D.; writing—original draft preparation, G.D.; writing—review and editing, G.D., D.I., J.W. and L.Z.; visualisation, G.D.; supervision, D.I., J.W., and L.Z.; funding acquisition, L.Z..

Appendix D. A Kriging approach to model updating for damage detection

Conceptualisation, G.D.; methodology, G.D.; software, G.D.; validation, G.D.; formal analysis, G.D.; investigation, G.D.; resources, D.I., J.W. and L.Z.; data curation, G.D.; writing—original draft preparation, G.D.; writing—review and editing, G.D., D.I., J.W. and L.Z.; visualisation, G.D., D.I. and J.W.; supervision, D.I., J.W., and L.Z.; funding acquisition, L.Z..

Appendix E. Ground vibration testing of a flexible wing with revolving clamp

Conceptualisation, G.D., L.Z and A.P.; methodology, G.D., L.Z. and A.P.; software, L.Z and G.D.; validation, G.D.; formal analysis, G.D.; investigation, G.D.; resources, D.I., J.W. and L.Z.; data curation, G.D.; writing—original draft preparation, G.D.; writing—review and editing, G.D., D.I., J.W., L.Z., and A.P.; visualisation, G.D.; supervision, D.I., J.W., and L.Z.; funding acquisition, L.Z..

Appendix B

Ground Vibration Testing of a Flexible Wing: A Benchmark and Case Study[1]

Table B.1: Twin spar: identified modal parameters.

	Low Input			Medium Input			High Input		
Mode	**1st**	**2nd**	**3rd**	**1st**	**2nd**	**3rd**	**1st**	**2nd**	**3rd**
ω_n	4.731	24.733	75.939	4.742	25.029	75.124	4.738	25.087	75.106
ζ_n	0.013	0.010	0.017	0.027	0.021	0.021	0.029	0.016	0.022
$\boldsymbol{\phi}_n$(1R)	0.137	0.531	0.626	0.138	0.525	0.580	0.149	0.550	0.268
$\boldsymbol{\phi}_n$(1L)	0.131	0.497	0.614	0.132	0.521	0.624	0.141	0.553	0.267
$\boldsymbol{\phi}_n$(2R)	0.303	0.744	0.056	0.303	0.746	0.074	0.309	0.809	0.069
$\boldsymbol{\phi}_n$(2L)	0.303	0.706	0.111	0.300	0.743	0.098	0.306	0.806	0.069
$\boldsymbol{\phi}_n$(3R)	0.662	0.152	-0.765	0.664	0.142	-0.693	0.664	0.123	-0.449
$\boldsymbol{\phi}_n$(3L)	0.640	0.117	-0.649	0.642	0.137	-0.656	0.669	0.126	-0.423
$\boldsymbol{\phi}_n$(4R)	0.995	-0.967	0.911	0.996	-0.997	0.977	0.9986	-1	0.965
$\boldsymbol{\phi}_n$(4L)	1	-1	1	1	-1	1	1	-0.997	1

[1]This is an adapted version of the Appendix for the following Open Access journal article: Dessena, G., Ignatyev, D. I., Whidborne, J. F., Pontillo, A., Zanotti Fragonara, L. (2022). Ground vibration testing of a flexible wing: A benchmark and case study. Aerospace, 9(8), 438. The final authenticated version is available at: https://doi.org/10.3390/aerospace9080438

Table B.2: Main spar: identified modal parameters.

	Low Input			**Medium Input**			**High Input**		
Mode	**1st**	**2nd**	**3rd**	**1st**	**2nd**	**3rd**	**1st**	**2nd**	**3rd**
ω_n	4.855	26.966	76.851	4.866	27.050	76.195	4.876	27.057	75.805
ζ_n	0.033	0.010	0.014	0.029	0.016	0.020	0.029	0.014	0.022
$\boldsymbol{\phi}_n$(1R)	0.159	0.484	0.650	0.157	0.481	0.607	0.126	0.442	0.784
$\boldsymbol{\phi}_n$(1L)	0.171	0.500	0.708	0.160	0.487	0.641	0.116	0.435	0.918
$\boldsymbol{\phi}_n$(2R)	0.317	0.639	0.028	0.325	0.637	0.025	0.297	0.587	0.397
$\boldsymbol{\phi}_n$(2L)	0.302	0.680	0.104	0.306	0.656	0.071	0.277	0.603	0.438
$\boldsymbol{\phi}_n$(3R)	0.660	0.131	-0.755	0.679	0.133	-0.722	0.728	0.148	-0.834
$\boldsymbol{\phi}_n$(3L)	0.646	0.156	-0.656	0.663	0.144	-0.686	0.702	0.153	-0.749
$\boldsymbol{\phi}_n$(4R)	1	-1	0.942	1	-1	0.999	1	-1	0.951
$\boldsymbol{\phi}_n$(4L)	0.999	-0.977	1	0.999	-0.988	1	0.995	-0.992	1

Table B.3: Spar and tube: identified modal parameters.

	Low Input			**Medium Input**			**High Input**		
Mode	**1st**	**2nd**	**3rd**	**1st**	**2nd**	**3rd**	**1st**	**2nd**	**3rd**
ω_n	5.252	25.933	76.242	5.151	25.958	75.770	5.163	25.941	75.135
ζ_n	0.022	0.014	0.017	0.030	0.011	0.034	0.036	0.010	0.034
$\boldsymbol{\phi}_n$(1R)	0.165	0.486	0.337	0.161	0.494	0.286	0.163	0.494	0.515
$\boldsymbol{\phi}_n$(1L)	0.158	0.439	0.658	0.153	0.441	0.595	0.156	0.440	0.798
$\boldsymbol{\phi}_n$(2R)	0.323	0.621	-0.185	0.318	0.631	-0.205	0.322	0.630	-0.173
$\boldsymbol{\phi}_n$(2L)	0.307	0.584	0.199	0.301	0.587	0.257	0.306	0.585	0.232
$\boldsymbol{\phi}_n$(3R)	0.672	0.107	-0.849	0.662	0.116	-0.823	0.672	0.112	-0.918
$\boldsymbol{\phi}_n$(3L)	0.646	0.0645	-0.320	0.663	0.072	-0.322	0.655	-0.068	-0.460
$\boldsymbol{\phi}_n$(4R)	1	-0.975	0.576	0.997	-0.967	0.595	0.999	-0.967	0.647
$\boldsymbol{\phi}_n$(4L)	0.999	-1	1	1	-1	1	1	-1	1

Table B.4: Full wing: identified modal parameters.

	Low Input			**Medium Input**			**High Input**		
Mode	**1st**	**2nd**	**4th**	**1st**	**2nd**	**4th**	**1st**	**2nd**	**4th**
ω_n	3.187	11.752	17.447	3.164	11.267	17.070	3.139	11.196	16.988
ζ_n	0.024	0.047	0.037	0.018	0.060	0.041	0.018	0.065	0.042
$\boldsymbol{\phi}_n$(1R)	0.187	1	0.090	0.187	1	0.089	0.192	1	0.086
$\boldsymbol{\phi}_n$(1L)	0.168	0.047	-0.474	0.174	0.047	-0.454	0.180	0.049	-0.420
$\boldsymbol{\phi}_n$(2R)	0.328	0.879	-0.204	0.329	0.895	-0.234	0.338	0.892	-0.241
$\boldsymbol{\phi}_n$(2L)	0.289	0.040	-0.682	0.278	0.041	-0.636	0.285	0.033	-0.572
$\boldsymbol{\phi}_n$(3R)	0.673	0.409	0.181	0.674	0.407	0.185	0.626	-0.204	-0.217
$\boldsymbol{\phi}_n$(3L)	0.624	-0.172	-0.288	0.620	-0.179	-0.250	0.655	-0.068	-0.460
$\boldsymbol{\phi}_n$(4R)	1	-0.195	1	1	-0.189	1	1	-0.297	1
$\boldsymbol{\phi}_n$(4L)	0.981	-0.640	0.610	0.986	-0.639	0.642	0.988	-0.712	0.663

Appendix C

An Iterative Approach for the Model Updating of Flexible Wings

Table C.1: Lumped masses position for the modelling of the XB-2 wing

	Position [cm]					Position [cm]			
Mass #	X	Y	Z	**Mass [g]**	**Mass #**	X	Y	Z	**Mass [g]**
1	13.987	0.297	5.139	74.108	25	68.500	-0.107	3.781	8.647
2	17.000	-0.044	3.756	12.836	26	69.998	-0.108	3.748	17.597
3	18.499	-0.045	3.729	26.185	27	71.499	-0.110	3.713	8.499
4	20.000	-0.047	3.701	12.677	28	72.998	-0.111	3.678	17.293
5	21.499	-0.049	3.672	25.845	29	74.500	-0.113	3.646	8.351
6	23.000	-0.050	3.646	12.517	30	75.998	-0.115	3.611	16.988
7	19.499	-0.052	3.618	25.518	31	77.998	-0.117	3.565	16.778
8	26.000	-0.053	3.589	12.346	32	80.052	-0.132	4.292	19.305
9	27.499	-0.055	3.563	25.190	33	86.933	0.326	3.954	79.010
10	29.000	-0.056	3.535	12.187	34	93.941	-0.146	3.929	17.831
11	32.484	0.269	4.841	79.642	35	95.499	-0.135	3.167	7.303
12	36.247	-0.109	6.483	33.263	36	96.992	-0.137	3.228	14.602
13	37.752	-0.110	6.422	33.111	37	98.499	-0.139	3.291	6.930
14	39.000	-0.066	3.350	11.639	38	99.998	-0.140	3.257	14.075
15	40.498	-0.068	3.324	23.739	39	101.499	-0.142	3.221	6.784
16	42.000	-0.069	3.296	11.480	40	102.998	-0.144	3.184	13.069
17	43.492	-0.073	3.398	22.955	41	104.499	-0.145	3.151	66.382
18	45.000	-0.075	3.508	10.895	42	105.997	-0.147	3.115	13.467
19	46.249	-0.076	3.483	16.673	43	107.997	-0.149	3.055	13.244
20	47.998	-0.079	3.447	22.031	44	109.746	-0.166	4.174	18.825
21	50.042	-0.096	4.294	24.582	45	111.505	-0.167	4.090	25.015
22	56.191	0.263	4.721	153.036	46	126.925	0.040	3.987	188.721
23	64.993	-0.132	5.668	39.078	47	146.455	-0.112	1.977	66.795
24	67.004	-0.134	5.578	38.809					

Table C.2: Modal parameters, ω_n and $\boldsymbol{\phi}_n$, extracted from the preliminary FEMs.

	Spar			**Torque box**			**XB-2 Wing**	
Mode	**1st**	**2nd**	**3rd**	**1st**	**2nd**	**3rd**	**1st**	**3rd**
ω_n	5.447	30.597	88.757	5.397	31.425	86.344	3.539	17.774
$\boldsymbol{\phi}_n$(1R)	0.0793	-0.329	0.545	0.099	-0.366	-0.498	0.080	-0.289
$\boldsymbol{\phi}_n$(1L)	0.079	-0.329	0.545	0.099	-0.366	-0.484	0.080	-0.286
$\boldsymbol{\phi}_n$(2R)	0.218	-0.623	0.470	0.247	-0.614	-0.259	0.215	-0.536
$\boldsymbol{\phi}_n$(2L)	0.218	-0.623	0.470	0.247	-0.614	-0.243	0.215	-0.534
$\boldsymbol{\phi}_n$(3R)	0.540	-0.396	-0.644	0.562	-0.329	0.634	0.532	-0.328
$\boldsymbol{\phi}_n$(3L)	0.540	-0.396	-0.644	0.562	-0.329	0.653	0.532	-0.326
$\boldsymbol{\phi}_n$(4R)	1	1	1	1	1	-1	1	1
$\boldsymbol{\phi}_n$(4L)	1	1	1	1	1	-0.983	1	1

Table C.3: Modal parameters, ω_n and $\boldsymbol{\phi}_n$, extracted from the FEMs with the bottom-up approach.

	Spar			**Torque box**			**XB-2 Wing**	
Mode	**1st**	**2nd**	**3rd**	**1st**	**2nd**	**3rd**	**1st**	**3rd**
ω_n	4.855	26.864	80.624	5.658	32.663	82.992	3.187	17.448
$\boldsymbol{\phi}_n$(1R)	0.096	-0.346	0.5666	0.093	-0.360	-0.422	0.092	-0.312
$\boldsymbol{\phi}_n$(1L)	0.096	-0.346	0.566	0.093	-0.360	-0.422	0.092	-0.309
$\boldsymbol{\phi}_n$(2R)	0.248	-0.555	0.211	0.239	-0.620	-0.194	0.238	-0.524
$\boldsymbol{\phi}_n$(2L)	0.248	-0.555	0.211	0.239	-0.620	-0.194	0.238	-0.521
$\boldsymbol{\phi}_n$(3R)	0.569	-0.184	-0.620	0.556	-0.358	0.629	0.555	-0.265
$\boldsymbol{\phi}_n$(3L)	0.569	-0.184	-0.620	0.556	-0.358	0.629	0.555	-0.263
$\boldsymbol{\phi}_n$(4R)	1	1	1	1	1	-1	1	0.999
$\boldsymbol{\phi}_n$(4L)	1	1	1	1	1	-1	1	1

Table C.4: Modal parameters, ω_n and $\boldsymbol{\phi}_n$, extracted from the FEMs with the top-down approach.

	Spar			**Torque box**			**XB-2 Wing**	
Mode	**1st**	**2nd**	**3rd**	**1st**	**2nd**	**3rd**	**1st**	**3rd**
ω_n	5.062	31.775	95.269	5.354	31.092	68.926	3.187	17.447
$\boldsymbol{\phi}_n$(1R)	0.096	-0.387	0.632	0.096	-0.373	-0.178	0.096	-0.311
$\boldsymbol{\phi}_n$(1L)	0.096	-0.387	0.632	0.096	-0.373	-0.178	0.095	-0.305
$\boldsymbol{\phi}_n$(2R)	0.247	-0.653	0.407	0.246	-0.623	0.189	0.244	-0.496
$\boldsymbol{\phi}_n$(2L)	0.247	-0.653	0.407	0.246	-0.623	0.189	0.244	-0.491
$\boldsymbol{\phi}_n$(3R)	0.566	-0.332	-0.658	0.564	-0.307	0.647	0.562	-0.184
$\boldsymbol{\phi}_n$(3L)	0.566	-0.332	-0.658	0.564	-0.307	0.647	0.562	-0.180
$\boldsymbol{\phi}_n$(4R)	1	1	1	1	1	-1	1	0.998
$\boldsymbol{\phi}_n$(4L)	1	1	1	1	1	-1	1	1

Table C.5: Optimisation parameters results for phase 1 (bottom-up) and phase 2 (top-down) FEMU.

	Parameters	
	Phase 1	Phase 2
x_1	0.629	0.678
x_2	1.370	1.337
x_3	0.834	0.974
x_4	0.683	1.007
x_5	1.190	1.056
x_6	1.400	0.919
x_7	0.798	0.605
x_8	1.400	1.400
x_9	0.601	1.147
x_{10}	0.753	0.670
x_{11}	1.373	0.674
x_{12}	1.400	1.400
x_{13}	0.863	0.600
x_{14}	0.694	1.400
x_{15}	1.065	1.167

Appendix D

A Kriging Approach to Model Updating for Damage Detection[1]

Abstract

For complex or large structures, the model updating process can be long and tedious and numerical methods can be computationally expensive. Hence, practitioners and researchers often resort to meta-modelling techniques when large problems are met. Even so, traditional methodologies, such as the Efficient Global Optimisation, can be slow and give sub-optimal results. This work proposes a new methodology for the model updating of numerical systems based on a novel Kriging approach for the scope of damage detection and quantification. The framework proposed is based on a global-local optimisation strategy recently developed by the authors, the refined Efficient Global Optimisation, herein used to tweak finite element models' parameters to match the modal data extracted from a numerical system by using the residuals of the modified total modal assurance

[1]This Appendix chapter is an adapted version of the preprint of the following work: Dessena, G., Ignatyev, D.I., Whidborne, J.F., Zanotti Fragonara, L. (2023). A Kriging Approach to Model Updating for Damage Detection. In: Rizzo, P., Milazzo, A. (eds) European Workshop on Structural Health Monitoring. EWSHM 2022. Lecture Notes in Civil Engineering, vol 254. Springer, Cham reproduced with permission of Springer Nature. The final authenticated version is available online at: http://dx.doi.org/10.1007/978-3-031-07258-1_26

criterion. The main advantage to existing direct optimisation and meta-modelling frameworks is the more efficient use of computational effort for higher dimensional problems, which is verified with the use of a numerical system.

D.1 Introduction

Damage is considered a change in a system, or structure, which compromises or influences its operational capability [1] and as such is a key driver, being strictly related to reliability and safety [2], in engineering design and operations. Hence, a plethora of methods for damage detection, commonly referred as structural health monitoring (SHM), have been proposed and implemented [3]. Nevertheless, the most prominent techniques are vibration-based approaches [4], which can be direct such as, [5, 6], or *indirect*, such as [7, 8]. The latter approach, known as model-based SHM, is the focus of this work, which ultimate goal is to present a new method based on an enhanced surrogate modelling technique developed by the authors, the refined Efficient Global Optimisation (rEGO). For this aim, a numerical 9-DoF mass-spring-damper system is generated with four damage scenarios. The task for the new method is to tune, or update, a finite element model (FEM) of the undamaged scenario to a damaged scenario and by matching the modal response, intended as natural frequencies and mode shapes, using the residuals of the modified total modal assurance criterion (MTMAC) [9], to localise and quantify the damage.

The remainder of this section is focused on the background related to FEM updating, surrogate modelling, and their combined implementation. On the other hand, the remainder of this work is structured as follows. Appendix D.2 introduces rEGO, the FEM updating workflow, the numerical system, and the damage detection capabilities, while Appendix D.3 shows the obtained results, discusses its merits and delivers the closing remarks by introducing the future opportunities

for this technique.

D.1.1 Background

FEM updating is defined as the mathematical process by which a baseline FEM of the previously undamaged structure is tuned to achieve a good agreement with the damaged structure [10]. According to [11, 12], model updating can be split in two categories: direct and indirect. Direct techniques, such as matrix update, optimal matrix, and eigenstructure assignment, use modal characteristics to update the FEM and are regarded as efficient and accurate methods; however, the requirement for precise measurements, the sensitivity to noise, the impossibility of using truncated data and the possibility of losing symmetry in the FEM matrix do not make them suitable candidates for damage detection applications via FEM updating. On the other hand, indirect, or iterative, methods can overcome the aforementioned problems [13]. Iterative methods can be divided in four main categories [13]: (i) sensitivity-based, (ii) computational intelligence-based, (iii) response surface method (RSM), and (iv) Bayesian or Monte-Carlo approaches. Only RSM methods for are discussed beyond this point as they are the focus of this work. Nevertheless, the interested reader is referred to [10] for a more profound review of the remaining approaches.

In damage detection, RSMs are used to achieve an approximation of the structural response to a given objective function [14]; generally, the objective functions target modal data or time or frequency response. RSMs are widely used in many fields of engineering and, most notably, in computational design, as their approximations can be used successfully for the research of an optimal design [15]. A general RSM procedure is defined:

1. The design of experiment (DoE) is drawn to collect a number of samples from the goal function with strategic sampling;

2. The chosen RSM is fitted to the data obtained through the DoE and a predictor is established

3. The RSM can be updated with new results strategically, such as computing the actual value of the expected minimum.

4. Iterating between points 2 and 3 until convergence is reached

It goes without saying that a minimal implementation could stop after point 2, but usually such minimal implementation does not meet the set standards. While it is not the purpose of this work to give a thorough review on meta-modelling, or RSM, the interested reader is referred to [16] for a complete scrutiny on the subject with a focus on Gaussian processes, also the core of this work. Within the realm of meta-modelling, Gaussian processes have received great attention in the two decades or so [14, 16, 17]; however, one of the most used techniques, Kriging, originated outside engineering, in geostatistics, in the 1950s [18]. As a stochastic-based meta-modelling technique, it is based on the relationship between the sample data (input) $\boldsymbol{X}$ and the observed response (output) $\boldsymbol{Y}$. For the sake of brevity, the full mathematical background on Kriging is not presented here, but the interested reader can consult [16, 17] for a more comprehensive review.

Returning to the RSM procedure, after outlining the concept of Kriging, the second point of the list is clear. However, points 1, 3, and 4 are still to be explored. The DoE is usually carried out by selecting strategically a number of points equal to ten times the number of variables [15]. One of the most efficient strategies[16] is the Morris–Mitchell optimal latin hypercube (LH) [19, 20], which ensures uniform spreading of the sample points and is used throughout this work. The reader interested in a more broad review of sampling strategies is directed to [21]. The Efficient Global Optimization (EGO) [17] is the cornerstone of the meta-modelling via Kriging. Particularly, [17] introduced a new quantity, the Expected Improvement (EI), to aid the updating of the RSM generated with Kriging.

Simply speaking, the EI is the measure of how much the minimum of a function can be improved if a point at a given location is searched. In fact, the maximum absolute value of EI, along the function, is used to identify the infill point for the Kriging model. For the mathematical formulation of the EI reference is made to [16, 17]. The EI is treated in this work as the informing parameter for updating the RSM model. While EGO was a pioneering strategy when released, the aforementioned classical structure was followed. The main drawback of EGO is its global only optimisation capability, which does not allow for the full convergence of the optimisation process, resulting in sub-optimal results. The authors propose to solve this constraint with a modified EGO [22], which offers a global-local search capability, allowing its application to damage detection. The modified EGO, or refined Efficient Global Optimisation (rEGO), is introduced in Appendix D.2.

D.2 Methods

In this Section the rEGO workflow is introduced alongside its implementation for damage detection and, finally, the numerical system and the computational experiment setup are described.

D.2.1 The refined Efficient Global Optimisation

In order to enhance the capability of EGO to a global-local optimisation technique, rEGO introduces a refinement and selection technique. The refinement technique deals with an active reduction of the search domain, which is halved each time the main stopping criterion (ε_1), linked to EI, is achieved and the number of sample points is more that ten times the variables. The selection, inspired by multi-objective optimisation [15] and the Pareto fronts dominance [23], is chained to the refinement and promotes the selection of single points from clusters within the new refined search space. This retains only dominant points, keeps the number

of sample points down and, hence, maintains the search to be computationally efficient.

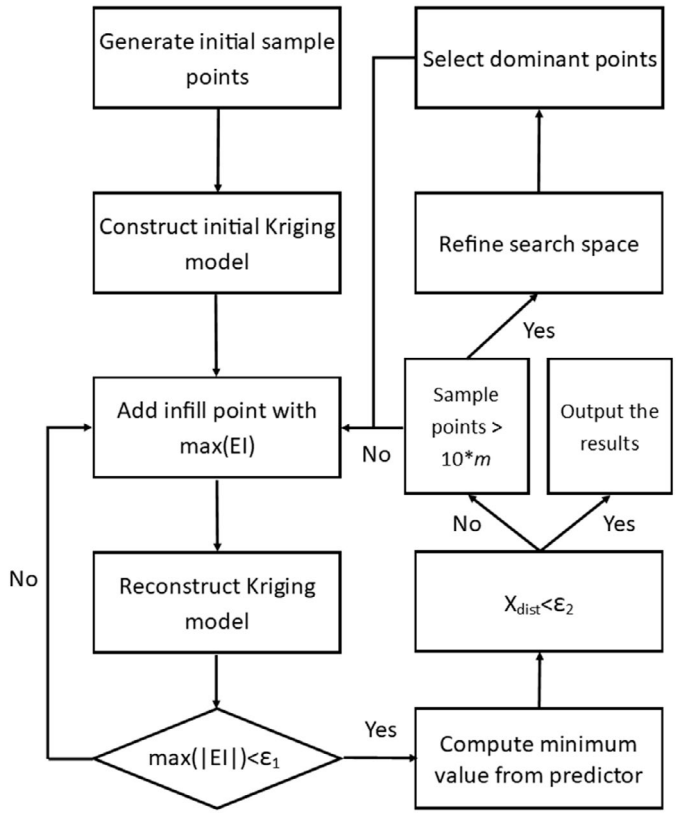

Figure D.1: rEGO workflow. m stands for the number of variables.(retrieved from [22])

The workflow in Figure D.1 outlines the general working principles of rEGO. The left column of the workflow represents a typical EGO algorithm, while the right column highlights the aforementioned improvements implemented by the authors. The second stopping criterion, ε_2, is a measure of local convergence, as it is based on the Euclidean distance between the variables of proposed minima (x_{dist}), in an hill climbing fashion. If the ε_2 condition is satisfied the algorithm terminates; otherwise, the number of sample points is taken under consideration and if its number is ten times the number of variables the search space is refined. Ensuring a set number of points within the search space is pivotal to guarantee the exploration of the search space. In fact, while [17] states that obtaining at least $\max(|(EI)|) < 1\%$ is a sign of good exploration, sometimes issues might arise with

a low number of samples. Hence, drawing from the experience of sampling [16], the minimum size requirement for the data pool was established to be ten times the number of variables. The two requirements, EI and data pool size, ensure a good exploration of the design space and the viability of the refinement and selection technique.

D.2.2 Damage Detection via Model Updating

Having outlined the principles behind rEGO, the model updating and, so, the damage detection routine are described. As a model-based technique a baseline, or undamaged, FEM is generated and then the data obtained from damage scenarios are used to update the model and identify the changes in parameters which identify the damage. Modal data, natural frequencies (ω_n) and mode shapes($\boldsymbol{\phi}_n$), are taken into consideration within this work as the MTMAC residual is used. The MTMAC residuals is presented below.

$$\text{MTMAC}_{\text{res}} = 1 - \prod_{i=1}^{n} \frac{\text{MAC}(\boldsymbol{\phi}_i^E, \boldsymbol{\phi}_i^N)}{\left(1 + \frac{|\omega_i^N - \omega_i^E|}{|\omega_i^N + \omega_i^E|}\right)} \tag{D.1}$$

MAC, stands for the usual modal assurance criterion [24], n is the total number of modes under consideration, superscript E denotes for experimental results and superscript N for numerical. For the purpose of this work, N stands for the updated model and E for the damaged data. The $\text{MTMAC}_{\text{res}}$ can return results only between 0 and 1, with 0 being the value that represents full agreement. The task of the rEGO is to tune the parameters of a given model to minimise the $\text{MTMAC}_{\text{res}}$ response and extract the damage extend and location.

The system selected for the numerical verification of rEGO as a damage detection technique is the 9 DoF mass-spring-damper system shown in Figure D.2. In the undamaged system, all masses (m_{1-9}) are set to 1 kg and the springs' stiff-

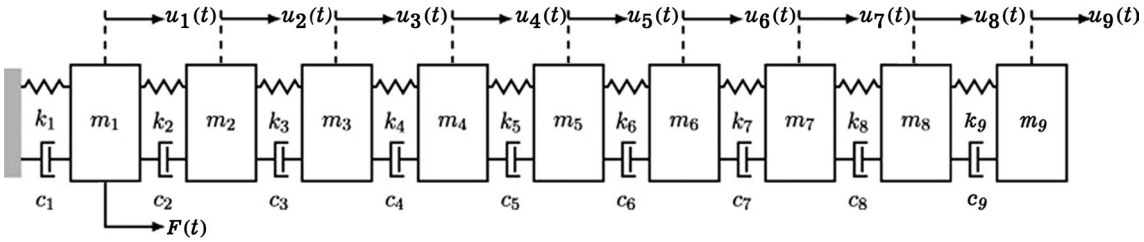

Figure D.2: 9 DoF mass-spring damper system.(retrieved from [5])

ness is $k_{1-9} = 10$ kNm^{-1}. The damping is defined as the damping ratio (ζ_n) and it is set to 1%. Changes in damping are not considered within this study and the given value stays constant for all scenarios. The modal parameters are extracted through eigenanalysis and ζ_n is used for adjusting the values of ω_n of the damped system. The mass and stiffness matrices are built according to usual practice for such systems.

This work considers 4 damage scenarios, listed in Table D.1. For all the damaged cases only the stiffness properties, as the scope of this work is solely damage detection, are tuned by the ratio of the optimisation variables ($\boldsymbol{x}$) to the baseline stiffness values, e.g. for a 10% damage at the second element k_2 is given by $x_2 \times k_2$, where x_2 should be 0.9 at convergence. The optimisation search bounds are set between $[0.7, 1]$ and 9 variables are searched to match the modal response. The MTMAC takes into considerations only ω_n and $\boldsymbol{\phi}_n$, so it is ben-

Table D.1: Damage scenarios of the 9 DoF system.

Scenario #	Damage
1	Undamaged
2	10% stiffness reduction in the fourth element.
3	25% stiffness reduction in the fourth element.
4	25% stiffness reduction in the fourth element and 10% stiffness reduction in the seventh element.
5	25% stiffness reduction in the second element, 10% stiffness reduction in the fourth element and 10% stiffness reduction in the seventh element.

eficial to report in Table D.2 the computed ω_n and in Figure D.3 the $\boldsymbol{\phi}_n$. From Table D.2 and Figure D.3 the difference induced by damage are quite evident.

These changes are detected via rEGO and, for comparison purposes, with genetic algorithm (GA) and EGO. The rEGO stopping criteria were: $\varepsilon_1 = 0.1\%$ (to ensure further exploration of the design space) and $\varepsilon_2 = 10^{-4}$. The same value of ε_1 is also selected as the EGO stopping criterion, while for the GA a function tolerance of 10^{-4} and a maximum generation number of 100 are selected. The other properties of the GA are unchanged from the standard function ga offered in MATLAB. GAs are not discussed in depth in this work as they are a well established method and are only used for benchmarking purposes. For all methods a Morris–Mitchell optimal LH with a number of samples ten times the number of variables is selected to define the starting population. Each optimisation run, on each scenario, for each method is run ten times for statistical significance.

Table D.2: Computed natural frequencies in Hz of 9 DoF mass-spring damper system.

	Natural Frequencies [Hz]				
Scenario #	**1**	**2**	**3**	**4**	**5**
Mode #					
1	2.629	2.349	2.371	2.686	2.422
2	7.814	7.226	7.355	7.875	7.485
3	12.786	12.179	11.980	12.656	12.196
4	17.409	17.091	16.962	17.052	16.323
5	21.558	20.957	20.945	20.986	20.399
6	25.118	24.152	23.903	24.332	23.972
7	27.993	27.416	27.306	27.250	26.260
8	30.105	29.285	28.886	29.674	28.526
9	31.395	30.788	30.760	31.274	30.898

D.3 Results and Conclusions

This section shows the results obtained for the numerical study on the 9 DoF system by comparing the results obtained for the damage detection via model updating using rEGO, EGO and GA. Particular attention is paid to the detection of stiffness changes and to the number of function evaluations needed to reach a

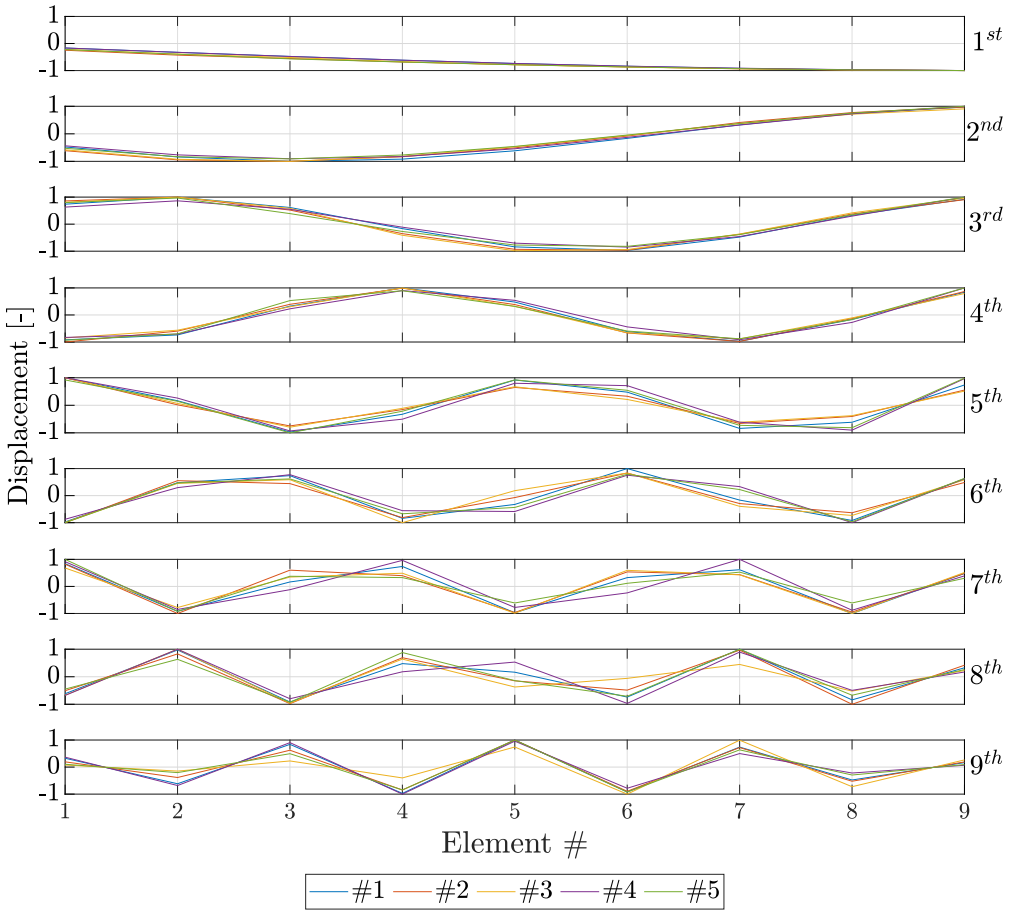

Figure D.3: 9 DoF mass-spring damper system mode shapes for all scenarios. The legend refers to the scenario # and the label at the right of the plot to the mode.

solution by each routine.

The results of the damage detection routine are presented in Figure D.4 as bar plots, identified as the mean (μ) parameter $\boldsymbol{x}$ change, identified as damage, over ten iterations for the rEGO, EGO , and GA implementation. Only the μ values are reported for conciseness and clarity. Table D.3 presents the function evaluations to convergence for each scenario. The values are presented taking into consideration the minimum and maximum evaluations needed and the μ over the ten iterations. Notably, GAs' maxima are the same for all scenarios, meaning that the hard limit for maximum generations was met in at least one realisation for the given scenarios.

From Figure D.4 it is clear that rEGO has an advantage over EGO for dam-

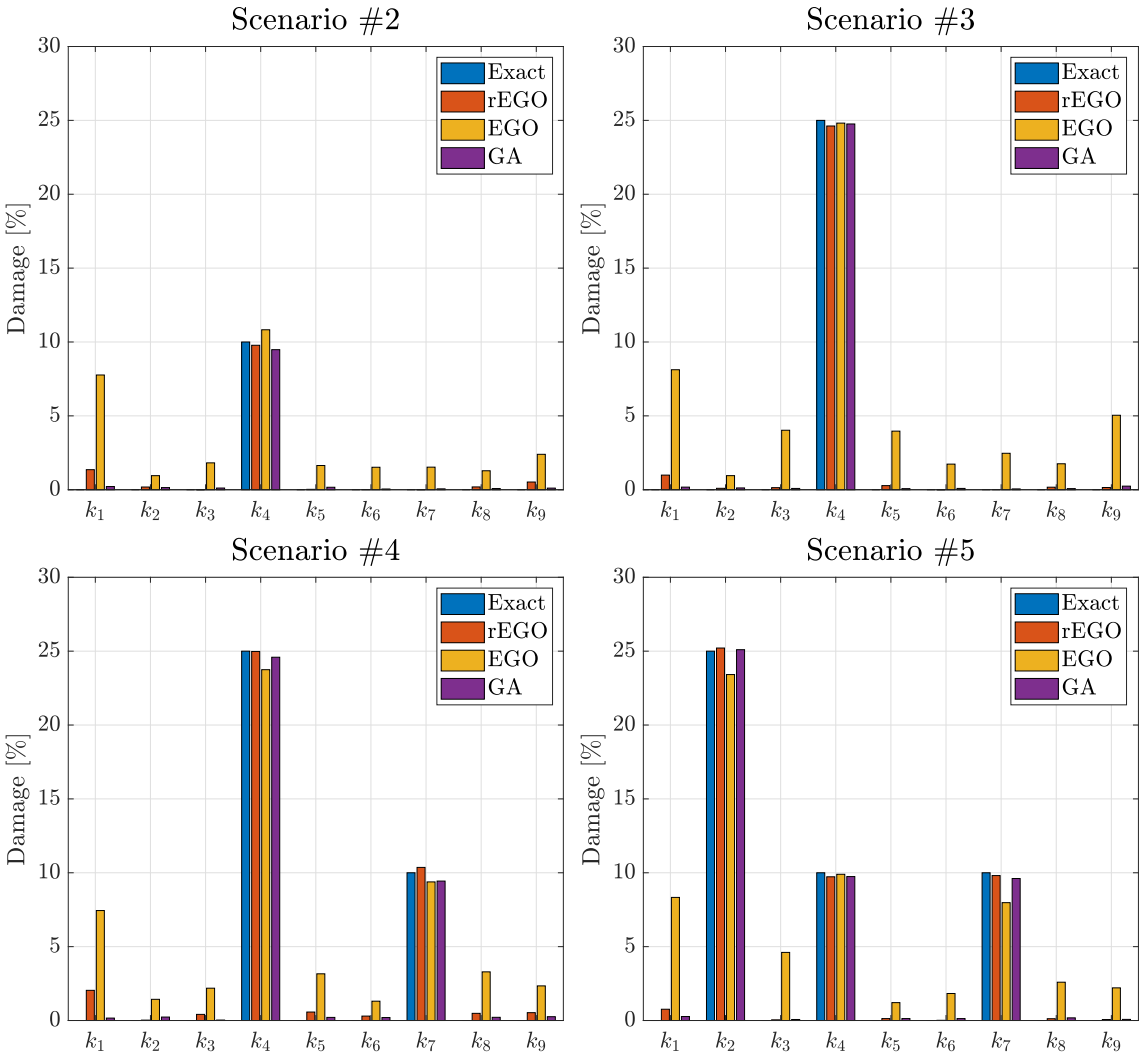

Figure D.4: The mean values, over 10 iterations, of the identified damage by rEGO, EGO, and GA vs the exact value.

Table D.3: Number of function evaluations for convergence.

Scenario	**#2**			**#3**			**#4**			**#5**		
	min	μ	max	min	μ	max	min	μ	max	min	μ	max
rEGO	159	281	382	172	286	494	274	329	391	217	331	433
EGO	104	115	131	100	111	130	103	112	129	100	106	119
GA	15600	17899	19210	15410	17424	19210	15030	16778	19210	13700	16778	19210

age detection. For all instances the damage estimated via rEGO is closer to the exact value than the one calculated via EGO. Also rEGO, detects damage as as well as GA; however, rEGO had the tendency to detect a slight, even imperceptible, damage where there was none. This is most evident in the first element of scenarios #2 and #4. Even EGO has this issue, but it is more evident and happens for all cases. Generally the GA is better at detecting undamaged locations,

but at the price of a many more evaluations. As shown in Table D.3, the evaluations for the GA driven search are of two order of magnitude higher than rEGO and EGO. EGO, unsurprisingly, reaches convergence with the fewest evaluations, while rEGO is able to do so with two or three times the evaluations, depending on the scenario, but, as said above, with much more success than EGO.

Concluding, rEGO proved to be a clear enhancement over EGO and an excellent compromise over the computationally expensive GA for model-based damage detection. The future plan is to implement it on existing benchmarks and experimental data to further validate its credibility for the employment in the monitoring of real structures. rEGO itself can also be used in any other domain which requires a RSM, such as computational engineering design.

References

[1] C. R. Farrar, S. W. Doebling, and D. A. Nix, "Vibration–based structural damage identification," *Philosophical Transactions of the Royal Society of London. Series A: Mathematical, Physical and Engineering Sciences*, vol. 359, no. 1778, N. A. J. Lieven and D. J. Ewins, Eds., pp. 131–149, 2001, ISSN: 1364-503X, DOI: 10.1098/rsta.2000.0717 (cit. on p. 273).

[2] C. S. Wang, F. Wu, and F.-K. Chang, "Structural health monitoring from fiber-reinforced composites to steel-reinforced concrete," *Smart Materials and Structures*, vol. 10, no. 3, pp. 548–552, 2001, ISSN: 0964-1726, DOI: 10.1088/0964-1726/10/3/318 (cit. on p. 273).

[3] P. Cawley, "Structural health monitoring: Closing the gap between research and industrial deployment," *Structural Health Monitoring*, vol. 17, no. 5, pp. 1225–1244, 2018, ISSN: 1475-9217, DOI: 10.1177/1475921717750047 (cit. on p. 273).

[4] A. Rytter, "Vibrational based inspection of civil engineering structures," Ph.D. dissertation, Aalborg University, 1993 (cit. on p. 273).

[5] G. Dessena, M. Civera, L. Zanotti Fragonara, D. I. Ignatyev, and J. F. Whidborne, "A Loewner-based system identification and structural health monitoring approach for mechanical systems," *Structural Control and Health Monitoring [Accepted]*, p. 17, 2023 (cit. on pp. 273, 279).

[6] M. Civera, G. Calamai, and L. Zanotti Fragonara, "System identification via Fast Relaxed Vector Fitting for the Structural Health Monitoring of masonry bridges," *Structures*, vol. 30, no. January, pp. 277–293, 2021, ISSN: 23520124, DOI: 10.1016/j.istruc.2020.12.073 (cit. on p. 273).

[7] F. Shadan, F. Khoshnoudian, and A. Esfandiari, "A frequency response-based structural damage identification using model updating method," *Structural Control and Health Monitoring*, vol. 23, no. 2, pp. 286–302, 2016, ISSN: 15452255, DOI: 10.1002/stc.1768 (cit. on p. 273).

[8] X. Yang, X. Guo, H. Ouyang, and D. Li, "A Kriging model based finite element model updating method for damage detection," *Applied Sciences*, vol. 7, no. 10, p. 1039, 2017, ISSN: 2076-3417, DOI: 10.3390/app7101039 (cit. on p. 273).

[9] R. Perera and R. Torres, "Structural damage detection via modal data with genetic algorithms," *Journal of Structural Engineering*, vol. 132, no. 9, pp. 1491–1501, 2006, ISSN: 0733-9445, DOI: 10.1061/(ASCE)0733-9445(2006)132:9(1491) (cit. on p. 273).

[10] T. Marwala, *Finite-element-model Updating Using Computional Intelligence Techniques*. London: Springer London, 2010, ISBN: 978-1-84996-322-0, DOI: 10.1007/978-1-84996-323-7 (cit. on p. 274).

[11] M. I. Friswell and J. E. Mottershead, *Finite Element Model Updating in Structural Dynamics* (Solid Mechanics and its Applications). Dordrecht:

Springer Netherlands, 1995, vol. 38, ISBN: 978-90-481-4535-5, DOI: 10.1007/978-94-015-8508-8 (cit. on p. 274).

[12] J. Mottershead and M. Friswell, "Model updating in structural dynamics: A survey," *Journal of Sound and Vibration*, vol. 167, no. 2, pp. 347–375, 1993, ISSN: 0022460X, DOI: 10.1006/jsvi.1993.1340 (cit. on p. 274).

[13] N. F. Alkayem, M. Cao, Y. Zhang, M. Bayat, and Z. Su, "Structural damage detection using finite element model updating with evolutionary algorithms: a survey," *Neural Computing and Applications*, vol. 30, no. 2, pp. 389–411, 2018, ISSN: 0941-0643, DOI: 10.1007/s00521-017-3284-1 (cit. on p. 274).

[14] W.-X. Ren and H.-B. Chen, "Finite element model updating in structural dynamics by using the response surface method," *Engineering Structures*, vol. 32, no. 8, pp. 2455–2465, 2010, ISSN: 01410296, DOI: 10.1016/j.engstruct.2010.04.019 (cit. on pp. 274, 275).

[15] I. Voutchkov and A. Keane, "Multi-Objective Optimization Using Surrogates," in *Computational Intelligence in Optimization*, Y. Tenne and C.-K. Goh, Eds., Berlin: Springer, 2010, ch. 7, pp. 155–175, DOI: 10.1007/978-3-642-12775-5_7 (cit. on pp. 274–276).

[16] A. I. J. Forrester, A. Sóbester, and A. J. Keane, *Engineering Design via Surrogate Modelling*. Wiley, 2008, ISBN: 9780470060681, DOI: 10.1002/9780470770801 (cit. on pp. 275, 276, 278).

[17] D. R. Jones, M. Schonlau, and W. J. Welch, "Efficient global optimization of expensive black-box functions," *Journal of Global Optimization*, vol. 13, pp. 455–492, 1998, DOI: 10.1023/A:1008306431147 (cit. on pp. 275–277).

[18] D. G. Krige, "A statistical approach to some basic mine valuation problems on the Witwatersrand," *Journal of the Chemical, Metallurgical and Mining Society of South Africa*, vol. 52, no. 6, pp. 119–139, 1951 (cit. on p. 275).

[19] M. D. McKay, R. J. Beckman, and W. J. Conover, "A comparison of three methods for selecting values of input variables in the analysis of output from a computer code," *Technometrics*, vol. 21, no. 2, p. 239, 1979, ISSN: 00401706, DOI: 10.2307/1268522 (cit. on p. 275).

[20] M. D. Morris and T. J. Mitchell, "Exploratory designs for computational experiments," *Journal of Statistical Planning and Inference*, vol. 43, no. 3, pp. 381–402, 1995, ISSN: 03783758, DOI: 10.1016/0378-3758(94)00035-T (cit. on p. 275).

[21] A. Lye, A. Cicirello, and E. Patelli, "Sampling methods for solving Bayesian model updating problems: A tutorial," *Mechanical Systems and Signal Processing*, vol. 159, p. 107 760, 2021, ISSN: 08883270, DOI: 10.1016/j.ymssp.2021.107760 (cit. on p. 275).

[22] G. Dessena, D. I. Ignatyev, J. F. Whidborne, and L. Zanotti Fragonara, "A global-local meta-modelling technique for model updating," *[Submitted to] Computer Methods in Applied Mechanics and Engineering*, 2023 (cit. on pp. 276, 277).

[23] K. Deb, A. Pratap, S. Agarwal, and T. Meyarivan, "A fast and elitist multiobjective genetic algorithm: NSGA-II," *IEEE Transactions on Evolutionary Computation*, vol. 6, no. 2, pp. 182–197, 2002, ISSN: 1089778X, DOI: 10.1109/4235.996017 (cit. on p. 276).

[24] D. L. Brown, R. J. Allemang, R. Zimmerman, and M. Mergeay, "Parameter estimation techniques for modal analysis," in *1979 Automotive Engineering Congress and Exposition*, Univ.of Cincinnati, 1979, p. 19, DOI: 10.4271/790221 (cit. on p. 278).

Appendix E

Ground Vibration Testing of a High Aspect Ratio wing with Revolving Clamp[1]

Abstract

The advancements in the aeronautical industry and research on materials and manufacturing methods in the last 70 years have been shifting the paradigm of wing design to high aspect ratio flexible wings. These wings can show a varying behaviour in different operating conditions, as per the nature of their geometry and materials. This work proposes a case study of a high aspect ratio flexible wing in order to study the effect of operating conditions on its structural properties. To test different operating conditions on the ground, a revolving clamp is designed to attach the specimen to a clamp-on shaker. A clear relationship between the wing's modal properties, and so structural properties, and the angle the clamp

[1]This Appendix chapter is an adapted version of the following Conference Proceeding: Dessena, G., Ignatyev, D.I., Whidborne, J.F., Pontillo, A., Zanotti Fragonara, L. (2022). *In:* 33rd Congress of the International Council of the Aeronautical Sciences (ICAS) – Stockholm, 4–9 September 2022. The final authenticated version is available online at: http://www.doi.org/10.17862/cranfield.rd.20486229

sets is found.

E.1 Introduction

During flight operations an aircraft is subject to multiple external factors, from loads to environmental conditions. Estimating the complete behaviour of a flexible high aspect ratio (HAR) wing in such environment is not a trivial task and involves careful modelling and testing to ensure compliance with regulations. This work aims to discover the relationship between the change in environmental conditions and structural properties by modal analysis, in particular by detecting the induced change on the modal parameters. For this, a revolving clamp for a clamp-on shaker was designed, the clamp allows to change the setting angle (α_{gvt}) of a HAR wing while on the shaker and to run ground vibration testing (GVT) of the wing at different α_{gvt}s. In this sense, the change in the α_{gvt} of the clamp is meant to simulate, on the ground, the wing's deflection by inducing different deformations on the specimen thanks to the altered influence of gravity. The specimen used in this testing campaign is a wing from Cranfield University's Beam Reduction and Dynamic Scaling (BeaRDS) project [1–4], which is a HAR flexible wing, made of aluminium, stainless steel, and 3D printed plastics, developed as a dynamically scaled model of a narrow body civil jet airliner and known as eXperimental BeaRDS 2 (XB-2). Within this work, only the vertical and torsional displacements are considered and, particularly, the first three modes' modal parameters, where vertical displacement is dominant, are extracted.

The experimental setup and its results are the focus of this work, which also includes some reference to the future use of the generated data.

The increasing awareness for the need of a greener aviation and the promise of lighter and more efficient structures is pushing a new paradigm in wing design: flexible HAR wings. Not only is this revolution focusing on the design, but, as a

process that started more than 70 years ago, also on materials. In fact, new ultra-light and customisable composite materials are the enabling technology [5] of the modern configurations. However, all these ingredients create a reduction in stiffness and modal frequencies of the structure, causing a decrease in aeroelastic phenomena onset speeds, which if overlooked, can create several, even catastrophic [6], problems. Nevertheless, the designers have two main instruments in their hands to prevent these occurrences: GVT and finite element modelling (FEM). The former is the main focus of this work.

In aeronautics, the term GVT replaces the term Experimental Modal Analysis and the most common targets of GVT are the whole craft [7], wings [8] and helicopter blades [9]. The main purposes of GVT in aeronautics is to update, or validate, the specimen's finite element model (FEM) [10, 11], which in turn can be used to characterise the aeroelastic onset speeds [7]. These objectives are usually obtained by extracting the modal parameters, namely natural frequencies (ω_n), damping ratios (ζ_n), and mode shapes ($\boldsymbol{\phi}_n$), from the experimental data [7, 12, 13]. However, for flexible wings, sometimes, more involved testing techniques have to be employed in order to characterise some particular response of the wing, such as damping [14] or non-linearities [15]. Nevertheless, a band-limited random verification is sufficient to achieve the goal of this work [16]. The mean for extracting modal parameters are system identification (SI) techniques [17] which create a model from the measured data, which can be in two domains: time and frequency. Depending on the domain, some SI methods are preferred over other, such as numerical algorithms for subspace state space system identification in time domain and least-squares complex exponential, or rational fractional polynomial, in the frequency domain. For the purpose of this work a frequency domain technique, the Loewner Framework (LF), recently introduced by some of the authors for mechanical systems [18–20] is the method of choice.

The remainder of this work is structured as follows. In Section 2, the specimen,

the clamp, and the experimental setup are discussed in detail and in Section 3 The results are outlined and, finally, in Section 4 the conclusions and future works are presented.

E.2 Methods

In this section the specimen tested, the XB-2 wing, and its motivation are introduced. In addition, the revolving clamp design and mechanism are explained prior to describing the experimental setup and the data collection and processing procedure.

E.2.1 Beam Reduction and Dynamic Scaling High Aspect Ratio Wing

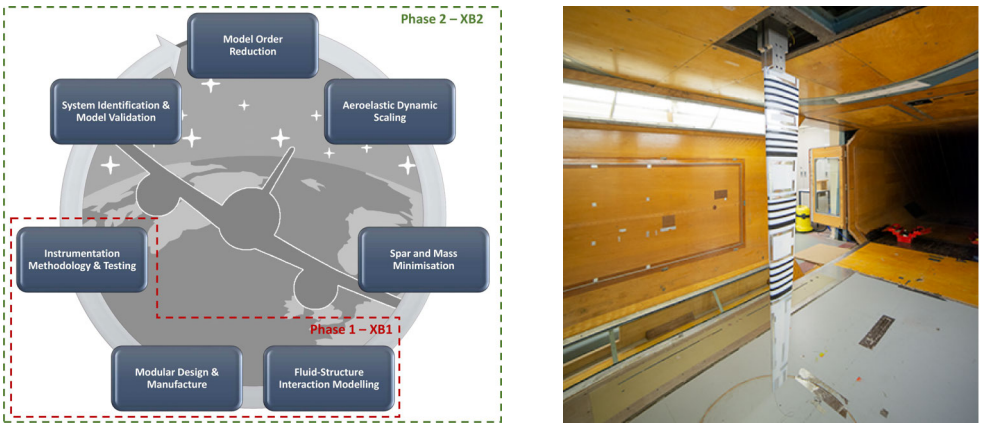

(a) (b)

Figure E.1: BeaRDS work flow (retrieved from [1]) and XB-2 in the 8'x6' Cranfield University wind tunnel (retrieved from [4]).

The BeaRDS framework, Figure E.1a, was a project from Cranfield University which aimed to create a work flow for the design, testing and modelling of flexible wings based on dynamically scaled prototypes. For the scope of validating the framework, the XB-2 HAR wing was designed and manufactured to be tested in the Cranfield University's 8'x6' wind tunnel. The wing has 4 main parts: the main

spar, the stiffening tube, the added masses and skin. Since the only purpose of the masses was for the dynamic scaling of a narrow body civil airliner [2] and, so, outside the scope of this study, they were removed for this round of testing.

XB-2's spar is machined out of two 6082-T6 Aluminium blocks and the tube and the linkages are made out of stainless steel, while the skin is made of strips of 3D printed Digital-ABS [21] and Agilus 30 [22], a rubber-like material. In the skin, the Agilus 30 black strips, in Figure E.1b, alternate the white Digital ABS sections, allowing the skin to flex considerably and retaining structural continuity. Notably the wing's skin is printed in only three sections thanks to Polyjet technology [23] that allows for the use of different materials within the same print. Table E.1 recaps the materials properties of interest.

Table E.1: Materials' properties.

Material	**Young Modulus [GPa]**	**Poisson Ratio [-]**	**Density [kgm^{-3}]**
6082-T6 Aluminium	70	0.33	2700
Stainless Steel	193	0.33	8000
Digital ABS	2.6-3.0	0.33 [24]	1170-1180
Agilus 30	NA	NA	1140

Figure E.2: The spar and tube assembly (retrieved from [8]).

The torque box of the wing is made of the spar and tube assembly, in Figure E.2, and it is responsible to carry the loads transferred from the skin. The mass of the spar and tube assembly is 1.362 kg. The spar was machined from two separate aluminium blocks, welded at mid-span and secured with a set of four I-plates bolted to the two sub-parts to ensure continuity. The spar features a Saint George's cross-like cross section, which changes proportions linearly along the span, and a rectangular cross section in the root section, which is used as a clamping point by the revolving clamp. The overall length of the spar is 1.45 m,

while the suspended span when clamped is 1.325 m.

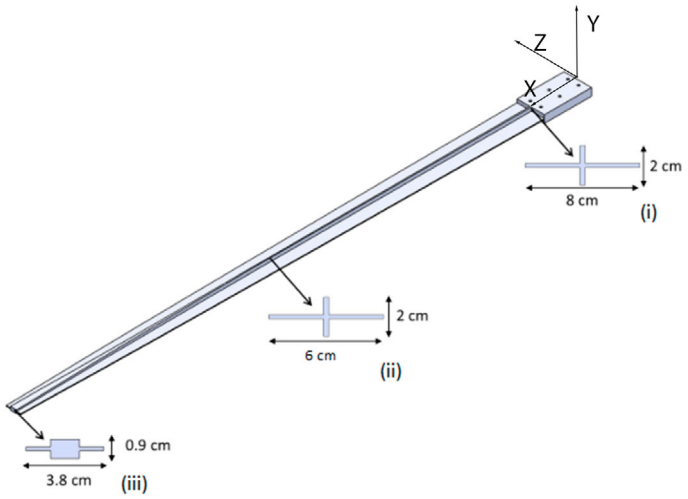

Figure E.3: Spar's CAD model with section view at the location of interest: (i) root, (ii) mid-span, and (iii) tip (adapted from [2]).

Three positions within the clamp define the cross section, (i) the root, (ii) the mid-span, and (iii) the tip, whose shapes are shown in Figure E.3. The tube, having an outer diameter of 10 mm, a thickness of 1 mm and being 550 mm long is connected to the spar at three points and is located aft of the spar and was added to improve bending and torsional stiffness. The complete wing assembly comprising spar, tube, and skin weights 3.024 kg and has a overall span of 1.5 m featuring a root chord of 236 mm and a tip chord of 83 mm with a leading edge (LE) sweep of 14.9°. The reader interested in a more profound review of BeaRDS and the specimen is referred to [1–4, 8, 20], while Table E.2 recaps XB-2's physical properties.

Table E.2: XB-2 wing properties

Property	**Details**	**Unit**
Semi span	1.5	m
Root chord	236	mm
Tip chord	83	mm
LE sweep	14.9	^{o}
Mass	3.024	kg

E.2.2 The Revolving Clamp

This work is based on the possibility of running GVT of the XB-2 wing at different α_{gvt}s. Hence, a suitable device had to be designed and the revolving clamp, in Figure E.4a, was conceived.

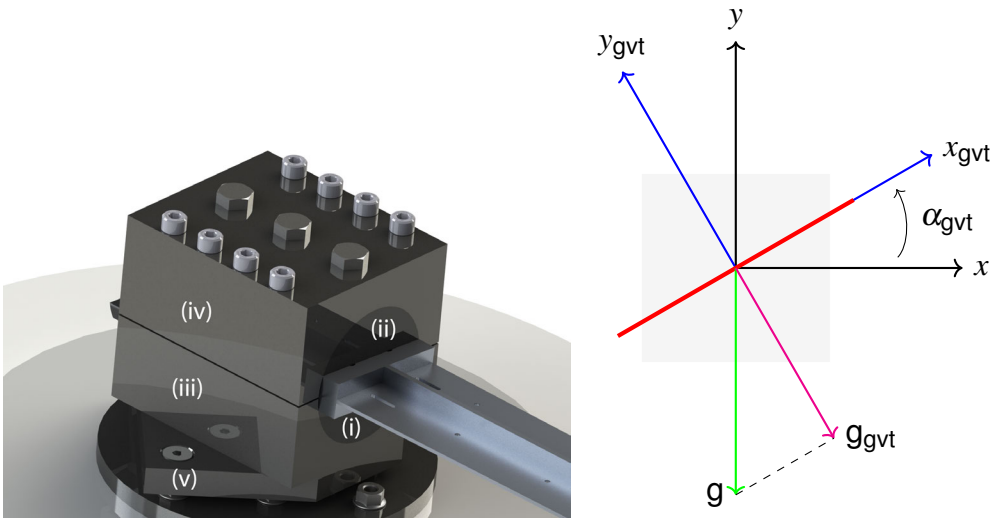

(a) (b)

Figure E.4: Figure E.4a shows the rendering of the revolving clamp mounted on the shaker with labelled parts: (i) the lower sock, (ii) the upper sock, (iii) the lower end, (iv) the upper end, and (v) the base plate. A schematic demonstrating the effect of α_{gvt} over gravity loads on the specimen is shown in Figure E.4b.

The clamp consists of five parts: (i) the lower sock, (ii) the upper sock, (iii) the lower end, (iv) the upper end, and (v) the base plate. The lower and upper sock are clamped directly to the wing's root using four M6 cap head socket bolts, then the two socks and the specimen are secured between the lower and upper end. The lower end is directly bolted to the base plate with three M8 socket countersunk bolts and serves as an adaptor for the fixings on the shaker and is secured to it with seven M8 socket countersunk bolts. The upper end clamps the specimen to the lower end clamp with 8 M8 cap head socket bolts, the four bolts at the corners are bolted to the lower end end clamp, while the four inboard to directly to the base plate. Finally, three M10 hexagonal bolts are placed in the upper clamp to further constrain the sock assembly from rotating or slipping.

The specimen α_{gvt} is adjusted by untightening the bolts on the upper end clamp and setting the specimen to the required angle by placing an inclinometer over the extruded tab of the lower sock. The clamp, excluding the base plate, was machined from a single block of aluminium and its mass, excluding the fixings, is 3.583 kg. The fixings weight is 0.606 kg, giving a total mass of 4.189 kg.

The motivation behind the revolving clamp is to change the effect of gravity on the static configuration of the wing. In fact, the effective downward, normal to the wing inclination, effect of gravity decreases. This is clearly depicted in E.4b, where the phenomenon is graphically described. The black axes are the global axis, while the blue axes are the local axis relative to the inclined wing and the red thick line identifies the wing's profile. The actual gravity vector g is the green arrow and the relative gravity on the inclined wing ($g_{\alpha_{gvt}}$) is the pink arrow. From simple trigonometry the relationship between the two is the following:

$$g_{\alpha_{gvt}} = g \times \cos(\alpha_{gvt}) \tag{E.1}$$

Summarising, the increase in the wing's inclination angle decreases g_{gvt} and so the wing's deflection from it's own weight.

E.2.3 Experimental Setup and Data Processing

The testing campaign involves the XB-2 wing at three different setting angles (α_{gvt}s): 0, 5, and 10°. The specimen is excited with a random vibration excitation at three different inputs for 20 min. However, only 18 min are considered while post-processing the data to exclude any transients.

A Data Physics® Signal Force™ modal shaker controlled by its DP760™ close-loop control software, running on a consumer grade laptop, drives the specimen. Eight accelerometers are attached to the specimen and another on the clamp's lower sock, for feedback purposes. The accelerometer at the clamp is

Table E.3: Accelerometers specifications.

ID #	AccelerometersModel	Sensitivity [mVg^{-1}]	Mass [g]
0	PCB Piezotronics® model: 356B18	995	25
1R	PCB Piezotronics® model: 356A16	96.50	7.4
1L	Isotron® accelerometer model 7251A	10.30	10.5
2R	PCB Piezotronics® model: 356A16	97.20	7.4
2L	Isotron® accelerometer model 7251A	10.08	10.5
3R	PCB Piezotronics® model: 356A45	100.20	4.2
3L	Isotron® accelerometer model 7251A	10.34	10.5
4R	Brüel & Kjær® accelerometer type 4507-002	94.12	4.8
4L	Brüel & Kjær® accelerometer type 4507-002	95.52	4.8

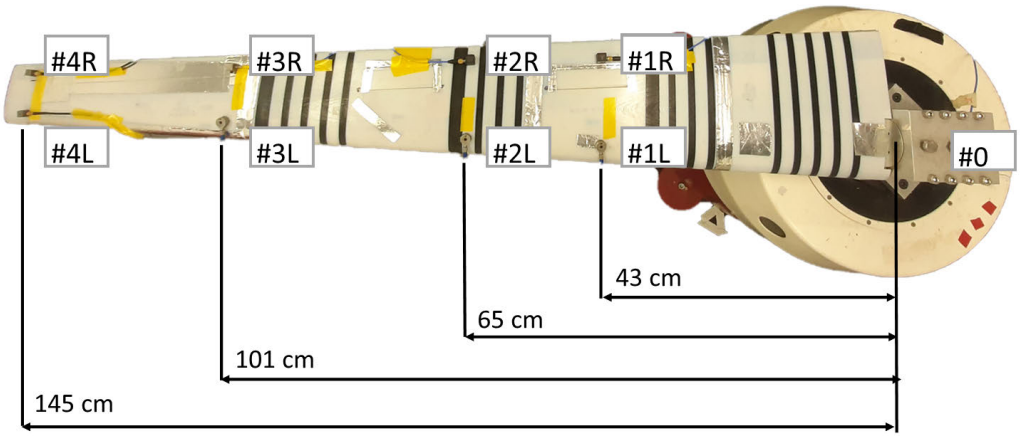

Figure E.5: Accelerometers locations (retrieved from [8]). Note that the accelerometers do not appear aligned due to the optical effect of the camera lens.

positioned in such a way to record the vertical acceleration normal to the wing inclination, this ensures that even at different amplitudes the shaker delivers the same output in the direction normal to the wing's direction. The accelerometers' span-wise locations are decided using a sensor placement routine based on a genetic algorithm[25]: a FEM model was employed as a baseline and a genetic algorithm minimised the sum of the off-diagonal terms of the Auto-Modal Assurance Criterion (Auto-MAC) by changing the sensors position along the span. The accelerometer positions are shown in Figure E.5 and their characteristics in Table E.3. The experimental setup is completed by a desktop machine that collects the data from a National Instruments cDAQ-9174, to which the accelerometers are connected, via a LabVIEW program, as shown in Figure E.6.

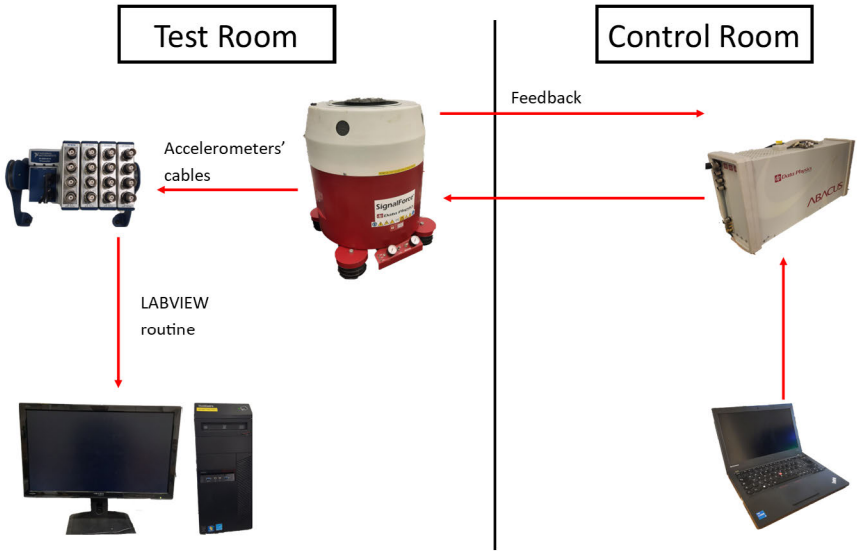

Figure E.6: Testing setup (retrieved from [8]).

The wing is excited with a random verification at different input amplitudes. The amplitudes are considered normal to the wing's inclination and are, from now on, always referred as Low, Medium, and High. They, relatively, correspond to 0.649, 0.919, and 1.590 RMS (Root mean square) ms^{-2}. To ensure the highest precision and repeatability, the tests are repeated 5 times for each input scenario at each α_{gvt} totalling 45 cases. The nine input and α_{gvt} cases are summarised in Table E.4.

Table E.4: Test cases for the XB-2 wing considering input amplitude and α_{gvt}.

Case	Input	α_{gvt} [°]
1	Low	0
2	Medium	0
3	High	0
4	Low	5
5	Medium	5
6	High	5
7	Low	10
8	Medium	10
9	High	10

For all scenarios the random input signal is bandwidth limited between 2 and 100 Hz and lasts 20 min and was down-sampled to 256 Hz from the original sampling frequency (f_s) of 5120 Hz. Then, the Frequency Response Functions

(FRFs) are generated by taking the Fast Fourier Transform of all time histories, relative to channel #1-8 and dividing them by the input, channel # 0. Prior to identification, the FRFs are smoothed with the MATLAB built-in function `smoothdata` by setting the moving average window length to 60.

E.3 Results and Discussion

In this section the results of the 45 independent cases are presented. First, a single case is deeply investigated in detail then the remaining cases are presented focusing in the relationship between α_{gvt}, input amplitude and modal parameters. In Figure E.7, the FRFs for Case 1 are shown. All channels are superimposed for conciseness, showing the peaks of the first three vertical dominant modes. While only three modes are detected, within this work they are going to be referred as first, second, and fourth because it was found in a previous testing campaign [8] that a horizontal dominant mode can be found around 14 Hz.

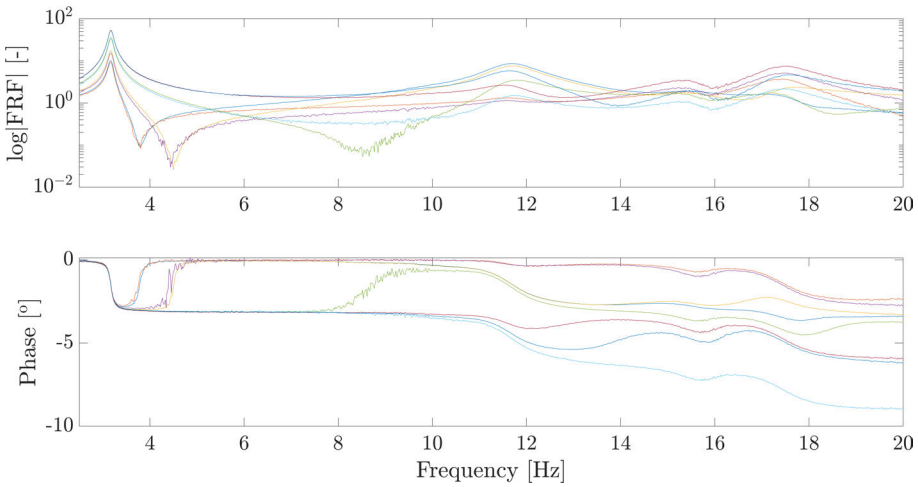

Figure E.7: Case 1: FRFs relative to channels #1-8 of of a single realisation of the low input 0° α_{gvt} case. All channels superimposed for conciseness.

The modal parameters are extracted via LF using a stabilisation diagram for the 45 instances and then the results of the five instances within the same case are averaged to obtain the modal parameters. Figure E.8 shows the stabilisation

diagram of the first instance for Case 1 and clearly shows the first three vertical dominant modes by superimposing the stable modes, between LF's order 6 and 200, to the FRFs relative to channels # 2, 4, 6, and 8. The modes are regarded as stable when the difference in ω_n (Δf) is within 1%, that of ζ_n is 10% and Modal Assurance Criterion (MAC) [26] value over 0.95 within the preceding ten.

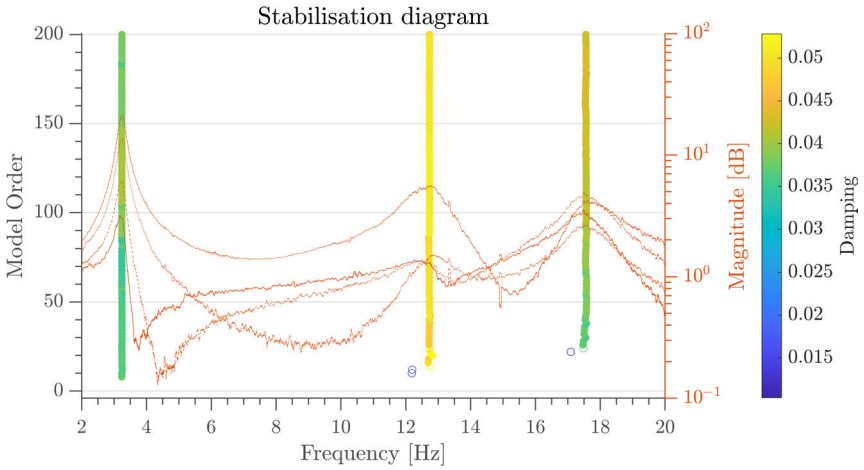

Figure E.8: Case 1, first instance: stabilisation diagram computed with the following parameters: $\Delta f = 1\%$, $\Delta\zeta = 10\%$ and $\Delta\text{MAC} = 0.95$.

In Table E.5 the identified modal parameters, ω_n and ζ_n, of Cases 1, 2, and 3 are presented. As these cases refer to the same α_{gvt}, the decrease in ω_n over the increase in input amplitude shows that the wing, contrary to usual expectations for a beam-like structure, features a softening behaviour. On the other hand, ζ_n remains roughly constant for all inputs, only ζ_4 is considerably larger for Case 3.

Table E.5: Cases 1, 2, and 3: average value, over five instances, of natural frequency and damping ratio parameters.

Case	***1***		***2***		***3***	
Mode	ω_n	ζ_n	ω_n	ζ_n	ω_n	ζ_n
1st Bending	3.21	0.035	3.20	0.023	3.17	0.018
2nd Coupled	12.50	0.053	11.92	0.053	11.76	0.055
4th Coupled	17.36	0.045	17.15	0.045	17.05	0.057

For the same Cases taken under consideration in Table E.5, Figure E.9 shows $\boldsymbol{\phi}_{1,2,4}$, which are superimposed to the baseline shape for a clearer visualisation.

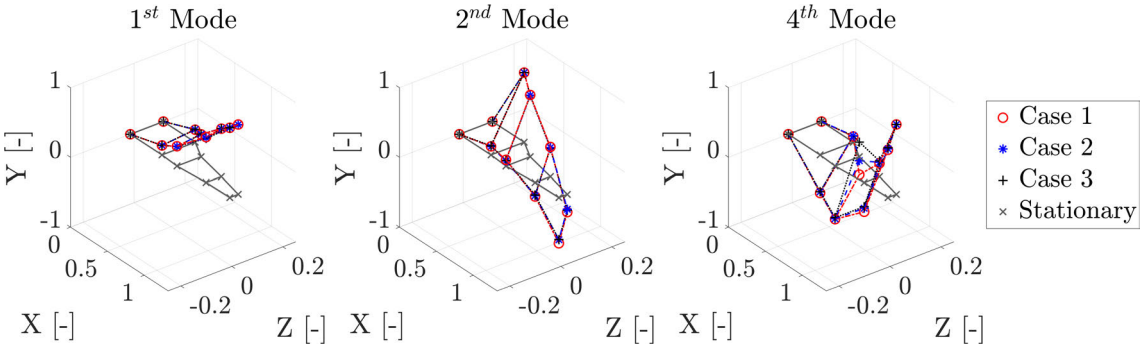

Figure E.9: Case 1, 2, and 3: mode shapes of the first three vertically dominant modes.

The result for first three cases, which take into consideration a $\alpha_{\text{gvt}} = 0^{\text{o}}$ and the three input levels, show that the structure's modal response is influenced by the input amplitude. In particular, the behaviour detected for this particular wing is softening, which means that as the input amplitude increases the ω_n decrease. This kind of behaviour is easily detectable [16] with the band-limited random verification of this series of test. As it is usually the case for lightly nonlinear structure, the ζ_n and $\boldsymbol{\phi}_n$ are not massively influenced by the input amplitude. Nevertheless, the only difference concerning $\boldsymbol{\phi}_n$ is found in the fourth mode, where the displacement linked to channel #3L fluctuates.

Given the dependency of the modal response to input amplitude, the results for the nine cases under scrutiny are presented in a way that takes into consideration the different amplitudes. In Figure E.10, first, Figure E.10a, compares the ω_n for the low input amplitude, then, Figure E.10b, those for the medium input and, finally, Figure E.10c reports on the ω_n for the high input amplitude. The boxplots used reports the results for all 45 instances. In fact, for each case the median value is represented by a red line, the bottom and top blue edges of the box indicate the 25th and 75th percentiles and the whiskers the largest and smallest data points not considered outliers, while the red plus symbol indicates the outlier values. These give a statistical significance to the results and gives an indication of their trustworthiness. The boxplots are also accompanied by a regression line,

in black, to highlight the ω_n trend in relation to α_{gvt}. For all the cases compared, exception made for the first mode at $\alpha_{\text{gvt}} = 5^{\text{o}}$ and high input amplitude, the ω_n decrease as α_{gvt} increases. While the results only consider structural effects, they follow the same trend of aero-structural theory [27]. In fact, an increase in natural frequencies is expected when flight speed increases. In the same way, when the setting angle is changed g_{gvt} is always smaller than g, as per Equation E.1, and hence a smaller a deflection and ω_n are obtained.

The results for ζ_n are presented in the same way as per ω_n in Figure E.11. Generally, damping ratios can be said to decrease over α_{gvt}, just as it is for ω_n. However, for a single instance, the second mode of the medium input scenario at $\alpha_{\text{gvt}} = 5^{\text{o}}$, this is not the case. Also, damping seems to be less influenced, without a clear trend, by the input amplitude. With the same consideration on gravity-induced deflection, the results are consistent from what is expected from theory [27] and experimental surveys [28] for a full wing.

Lastly, the $\boldsymbol{\phi}_n$ are compared. Since a visual comparison of the all $\boldsymbol{\phi}_n$ for all cases is not efficient nor concise. Hence, the MAC value, relative to Case 1, is computed for the modes of all scenario. Only the diagonal terms of the MAC matrices are reported in Table E.6, as the off-diagonal values are negligible. Since, the minimum value is found to be 0.85, it can be said that a good correlation exists between all respective ϕ_n [12]. Notably, the third mode's correlation slightly diminishes for all cases. In fact this is true for Cases 1-3 as well. By inspection of Figure E.9, it is trivial to detect a discrepancy at the channel #3L's position. This happens for the remaining cases as well and more notably for the highest input amplitude. However, all the respective modes are sufficiently correlated and no major variation is evident in their trajectories when compared.

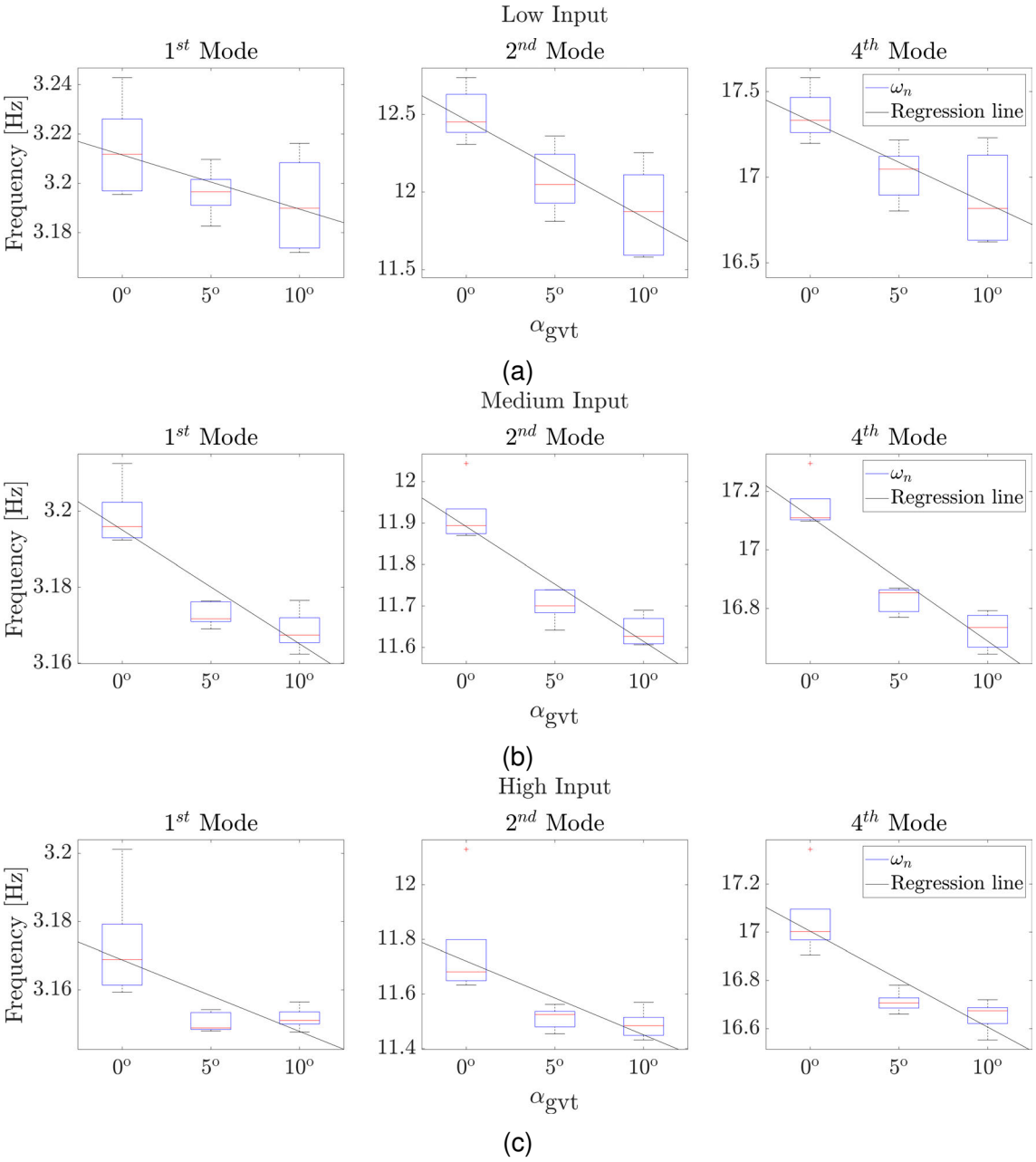

Figure E.10: Investigation on the effect of α_{gvt} on the natural frequencies. Figure E.10a refers to the low input scenario, Figure E.10b to the medium input and Figure E.10c to the high input.

E.4 Conclusions and Future Works

In this work, a high aspect ratio flexible wing undergoes ground vibration testing at three different inclination angles and input amplitudes on a revolving clamp to asses the relationship between the setting angle and its modal properties. A total

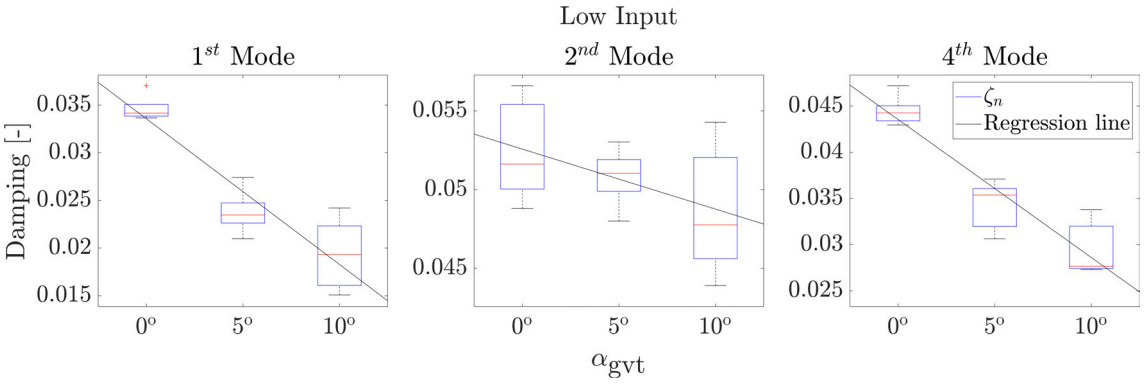

(a)

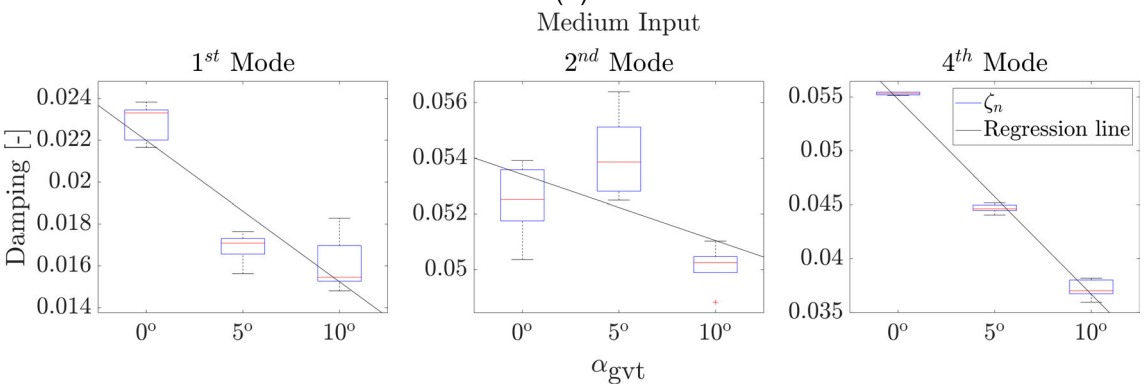

(b)

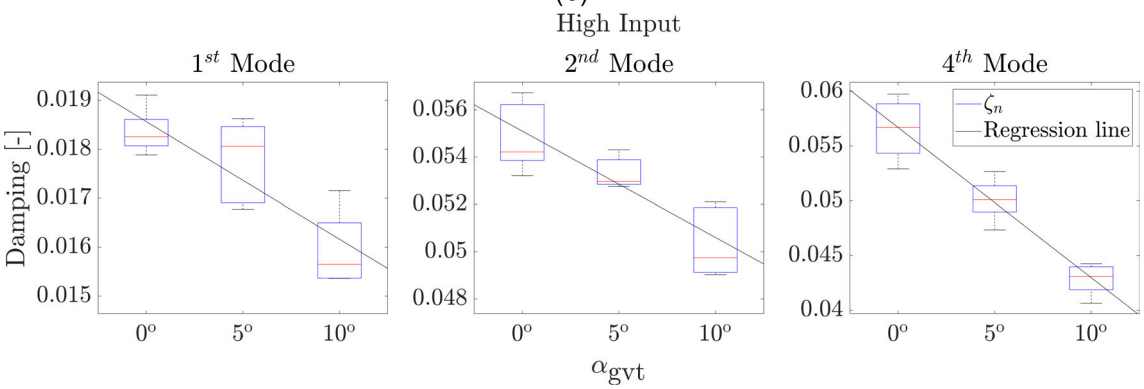

(c)

Figure E.11: Investigation on the effect of α_{gvt} on the damping ratios. Figure E.11a refers to the low input scenario, Figure E.11b to the medium input and Figure E.11c to the high input.

of 45 test is run, which includes 5 instances for each setting angle and amplitude scenario. The modal parameters are extracted with the Loewner Framework, a technique recently introduced for mechanical systems by some of the authors, via stabilisation diagrams up to order $k = 200$. The five instances available for each case give a statistical significance to the results and ensure the meeting of

Table E.6: Diagonal value of the MAC matrices between the computed mode shapes of Case 1 and all other cases.

	MAC Value [-]						
	Mode				Mode		
Case	1st	2nd	4th	**Case**	1st	2nd	4th
2	1	1	0.98	6	1	1	0.85
3	1	1	0.91	7	1	1	0.99
4	1	1	1	8	1	1	.99
5	1	1	1	9	1	1	.91

repeatability requirements.

From the results, a clear relationship between the setting angle and modal parameters, particularly natural frequencies and damping ratios emerges. This has a direct link to the wing's stationary deflection, linked to gravity, whose effect decreases inversely to the setting angle. Both natural frequencies and damping ratios are found to decrease as the setting angle increases indicating that a greater stationary deflection is proportional to an increase in those quantities. Also, it was found that the wing shows a softening behaviour: the natural frequencies decrease as the input amplitude increases. Moreover, it is shown that the mode shapes are pretty much unchanged when the setting angle is changed, but, particularly the fourth mode, it is influenced by input amplitude, . These relationships can be used to build a wing's finite element model to study its aeroelastic properties and also to assess the feasibility of this testing procedure to, or in part, substitute, when paired with computational fluid dynamics techniques, wind tunnel testing for flutter and divergence onset speeds characterisation.

References

[1] A. Pontillo *et al.*, "Flexible high aspect ratio wing: low cost experimental model and computational framework," in *2018 AIAA Atmospheric Flight Mechanics Conference*, Kissimmee, FL: American Institute of Aeronau-

tics and Astronautics, 2018, pp. 1–15, ISBN: 978-1-62410-525-8, DOI: 10.2514/6.2018-1014 (cit. on pp. 288, 290, 292).

[2] S. Y. Yusuf, D. Hayes, A. Pontillo, M. A. Carrizales, G. X. Dussart, and M. M. Lone, "Aeroelastic Scaling for Flexible High Aspect Ratio Wings," in *AIAA Scitech 2019 Forum*, Reston, Virginia: American Institute of Aeronautics and Astronautics, 2019, pp. 1–14, ISBN: 978-1-62410-578-4, DOI: 10.2514/6.2019-1594 (cit. on pp. 288, 291, 292).

[3] D. Hayes, A. Pontillo, S. Y. Yusuf, M. M. Lone, and J. Whidborne, "High aspect ratio wing design using the minimum energy destruction principle," in *AIAA Scitech 2019 Forum*, Kissimmee, FL: American Institute of Aeronautics and Astronautics, 2019, ISBN: 978-1-62410-578-4, DOI: 10.2514/6.2019-1592 (cit. on pp. 288, 292).

[4] A. Pontillo, "High Aspect Ratio Wings on Commercial Aircraft: a Numerical and Experimental approach," PhD Thesis, Cranfield University, 2020 (cit. on pp. 288, 290, 292).

[5] S. Malik, S. Ricci, and L. Riccobene, "Aeroelastic analysis of a slender wing," *CEAS Aeronautical Journal*, vol. 11, no. 4, pp. 917–927, 2020, ISSN: 1869-5582, DOI: 10.1007/s13272-020-00459-6 (cit. on p. 289).

[6] T. E. Noll *et al.*, "Technical findings , lessons learned , and recommendations resulting from the helios prototype vehicle mishap," in *UAV Design Processes / Design Criteria for Structures. Meeting Proceedings RTO-MP-AVT-145, Paper 3.4*, Neuilly-sur-Seine, France: RTO, 2007, pp. 3.4–1 – 3.4–18 (cit. on p. 289).

[7] C. R. Pickrel, "Airplane ground vibration testing - Nominal modal model correlation," *Sound and Vibration*, vol. 36, no. 11, pp. 18–25, 2002, ISSN: 00381810 (cit. on p. 289).

[8] G. Dessena, D. I. Ignatyev, J. F. Whidborne, A. Pontillo, and L. Zanotti Fragonara, "Ground vibration testing of a flexible wing: a benchmark and case study," *Aerospace*, vol. 9, no. 8, p. 438, 2022, ISSN: 2226-4310, DOI: 10.3390/aerospace9080438 (cit. on pp. 289, 291, 292, 295–297).

[9] S. Weber *et al.*, "Application of fibre optic sensing systems to measure rotor blade structural dynamics," *Mechanical Systems and Signal Processing*, vol. 158, p. 107 758, 2021, ISSN: 08883270, DOI: 10.1016/j.ymssp.2021.107758 (cit. on p. 289).

[10] B. Sharqi and C. E. Cesnik, "Finite Element Model Updating for Very Flexible Wings," in *AIAA SCITECH 2022 Forum*, San Diego, CA: American Institute of Aeronautics and Astronautics, 2022, pp. 1–23, ISBN: 978-1-62410-631-6, DOI: 10.2514/6.2022-1185 (cit. on p. 289).

[11] G. Dessena, D. I. Ignatyev, J. F. Whidborne, and L. Zanotti Fragonara, "A Kriging Approach to Model Updating for Damage Detection," in *EWSHM 2022*, P. Rizzo and A. Milazzo, Eds., LNCE 254, Singapore: Springer, 2023, ch. 26, pp. 245–255, DOI: 10.1007/978-3-031-07258-1_26 (cit. on p. 289).

[12] D. J. Ewins, *Modal Testing Theory, Practice and Application*, 2nd. Baldock, UK: Research Studies Press, 2000, p. 562, ISBN: 978-0-863-80218-4 (cit. on pp. 289, 300).

[13] C. R. Pickrel, "A practical approach to modal pretest design," *Mechanical Systems and Signal Processing*, vol. 13, no. 2, pp. 271–295, 1999, ISSN: 08883270, DOI: 10.1006/mssp.1998.1212 (cit. on p. 289).

[14] M. Civera, S. Grivet-Talocia, C. Surace, and L. Zanotti Fragonara, "A generalised power-law formulation for the modelling of damping and stiffness nonlinearities," *Mechanical Systems and Signal Processing*, vol. 153, p. 107 531,

2021, ISSN: 10961216, DOI: 10.1016/j.ymssp.2020.107531 (cit. on p. 289).

[15] M. Civera, L. Zanotti Fragonara, and C. Surace, "Using video processing for the full-field identification of backbone curves in case of large vibrations," *Sensors*, vol. 19, no. 10, p. 2345, 2019, ISSN: 1424-8220, DOI: 10.3390/s19102345 (cit. on p. 289).

[16] K. Worden and G. R. Tomlinson, *Nonlinearity in Structural Dynamics Detection, Identification and Modelling*. Bristol, UK: Institute of Physics Publishing, 2001, ISBN: 0750303565 (cit. on pp. 289, 299).

[17] L. Ljung, *System Identification: Theory for the User*, First. Englewood Cliffs, NJ: P T R Prentice Hall, 1987 (cit. on p. 289).

[18] G. Dessena, M. Civera, L. Zanotti Fragonara, D. I. Ignatyev, and J. F. Whidborne, "A Loewner-based system identification and structural health monitoring approach for mechanical systems," *Structural Control and Health Monitoring [Accepted]*, p. 17, 2023 (cit. on p. 289).

[19] G. Dessena, M. Civera, D. I. Ignatyev, J. F. Whidborne, and L. Zanotti Fragonara, "On the accuracy and computational efficiency of the Loewner Framework for mechanical systems," *in preparation*, 2023 (cit. on p. 289).

[20] G. Dessena, M. Civera, A. Pontillo, D. I. Ignatyev, J. F. Whidborne, and L. Zanotti Fragonara, "Comparative Study on Novel Modal Parameters Extraction Methods for Aeronautical Structures," *in preparation*, 2023 (cit. on pp. 289, 292).

[21] Stratasys, *Digital ABS plus*, 2021, [Online]. Available: https://www.stratasys.com/it/materials/search/digital-abs-plus (visited on 2021) (cit. on p. 291).

[22] Stratasys, *Agilus 30*, 2021, [Online]. Available: https://www.stratasys.com/materials/search/agilus30 (cit. on p. 291).

[23] N. P. Macdonald, J. M. Cabot, P. Smejkal, R. M. Guijt, B. Paull, and M. C. Breadmore, "Comparing Microfluidic Performance of Three-Dimensional (3D) Printing Platforms," *Analytical Chemistry*, vol. 89, no. 7, pp. 3858–3866, 2017, ISSN: 15206882, DOI: 10.1021/acs.analchem.7b00136 (cit. on p. 291).

[24] A. J. Keane, A. Sóbester, and J. P. Scanlan, *Small Unmanned Fixed-wing Aircraft Design*. Chichester, UK: John Wiley & Sons, 2017, ISBN: 9781119406303, DOI: 10.1002/9781119406303 (cit. on p. 291).

[25] A. Schulze, J. Zierath, S.-E. Rosenow, R. Bockhahn, R. Rachholz, and C. Woernle, "Optimal sensor placement for modal testing on wind turbines," *Journal of Physics: Conference Series*, vol. 753, no. 7, p. 072 031, 2016, ISSN: 1742-6588, DOI: 10.1088/1742-6596/753/7/072031 (cit. on p. 295).

[26] R. J. Allemang and D. L. Brown, "A correlation coefficient for modal vector analysis," in *Proceedings of the 1st International Modal Analysis Conference*, Orlando: Union Coll, 1982, pp. 110–116 (cit. on p. 298).

[27] J. R. Wright and J. E. Cooper, *Introduction to Aircraft Aeroelasticity and Loads*. Chichester, UK: John Wiley & Sons, 2014, ISBN: 9781118700440, DOI: 10.1002/9781118700440 (cit. on p. 300).

[28] I. Tsatsas, A. Pontillo, and M. Lone, "Aeroelastic damping estimation for a flexible high-aspect-ratio wing," *Journal of Aerospace Engineering*, vol. 35, no. 2, pp. 1–27, 2022, ISSN: 0893-1321, DOI: 10.1061/(ASCE)AS.1943-5525.0001390 (cit. on p. 300).

Global Bibliography

R. M. Ajaj, M. S. Parancheerivilakkathil, M. Amoozgar, M. I. Friswell, and W. J. Cantwell, "Recent developments in the aeroelasticity of morphing aircraft," *Progress in Aerospace Sciences*, vol. 120, no. February, p. 100 682, 2021, ISSN: 03760421, DOI: 10.1016/j.paerosci.2020.100682 (cit. on p. 103).

N. F. Alkayem, M. Cao, Y. Zhang, M. Bayat, and Z. Su, "Structural damage detection using finite element model updating with evolutionary algorithms: a survey," *Neural Computing and Applications*, vol. 30, no. 2, pp. 389–411, 2018, ISSN: 0941-0643, DOI: 10.1007/s00521-017-3284-1 (cit. on pp. 18, 175, 177, 219, 274).

R. J. Allemang and D. L. Brown, "A correlation coefficient for modal vector analysis," in *Proceedings of the 1st International Modal Analysis Conference*, Orlando: Union Coll, 1982, pp. 110–116 (cit. on pp. 28, 111, 149, 220, 223, 298).

B. Anderson and A. Antoulas, "Rational interpolation and state-variable realizations," *Linear Algebra and its Applications*, vol. 137-138, no. C, pp. 479–509, 1990, ISSN: 00243795, DOI: 10.1016/0024-3795(90)90140-8 (cit. on p. 21).

A. C. Antoulas, "A tutorial introduction to the Loewner framework for model reduction," in *9th Elgersburg Workshop Mathematische Systemtheorie*, 2014 (cit. on p. 21).

A. C. Antoulas, S. Lefteriu, and A. C. Ionita, "A Tutorial Introduction to the Loewner Framework for Model Reduction," in *Model Reduction and Approximation*, Philadel-

phia, PA: Society for Industrial and Applied Mathematics, 2017, ch. 8, pp. 335–376, DOI: 10.1137/1.9781611974829.ch8 (cit. on pp. 20, 21, 26, 100).

M. Baruch, "Optimization procedure to correct stiffness and flexibility matrices using vibration tests," *AIAA Journal*, vol. 16, no. 11, pp. 1208–1210, 1978, ISSN: 0001-1452, DOI: 10.2514/3.61032 (cit. on p. 175).

R. L. Bisplinghoff, H. Ashley, and R. L. Halfman, *Aeroelasticity*. 1996, p. 860, ISBN: 9780486691893 (cit. on p. 105).

R. D. Blevins, "Formulas for Dynamics, Acoustics and Vibration," *Formulas for Dynamics, Acoustics and Vibration*, pp. 1–448, 2015, DOI: 10.1002/9781119038122 (cit. on p. 68).

G. Boscato, S. Russo, R. Ceravolo, and L. Z. Fragonara, "Global sensitivity-based model updating for heritage structures," *Computer-Aided Civil and Infrastructure Engineering*, vol. 30, no. 8, pp. 620–635, 2015, ISSN: 14678667, DOI: 10.1111/mice.12138 (cit. on p. 176).

A. Bovsunovsky and C. Surace, "Non-linearities in the vibrations of elastic structures with a closing crack: A state of the art review," *Mechanical Systems and Signal Processing*, vol. 62-63, pp. 129–148, 2015, ISSN: 08883270, DOI: 10.1016/j.ymssp.2015.01.021 (cit. on pp. 39, 194).

G. E. P. Box and K. B. Wilson, "On the Experimental Attainment of Optimum Conditions," *Journal of the Royal Statistical Society. Series B (Methodological)*, vol. 13, no. 1, pp. 1–45, 1951, ISSN: 00359246, [Online]. Available: http://www.jstor.org/stable/2983966 (cit. on p. 178).

M. Bras, S. Warwick, and A. Suleman, "Aeroelastic evaluation of a flexible high aspect ratio wing UAV: Numerical simulation and experimental flight validation," *Aerospace Science and Technology*, vol. 122, p. 107 400, 2022, ISSN: 12709638, DOI: 10.1016/j.ast.2022.107400 (cit. on p. 102).

D. L. Brown, R. J. Allemang, R. Zimmerman, and M. Mergeay, "Parameter estimation techniques for modal analysis," in *1979 Automotive Engineering Congress and Exposition*, Univ.of Cincinnati, 1979, p. 19, DOI: 10.4271/790221 (cit. on pp. 18, 62, 278).

A. Cancelli, S. Laflamme, A. Alipour, S. Sritharan, and F. Ubertini, "Vibration-based damage localization and quantification in a pretensioned concrete girder using stochastic subspace identification and particle swarm model updating," *Structural Health Monitoring*, vol. 19, no. 2, pp. 587–605, 2020, ISSN: 1475-9217, DOI: 10.1177/1475921718820015 (cit. on pp. 18, 101).

F. Cao and Y. Ge, "Air-induced nonlinear damping and added mass of vertically vibrating bridge deck section models under zero wind speed," *Journal of Wind Engineering and Industrial Aerodynamics*, vol. 169, no. June, pp. 217–231, 2017, ISSN: 01676105, DOI: 10.1016/j.jweia.2017.07.022 (cit. on pp. 144, 152, 153).

R. Cardoso, A. Cury, and F. Barbosa, "A robust methodology for modal parameters estimation applied to SHM," *Mechanical Systems and Signal Processing*, vol. 95, pp. 24–41, 2017, ISSN: 08883270, DOI: 10.1016/j.ymssp.2017.03.021 (cit. on p. 18).

P. Cawley, "Structural health monitoring: Closing the gap between research and industrial deployment," *Structural Health Monitoring*, vol. 17, no. 5, pp. 1225–1244, 2018, ISSN: 1475-9217, DOI: 10.1177/1475921717750047 (cit. on pp. 102, 175, 273).

J. Cecrdle, "Updating of aircraft structure dynamic model to ground vibration test results," in *29th Congress of the International Council of the Aeronautical Sciences*, St. Petersburg, Russia, 2014, pp. 1–7, ISBN: 3-932182-80-4 (cit. on p. 220).

J. Cecrdle, “Updating of jet trainer aircraft dynamic model to results of ground vibration test,” in *33rd Congress of the International Council of the Aeronautical Sciences*, Stockholm, Sweden, 2022, pp. 1–9 (cit. on p. 220).

M. T. A. Chaudhary and Y. Fujino, “System identification of bridges using recorded seismic data and its application in structural health monitoring,” *Structural Control and Health Monitoring*, vol. 15, no. 7, pp. 1021–1035, 2008, ISSN: 15452255, DOI: 10.1002/stc.249 (cit. on p. 15).

C. Chiodi, G. Coppotelli, and J. V. Covioli, “Identification of the static and dynamic numerical model of a jet aircraft wing from experimental tests,” *AIAA Scitech 2021 Forum*, no. January, pp. 1–21, 2021, DOI: 10.2514/6.2021-1498 (cit. on p. 220).

A. K. Chopra, *Dynamics of Structures: Theory and Applications to Earthquake Engineering*, 4th Editio. Upper Saddle River, NJ: Prentice Hall, 2011, p. 992 (cit. on p. 196).

M. Civera, G. Calamai, and L. Zanotti Fragonara, “Experimental modal analysis of structural systems by using the fast relaxed vector fitting method,” *Structural Control and Health Monitoring*, vol. 28, no. 4, pp. 1–23, 2021, ISSN: 1545-2255, DOI: 10.1002/stc.2695 (cit. on pp. 15, 20, 40, 42, 44, 98, 108, 193, 220).

M. Civera, G. Calamai, and L. Zanotti Fragonara, “System identification via Fast Relaxed Vector Fitting for the Structural Health Monitoring of masonry bridges,” *Structures*, vol. 30, no. January, pp. 277–293, 2021, ISSN: 23520124, DOI: 10.1016/j.istruc.2020.12.073 (cit. on pp. 15, 19, 20, 84, 95, 98, 102, 175, 273).

M. Civera, L. Z. Fragonara, and C. Surace, “A Computer Vision-Based Approach for Non-contact Modal Analysis and Finite Element Model Updating,” in *EW-*

SHM 2020, LNCE 127, vol. 127, 2021, pp. 481–493, ISBN: 9783030645939, DOI: 10.1007/978-3-030-64594-6_47 (cit. on p. 220).

M. Civera, S. Grivet-Talocia, C. Surace, and L. Zanotti Fragonara, "A generalised power-law formulation for the modelling of damping and stiffness nonlinearities," *Mechanical Systems and Signal Processing*, vol. 153, p. 107 531, 2021, ISSN: 10961216, DOI: 10.1016/j.ymssp.2020.107531 (cit. on pp. 62, 126, 142–144, 150, 152, 289).

M. Civera, V. Mugnaini, and L. Zanotti Fragonara, "Machine learning-based automatic operational modal analysis: A structural health monitoring application to masonry arch bridges," *Structural Control and Health Monitoring*, no. May, pp. 1–23, 2022, ISSN: 1545-2255, DOI: 10.1002/stc.3028 (cit. on pp. 15, 39, 60, 94).

M. Civera and C. Surace, "A Comparative Analysis of Signal Decomposition Techniques for Structural Health Monitoring on an Experimental Benchmark," *Sensors*, vol. 21, no. 5, p. 1825, 2021, ISSN: 1424-8220, DOI: 10.3390/s21051825 (cit. on p. 39).

M. Civera, L. Zanotti Fragonara, and C. Surace, "Using video processing for the full-field identification of backbone curves in case of large vibrations," *Sensors*, vol. 19, no. 10, p. 2345, 2019, ISSN: 1424-8220, DOI: 10.3390/s19102345 (cit. on pp. 1, 39, 59, 142, 143, 150, 151, 153, 289).

L. Colo, G. Broux, and E. Garrigues, "A new flutter prediction algorithm to avoid P-K method shortcomings," in *International Forum on Aeroelasticity and Structural Dynamics 2019, IFASD 2019*, Savannah, Georgia, 2019, pp. 1–19 (cit. on p. 106).

G. Coppotelli, F. D. Giandomenico, C. Groth, S. Porziani, A. Chiappa, and M. E. Biancolini, "On the structural updating using operational responses of a realis-

tic wing model: The ribes test article," in *8th IOMAC - International Operational Modal Analysis Conference, Proceedings*, 2019 (cit. on p. 220).

A. Da Ronch, K. Badcock, Y. Wang, A. Wynn, and R. Palacios, "Nonlinear Model Reduction for Flexible Aircraft Control Design," in *AIAA Atmospheric Flight Mechanics Conference*, Minneapolis, Minnesota: American Institute of Aeronautics and Astronautics, 2012, pp. 1–23, ISBN: 978-1-62410-184-7, DOI: 10.2514/6.2012-4404 (cit. on p. 142).

F. De Florio, *Airworthiness*. Elsevier, 2011, ISBN: 9780080968025, DOI: 10.1016/C2010-0-65567-2 (cit. on pp. 60, 101, 219).

K. Deb, A. Pratap, S. Agarwal, and T. Meyarivan, "A fast and elitist multiobjective genetic algorithm: NSGA-II," *IEEE Transactions on Evolutionary Computation*, vol. 6, no. 2, pp. 182–197, 2002, ISSN: 1089778X, DOI: 10.1109/4235.996017 (cit. on pp. 182, 222, 276).

D. Deschrijver, M. Mrozowski, T. Dhaene, and D. De Zutter, "Macromodeling of Multiport Systems Using a Fast Implementation of the Vector Fitting Method," *IEEE Microwave and Wireless Components Letters*, vol. 18, no. 6, pp. 383–385, 2008, ISSN: 1531-1309, DOI: 10.1109/LMWC.2008.922585 (cit. on p. 97).

G. Dessena, *A tutorial on the Loewner-based system identification and structural health monitoring approach for mechanical systems.* Cranfield, 2022, DOI: 10.17862/cranfield.rd.16636279 (cit. on pp. 26, 100, 148, 220).

G. Dessena, *A tutorial on the refined Efficient Global Optimisation*, Cranfield, UK, 2022, DOI: 10.17862/cranfield.rd.21163750 (cit. on p. 223).

G. Dessena, *Data supporting: Ground Vibration Testing of a Flexible Wing: A Benchmark and Case Study*, 2022, DOI: 10.17862/cranfield.rd.19077023 (cit. on p. 71).

G. Dessena, M. Civera, D. I. Ignatyev, J. F. Whidborne, and L. Zanotti Fragonara, "On the accuracy and computational efficiency of the Loewner Framework for mechanical systems," *in preparation*, 2023 (cit. on pp. 100, 122, 148, 195, 289).

G. Dessena, M. Civera, A. Pontillo, D. I. Ignatyev, J. F. Whidborne, and L. Zanotti Fragonara, "Comparative Study on Novel Modal Parameters Extraction Methods for Aeronautical Structures," *in preparation*, 2023 (cit. on pp. 61, 146, 148, 195, 226, 231, 289, 292).

G. Dessena, M. Civera, L. Zanotti Fragonara, D. I. Ignatyev, and J. F. Whidborne, "A Loewner-based system identification and structural health monitoring approach for mechanical systems," *Structural Control and Health Monitoring [Accepted]*, p. 17, 2023 (cit. on pp. 60, 95, 96, 100, 101, 108, 123, 195, 273, 279, 289).

G. Dessena, D. I. Ignatyev, J. F. Whidborne, A. Pontillo, and L. Zanotti Fragonara, "Ground vibration testing of a flexible wing: a benchmark and case study," *Aerospace*, vol. 9, no. 8, p. 438, 2022, ISSN: 2226-4310, DOI: 10.3390/aerospace9080438 (cit. on pp. 15, 94, 119, 121–123, 144, 146–149, 155, 156, 162, 220, 226, 227, 229, 231, 236, 289, 291, 292, 295–297).

G. Dessena, D. I. Ignatyev, J. F. Whidborne, A. Pontillo, and L. Zanotti Fragonara, "Ground vibration testing of a high aspect ratio wing with revolving clamp," in *33rd Congress of the International Council of the Aeronautical Sciences*, Stockholm, Sweden, 2022, DOI: 10.17862/cranfield.rd.20486229 (cit. on pp. 144, 146, 147, 149, 153, 155, 162, 226, 231).

G. Dessena, D. I. Ignatyev, J. F. Whidborne, and L. Zanotti Fragonara, "A global-local meta-modelling technique for model updating," *[Submitted to] Computer Methods in Applied Mechanics and Engineering*, 2023 (cit. on pp. 94, 219, 222, 223, 233, 276, 277).

G. Dessena, D. I. Ignatyev, J. F. Whidborne, and L. Zanotti Fragonara, "A Kriging Approach to Model Updating for Damage Detection," in *EWSHM 2022*, P. Rizzo and A. Milazzo, Eds., LNCE 254, Singapore: Springer, 2023, ch. 26, pp. 245–255, DOI: 10.1007/978-3-031-07258-1_26 (cit. on pp. 18, 60, 182, 219, 223, 233, 289).

G. Dessena, A. Pontillo, D. I. Ignatyev, J. F. Whidborne, and L. Zanotti Fragonara, "Identification of Nonlinearity Sources in a Flexible Wing: a Case Study," *in preparation*, 2023 (cit. on p. 231).

F. Dezi, F. Gara, and D. Roia, "Dynamic Characterization of Open-ended Pipe Piles in Marine Environment," in *Applied Studies of Coastal and Marine Environments*, InTech, 2016, pp. 169–204, DOI: 10.5772/62055 (cit. on pp. 17, 62, 95, 148, 231).

M. Donà, A. Palmeri, M. Lombardo, and A. Cicirello, "An efficient two-node finite element formulation of multi-damaged beams including shear deformation and rotatory inertia," *Computers and Structures*, vol. 147, pp. 96–106, 2015, ISSN: 00457949, DOI: 10.1016/j.compstruc.2014.10.002 (cit. on p. 101).

T. Dossogne *et al.*, "Nonlinear ground vibration identification of an F-16 aircraft - Part II: Understanding nonlinear behaviour in aerospace structures using sine-sweep testing," *International Forum on Aeroelasticity and Structural Dynamics, IFASD 2015*, pp. 1–19, 2015 (cit. on p. 61).

D. J. Ewins, *Modal Testing Theory, Practice and Application*, 2nd. Baldock, UK: Research Studies Press, 2000, p. 562, ISBN: 978-0-863-80218-4 (cit. on pp. 28, 61, 94, 111, 233, 289, 300).

C. R. Farrar, S. W. Doebling, and D. A. Nix, "Vibration–based structural damage identification," *Philosophical Transactions of the Royal Society of London. Series A: Mathematical, Physical and Engineering Sciences*, vol. 359, no. 1778,

N. A. J. Lieven and D. J. Ewins, Eds., pp. 131–149, 2001, ISSN: 1364-503X, DOI: 10.1098/rsta.2000.0717 (cit. on pp. 15, 18, 101, 175, 273).

C. R. Farrar and K. Worden, "An introduction to structural health monitoring," *Philosophical Transactions of the Royal Society A: Mathematical, Physical and Engineering Sciences*, vol. 365, no. 1851, pp. 303–315, 2007, ISSN: 1364503X, DOI: 10.1098/rsta.2006.1928 (cit. on p. 18).

W. Favoreel, B. De Moor, and P. Van Overschee, "Subspace state space system identification for industrial processes," *Journal of Process Control*, vol. 10, no. 2-3, pp. 149–155, 2000, ISSN: 09591524, DOI: 10.1016/S0959-1524(99)00030-X (cit. on p. 17).

C. Fei, H. Liu, S. Li, H. Li, L. An, and C. Lu, "Dynamic parametric modeling-based model updating strategy of aeroengine casings," *Chinese Journal of Aeronautics*, vol. 34, no. 12, pp. 145–157, 2021, ISSN: 10009361, DOI: 10.1016/j.cja.2020.10.036 (cit. on p. 219).

E. Figueiredo, G. Park, C. R. Farrar, K. Worden, and J. Figueiras, "Machine learning algorithms for damage detection under operational and environmental variability," *Structural Health Monitoring*, vol. 10, no. 6, pp. 559–572, 2011, ISSN: 1475-9217, DOI: 10.1177/1475921710388971 (cit. on pp. 39, 41).

E. Figueiredo, G. Park, J. Figueiras, C. Farrar, and K. Worden, "Structural health monitoring algorithm comparisons using standard data sets," Los Alamos National Laboratory (LANL), Los Alamos, NM (United States), Tech. Rep., 2009, DOI: 10.2172/961604 (cit. on pp. 39–42, 44, 174, 193, 195–199).

A. I. J. Forrester, A. Sóbester, and A. J. Keane, *Engineering Design via Surrogate Modelling*. Wiley, 2008, ISBN: 9780470060681, DOI: 10.1002/9780470770801 (cit. on pp. 178, 180, 181, 185, 221, 223, 275, 276, 278).

A. I. Forrester, A. Sóbester, and A. J. Keane, "Multi-fidelity optimization via surrogate modelling," *Proceedings of the Royal Society A: Mathematical, Physical*

and Engineering Sciences, vol. 463, no. 2088, pp. 3251–3269, 2007, ISSN: 14712946, DOI: 10.1098/rspa.2007.1900 (cit. on pp. 179, 221–223).

M. I. Friswell and J. E. Mottershead, *Finite Element Model Updating in Structural Dynamics* (Solid Mechanics and its Applications). Dordrecht: Springer Netherlands, 1995, vol. 38, ISBN: 978-90-481-4535-5, DOI: 10.1007/978-94-015-8508-8 (cit. on pp. 177, 219, 274).

Y. Gao and B. F. Spencer, "Damage localization under ambient vibration using changes in flexibility," *Earthquake Engineering and Engineering Vibration*, vol. 1, no. 1, pp. 136–144, 2002, ISSN: 1671-3664, DOI: 10.1007/s11803-002-0017-x (cit. on p. 190).

L. Gelman, I. Petrunin, C. Parrish, and M. Walters, "Novel health monitoring technology for in-service diagnostics of intake separation in aircraft engines," *Structural Control and Health Monitoring*, vol. 27, no. 5, pp. 1–14, 2020, ISSN: 15452263, DOI: 10.1002/stc.2479 (cit. on p. 18).

M. Girardi, C. Padovani, D. Pellegrini, M. Porcelli, and L. Robol, "Finite element model updating for structural applications," *Journal of Computational and Applied Mathematics*, vol. 370, p. 112 675, 2020, ISSN: 03770427, DOI: 10.1016/j.cam.2019.112675, arXiv: 1801.09122 (cit. on p. 174).

D. Göge, "Automatic updating of large aircraft models using experimental data from ground vibration testing," *Aerospace Science and Technology*, vol. 7, no. 1, pp. 33–45, 2003, ISSN: 12709638, DOI: 10.1016/S1270-9638(02)01184-7 (cit. on p. 60).

D. E. Goldberg, *Genetic Algorithms in Search, Optimization and Machine Learning*. Boston, MA: Addison-Wesley Longman, 1989, p. 372, ISBN: 978-0-201-15767-3 (cit. on p. 177).

I. V. Gosea and A. C. Antoulas, "Model reduction of linear and nonlinear systems in the Loewner framework: A summary," in *2015 European Control Conference*

(ECC), IEEE, 2015, pp. 345–349, ISBN: 978-3-9524-2693-7, DOI: 10.1109/ECC.2015.7330568 (cit. on p. 99).

S. Grivet-Talocia and B. Gustavsen, *Passive Macromodeling: Theory and Applications*. Wiley, 2016, p. 869 (cit. on pp. 98, 99).

B. Gustavsen, "Relaxed Vector Fitting Algorithm for Rational Approximation of Frequency Domain Responses," in *2006 IEEE Workship on Signal Propagation on Interconnects*, IEEE, 2006, pp. 97–100, ISBN: 1-4244-0454-1, DOI: 10.1109/SPI.2006.289202 (cit. on pp. 20, 98).

B. Gustavsen and A. Semlyen, "Rational approximation of frequency domain responses by vector fitting," *IEEE Transactions on Power Delivery*, vol. 14, no. 3, pp. 1052–1061, 1999, ISSN: 08858977, DOI: 10.1109/61.772353 (cit. on pp. 20, 97).

G. Haller and S. Ponsioen, "Nonlinear normal modes and spectral submanifolds: existence, uniqueness and use in model reduction," *Nonlinear Dynamics*, vol. 86, no. 3, pp. 1493–1534, 2016, ISSN: 0924-090X, DOI: 10.1007/s11071-016-2974-z (cit. on p. 143).

G. J. Hancock, J. R. Wright, and A. Simpson, "On the teaching of the principles of wing flexure-torsion flutter," *Aeronautical Journal*, pp. 285–305, 89 1985, DOI: 10.1017/S0001924000015050 (cit. on p. 103).

D. Hayes, A. Pontillo, S. Y. Yusuf, M. M. Lone, and J. Whidborne, "High aspect ratio wing design using the minimum energy destruction principle," in *AIAA Scitech 2019 Forum*, Kissimmee, FL: American Institute of Aeronautics and Astronautics, 2019, ISBN: 978-1-62410-578-4, DOI: 10.2514/6.2019-1592 (cit. on pp. 1, 59, 63, 119, 145, 224, 226, 288, 292).

F. Hemez and S. W. Doebling, "Review and assessment of model updating for non-linear, transient dynamics," *Mechanical Systems and Signal Processing*,

vol. 15, no. 1, pp. 45–74, 2001, ISSN: 08883270, DOI: 10.1006/mssp.2000.1351 (cit. on p. 101).

X. Hu, "Effects of stinger axial dynamics and mass compensation methods on experimental modal analysis," PhD Thesis, Iowa State University, Digital Repository, Ames, 1992, DOI: 10.31274/rtd-180813-9382 (cit. on pp. 69, 81).

N. E. Huang and N. O. Attoh-Okine, *The Hilbert-Huang Transform in Engineering*, 1st Editio, N. E. Huang and N. O. Attoh-Okine, Eds. Boca Raton, FL: CRC Press, 2005, p. 328, ISBN: 9780429114311, DOI: 10.1201/9781420027532 (cit. on p. 152).

N. E. Huang *et al.*, "The empirical mode decomposition and the Hilbert spectrum for nonlinear and non-stationary time series analysis," *Proceedings of the Royal Society of London. Series A: Mathematical, Physical and Engineering Sciences*, vol. 454, no. 1971, pp. 903–995, 1998, ISSN: 1364-5021, DOI: 10.1098/rspa.1998.0193 (cit. on p. 152).

A. C. Ionita, *System identification*, 2013, [Online]. Available: http://aci.rice.edu/system-identification/ (visited on 2021) (cit. on p. 26).

A. C. Ionita and A. C. Antoulas, "Case Study: Parametrized Reduction Using Reduced-Basis and the Loewner Framework," in *Reduced Order Methods for Modeling and Computational Reduction*, A. Quarteroni and G. Rozza, Eds., Cham: Springer International Publishing, 2014, ch. 2, pp. 51–66, DOI: 10.1007/978-3-319-02090-7_2 (cit. on p. 16).

M. Jamil and X. S. Yang, "A literature survey of benchmark functions for global optimisation problems," *International Journal of Mathematical Modelling and Numerical Optimisation*, vol. 4, no. 2, p. 150, 2013, ISSN: 2040-3607, DOI: 10.1504/IJMMNO.2013.055204 (cit. on p. 185).

D. R. Jones, M. Schonlau, and W. J. Welch, "Efficient global optimization of expensive black-box functions," *Journal of Global Optimization*, vol. 13, pp. 455–

492, 1998, DOI: 10.1023/A:1008306431147 (cit. on pp. 173, 177, 178, 180, 181, 183, 184, 221–223, 275–277).

R. Kamakoti and W. Shyy, "Fluid-structure interaction for aeroelastic applications," *Progress in Aerospace Sciences*, vol. 40, no. 8, pp. 535–558, 2004, ISSN: 03760421, DOI: 10.1016/j.paerosci.2005.01.001 (cit. on p. 103).

D. S. Karachalios, I. V. Gosea, and A. C. Antoulas, "The Loewner framework for nonlinear identification and reduction of Hammerstein cascaded dynamical systems," *PAMM*, vol. 20, no. 1, pp. 2020–2022, 2021, ISSN: 1617-7061, DOI: 10.1002/pamm.202000337 (cit. on p. 20).

A. Keane and J. Scanlan, "Design search and optimization in aerospace engineering," *Philosophical Transactions of the Royal Society A: Mathematical, Physical and Engineering Sciences*, vol. 365, no. 1859, pp. 2501–2529, 2007, ISSN: 1364-503X, DOI: 10.1098/rsta.2007.2019 (cit. on pp. 177, 221).

A. J. Keane, A. Sóbester, and J. P. Scanlan, *Small Unmanned Fixed-wing Aircraft Design*. Chichester, UK: John Wiley & Sons, 2017, ISBN: 9781119406303, DOI: 10.1002/9781119406303 (cit. on pp. 60, 64, 94, 95, 120, 126, 129, 146, 226, 291).

G. Kerschen, M. Peeters, J. C. Golinval, and C. Stéphan, "Nonlinear modal analysis of a full-scale aircraft," *Journal of Aircraft*, vol. 50, no. 5, pp. 1409–1419, 2013, ISSN: 0021-8669, DOI: 10.2514/1.C031918 (cit. on p. 62).

G. Kerschen, L. Soula, J. B. Vergniaud, and A. Newerla, "Assessment of Nonlinear System Identification Methods using the SmallSat Spacecraft Structure," in *Conference Proceedings of the Society for Experimental Mechanics Series*, vol. 1, 2011, pp. 203–219, ISBN: 9781441993014, DOI: 10.1007/978-1-4419-9302-1_18 (cit. on p. 61).

G. Kerschen, K. Worden, A. F. Vakakis, and J.-C. Golinval, "Past, present and future of nonlinear system identification in structural dynamics," *Mechanical*

Systems and Signal Processing, vol. 20, no. 3, pp. 505–592, 2006, ISSN: 08883270, DOI: 10.1016/j.ymssp.2005.04.008 (cit. on pp. 61, 142).

B. Kramer and S. Gugercin, "Tangential interpolation-based eigensystem realization algorithm for MIMO systems," *Mathematical and Computer Modelling of Dynamical Systems*, vol. 22, no. 4, pp. 282–306, 2016, ISSN: 1387-3954, DOI: 10.1080/13873954.2016.1198389 (cit. on pp. 21, 100).

D. G. Krige, "A statistical approach to some basic mine valuation problems on the Witwatersrand," *Journal of the Chemical, Metallurgical and Mining Society of South Africa*, vol. 52, no. 6, pp. 119–139, 1951 (cit. on pp. 173, 177, 178, 275).

S. Lefteriu and A. C. Antoulas, "Modeling multi-port systems from frequency response data via tangential interpolation," in *2009 IEEE Workshop on Signal Propagation on Interconnects*, IEEE, 2009, pp. 1–4, ISBN: 978-1-4244-4490-8, DOI: 10.1109/SPI.2009.5089847 (cit. on pp. 15, 16, 19, 20, 26, 100).

S. Lefteriu and A. C. Antoulas, "A new approach to modeling multiport systems from frequency-fomain data," *IEEE Transactions on Computer-Aided Design of Integrated Circuits and Systems*, vol. 29, no. 1, pp. 14–27, 2010, ISSN: 0278-0070, DOI: 10.1109/TCAD.2009.2034500 (cit. on pp. 15, 16, 19, 24, 26, 100).

K. J. Lemler and W. H. Semke, "Application of modal testing and analysis techniques on a sUAV," in *Conference Proceedings of the Society for Experimental Mechanics Series*, vol. 6, 2013, pp. 47–57, ISBN: 9781461465454, DOI: 10.1007/978-1-4614-6546-1_5 (cit. on p. 60).

L. Ljung, *System Identification: Theory for the User*, First. Englewood Cliffs, NJ: P T R Prentice Hall, 1987 (cit. on pp. 96, 289).

L. Ljung, T. Chen, and B. Mu, "A shift in paradigm for system identification," *International Journal of Control*, vol. 93, no. 2, pp. 173–180, 2020, ISSN: 13665820, DOI: 10.1080/00207179.2019.1578407 (cit. on p. 94).

J. M. Londoño, J. E. Cooper, and S. A. Neild, "Identification of systems containing nonlinear stiffnesses using backbone curves," *Mechanical Systems and Signal Processing*, vol. 84, pp. 116–135, 2017, ISSN: 10961216, DOI: 10.1016/j.ymssp.2016.02.008 (cit. on p. 142).

K. Löwner, "Über monotone matrixfunktionen," *Mathematische Zeitschrift*, vol. 38, no. 1, pp. 177–216, 1934, ISSN: 0025-5874, DOI: 10.1007/BF01170633 (cit. on pp. 20, 100).

P. Lubrina, S. Giclais, C. Stephan, M. Boeswald, Y. Govers, and N. Botargues, "AIRBUS A350 XWB GVT: State-of-the-Art Techniques to Perform a Faster and Better GVT Campaign," in *Topics in Modal Analysis II, Volume 8. Conference Proceedings of the Society for Experimental Mechanics Series*, R. Allemang, Ed., vol. 45, Orlando, FL.: Springer, Cham, 2014, pp. 243–256, DOI: 10.1007/978-3-319-04774-4_24 (cit. on pp. 60, 95).

A. Lye, A. Cicirello, and E. Patelli, "Sampling methods for solving Bayesian model updating problems: A tutorial," *Mechanical Systems and Signal Processing*, vol. 159, p. 107 760, 2021, ISSN: 08883270, DOI: 10.1016/j.ymssp.2021.107760 (cit. on pp. 179, 275).

N. P. Macdonald, J. M. Cabot, P. Smejkal, R. M. Guijt, B. Paull, and M. C. Breadmore, "Comparing Microfluidic Performance of Three-Dimensional (3D) Printing Platforms," *Analytical Chemistry*, vol. 89, no. 7, pp. 3858–3866, 2017, ISSN: 15206882, DOI: 10.1021/acs.analchem.7b00136 (cit. on pp. 145, 226, 291).

N. M. M. Maia, "Extraction of valid modal properties from measured data in structural vibrations," PhD Thesis, Imperial College London, 1988, p. 380 (cit. on pp. 18, 62, 96).

S. Malik, S. Ricci, and L. Riccobene, "Aeroelastic analysis of a slender wing," *CEAS Aeronautical Journal*, vol. 11, no. 4, pp. 917–927, 2020, ISSN: 1869-5582, DOI: 10.1007/s13272-020-00459-6 (cit. on pp. 1, 142, 220, 289).

D. Martucci, M. Civera, and C. Surace, "The Extreme Function Theory for Damage Detection: An Application to Civil and Aerospace Structures," *Applied Sciences*, vol. 11, no. 4, p. 1716, 2021, ISSN: 2076-3417, DOI: 10.3390/app11041716 (cit. on p. 39).

T. Marwala, *Finite-element-model Updating Using Computional Intelligence Techniques*. London: Springer London, 2010, ISBN: 978-1-84996-322-0, DOI: 10.1007/978-1-84996-323-7 (cit. on pp. 176–178, 219, 274).

T. Marwala and S. Sibisi, "Finite element model updating using bayesian framework and modal properties," *Journal of Aircraft*, vol. 42, no. 1, pp. 275–278, 2005, ISSN: 0021-8669, DOI: 10.2514/1.11841 (cit. on p. 176).

F. Mastroddi, L. M. Travaglini, and S. Gemma, "Multi-objective Optimization for the Design of an Unconventional Sun-Powered High-Altitude-Long-Endurance Unmanned Vehicle," *Aerotecnica Missili & Spazio*, vol. 97, no. 2, pp. 68–84, 2018, ISSN: 0365-7442, DOI: 10.1007/BF03405802 (cit. on p. 142).

A. Mayo and A. Antoulas, "A framework for the solution of the generalized realization problem," *Linear Algebra and its Applications*, vol. 425, no. 2-3, pp. 634–662, 2007, ISSN: 00243795, DOI: 10.1016/j.laa.2007.03.008 (cit. on pp. 21, 23, 26, 100).

M. D. McKay, R. J. Beckman, and W. J. Conover, "A comparison of three methods for selecting values of input variables in the analysis of output from a computer code," *Technometrics*, vol. 21, no. 2, p. 239, 1979, ISSN: 00401706, DOI: 10.2307/1268522 (cit. on pp. 179, 275).

J. Meinguet, *On the solubility of the Cauchy interpolation problem* (Institut de Mathématique Pure et Appliquée Louvain: Rapport). Univ. Cathol., 1969 (cit. on p. 21).

M. Mihaila-Andres, P.-V. Rosu, C. Larco, M. Demsa, L. Constantin, and R. Pahonie, "Preliminary design of aeroelastically tailored wing box structures with

bend-twist coupling," *ITM Web of Conferences*, vol. 24, N. Bardis, Ed., p. 02 010, 2019, ISSN: 2271-2097, DOI: 10.1051/itmconf/20192402010 (cit. on p. 220).

P. Milillo, G. Giardina, D. Perissin, G. Milillo, A. Coletta, and C. Terranova, "Pre-Collapse Space Geodetic Observations of Critical Infrastructure: The Morandi Bridge, Genoa, Italy," *Remote Sensing*, vol. 11, no. 12, p. 1403, 2019, ISSN: 2072-4292, DOI: 10.3390/rs11121403 (cit. on p. 101).

V. V. Moca, H. Bârzan, A. Nagy-Dăbâcan, and R. C. Mureșan, "Time-frequency super-resolution with superlets," *Nature Communications*, vol. 12, no. 1, pp. 1–18, 2021, ISSN: 20411723, DOI: 10.1038/s41467-020-20539-9 (cit. on p. 151).

H. Moravej, S. Jamali, T. H. Chan, and A. Nguyen, "Finite element model updating of civil engineering infrastructures: A literature review," in *SHMII 2017 - 8th International Conference on Structural Health Monitoring of Intelligient Infrastructure, Proceedings*, 2017, pp. 1139–1150, ISBN: 9781925553055 (cit. on p. 174).

M. D. Morris and T. J. Mitchell, "Exploratory designs for computational experiments," *Journal of Statistical Planning and Inference*, vol. 43, no. 3, pp. 381–402, 1995, ISSN: 03783758, DOI: 10.1016/0378-3758(94)00035-T (cit. on pp. 179, 275).

J. Mottershead and M. Friswell, "Model updating in structural dynamics: A survey," *Journal of Sound and Vibration*, vol. 167, no. 2, pp. 347–375, 1993, ISSN: 0022460X, DOI: 10.1006/jsvi.1993.1340 (cit. on pp. 174, 177, 219, 274).

V. Mugnaini, L. Zanotti Fragonara, and M. Civera, "A machine learning approach for automatic operational modal analysis," *Mechanical Systems and Signal Processing*, vol. 170, no. February, p. 108 813, 2022, ISSN: 08883270, DOI: 10.1016/j.ymssp.2022.108813 (cit. on pp. 61, 94, 220).

F. Naeim and J. M. Kelly, *Design of Seismic Isolated Structures*. Hoboken, NJ, USA: John Wiley & Sons, Inc., 1999, p. 304, ISBN: 9780470172742, DOI: 10.1002/9780470172742 (cit. on pp. 105, 195).

A. H. Nayfeh and D. T. Mook, *Nonlinear Oscillations*. Wiley, 1995, ISBN: 9780471121428, DOI: 10.1002/9783527617586 (cit. on p. 144).

E. Neu, F. Janser, A. A. Khatibi, C. Braun, and A. C. Orifici, "Operational Modal Analysis of a wing excited by transonic flow," *Aerospace Science and Technology*, vol. 49, pp. 73–79, 2016, ISSN: 12709638, DOI: 10.1016/j.ast.2015.11.032 (cit. on p. 94).

P. Ni, J. Li, H. Hao, Q. Han, and X. Du, "Probabilistic model updating via variational Bayesian inference and adaptive Gaussian process modeling," *Computer Methods in Applied Mechanics and Engineering*, vol. 383, p. 113 915, 2021, ISSN: 00457825, DOI: 10.1016/j.cma.2021.113915 (cit. on p. 174).

H. B. Nielsen, S. N. Lophaven, and J. Søndergaard, "DACE - A MATLAB Kriging Toolbox," Informatics and Mathematical Modelling, Technical University of Denmark, DTU, Tech. Rep., 2002, [Online]. Available: https://orbit.dtu.dk/en/publications/dace-a-matlab-kriging-toolbox (cit. on p. 184).

J. P. Nöel, L. Renson, G. Kerschen, B. Peeters, S. Manzato, and J. Debille, "Nonlinear dynamic analysis of an F-16 aircraft using GVT data," in *IFASD 2013 - International Forum on Aeroelasticity and Structural Dynamics*, 2013, pp. 1–13 (cit. on pp. 2, 60, 62).

J. Noël and G. Kerschen, "Nonlinear system identification in structural dynamics: 10 more years of progress," *Mechanical Systems and Signal Processing*, vol. 83, pp. 2–35, 2017, ISSN: 08883270, DOI: 10.1016/j.ymssp.2016.07.020 (cit. on pp. 61, 142).

T. E. Noll *et al.*, "Technical findings , lessons learned , and recommendations resulting from the helios prototype vehicle mishap," in *UAV Design Processes /*

Design Criteria for Structures. Meeting Proceedings RTO-MP-AVT-145, Paper 3.4, Neuilly-sur-Seine, France: RTO, 2007, pp. 3.4–1 – 3.4–18 (cit. on p. 289).

Noviello, Dimino, Concilio, Amoroso, and Pecora, "Aeroelastic Assessments and Functional Hazard Analysis of a Regional Aircraft Equipped with Morphing Winglets," *Aerospace*, vol. 6, no. 10, p. 104, 2019, ISSN: 2226-4310, DOI: 10.3390/aerospace6100104 (cit. on p. 61).

A. Pagani, R. Azzara, E. Carrera, and E. Zappino, "Static and dynamic testing of a full-composite VLA by using digital image correlation and output-only ground vibration testing," *Aerospace Science and Technology*, vol. 112, p. 106 632, 2021, ISSN: 12709638, DOI: 10.1016/j.ast.2021.106632 (cit. on p. 94).

A. Pagani and E. Carrera, "Unified formulation of geometrically nonlinear refined beam theories," *Mechanics of Advanced Materials and Structures*, vol. 25, no. 1, pp. 15–31, 2018, ISSN: 15376532, DOI: 10.1080/15376494.2016.1232458 (cit. on pp. 83, 144, 156, 162).

R. Pecora, F. Amoroso, R. Palumbo, M. Arena, G. Amendola, and I. Dimino, "Preliminary aeroelastic assessment of a large aeroplane equipped with a camber-morphing aileron," in *Industrial and Commercial Applications of Smart Structures Technologies 2017*, D. J. Clingman, Ed., vol. 10166, 2017, 101660E, ISBN: 9781510608177, DOI: 10.1117/12.2260008 (cit. on p. 61).

M. Peeters, G. Kerschen, and J. C. Golinval, "Modal testing of nonlinear vibrating structures based on nonlinear normal modes: Experimental demonstration," *Mechanical Systems and Signal Processing*, vol. 25, no. 4, pp. 1227–1247, 2011, ISSN: 08883270, DOI: 10.1016/j.ymssp.2010.11.006 (cit. on p. 143).

M. Peeters, G. Kerschen, and J. Golinval, "Dynamic testing of nonlinear vibrating structures using nonlinear normal modes," *Journal of Sound and Vibration*, vol. 330, no. 3, pp. 486–509, 2011, ISSN: 0022460X, DOI: 10.1016/j.jsv.2010.08.028 (cit. on pp. 143, 150, 162).

R. Perera and R. Torres, "Structural damage detection via modal data with genetic algorithms," *Journal of Structural Engineering*, vol. 132, no. 9, pp. 1491–1501, 2006, ISSN: 0733-9445, DOI: 10.1061/(ASCE)0733-9445(2006)132:9(1491) (cit. on pp. 177, 190, 223, 273).

V. Picheny, T. Wagner, and D. Ginsbourger, "A benchmark of kriging-based infill criteria for noisy optimization," *Structural and Multidisciplinary Optimization*, vol. 48, no. 3, pp. 607–626, 2013, ISSN: 16151488, DOI: 10.1007/s00158-013-0919-4 (cit. on p. 185).

C. R. Pickrel, "A practical approach to modal pretest design," *Mechanical Systems and Signal Processing*, vol. 13, no. 2, pp. 271–295, 1999, ISSN: 08883270, DOI: 10.1006/mssp.1998.1212 (cit. on p. 289).

C. R. Pickrel, "Airplane ground vibration testing - Nominal modal model correlation," *Sound and Vibration*, vol. 36, no. 11, pp. 18–25, 2002, ISSN: 00381810 (cit. on p. 289).

R. Pintelon and J. Schoukens, *System Identification : A Frequency Domain Approach*, 2nd. Hoboken, NJ: John Wiley, 2012 (cit. on p. 96).

A. Pontillo, "High Aspect Ratio Wings on Commercial Aircraft: a Numerical and Experimental approach," PhD Thesis, Cranfield University, 2020 (cit. on pp. 1, 59, 63, 119, 145, 146, 224, 226, 288, 290, 292).

A. Pontillo *et al.*, "Flexible high aspect ratio wing: low cost experimental model and computational framework," in *2018 AIAA Atmospheric Flight Mechanics Conference*, Kissimmee, FL: American Institute of Aeronautics and Astronautics, 2018, pp. 1–15, ISBN: 978-1-62410-525-8, DOI: 10.2514/6.2018-1014 (cit. on pp. 1, 59, 63, 119, 145, 224, 226, 288, 290, 292).

J. Qian, Y. Cheng, J. Zhang, J. Liu, and D. Zhan, "A parallel constrained efficient global optimization algorithm for expensive constrained optimization

problems," *Engineering Optimization*, vol. 53, no. 2, pp. 300–320, 2021, ISSN: 10290273, DOI: 10.1080/0305215X.2020.1722118 (cit. on p. 184).

S. J. Qin, "An overview of subspace identification," *Computers & Chemical Engineering*, vol. 30, no. 10-12, pp. 1502–1513, 2006, ISSN: 00981354, DOI: 10.1016/j.compchemeng.2006.05.045 (cit. on p. 17).

D. Quero, P. Vuillemin, and C. Poussot-Vassal, "A generalized state-space aeroservoelastic model based on tangential interpolation," *Aerospace*, vol. 6, no. 1, p. 9, 2019, ISSN: 2226-4310, DOI: 10.3390/aerospace6010009 (cit. on pp. 19, 22, 94).

L. Rastrigin, *Systems of External Control*. Moscow: Mir, 1974 (cit. on p. 185).

W.-X. Ren and H.-B. Chen, "Finite element model updating in structural dynamics by using the response surface method," *Engineering Structures*, vol. 32, no. 8, pp. 2455–2465, 2010, ISSN: 01410296, DOI: 10.1016/j.engstruct.2010.04.019 (cit. on pp. 174, 177, 178, 274, 275).

E. Reynders, R. Pintelon, and G. De Roeck, "Uncertainty bounds on modal parameters obtained from stochastic subspace identification," *Mechanical Systems and Signal Processing*, vol. 22, no. 4, pp. 948–969, 2008, ISSN: 08883270, DOI: 10.1016/j.ymssp.2007.10.009 (cit. on p. 19).

M. Richardson and B. Schwarz, "Modal parameter estimation from operating data," *Sound and Vibration Magazine*, 2003, ISSN: 15410161 (cit. on p. 15).

M. H. Richardson and D. L. Formenti, "Global curve fitting of frequency response measurements using the rational fraction polynomial method.," *Proceedings of the International Modal Analysis Conference & Exhibit*, vol. 1, pp. 390–397, 1985 (cit. on p. 20).

P. Rizzo and A. Enshaeian, "Challenges in bridge health monitoring: a review," *Sensors*, vol. 21, no. 13, p. 4336, 2021, ISSN: 1424-8220, DOI: 10.3390/s21134336 (cit. on pp. 18, 60).

R. Rocchetta, M. Broggi, Q. Huchet, and E. Patelli, "On-line Bayesian model updating for structural health monitoring," *Mechanical Systems and Signal Processing*, vol. 103, pp. 174–195, 2018, ISSN: 10961216, DOI: 10.1016/j.ymssp.2017.10.015 (cit. on p. 177).

R. M. Rosenberg, "The Normal Modes of Nonlinear n-Degree-of-Freedom Systems," *Journal of Applied Mechanics*, vol. 29, no. 1, pp. 7–14, 1962, ISSN: 0021-8936, DOI: 10.1115/1.3636501 (cit. on p. 143).

R. G. J. Ross, "Synthesis of stiffness and mass matrices from experimental vibration modes," *SAE Transactions*, vol. 80, no. 4, pp. 2627–2635, 1971, [Online]. Available: https://www.jstor.org/stable/44650348 (cit. on p. 175).

R. Roy, M. Gherlone, and C. Surace, "A shape sensing methodology for beams with generic cross-sections: Application to airfoil beams," *Aerospace Science and Technology*, vol. 110, p. 106 484, 2021, ISSN: 12709638, DOI: 10.1016/j.ast.2020.106484 (cit. on p. 101).

A. Rytter, "Vibrational based inspection of civil engineering structures," Ph.D. dissertation, Aalborg University, 1993 (cit. on pp. 15, 18, 99, 101, 102, 108, 115, 116, 175, 273).

C. Schneider and W. Werner, "Some new aspects of rational interpolation," *Mathematics of Computation*, vol. 47, no. 175, p. 285, 1986, ISSN: 00255718, DOI: 10.2307/2008095 (cit. on p. 21).

A. Schulze, J. Zierath, S.-E. Rosenow, R. Bockhahn, R. Rachholz, and C. Woernle, "Optimal sensor placement for modal testing on wind turbines," *Journal of Physics: Conference Series*, vol. 753, no. 7, p. 072 031, 2016, ISSN: 1742-6588, DOI: 10.1088/1742-6596/753/7/072031 (cit. on pp. 70, 147, 230, 295).

F. Shadan, F. Khoshnoudian, and A. Esfandiari, "A frequency response-based structural damage identification using model updating method," *Structural Con-*

trol and Health Monitoring, vol. 23, no. 2, pp. 286–302, 2016, ISSN: 15452255, DOI: 10.1002/stc.1768 (cit. on p. 273).

B. Sharqi and C. E. Cesnik, "Finite Element Model Updating for Very Flexible Wings," in *AIAA SCITECH 2022 Forum*, San Diego, CA: American Institute of Aeronautics and Astronautics, 2022, pp. 1–23, ISBN: 978-1-62410-631-6, DOI: 10.2514/6.2022-1185 (cit. on p. 289).

S. Shaw and C. Pierre, "Non-linear normal modes and invariant manifolds," *Journal of Sound and Vibration*, vol. 150, no. 1, pp. 170–173, 1991, ISSN: 0022460X, DOI: 10.1016/0022-460X(91)90412-D (cit. on p. 143).

J. Sidhu and D. J. Ewins, "Correlation of finite element and modal test studies of a practical structure," in *Proceedings of the 2nd IMAC*, Orlando, FL, 1984, pp. 756–762 (cit. on p. 175).

B. R. Smith, "The quadratically damped oscillator: A case study of a non-linear equation of motion," *American Journal of Physics*, vol. 80, no. 9, pp. 816–824, 2012, ISSN: 0002-9505, DOI: 10.1119/1.4729440 (cit. on p. 144).

A. Sóbester and A. I. J. Forrester, *Aircraft Aerodynamic Design: Geometry and Optimization*. Wiley, 2014, p. 264 (cit. on p. 181).

A. Sóbester, A. I. Forrester, D. J. Toal, E. Tresidder, and S. Tucker, "Engineering design applications of surrogate-assisted optimization techniques," *Optimization and Engineering*, vol. 15, no. 1, pp. 243–265, 2014, ISSN: 15732924, DOI: 10.1007/s11081-012-9199-x (cit. on pp. 178, 181).

H. Sohn, C. R. Farrar, D. D. Shunk, D. W. Stinemates, B. R. Nadler, and J. Czarnecki, "A Review of Structural Health Monitoring Literature: 1996–2001," Los Alamos National Laboratory (LANL), Los Alamos, CA, Tech. Rep., 2004 (cit. on pp. 18, 102, 175).

M. Song, L. Renson, B. Moaveni, and G. Kerschen, "Bayesian model updating and class selection of a wing-engine structure with nonlinear connections using nonlinear normal modes," *Mechanical Systems and Signal Processing*, vol. 165, no. December 2020, p. 108 337, 2022, ISSN: 10961216, DOI: 10.1016/j.ymssp.2021.108337 (cit. on p. 143).

F. R. Spitznogle, J. M. Barrett, C. I. Black, T. W. Ellis, and W. L. LaFuze, "Representation and analysis of sonar signals. Volume I. Improvements in the Complex Exponential signal analysis computational algorithm.," Office of Naval Research- Contract No. NOOO14-69-C0315,1971, Tech. Rep., 1971, p. 47 (cit. on pp. 18, 60, 62, 148, 231).

F. R. Spitznogle and A. H. Quazi, "Representation and analysis of time-limited signals using a Complex Exponential algorithm," *The Journal of The Acoustical Society of America*, vol. 47, no. 5 (Part I), pp. 1150–1155, 1970 (cit. on pp. 18, 60, 62, 148, 231).

Stratasys, *Agilus 30*, 2021, [Online]. Available: https://www.stratasys.com/materials/search/agilus30 (cit. on pp. 63, 119, 145, 291).

Stratasys, *Digital ABS plus*, 2021, [Online]. Available: https://www.stratasys.com/it/materials/search/digital-abs-plus (visited on 2021) (cit. on pp. 63, 119, 145, 291).

C. J. Stull, C. J. Earls, and P.-S. Koutsourelakis, "Model-based structural health monitoring of naval ship hulls," *Computer Methods in Applied Mechanics and Engineering*, vol. 200, no. 9-12, pp. 1137–1149, 2011, ISSN: 00457825, DOI: 10.1016/j.cma.2010.11.018 (cit. on p. 175).

W. Su and C. E. Cesnik, "Dynamic response of highly flexible flying wings," *Collection of Technical Papers - AIAA/ASME/ASCE/AHS/ASC Structures, Structural Dynamics and Materials Conference*, vol. 1, no. May, pp. 412–435, 2006, ISSN: 02734508, DOI: 10.2514/6.2006-1636 (cit. on p. 103).

W. Su and C. E. Cesnik, "Nonlinear aeroelasticity of a very flexible blended-wing-body aircraft," *Journal of Aircraft*, vol. 47, no. 5, pp. 1539–1553, 2010, ISSN: 15333868, DOI: 10.2514/1.47317 (cit. on p. 103).

C. Surace, K. Worden, and G. R. Tomlinson, "An improved nonlinear model for an automotive shock absorber," *Nonlinear Dynamics*, vol. 3, no. 6, pp. 413–429, 1992, ISSN: 0924-090X, DOI: 10.1007/BF00045646 (cit. on p. 142).

S. Surjanovic and D. Bingham, *Virtual Library of Simulation Experiments: Test Functions and Dataset*, 2013, [Online]. Available: http://www.sfu.ca/$%5Csim$ssurjano/optimization.html (visited on 2022) (cit. on p. 185).

J. Taghipour, M. Dardel, and M. H. Pashaei, *Nonlinear vibration mitigation of a flexible rotor shaft carrying a longitudinally dispositioned unbalanced rigid disc*. Springer Netherlands, 2021, vol. 104, pp. 2145–2184, ISBN: 0123456789, DOI: 10.1007/s11071-021-06428-w (cit. on p. 158).

A. Teughels and G. De Roeck, "Damage detection and parameter identification by finite element model updating," *Archives of Computational Methods in Engineering*, vol. 12, no. 2, pp. 123–164, 2005, ISSN: 1134-3060, DOI: 10.1007/BF03044517 (cit. on p. 176).

I. Tsatsas, A. Pontillo, and M. Lone, "Aeroelastic damping estimation for a flexible high-aspect-ratio wing," *Journal of Aerospace Engineering*, vol. 35, no. 2, pp. 1–27, 2022, ISSN: 0893-1321, DOI: 10.1061/(ASCE)AS.1943-5525.0001390 (cit. on pp. 61, 62, 146, 163, 300).

N. Tsushima, M. Tamayama, H. Arizono, and K. Makihara, "Geometrically nonlinear aeroelastic characteristics of highly flexible wing fabricated by additive manufacturing," *Aerospace Science and Technology*, vol. 117, p. 106 923, 2021, ISSN: 12709638, DOI: 10.1016/j.ast.2021.106923 (cit. on p. 95).

S. Urasaki and H. Yabuno, "Identification method for backbone curve of cantilever beam using van der Pol-type self-excited oscillation," *Nonlinear Dynamics*,

vol. 103, no. 4, pp. 3429–3442, 2021, ISSN: 0924-090X, DOI: 10.1007/s11071-020-05945-4 (cit. on p. 144).

P. Van Overschee and B. De Moor, "N4SID: Subspace algorithms for the identification of combined deterministic-stochastic systems," *Automatica*, vol. 30, no. 1, pp. 75–93, 1994, ISSN: 00051098, DOI: 10.1016/0005-1098(94)90230-5 (cit. on pp. 17, 95–97).

T. Verhulst, D. Judt, C. Lawson, Y. Chung, O. Al-Tayawe, and G. Ward, "Review for State-of-the-Art Health Monitoring Technologies on Airframe Fuel Pumps," *International Journal of Prognostics and Health Management*, vol. 13, no. 1, pp. 1–20, 2022, ISSN: 2153-2648, DOI: 10.36001/ijphm.2022.v13i1.3134 (cit. on p. 60).

I. Voutchkov and A. Keane, "Multi-Objective Optimization Using Surrogates," in *Computational Intelligence in Optimization*, Y. Tenne and C.-K. Goh, Eds., Berlin: Springer, 2010, ch. 7, pp. 155–175, DOI: 10.1007/978-3-642-12775-5_7 (cit. on pp. 182, 222, 274–276).

C. S. Wang, F. Wu, and F.-K. Chang, "Structural health monitoring from fiber-reinforced composites to steel-reinforced concrete," *Smart Materials and Structures*, vol. 10, no. 3, pp. 548–552, 2001, ISSN: 0964-1726, DOI: 10.1088/0964-1726/10/3/318 (cit. on pp. 101, 273).

J. Wang and C. Wang, "Structural model updating of frequency response function based on Kriging model," in *2016 3rd International Conference on Information Science and Control Engineering (ICISCE)*, IEEE, 2016, pp. 640–644, ISBN: 978-1-5090-2535-0, DOI: 10.1109/ICISCE.2016.142 (cit. on p. 178).

J. Wang, C. Wang, and J. Zhao, "Structural dynamic model updating based on kriging model using frequency response data," *Journal of Vibroengineering*, vol. 18, no. 6, pp. 3484–3498, 2016, ISSN: 13928716, DOI: 10.21595/jve.2016.16973 (cit. on p. 178).

W. Wang, X. Zhang, D. Hu, D. Zhang, and P. Allaire, "A novel none once per revolution blade tip timing based blade vibration parameters identification method," *Chinese Journal of Aeronautics*, vol. 33, no. 7, pp. 1953–1968, 2020, ISSN: 10009361, DOI: 10.1016/j.cja.2020.01.014 (cit. on p. 220).

Y. Wang, A. Wynn, and R. Palacios, "Nonlinear aeroelastic control of very flexible aircraft using model updating," *Journal of Aircraft*, vol. 55, no. 4, pp. 1551–1563, 2018, ISSN: 15333868, DOI: 10.2514/1.C034684 (cit. on p. 220).

Z. Wang, R. Lin, and M. Lim, "Structural damage detection using measured FRF data," *Computer Methods in Applied Mechanics and Engineering*, vol. 147, no. 1-2, pp. 187–197, 1997, ISSN: 00457825, DOI: 10.1016/S0045-7825(97)00013-3 (cit. on p. 176).

S. Weber *et al.*, "Application of fibre optic sensing systems to measure rotor blade structural dynamics," *Mechanical Systems and Signal Processing*, vol. 158, p. 107 758, 2021, ISSN: 08883270, DOI: 10.1016/j.ymssp.2021.107758 (cit. on pp. 60, 95, 289).

Wei Fan and Pizhong Qiao, "Vibration-based damage identification methods: A Review and comparative study," *Structural Health Monitoring*, vol. 10, no. 1, pp. 83–111, 2011, ISSN: 1475-9217, DOI: 10.1177/1475921710365419 (cit. on pp. 18, 101).

D. Whitley, "A genetic algorithm tutorial," *Statistics and Computing*, vol. 4, no. 2, 1994, ISSN: 0960-3174, DOI: 10.1007/BF00175354 (cit. on pp. 182, 222).

K. Worden and G. R. Tomlinson, *Nonlinearity in Structural Dynamics Detection, Identification and Modelling*. Bristol, UK: Institute of Physics Publishing, 2001, ISBN: 0750303565 (cit. on pp. 61, 142, 150, 162, 289, 299).

J. R. Wright and J. E. Cooper, *Introduction to Aircraft Aeroelasticity and Loads*. Chichester, UK: John Wiley & Sons, 2014, ISBN: 9781118700440, DOI: 10.1002/9781118700440 (cit. on pp. 94, 102–106, 127, 300).

J. Xing, Y. Luo, and Z. Gao, "A global optimization strategy based on the Kriging surrogate model and parallel computing," *Structural and Multidisciplinary Optimization*, vol. 62, no. 1, pp. 405–417, 2020, ISSN: 16151488, DOI: 10.1007/s00158-020-02495-6 (cit. on pp. 182, 222).

Y. Xu, D. Cao, C. Shao, and H. Lin, "Effects of the pylon–store system on the nonlinear aeroelastic responses of a slender wing," *Nonlinear Dynamics*, vol. 95, no. 2, pp. 1471–1494, 2019, ISSN: 0924-090X, DOI: 10.1007/s11071-018-4639-6 (cit. on p. 142).

L. Yang, Z. Mao, S. Wu, X. Chen, and R. Yan, "Nonlinear dynamic behavior of rotating blade with breathing crack," *Frontiers of Mechanical Engineering*, vol. 16, no. 1, pp. 196–220, 2021, ISSN: 20950241, DOI: 10.1007/s11465-020-0609-z (cit. on pp. 83, 144, 156, 163).

X. Yang, X. Guo, H. Ouyang, and D. Li, "A Kriging model based finite element model updating method for damage detection," *Applied Sciences*, vol. 7, no. 10, p. 1039, 2017, ISSN: 2076-3417, DOI: 10.3390/app7101039 (cit. on pp. 177–179, 219, 273).

H. Yin, J. Ma, K. Dong, Z. Peng, P. Cui, and C. Yang, "Model updating method based on Kriging model for structural dynamics," *Shock and Vibration*, vol. 2019, pp. 1–12, 2019, ISSN: 1070-9622, DOI: 10.1155/2019/8086024 (cit. on p. 178).

S. Y. Yusuf, "On System Identification and Dynamic Scaling of a Flexible Aircraft," PhD Thesis, Cranfield University, 2019 (cit. on pp. 1, 145, 224, 226).

S. Y. Yusuf, D. Hayes, A. Pontillo, M. A. Carrizales, G. X. Dussart, and M. M. Lone, "Aeroelastic Scaling for Flexible High Aspect Ratio Wings," in *AIAA Scitech 2019 Forum*, Reston, Virginia: American Institute of Aeronautics and Astronautics, 2019, pp. 1–14, ISBN: 978-1-62410-578-4, DOI: 10.2514/6.2019-1594 (cit. on pp. 1, 59, 63, 65, 67, 69, 81, 82, 84, 119, 145, 146, 156, 162, 163, 224, 226, 227, 288, 291, 292).

J. Zacharias, C. Hartmann, and A. Delgado, "Damage detection on crates of beverages by artificial neural networks trained with finite-element data," *Computer Methods in Applied Mechanics and Engineering*, vol. 193, no. 6-8, pp. 561–574, 2004, ISSN: 00457825, DOI: 10.1016/j.cma.2003.10.009 (cit. on p. 175).

L. Zadeh, "On the identification problem," *IRE Transactions on Circuit Theory*, vol. 3, no. 4, pp. 277–281, 1956, ISSN: 0096-2007, DOI: 10.1109/TCT.1956.1086328 (cit. on p. 16).

L. Zanotti Fragonara *et al.*, "Dynamic investigation on the Mirandola bell tower in post-earthquake scenarios," *Bulletin of Earthquake Engineering*, vol. 15, no. 1, pp. 313–337, 2017, ISSN: 1570-761X, DOI: 10.1007/s10518-016-9970-z (cit. on pp. 62, 94, 174).

D. Zhan, *The standard and parallel efficient global optimization (EGO) algorithms*, 2017, [Online]. Available: https://github.com/zhandawei/Single_objective_EGO_algorithms (visited on 2022) (cit. on p. 184).

J. Zhang *et al.*, "Aeroelastic model and analysis of an active camber morphing wing," *Aerospace Science and Technology*, vol. 111, p. 106 534, 2021, ISSN: 12709638, DOI: 10.1016/j.ast.2021.106534 (cit. on p. 127).

W. Zhang, Z. Lv, Q. Diwu, and H. Zhong, "A flutter prediction method with low cost and low risk from test data," *Aerospace Science and Technology*, vol. 86, pp. 542–557, 2019, ISSN: 12709638, DOI: 10.1016/j.ast.2019.01.043 (cit. on p. 60).

W. Zhao, N. Muthirevula, R. K. Kapania, A. Gupta, C. D. Regan, and P. J. Seiler, "A Subcomponent-based Finite Element Model Updating for a Composite Flying-wing Aircraft," in *AIAA Atmospheric Flight Mechanics Conference*, Grapevine, Texas: American Institute of Aeronautics and Astronautics, 2017, ISBN: 978-1-62410-448-0, DOI: 10.2514/6.2017-1393 (cit. on p. 220).

X. Zhi-Qian, P. Jian-Wen, W. Jin-Ting, and C. Fu-Dong, "Improved approach for vibration-based structural health monitoring of arch dams during seismic events and normal operation," *Structural Control and Health Monitoring*, vol. 29, no. 7, pp. 1–19, 2022, ISSN: 1545-2255, DOI: 10.1002/stc.2955 (cit. on p. 15).

X. Zhou and R. Huang, "Efficient nonlinear aeroelastic analysis of a morphing wing via parameterized fictitious mode method," *Nonlinear Dynamics*, vol. 105, no. 1, pp. 1–23, 2021, ISSN: 0924-090X, DOI: 10.1007/s11071-021-06577-y (cit. on p. 142).

D. C. Zimmerman and M. Kaouk, "Eigenstructure assignment approach for structural damage detection," *AIAA Journal*, vol. 30, no. 7, pp. 1848–1855, 1992, ISSN: 0001-1452, DOI: 10.2514/3.11146 (cit. on p. 175).